CONFORMATIONAL CONTROL OF ORGANIC CONJUGATED MOLECULES AND MACROMOLECULES THROUGH DYNAMIC NONCOVALENT BONDS

A Dissertation

by

CONGZHI ZHU

Submitted to the Office of Graduate and Professional Studies of
Texas A&M University
in partial fulfillment of the requirements for the degree of

DOCTOR OF PHILOSOPHY

Chair of Committee,	Lei Fang
Committee Members,	Karen L. Wooley
	François P. Gabbaï
	Jodie L. Lutkenhaus
Head of Department,	Simon W. North

May 2019

Major Subject: Chemistry

ABSTRACT

Torsional conformation of the backbone of a π-conjugated molecule or macromolecule shapes its solubility, optical and electronic characteristics, rheological behaviors, solid-state properties, and ultimately materials performances. This dissertation focuses on the on-demand control over the conformation of π-conjugated molecules and macromolecules using dynamic intramolecular noncovalent bonds, such as hydrogen bonds and B←N coordinate bonds. Those dynamic bonds bridged building units in a π-conjugated system so that desired conformations can be induced and then perturbed in a controlled manner. Through such an active manipulation over molecular conformation, optical band gaps, electrochemical properties, solubilities, and processabilities of organic conjugated materials can be tuned on demand.

This dissertation begins with a brief introduction of the development of organic conjugated molecules and macromolecules involving a variety of bridging noncovalent bonds (Chapter I). Challenges in this specific field are identified and discussed for future breakthroughs in exploiting the promising potential of these dynamic-noncovalent-bond-bridged π-conjugated organic materials.

Chapter II describes an example of conformational control in a conjugated molecule using intramolecular hydrogen bonds to achieve tailored molecular, supramolecular, and solid-state properties. The fully coplanar conformation of such molecules led to short π–π stacking distances, strong yet controllable aggregation in solution phase, and solid-state self-assembly into one-dimensional nano-/microfibers.

Shown in Chapter III, this molecular design is expanded into a macromolecular π-conjugated system. A molecular engineering strategy of chemically inhibiting and regenerating intramolecular hydrogen bonds was developed to resolve the synthetic challenges and processing issues by controlling the backbone conformation.

Chapter IV and V discuss the incorporation of intramolecular B←N coordinate bonds into organic conjugated molecules. In Chapter IV, it is demonstrated that the dynamic nature of such coordination allowed for active manipulation of the optical properties by using competing Lewis basic solvents. Described in Chapter V, two rigid molecular constitutions were designed to accommodate redox-active units and B←N coordination into a compact structure. These molecules demonstrated multiple electron transfer processes and multicolor electrochromism. Comprehensive experimental and computational investigations revealed the underlying mechanism of the redox processes, and the critical role of B←N coordination in rendering such redox properties.

This dissertation is to understand the fundamental correlation between molecular conformation and materials properties of π-conjugated systems by employing dynamic noncovalent bonds. This dissertation discusses synthetic methodologies to incorporate dynamic noncovalent bonds into organic conjugated molecules and macromolecules. The molecular design principles and structure-property relationships between molecular conformation and materials properties were established. The active manipulation of intramolecular noncovalent bonds led to tunable molecular and supramolecular properties and enabled solution processing of rigid coplanar macromolecules.

DEDICATION

Di You

Yifei Zhu

Ling Sun

ACKNOWLEDGEMENTS

First and foremost, I thank my advisor Professor Lei Fang for guiding, encouraging, and supporting me through my entire graduate study. He gave me the intellectual freedom to explore chemistry, and taught me the way to be a professional scholar.

I would also like to thank Professors Karen L. Wooley, François Gabbaï and Jodie L. Lutkenhaus, who served on my committees, for providing important feedback and constructive criticism on my research projects. I am also grateful to all the staff in the Department of Chemistry and Material Characterization Facility at Texas A&M University for their kind support. Particularly, I am most grateful to Dr Nattamai Bhuvanesh. His excellent running of single crystal analysis is essential to my graduate research.

I also thank and acknowledge the past and present group members in the Fang group for being a constant source of encouragement. They are Dr Yang Zou, Dr Zi-Hao Guo, Dr Yen-Hao Lin, Dr Jongbok Lee, Dr Tianyu Yuan, Alex J. Kalin, Xiaozhou Ji, Chenxu Wang, Mariela Vazquez, Sai Che, Anthony U. Mu, Bailey K. Phillips, Che-Hsuan Chang, Yirui Cao, Bo-Ji Peng, and Chenxuan Li. These people always provide generous help and support when I am in need. Thanks also go to undergraduate students and visiting scholars, who worked with me. They are Kayla P. Baker, Jordan Lavoie, Lauren Kuffel and Dr Wei Hu.

I would like to express my gratitude to my collaborators outside the Fang group, including Professor Sarbajit Banerjee, Professor Oleg V. Ozerov, Professor Steven E. Wheeler, Professor Mohammed Al-Hashimi, Professor Xugang Guo, Dr Fei Li, Cheng-Han Yu. Special acknowledgement goes to Dr Yi Liu and his team at Molecular Foundry. Without their collaborative contributions, none of the research in this dissertation would be possible.

I am also grateful for financial assistance and awards from Texas A&M University including a Heep Graduate Fellowship, Eastman Travel Award Scholarship, and Derek and Christine Barton Graduate Endowment Scholar Award.

I am truly grateful to my parents for their eternal and unconditional support. Their love and encouragement is the biggest motivation in my life. Last but not the least, I am incredibly thankful to my wife, Di You. As of this writing, Di and I have been together for more than three years. We have shared many high and low points. Through every single past day, our binding grows stronger. Her love and support is never to be forgotten by me. I am so grateful and honored to be accompanied by her, and looking forward to spending the rest of my life with her.

CONTRIBUTORS AND FUNDING SOURCES

Contributors

This work was supervised by a dissertation committee consisting of Professors Lei Fang (chair of committee), Karen L. Wooley and François Gabbaï of the Department of Chemistry and Professor Jodie L. Lutkenhaus of the Department of Chemical Engineering.

The crystal structures of compounds **34**, **BN-Ph**, **BN-Ph$^{\bullet+}$SbCl$_6^-$**, **and BN-Ph^{2-} [CoCp*$_2^+$]$_2$** were determined and provided by Dr. Nattamai Bhuvanesh. The TEM image of **34** was provided by Mr. Rick Litteton at Microscopy and Imaging Center. The TGA depicted in Chapter III was conducted by Chenxu Wang. The absorption data in Figure 47b were provided by Anthony U. Mu. The EPR spectra in Chapter V were provided by Xiaozhou Ji.

All other work conducted for the dissertation was completed by the student independently.

Funding Sources

Graduate study was supported by a Heep Graduate Student Fellowship from Texas A&M University.

This work was also made possible by Texas A&M University, National Science Foundation under Award Number 1654029, and Welsh Foundation under Grant Number A-1898.

NOMENCLATURE

AFM	Atomic Force Microscopy
Boc	*t*-Butyloxycarbonyl
BTH	Benzo[*d*]thiazole
Cp	Cyclopentadienyl
Cp*	Pentamethylcyclopentadienyl
DFT	Density Functional Theory
DMAP	4-Dimethylaminopyridine
DMF	*N,N*-dimethylformamide
DMSO	Dimethyl Sulfoxide
DSC	Differential Scanning Calorimetry
EPR	Electron Paramagnetic Resonance
ESI	Electron Spray Ionization
Fc	Ferrocene
Fc^+	Ferrocenium
FET	Field Effect Transistor
FT-IR	Fourier Transformed Infrared Spectroscopy
GIWAXS	Glazing Incidence Wide-Angle X-Ray Scattering
HOMO	Highest Occupied Molecular Orbital
ICBZ	Indolo[3,2-*b*]carbazole
LUMO	Lowest Occupied Molecular Orbital

MS	Mass Spectroscopy
NBO	Natural Bond Orbital
NIR	Near-Infrared
NMR	Nuclear Magnetic Resonance
PCE	Power Conversion Efficiency
Ph	Phenyl
SEM	Scanning Electron Microscopy
SAED	Selected Area Electron Diffraction
SOMO	Singly Occupied Molecular Orbital
TBAF	Tetrabutylammonium Fluoride
$TBAPF_6$	Tetrabutylammonium Hexaflurophosphate
TD-DFT	Time-Dependent Density Functional Theory
TGA	Thermogravimetric Analysis
THF	Tetrahydrofuran
TEM	Transmission Electron Microscopy
XRD	X-Ray Diffraction

TABLE OF CONTENTS

Page

ABSTRACT ii

DEDICATION iv

ACKNOWLEDGEMENTS v

CONTRIBUTORS AND FUNDING SOURCES vii

NOMENCLATURE viii

TABLE OF CONTENTS x

LIST OF FIGURES xiii

LIST OF TABLES xxii

CHAPTER I INTRODUCTION 1

1.1 Molecular Conformation of π-Conjugated Molecules and Macromolecules 1
1.2 Intramolecular Dynamic Noncovalent Bonds in Conjugated Molecules and Macromolecules 4
1.2.1 Overview 4
1.2.2 Hydrogen Bond Promoted Coplanarity 6
1.2.3 B←N Coordinate Bond Promoted Coplanarity 12
1.2.4 Heteroatom Noncovalent Interactions Promoted Coplanarity 17
1.3 Challenges and Outlook 23

CHAPTER II MOLECULAR COPLANARITY AND SELF-ASSEMBLY PROMOTED BY INTRAMOLECULAR HYDROGEN BONDS 27

2.1 Introduction 27
2.2 Molecular Design 30
2.3 Synthesis and Characterization 31
2.4 Controllable Aggregation and Self-Assembly 37
2.5 Conclusion 42
2.6 Experimental Section 42
2.6.1 General Methods 42
2.6.2 Synthesis 43

2.6.3 NMR Spectra 49

CHAPTER III SYNTHESIS AND SOLUTION PROCESSING OF A RIGID POLYMER ENABLED BY ACTIVE MANIPULATION OF INTRAMOLECULAR HYDROGEN BONDS 56

3.1 Introduction 56
3.2 Molecular Design 58
3.3 Synthesis and Characterization 61
3.4 Active Manipulation of Hydrogen Bonds and Solution Processing 67
3.5 Conclusion 72
3.6 Experimental Section 73
3.6.1 General Methods 73
3.6.2 Synthesis 75
3.6.3 NMR Spectra 81
3.6.4 Size Exclusion Chromatography 87

CHAPTER IV LOW BAND GAP COPLANAR CONJUGATED MOLECULES FEATURING DYNAMIC INTRAMOLECULAR LEWIS ACID-BASE COORDINATION 88

4.1 Introduction 88
4.2 Molecular Design, Synthesis and Characterization 90
4.3 Dynamic Nature of B←N Coordination 95
4.4 Electronic Properties 99
4.5 Conclusion 104
4.6 Experimental Section 104
4.6.1 General Methods 104
4.6.2 Synthesis 105
4.6.3 UV-vis-NIR Sepctra 108
4.6.4 NMR Spectra 109

CHAPTER V EXTRAORDINARY REDOX ACTIVITIES IN LADDER-TYPE CONJUGATED MOLECULES ENABLED BY B←N COORDINATION-PROMOTED DELOCALIZATION AND HYPERCONJUGATION 114

5.1 Introduction 114
5.2 Molecular Design 116
5.3 Synthesis and Optical Properties 118
5.4 Redox and Electrochromic Properties 123
5.5 Mechanistic Investigation 131
5.6 Hyperconjugation 137
5.7 Conclusion 140
5.8 Experimental Section 141

5.8.1 General Methods 141
5.8.2 Synthesis 143
5.8.3 Redox Reactions 147
5.8.4 NMR Spectra 149
5.8.5 DFT Calculation 156
5.8.6 Electron Paramagnetic Resonance Spectra 158
5.8.7 X-ray Single Crystal Analysis 159

CHAPTER VI CONCLUSION 161

6.1 Hydrogen Bond Bridged Coplanar Conjugated Molecules and Macromolecules 161
6.1.1 Summary 161
6.1.2 Perspective 162
6.2 B←N Coordinate Bond Bridged Rigid Conjugated Molecules 164
6.2.1 Summary 164
6.2.2 Perspective 165

REFERENCES 167

LIST OF FIGURES

Page

Figure 1. Graphic representations of (a) a π-conjugated polymer connected with single strand of bonds, (b) a ladder-type π-conjugated polymer and (c) a conjugated polymer coplanarized by dynamic noncovalent bonds. 2

Figure 2. Graphic representations of two synthetic strategies to construct a conjugated polymer coplanarized by dynamic noncovalent bonds. 5

Figure 3. Synthesis of a π-conjugated oligomer **1** with intramolecular hydrogen bonds. 6

Figure 4. The chemical structure of diketopyrolopyrole-derived small molecule **2** and its single crystal structure showing intramolecular hydrogen bonds and the coplanar conformation. 7

Figure 5. (a) Synthesis and (b) GIWAXS diffraction maps of hydrogen bonded poly(*p*-phenylene vinylene) derivatives, **3**, **4**, and **5**. 9

Figure 6. Synthesis of **6** with a conformation fully controlled by intramolecular hydrogen bonds and the chemical structure of **7** with a partially controlled conformation. 10

Figure 7. The structures of coplanar oligo(phenylene ethynylene) **8** and the different conformation of **9** controlled by competitive intramolecular hydrogen bonds. 11

Figure 8. Synthetic examples of incorporating N→B coordinative bonds onto π-conjugated molecules. 14

Figure 9. Synthesis of π-conjugated polymers containing N→B coordinative bonds. 17

Figure 10. (a) The chemical structures of **21** and **22**; (b) single crystal structure and solid-state packing of **21**; (c) UV-vis absorption and (d) differential scanning calorimetric traces of **21** (in red) and **22**(in blue). 18

Figure 11. Synthesis of π-conjugated polymers **23**, **24**, **25**, **26**, **27**, and **28** with conformation controlled by S…F electrostatic interaction. 20

Figure 12. (a) Synthesis of **29**, **30**, and **31** featuring a partially coplanar conformation promoted by S…O electrostatic interactions; (b) the chemical and single crystal structure of **32**; (c) the chemical structure and DFT optimized

geometry of **33** featuring a fully coplanar conformation promoted by S…O electrostatic interactions and hydrogen bonds. 22

Figure 13. (a) An intramolecular hydrogen bonded 2-phenylpyridine derivative with a dihedral angle measured from the single crystal structure.[110] (b) A *p*-phenylene ethynylene derivative with a parallel linear hydrogen bond.[111] (c) The structural formula of **34** and the potential energy surface scan [B97D/6-31G(d,p)] of **34** by changing the dihedral angle between the hydrogen bond donating units and accepting units. (d) The structural formula and DFT optimized conformation [B3LYP/6-311G(d,p)] of **35**..... 28

Figure 14. Synthesis of the coplanar model compound **34** and its non-coplanar counterpart **35** 31

Figure 15. ^{1}H NMR spctra (500 MHz, 295 K) of (a) a mixture of 1-iodoanthraquinone and **39** in $CDCl_3$; (b) **34** in $CDCl_3$; (c) **34** in d_6-DMSO/$CDCl_3$ (v/v =1/7) and (d) **35** in $CDCl_3$. 32

Figure 16. The plot of the chemical shifts of Proton h in **34** in $CDCl_3$ (red) and d_6-benzene (blue) against temperature according to ^{1}H NMR (500 MHz) experiement results. The temeperature coefficients were calculated to be −3.7 ppb/K and −6.0 ppb/K, respectively. 33

Figure 17. FT-IR spectra of **34** (in red) and **35** (in blue) in the solid state at room temperature. 34

Figure 18. (a) Front view and (b) side view of single crystal structure of **34**. The thermal ellipsoids were scaled to the 50% probability level. (c) A side view of the packing mode of **34** in single crystal. The octyl chains and $C_2H_2Cl_4$ solvent molecules are omitted for clarity. 35

Figure 19. UV-vis absorption spectra of **34** (in red) and **35** (in blue) in toluene solution (1.0×10^{-5} mol/L) and in the solid state (spin-cast thin films on quartz substrates). 36

Figure 20. Cyclic voltammetry traces of **34** (in red) and **35** (in blue) in CH_2Cl_2 (concentration: 1.0×10^{-3} mol/L; scan rate: 100 mV/s)..... 36

Figure 21. DPV traces of **34** and **35** (1.0×10^{-4} mol/L) in CH_2Cl_2 with $TBAPF_6$ as the electrolyte. The scan period, width, and height were 100 ms, 10 ms, and 50 mV, respectively, with a potential increment of 10 mV. 37

Figure 22. The aromatic region of ^{1}H NMR spectra of **34** and **35** in $CDCl_3$ in different concentrations 38

Figure 23. (a) Temperature- and concentration-dependent ^{1}H NMR chemical shifts of proton *f* of **34**, fitted with the isodesmic model; the inset is a van't Hoff plot of aggregation constants at different temperatures. (b) Aggregation enthalpy of **34** in $CDCl_3$/d_6-DMSO mixed solvents while increasing the volume fraction of d_6-DMSO. 39

Figure 24. (a) SEM images of nano-/microfibers of **34** grown from slow evaporation of CH_2Cl_2 solutions. (b) TEM images of these fibers with the SAED pattern. 40

Figure 25. Powder X-ray diffraction map of fibers of **34** grown by slow evaporation in CH_2Cl_2. 41

Figure 26. SEM images showing aggregates of **35** grown by slow evaporation using (a) CH_2Cl_2 and by vapor diffusion using (b) CH_2Cl_2/diethyl ether, (c) $CHCl_3$/pentane, (d) THF/pentane, (e) toluene/hexane and (f) DMF/ethanol. ..41

Figure 27. ^{1}H (500 MHz), ^{13}C NMR (125 MHz) spectra of **34** in $CDCl_3$ at room temperature. 49

Figure 28. ^{1}H (500 MHz), ^{13}C NMR (125 MHz) spectra of **35** in $CDCl_3$ at room temperature. 50

Figure 29. ^{1}H (500 MHz), ^{13}C NMR (125 MHz) spectra of **37** in $CDCl_3$ at room temperature. 51

Figure 30. ^{1}H (500 MHz), ^{13}C NMR (125 MHz) spectra of **38** in $CDCl_3$ at room temperature. Proton *d* is overlapping with H_2O....52

Figure 31. ^{1}H (500 MHz), ^{13}C NMR (125 MHz) spectra of **39** in $CDCl_3$ at room temperature. 53

Figure 32. ^{1}H (500 MHz), ^{13}C NMR (125 MHz) spectra of **40** in $CDCl_3$ at room temperature. 54

Figure 33. ^{1}H-^{1}H COSY NMR (500 MHz) spectra of **34** in $CDCl_3$ at room temperature. 55

Figure 34. ^{1}H-^{1}H COSY NMR (500 MHz) spectra of **35** in $CDCl_3$ at room temperature. 55

Figure 35. (a) Example of intramolecular hydrogen bonds: crystal structure of a polypeptide with helical conformation induced by intramolecular hydrogen bonds[141] and (b) chemical structures and graphical representations of **HP** and **BocP**. 57

Figure 36. Structural formula and molecular geometry of a representative structural segment of **HP** backbone. 60

Figure 37. Structural formula and molecular geometry of a representative structural segment of **BocP** backbone. 61

Figure 38. Synthetic route to monomers **41** and **42**. 61

Figure 39. Two Synthetic Routes to **HP**: Route A: direct polymerization of monomer **41** without masking the hydrogen bonds. Route B: polymerization of Boc-protected monomer **42** followed by solid-state unmasking of the hydrogen bonds. 62

Figure 40. (a) Size exclusion chromatogram of **BocP** and the soluble fraction of **HP-A**. Inset is a photograph of HP-A and **BocP** (5 mg/mL) in 2-methyltetrahydrofuran at room temperature. (b) FT-IR spectra of **BocP** and **HP-B**. 63

Figure 41. ^{1}H (500 MHz) NMR spectrum of **BocP** in $CDCl_3$ at room temperature. 64

Figure 42. The TGA trace of **BocP**. Boc cleavage started at 130 °C. A weight loss of 9.1% was observed from 130 °C to 210 °C. The polymer further decomposed at 270 °C with an additional weight loss of 5%. 65

Figure 43. Thin films of **HP-B** on glass substrates at room temperature soaked in different organic solvents: (a) chloroform, (b) THF, (c) chlorobenzene, (d) chlorobenzene after heating at 120 °C for 2 hours. 66

Figure 44. Fourier transform infrared spectrum of **HP-A** in the solid state at room temperature. 67

Figure 45. UV-vis absorption of thin films (spin coated from a solution of 2 mg/mL **BocP** in chloroform at 1000 rpm) of **BocP** and **HP-B** on glass substrates. 68

Figure 46. Cyclic voltammogram of **BocP** and **HP-B** in the solid state. 69

Figure 47. (a) AFM images of thin films of **BocP** and **HP-B**; graphic representation of multilayer-film processing of solvent-resistant film of **HP-B**. (b) UV–vis spectra of the **HP-B** films after different numbers of processing cycles. Inset is the plot between the processing cycle numbers and absorption intensities at 376 nm. 70

Figure 48. GIWAXS patterns of (a) a **BocP** (as casted) thin film and (b) a **HP-B** (annealed) thin film. The thin film of **BocP** was prepared by spin coating a **BocP** solution (2.0 mg/mL in chlorobenzene) at a spinning rate of 1000 rpm

on silica wafer substrates. The thin film of **HP-B** was prepared by thermal annealing another thin film of **BocP** at 130 °C for 1 hour in a N_2-filled glovebox. 71

Figure 49. ^1H (300 MHz), ^{13}C (75 MHz) NMR spectra of **43** in $CDCl_3$ at room temperature. 81

Figure 50. ^1H (300 MHz), ^{13}C (75 MHz) NMR spectra of **44** in $CDCl_3$ at room temperature. 82

Figure 51. ^1H (300 MHz), ^{13}C (125 MHz) NMR spectra of **45** in $CDCl_3$ at room temperature. 83

Figure 52. ^1H (300 MHz), ^{13}C (125 MHz) NMR spectra of **46** in $CDCl_3$ at room temperature. 84

Figure 53. ^1H (300 MHz), ^{13}C (125 MHz) NMR spectra of monomer **41** in $CDCl_3$ at room temperature. 85

Figure 54. ^1H (500 MHz), ^{13}C (125 MHz) NMR spectra of monomer **42** in $CDCl_3$ at room temperature. 86

Figure 55. Size exclusion chromatogram of **BocP** (top: as prepared; bottom: purified after preparative SEC). 87

Figure 56. Two general strategies that are often invoked in the design and synthesis of low band gap π-conjugated organic compounds: incorporation of conjugated electron-donating and -accepting units in an alternating manner (left) and extension of the coherent π-electron delocalization (right). 89

Figure 57. Synthesis of B ← N bridged donor–acceptor–donor ladder-type molecules **48** and **50**. 91

Figure 58. ^{11}B NMR spectra of **48** (blue) and **50** (green) in $CDCl_3$, and a background ^{11}B NMR of D_2O (orange). The broad signal between 25 pm and -20 ppm is a result of glassy NMR probe containing boron. 93

Figure 59. Solution phase UV–vis–NIR spectra and calculated oscillator strength [B3LYP/6-311G(d,p)] of **48** (top) and **50** (bottom), in comparison to their precursors **47** and **49**. 94

Figure 60. Normailzed UV-vis absorption spectra of **48** in chloroform (9.9×10^{-6} M) and in solid state. 95

Figure 61. Charge transfer absorption of **48** (a) and **50** (b) in a variety of organic solvents and the correlation between optical band gaps of **48** (c) and **50** (d) with the Lewis basicities of organic solvents (enthalpies from complex formation with BF_3). 96

Figure 62. Plots of optical bandgaps of **48** (bottom) and **50** (top) against dielectric constants of organic solvents. 97

Figure 63. Chemical shift change of protons in the aromatic region of **48** in CD_2Cl_2 and d_8-THF against the temperature. 98

Figure 64. Cyclic voltammetry of **47–50**, 0.10 M $TBAPF_6$ in CH_3CN. (The comparison of reduction onsets and oxidation onsets for **48**, **50** and their precursors were shown in dotted lines.) 99

Figure 65. Cyclic voltammetry of **48** and **50**, 0.10 M $TBAPF_6$ in CH_2Cl_2. 100

Figure 66. HOMO, LUMO energy levels [experimental data and calculated values (in parentheses)], calculated molecular orbitals, and electrostatic potential map for **47–50** [B3LYP/6-311G(d,p)]. 101

Figure 67. Calculated LUMO+1 orbitals of **48** (left) and **50** (right) [B3LYP/6-311g(d,p)]. 103

Figure 68. Normalized absorption spectra of Compound **48** (top, concentration: 9.9×10^{-6} M) and Compound **50** (bottom, concentration: 9.7×10^{-6} M) in a series of organic solvents at room temperature. 108

Figure 69. ^1H (500 MHz), ^{13}C NMR (125 MHz) spectra of **47** in $CDCl_3$ at room temperature. 109

Figure 70. ^1H (500 MHz), ^{13}C NMR (75 MHz) spectra of **48** in $CDCl_3$ at room temperature. 110

Figure 71. ^1H (500 MHz), ^{13}C NMR (125 MHz) spectra of **49** in $CDCl_3$ and TFA at room temperature. 111

Figure 72. ^1H (500 MHz), ^{13}C NMR (125 MHz) spectra of **50** in $CDCl_3$ at room temperature. 112

Figure 73. ^1H NMR spectra of (a) freshly prepared $CDCl_3$ solution of **48**; (b) $CDCl_3$ solution of **48**, 10 min after adding water; (c) $CDCl_3$ solution of **48**, 2hrs after adding water. 113

Figure 74. (a) Designed ladder-type molecule featuring cruciform arrangement of redox-active units (reduction-active in blue and oxidation-active in red) and B ← N coordination that can rigidify and coplanarize the entire molecule; (b) representative orbital interactions of the boron center in the designed conjugated molecules.....116

Figure 75. Synthesis of **BN-F** and **BN-Ph**. 119

Figure 76. DFT calculation optimized geometry of compound **53**. Methyl groups were used to replace *t*-butyl groups for the simplicity of calculation. Hydrogen atoms were omitted for clarity. 120

Figure 77. Computed (a) HOMO, (b) LUMO of **BN-F**, and (c) HOMO, (d) LUMO of **BN-Ph** (isovalue = 0.03). Hydrogen atoms were omitted for clarity. 121

Figure 78. UV–vis–NIR absorption (solid lines) and emission (dashed lines) of (a) **BN-F** and (b) **BN-Ph** in CH_2Cl_2 with transition energies calculated by time-dependent DFT using B3LYP/6-311g(d,p) with CH_2Cl_2 CPCM solvation.....122

Figure 79. CV curves of (a) **BN-F**, (b) **BN-Ph**, and (c) 53 in CH_2Cl_2 [0.10 M $TBAPF_6$ as the electrolyte; Ag/AgCl as the reference electrode; scan rate = 100 mV/s]. The half-wave potentials of each redox process were noted in (a) **BN-F** and (b) **BN-Ph**. (d) Comproportionation equilibriums of radical cations and radical anions. 124

Figure 80. (a) Photographs of the **BN-Ph** solutions at different redox states in the presence of a honeycomb working electrode in a spectroelectrochemical cell (in CH_2Cl_2 with 0.10 M $TBAPF_6$). UV–vis–NIR absorption changes of the **BN-Ph** solutions upon stepwise applications of potentials on the honeycomb working electrode (step height = 0.05 V, vs Ag/AgCl) from (b) +0.70 to +1.05 V, (c) +1.25 to +1.50 V, (e) −0.70 to −1.05 V, and (f) −1.05 to −1.35 V. Molecular frontier orbitals and calculated transition energies with oscillator strengths of (d) **BN-Ph**$^{\bullet+}$ and (g) **BN-Ph**$^{\bullet-}$ [UB3LYP/6-311g(d,p) with CH_2Cl_2 CPCM solvation]. Multiple cycles of absorption changes of the **BN-Ph** solutions when the potential was switching between (h) 0.20, 1.10, and 1.50 V and (i) −0.30, −1.05, and −1.40 V. 126

Figure 81. (a) Photographs of the honeycomb electrode in CH_2Cl_2 with 0.10 M $TBAPF_6$ as the electrolyte for different redox states of **BN-F**. UV-vis absorption changes of **BN-F** in CH_2Cl_2 upon stepwise application of potentials from (b) +1000 mV to +1400 mV (step heigh: 100 mV), (c) +1500 mV to +2200 mV (step heigh: 100 mV), (d) −550 mV to −750 mV (step heigh: 50 mV) and (e) −750 mV to −1300 mV (step heigh: 100 mV) vs. Ag/AgCl. 130

Figure 82. (a) The redox-active core structure of **BN-Ph** labeled with bond indices from *a* to *q*; (b) DFT calculated lengths of the bonds *a*–*g* before and after oxidation; (c) DFT calculated lengths of the bonds *e* and *h*–*o* before and after reduction [B3LYP/6-311g(d,p)]; (d) calculated HOMA and NICS(1)$_{zz}$ values for the central ring "A" of **BN-Ph** in different redox states.131

Figure 83. Constitutional structures of the five different redox states of **BN-Ph**. 132

Figure 84. (a) DFT calculated lengths of the bonds *a*~*g* in **BN-Ph** before and after oxidation; (b) DFT calculated lengths of the bonds *e* and *h*~*o* in **BN-Ph** before and after reduction (B3LYP/TZVP with D3 version of Grimme's dispersion correction). Bond indices were shown in Figure 82a. 133

Figure 85. Single-crystal X-ray structures of (a) **BN-Ph**, (b) **BN-Ph$^{\bullet+}$SbCl$_6^-$**, and (c) **BN-Ph^{2-}[CoCp*$_2^+$]$_2$** and bond lengths of the area around the central ring "A". Hydrogen atoms and solvent molecules were omitted for clarity. Thermal ellipsoids are scaled to the 50% probability level. 134

Figure 86. EPR spectra of (a) **BN-Ph$^{\bullet+}$** in CH_2Cl_2 (0.13 mM) and (c) **BN-Ph$^{\bullet-}$** in acetonitrile (0.03 mM) at 288 K. DFT computed spin density maps (isovalue = 0.0008) of (b) **BN-Ph$^{\bullet+}$** and (d) **BN-Ph$^{\bullet-}$**[UB3LYP/6-311g++(d,p)]. 136

Figure 87. Calculated isotropic Fermi coupling constants of (a) **BN-F$^{\bullet+}$**, (b) **BN-F$^{\bullet-}$**, (c) **BN-Ph$^{\bullet+}$**, (d) **BN-Ph$^{\bullet-}$**.....137

Figure 88. NBO plots of hyperconjugative interactions in different redox states of **BN-Ph** (a, b, c, d) and **BN-F** (e, f, g, h). 140

Figure 89. ^{1}H (500 MHz), ^{13}C NMR (125 MHz) of **51** in $CDCl_3$ at 295 K. 149

Figure 90. ^{1}H (500 MHz), ^{13}C NMR (125 MHz) of **52** in $CDCl_3$ at 295 K. 150

Figure 91. ^{1}H (500 MHz), ^{13}C NMR (125 MHz) of **53** in $CDCl_3$ at 295 K. 151

Figure 92. ^{1}H (500 MHz) of **BN-F** in $CDCl_3$ at 295 K. 152

Figure 93. ^{1}H (500 MHz in CD_2Cl_2), ^{13}C NMR (125 MHz in $CDCl_3$) of **BN-Ph** at 295 K. 153

Figure 94. ^{1}H-^{1}H COSY NMR (500 MHz in $CDCl_3$) of **BN-F** at 323 K. 154

Figure 95. ^{1}H-^{1}H COSY NMR (500 MHz in CD_2Cl_2) of **BN-Ph** at 295 K. 155

Figure 96. ^{1}H-^{1}H COSY NMR (500 MHz in CD_3CN) of **BN-Ph^{2-}** at 295 K. 156

Figure 97. Spin density maps (isovalue = 0.0008) of (b) **BN-F**$^{\bullet+}$ and (d) **BN-F**$^{\bullet-}$ calculated at uB3LYP/6-311g++(d,p) level. Hydrogen atoms were omitted for clarity. 158

Figure 98. EPR spectra of (a) **BN-F**$^{\bullet+}$ in CH_2Cl_2 and (b) **BN-F**$^{\bullet-}$ in CH_2Cl_2 at 288 K. 158

Figure 99. Synthesis routes for (a) thiophene-derived building units with hydrogen bond donating moieties and (b) naphthalene diimide-thiophene copolymers with intramolecular hydrogen bonds. 163

Figure 100. Molecular design of *n*-type organic semiconducting materials with intramolecular B←N coordinate bonds. 166

LIST OF TABLES

Page

Table 1. Calculated energy levels and HOMO—LUMO transition energies of **48** at different dihedral angles [B3LYP/6-311g(d,p)]. 102

Table 2. Calculated energy levels and HOMO—LUMO transition energies of **50** at different dihedral angles [B3LYP/6-311g(d,p)]. 102

Table 3. Calculated transition energies [B3LYP/6-311g(d,p)] of **BN-Ph**$^{\bullet+}$ and **BN-Ph**$^{2+}$ based on the molecular geometries obtained at the level of B3LYP/6-311g(d,p).....127

Table 4. Calculated transition energies [B3LYP/6-311g(d,p)] of **BN-Ph**$^{\bullet-}$ and **BN-Ph**$^{2-}$ based on the molecular geometries obtained at the level of B3LYP/6-311g(d,p).....129

CHAPTER I

INTRODUCTION*

1.1 Molecular Conformation of π-Conjugated Molecules and Macromolecules

Molecular conformation represents one of the most important structural features for organic molecules, polymers and biological macromolecules. It plays a pivotal role in governing many of the key properties of molecular species, including solubility, mechanical/rheological behaviors, biological activities, optical and electronic characteristics. In a π-conjugated molecule or macromolecule, the torsional conformation between aromatic units determines not only the overall molecular shape, but also its optical and electronic properties.[1,2] A coplanar conjugated system is expected to possess better coherent conjugation along the backbone, giving rise to a lower band gap and faster intramolecular charge transport.[3] Coplanarity also favors small reorganization energy through charge transport and close intermolecular packing in the solid state,[4] which are anticipated to result in strong intermolecular electronic coupling and long exciton diffusion length.[5] Recent molecular dynamic simulations demonstrated that a coplanar backbone could improve the local ordering in the solid state and was resilient to the side-chain disorder.[6,7] It was also proposed, from a theoretical perspective, that amorphous polymers with a coplanar backbone can adopt efficient packing and lead to good charge transport in short length scales for photovoltaic devices.[8] Meanwhile, the strong π-π interactions between coplanar backbones can facilitate the self-assembly process in solution[9,10] and the formation of ordered nano-/micro-structures in the solid state.[11,12] These advantages render coplanarity an important structural feature for the development of the active components for organic semiconductors,[13-16] solar cells,[17,18] light emitting diodes,[19-21] and NIR materials.[22] Although examples with twisted

* Reprinted with permission from "Locking the Coplanar Conformation of π-Conjugated Molecules and Macromolecules Using Dynamic Noncovalent Bonds" Zhu, C.; Fang, L. *Macromol. Rapid Commun.* **2017**, 1700241. Copyright 2017 John Wiley and Sons.

backbones, such as N2200, were reported to exhibit good charge carrier mobility in electronic devices,[23,24] systematic literature survey demonstrated that the coplanar conformation was generally favorable in enhancing the charge transport properties of conjugated polymers. In this context, it would be ideal to take full control of the torsional conformation, in order to achieve desired properties and performances of π-conjugated molecules and macromolecules at the molecular level and as functional materials.

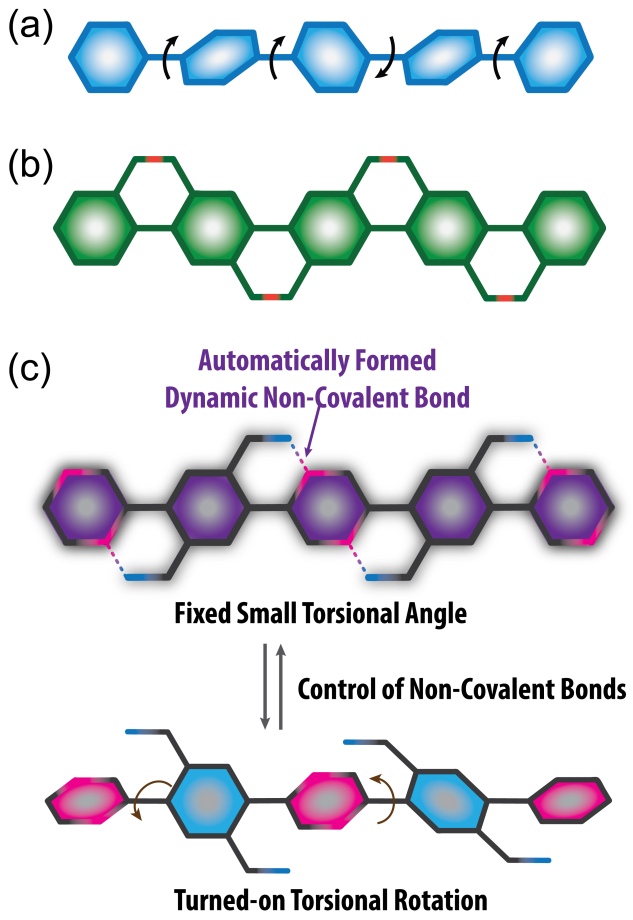

Figure 1. Graphic representations of (a) a π-conjugated polymer connected with single strand of bonds, (b) a ladder-type π-conjugated polymer and (c) a conjugated polymer coplanarized by dynamic noncovalent bonds.

Most of the known extended conjugated oligomers and polymers, however, are composed of multiple aromatic units linked by one strand of single bonds so that a

coplanar conformation is not always guaranteed (**Figure 1a**). The aromatic repeating units can adopt non-zero dihedral angles between the aromatic building blocks due to thermodynamic fluctuation and steric repulsion.[25] In a biphenyl system, for example, the torsional angle of the thermodynamically favored conformation is about 44° because of 2,2′-H,H steric repulsion.[26] Such a twisted backbone in conventional conjugated polymers shortens the coherent conjugation length[27], therefore limiting the transport of charge carriers and excitons with respect of electronic and optoelectronic application.[28] The torsional angle can often be reduced by π-π stacking interactions in the solid state. From a kinetic point of view, however, the low activation energy for dynamic torsional motion of a single bond (*e.g.*, ~3 kcal/mol in biphenyl)[29] makes it challenging to maintain a fixed conformation at room temperature and leads to less predictable materials performance. In order to pursue the desired individual/collective properties and material applications of π-conjugated molecules or macromolecules, it is essential to achieve full control of the torsional motion and draw a clear structure-property relationship in terms of torsional conformation. The prevailing strategy to achieve such a goal involves the construction of fused-ring constitutions, or so-called ladder-type molecules, by forming an additional strand of covalent bonds so that torsional motion is prohibited and a coplanar conformation is enforced (**Figure 1b**).[30-34] This method is efficient in affording excellent optoelectronic properties of individual molecules[35-37] and endorses strong intermolecular interactions,[32] which can be further translated into the formation of nano-/microscale assemblies in the solid state.[38,39] The covalently fused constitution, however, often leads to synthetic and processing challenges,[33] such as

structural defects and low solubilities. Moreover, the formation of covalent linkages is usually irreversible so that an active conformational control is not possible in covalent ladder-type molecules. In this context, the employment of dynamic noncovalent bond to manipulate the coplanar conformation of conjugated molecules and polymers is desirable for both fundamental investigations and practical applications of this class of materials (**Figure 1c**).

1.2 Intramolecular Dynamic Noncovalent Bonds in Conjugated Molecules and Macromolecules

1.2.1 Overview

Hydrogen bonds,[40,41] Lewis acid-base coordinative interactions,[42,43] metal coordination[44] and heteroatom noncovalent interactions,[18,45,4647] could serve as promising dynamic bridging interactions to induce the desired coplanarity in a π-conjugated molecule while enabling dynamic conformational control. Such a system is analogous to sophisticated biological macromolecules in nature such as proteins, in which intramolecular noncovalent bonds maintain the conformation and facilitate specific functions. A noncovalent conformational lock effect could be viewed as high energy barriers that prevents the low energy coplanar conformer from torsional rotation, contributed by the designed formation of noncovalent interactions.[8] Unlike covalent bonds, the thermodynamically driven formation of noncovalent bonds is reversible,[41,42,48] enabling on-demand control of molecular conformation and therefore active manipulation over molecular, supramolecular, and solid-state properties.[41]

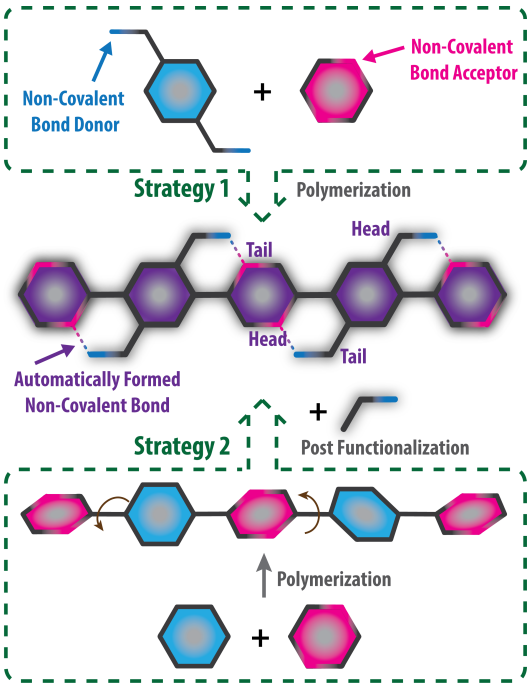

Figure 2. Graphic representations of two synthetic strategies to construct a conjugated polymer coplanarized by dynamic noncovalent bonds.

Two general synthetic strategies can be used to incorporate dynamic noncovalent bonds into π-conjugated systems, depending on whether the noncovalent bonding moieties are installed before or after the coupling step (**Figure 2**). The first strategy requires that the dynamic bond functionalities are pre-installed on building blocks and can tolerate the following polymerization. This strategy is advantageous in terms of ensuring the structural precision of the dynamically bonded conjugated backbone and minimizing the structural defects of the product. The second strategy involves a post-polymerization functionalization to introduce noncovalent bonding moieties into an already constructed conjugated backbone. High reactivity is demanded in the post-functionalization step to ensure a high conversion and further decrease structural defects.

Therefore, this strategy is more preferred for the synthesis of small molecules and oligomers, but is challenging to be applied in polymer synthesis due to the potential defects.

1.2.2 Hydrogen Bond Promoted Coplanarity

Among various types of noncovalent forces, the hydrogen bond stands out as an ideal interaction because of its tunable strength and directionality,[49] allowing for a precise control of conformation. In order to achieve the full control over an entire polymer chain, the hydrogen bond donating or accepting groups should be installed on both the head and the tail of each rigid building unit (**Figure 2**). Thus, the torsional angles with both adjacent units can be fixed to a near-zero value once hydrogen bonds are formed.

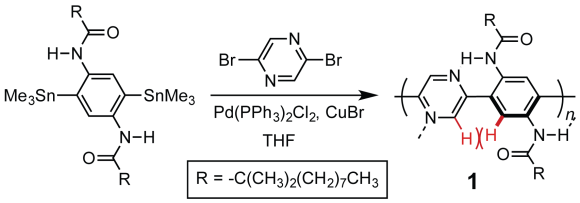

Figure 3. Synthesis of a π-conjugated oligomer 1 with intramolecular hydrogen bonds.

An early successful demonstration of this strategy was reported by Meijer et al. in the 1990s.[41] A benzene-based monomer was functionalized with two amide groups as hydrogen bond donors (**Figure 3**). The other monomer was derived from pyrazine, on which the nitrogen atoms served as the hydrogen bond acceptors. After Stille coupling

AA+BB polymerization between these two monomers, the intramolecular hydrogen bonds were formed spontaneously in a geometrically favorable six-member ring-like architecture. The molecular weight of this polymer was ~ 5.1 kg/mol, limited by the poor solubility induced by the rigid structure. The downfield shifted resonance signal (11.7 ppm) of the amide proton on ^{1}H NMR spectra and the weakened NH stretching on infrared spectra clearly confirmed the formation of intramolecular hydrogen bonds. However, the experimental band gap (2.78 eV) of **1** was higher than the density functional theory (DFT) calculated band gap (2.55 eV) using periodic boundary conditions.[50] Such a discrepancy is likely due to the low degree of polymerization. Subsequently, several other research groups adopted this hydrogen bond architecture to achieve the desired photophysical properties of conjugated oligomer/polymer systems.[51,52] Thanks to the coplanar conformation and the possible excited-state intramolecular proton transfer, these oligomers/polymers featuring hydrogen bonds exhibited all red-shifted absorption spectra and low-energy emission.

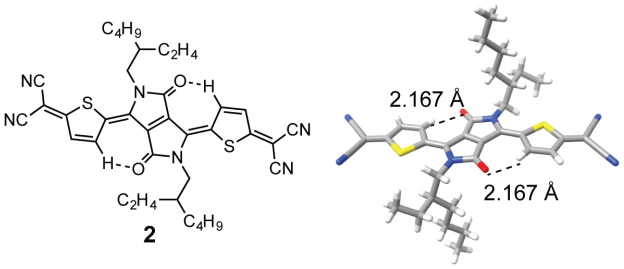

Figure 4. The chemical structure of diketopyrolopyrole-derived small molecule 2 and its single crystal structure showing intramolecular hydrogen bonds and the coplanar conformation.

Besides the classical hydrogen bonds, some non-traditional hydrogen bonds forming 6- or 7-membered ring architectures were recently found to play an important role in controlling the coplanar conformation of π-conjugated systems.[53,54] Such a hydrogen bonding event occurs between an electron-negative atom and a weak, non-traditional hydrogen bond donor, such as hydrogen attached to an aromatic unit. Computational investigation revealed that the binding energies in these non-traditional hydrogen bonds, (e.g., C−H…O, C−H…N and C−H…F interactions) ranged from 2.20 to 0.94 kcal/mol,[53,54] which were significantly weaker than the typical O−H…O or N−H…O hydrogen bonds. However, the favorable pre-organization and the short distance between the hydrogen bond donor and acceptor in a 6- or 7-membered ring architecture are able to promote the formation of these weak intramolecular hydrogen bonds, which further impose a profound impact on the conformation and the properties of π-conjugated systems. For example, the C−H…O hydrogen bonds widely exist in diketopyrolopyrole (DPP)-derived small molecules[40,55] and polymers.[56-59] In 2012, Liu and coworkers demonstrated this non-traditional hydrogen bond unambiguously in the single crystal structure of a DPP-based quinoidal molecule **2** (**Figure 4**).[40] This weak intramolecular interaction contributed to the coplanarity of **2** and conjugated polymers containing a similar building unit, leading to high performance of these materials as the semiconductor layer in FETs.[40,55-60]

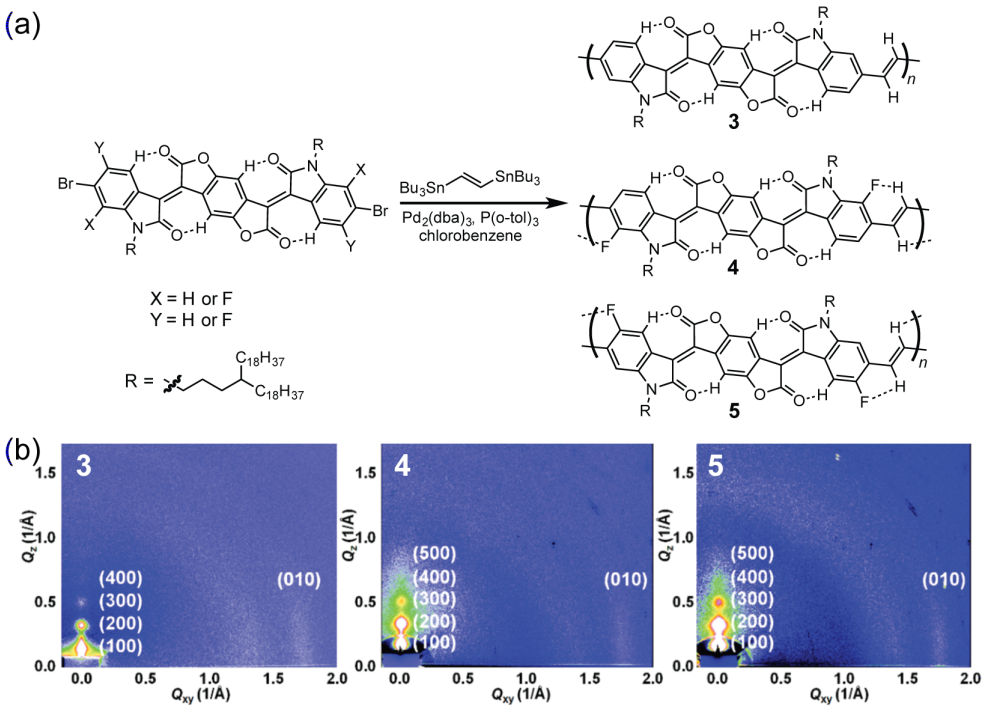

Figure 5. (a) Synthesis and (b) GIWAXS diffraction maps of hydrogen bonded poly(*p*-phenylene vinylene) derivatives, 3, 4, and 5.

In 2014, the Pei group reported the adoption of weak intramolecular C−H…O and C−H…F hydrogen bonds to achieve the conformational control of poly(*p*-phenylene vinylene) derivatives, **3**, **4**, and **5** (**Figure 5a**).[61] In each repeating unit of **3**, four pairs of hydrogen bonds were formed between protons on the phenyl rings and oxygen atoms on carbonyl groups, corroborated by the drastic downfield shift of their resonance signal on ^{1}H NMR.[54,61] These hydrogen bonds forced the benzodifurandione-based oligo(p-phenylene vinylene) (BDOPV) units to adopt a coplanar and rigid conformation with dihedral angles less than 8°. To further achieve conformational control over the entire polymer backbone, fluorine was introduced on the oxindolone part, which can form hydrogen bonds with the hydrogen atoms on the vinylene spacers.[54] Geometry

optimization through DFT calculations revealed coplanar conformation of **4** and **5**. Such a coplanar conformation was believed to induce strong aggregation and further promote a condensed packing mode in the solid state of **4** and **5** (**Figure 5b**). The coplanar conformation and shortened π–π stacking distances of **4** and **5** promoted the intramolecular and intermolecular charge transport, leading to high electron mobilities (1.70 $cm^2 V^{-1} s^{-1}$ for **4**and 0.81 $cm^2 V^{-1} s^{-1}$ for **5**) in FETs.

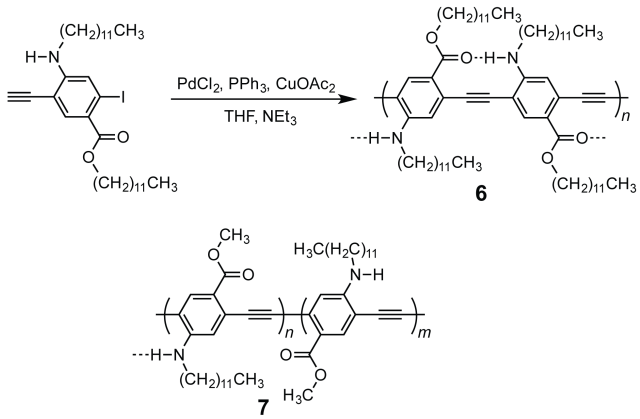

Figure 6. Synthesis of 6 with a conformation fully controlled by intramolecular hydrogen bonds and the chemical structure of 7 with a partially controlled conformation.

Besides the 6-/7-membered ring geometry, intramolecular hydrogen bonds can also be constructed parallel to the π-conjugated backbone in a linear manner. In this design, ethynylene units can be employed as spacers between aromatic units in the backbone in order to allow for enough spatial distance between the adjacent π-units, meanwhile preventing 2,2′-H,H steric repulsion between phenylene units.[11,48,62] Based on the aforementioned design strategy, Moroni et al. reported in 1997 the synthesis of a

hydrogen-bonded poly(phenylene ethynylene) **6** using Sonogashira coupling (**Figure 6**).[63] The polymer conformation was believed to be fully locked by intramolecular hydrogen bonds between the aromatic units. The measurement of nonlinear optical susceptibilities demonstrated that **6** had a higher third-order susceptibility than **7,** as a result of its fully coplanar conformation. Due to the strong π–π stacking interaction between the coplanar backbones/segments, **6** and **7** both suffered from low solubility in common organic solvents, preventing accurate determination of their molecular weights in solution phase.

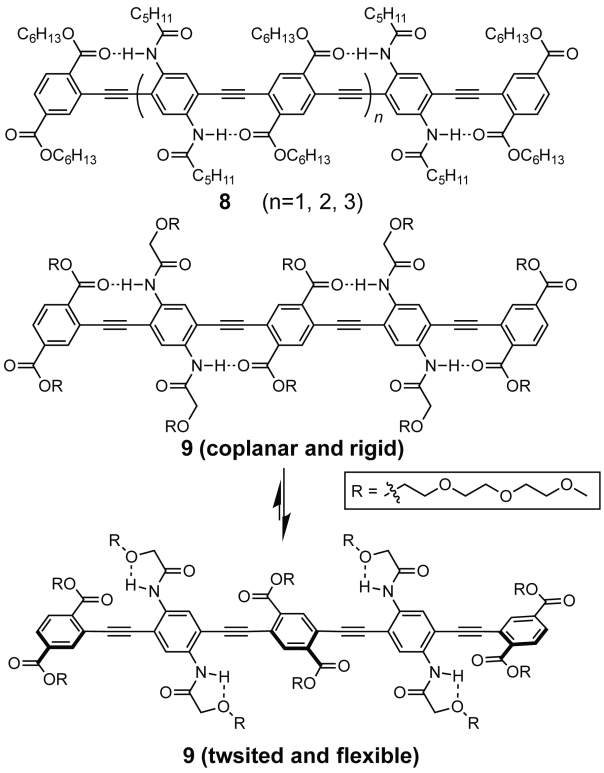

Figure 7. The structures of coplanar oligo(phenylene ethynylene) 8 and the different conformation of 9 controlled by competitive intramolecular hydrogen bonds.

In 2008, the Zhao group investigated the "conformation locking" effect on the optical properties of oligo(phenylene ethynylene)s.[48] A series of oligo(phenylene ethynylene)s **8** (**Figure 7**) with hydrogen-bond-promoted coplanar conformation were synthesized by step-wise Sonogashira coupling reactions. This study demonstrated that besides narrowed optical band gaps, the coplanarity and enhanced rigidity induced by intramolecular hydrogen bonds in **8** also contributed to smaller Stokes shifts compared to their non-hydrogen-bonded analogues. Later on, oligo(ethylene glycol) groups were further introduced as side chains in the structure of **9** (**Figure 7**).[64] The ^{1}H NMR spectra of **9** revealed hydrogen bond formation between the amide proton and the ether oxygen on the side chain. Such hydrogen bond formation competed with the hydrogen bond formed with the carbonyl oxygen. As a result, the conformation of **9** was more flexible and twisted, as evidenced by its broader UV-vis absorption band and decreased extinction coefficient.

1.2.3 B←N Coordinate Bond Promoted Coplanarity

Another class of promising dynamic interaction that can lock torsional conformation is N→B coordinative bonds. The synthetic challenge to this class of molecules is primarily the installation of a boron center onto a fused aromatic system. This objective can be achieved through 3 different methods: (i) lithium/boron exchange, (ii) directed electrophilic borylation, and (iii) hydroboration. Using the first method, namely the lithium/boron exchange reaction, Yamaguchi et al. functionalized thiophene-thiazole-based conjugated molecule **10** with dimesitylboryl moieties (**Figure 8**).[42] The

coplanarity of **10** was confirmed by single-crystal X-ray diffraction. The short distance of 1.67 Å between the nitrogen atom and the boron center indicated the strong interaction between the Lewis base (nitrogen) and the Lewis acid (boron). This coplanar molecule exhibited a smaller optical band gap compared to its non-coplanar precursor. Thanks to the excellent stability of such a tetra-coordinated boron center, **10** can be further functionalized to construct extended step-ladder molecule.[42] Since then, several examples of N→B coordination-promoted, ladder-type conjugated small molecules and oligomers have been reported, showing interesting photoisomerization[65] and fluorescence emission properties.[66,67] The second method involves a nitrogen-directed electrophilic borylation reaction so that an intramolecular N→B coordinative bond can be incorporated onto 2-phenylpyridine (**11** in **Figure 8**).[68] During this synthesis, the strong Lewis acidity of BBr_3 promoted the formation of Lewis acid-base adducts, followed by the substitution reaction on the spatially preferential aromatic carbon. The boron center in **11** can be further alkylated to **12** using organometallic reagents. Using the nitrogen-directed substitution strategy, Turner and co-workers recently developed a coplanar acceptor-donor-acceptor molecule **13** featuring N→B coordination (**Figure 8**).[69] Due to the donor-acceptor alternating structure and the coplanarity induced by intramolecular N→B coordination, **13** possessed a narrowed frontier orbital band gap and showed a strong emission reaching the red region of the visible light spectra. As shown in the single-crystal structure of **13**, the bulky phenyl groups on boron prevented the aggregate formation, affording a high quantum yield (33%) in the solid state.

Subsequently, compound **13** was employed as the emitter material in organic light emitting diodes, giving photoluminescence from 600 nm to 700 nm.

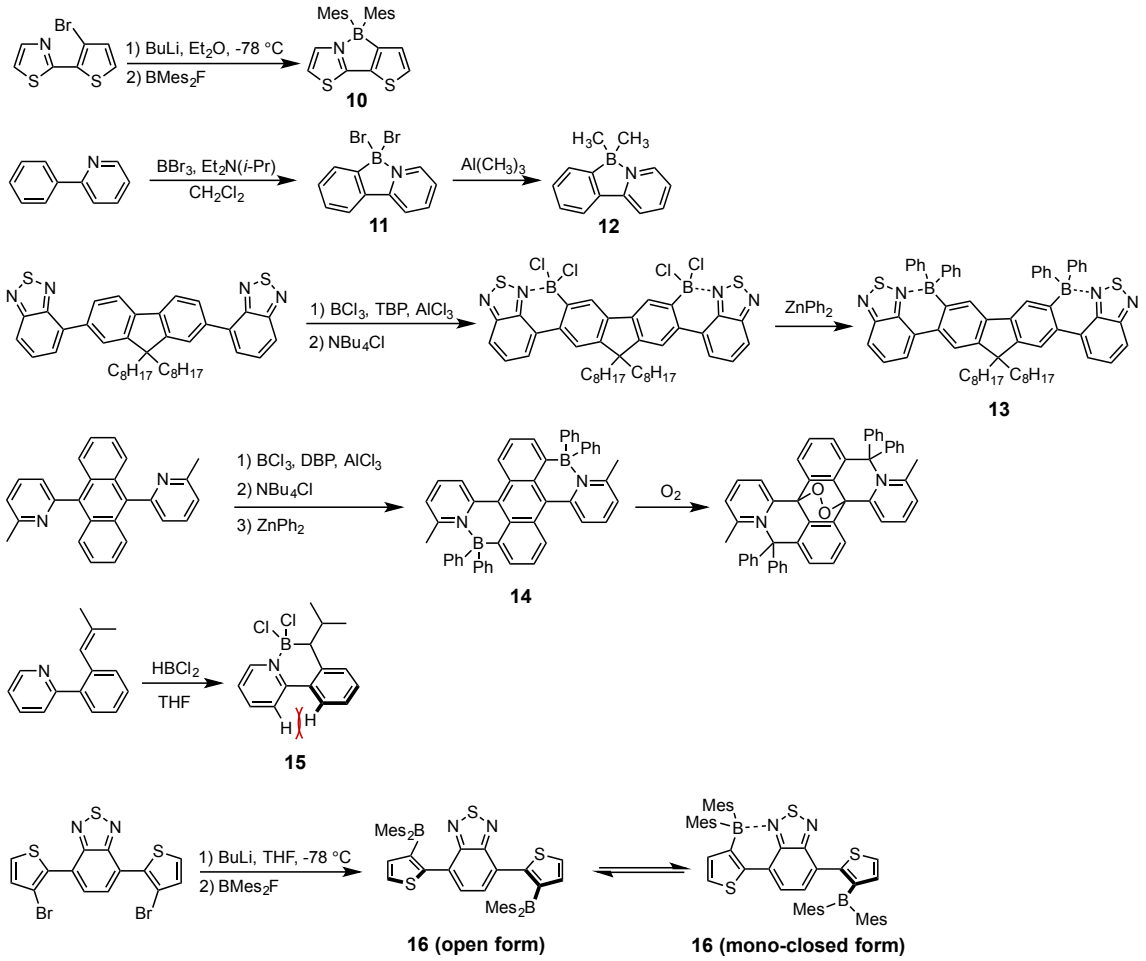

Figure 8. Synthetic examples of incorporating N→B coordinative bonds onto *π*-conjugated molecules.

In 2017, Jäkle *et al* adopted a similar synthetic method and incorporated N→B coordinative interactions into a conjugated backbone that was built upon a anthracene unit.[70] Compound **14** possessed a highly twisted backbone owing to the steric repulsion between the central anthracene and the flanking pyridine units (**Figure 8**). The

incoporation of N→B coordinative interactions into **14** rendered an enhanced electron affinity and a quinonoid type cross-conjugation in the LUMO level. Interestingly, upon the exposure to O_2, this compound underwent a structural transformation into endoperoxide compound, accompanied with a drastic color change.[70] Such a high reactivity of **14** towards O_2 was attributed to its strong absorption of visible light, its small singlet-triplet gap in the excited state, and the release of steric hindrance after the formation of peroxide.

In addition, classical hydroboration has also been introduced as a mild and atom-economic method for the preparation of ladder-type organoborane compounds (**15** in **Figure 8**).[71] The regioselectivity of such a hydroboration was controlled by the anti-Markovnikov effect of hydroboration.[72] The favorable six-membered ring geometry gave rise to a strong N→B coordinative interaction over 25 kcal/mol.[71] Although the conformation of **15** was rigidified by the N→B coordination, the single-crystal structures of **15** showed the dihedral angles between phenyl units and pyridine units to be around 20°,[72] presumably a result of 2,2′-H,H steric repulsion between the two adjacent phenyl units.

The dynamic nature and reversible formation of N→B coordinative interactions can be utilized to tune the backbone conformation, and the hence physical and electronic properties of conjugated π-systems. External stimuli, such as the presence of Lewis basic molecules and elevated temperatures, are expected to weaken the intramolecular N→B coordination by affecting the thermodynamic equilibrium. Wakamiya et al. developed thermochromic materials based on a N→B coordination bridged π-conjugated

molecule **16** (**Figure 8**).[73] Compared to the strong N→B coordinative bonds in **13** and **14** that shared a similar six-member ring architecture, the N→B coordination in **16** was much weaker because of the bulky mesitylene ligand. As a result, the energy difference between the open conformer and the "mono-closed" conformer was as small as 1.02 kcal/mol according to DFT calculations.[73] The coplanar and non-coplanar conformers co-existed in solution, and the temperature variation affected the equilibrium of forming N→B coordinative bonds and changed the population of each conformer. With intramolecular N→B coordination formed at low temperature, the "mono-closed" conformer exhibited a coplanar conjugated backbone and a greatly lowered LUMO level, giving rise to the low-energy absorption band at 575 nm.[73] Such a thermochromic behavior of **16** clearly demonstrated the dynamic nature of intramolecular N→B coordination.

As mentioned above, intramolecular N→B coordination has also been proven to significantly decrease the LUMO energy levels. [43,69,71,74] Such a unique characteristic was utilized by Wang et al. to develop a series of electron-deficient N→B bond bridged conjugated polymers **17**–**20** (**Figure 9**).[75,76] In these cases, two strands of intramolecular N→B coordinative bonds were installed onto a 2,2′-bipyridine unit to induce a coplanar conformation and deep-lying LUMO energy levels. After Stille coupling reaction with thiophene-based monomers, step-ladder polymers **17**–**20** with partially coplanarized conformation were synthesized. The coplanarity of these bipyridine units promoted condensed π–π stacking in the solid state and high electron transport mobilities up to 0.32 $cm^2 V^{-1} s^{-1}$.[75,76] These polymers were successfully incorporated as the active layer

in electronic devices. For example, **17** served as the electron acceptor material in organic solar cells,[75] and **18**–**20** were used as the *n*-type semiconducting materials in FETs.[76]

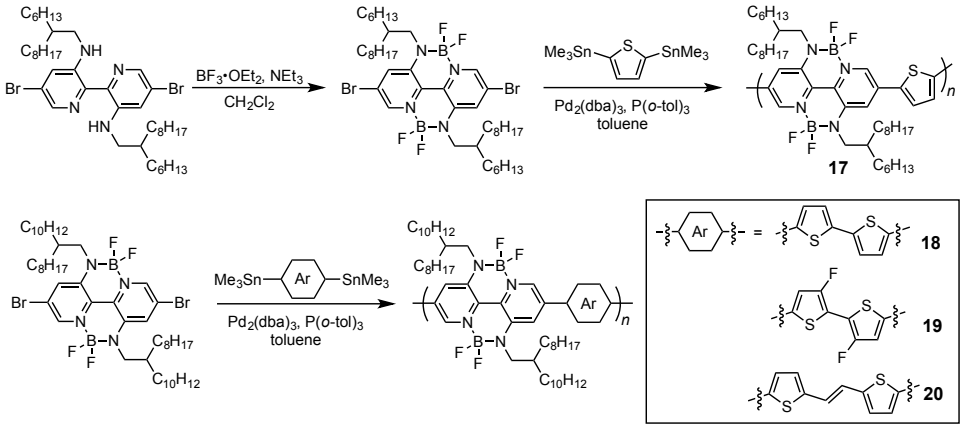

Figure 9. Synthesis of π-conjugated polymers containing N→B coordinative bonds.

1.2.4 Heteroatom Noncovalent Interactions Promoted Coplanarity

A variety of noncovalent interactions between sulfur and different electronegative atoms (N, O, F) have been utilized to control the polymer conformation of thiophene and thiophene-derived conjugated systems.[45,46,53,77-81] These noncovalent binding events were attributed to the partial donation of electron lone pairs of electronegative atoms to the unoccupied σ* orbital of a S−C bond.[82,83] Computational studies showed that the strength of this class of heteroatom interactions are around 0.5 kcal/mol,[53] much weaker than the traditional hydrogen bonds and N→B coordinative interaction. However, these interactions are proved to be capable of stabilizing the coplanar conformation of small molecules and polymers, especially in the solid state. In

fact, we noticed that at the early stage of the development of functional π-conjugated polymers, enhanced coplanarity of the conjugated backbones might be achieved unintentionally by introducing a number of heteroatoms that can in fact form these weak interactions. Moreover, in the past few years, it has become a popular research topic to apply these interactions through a sophisticated design for the purpose of planarizing the backbone conformation for high device performance.

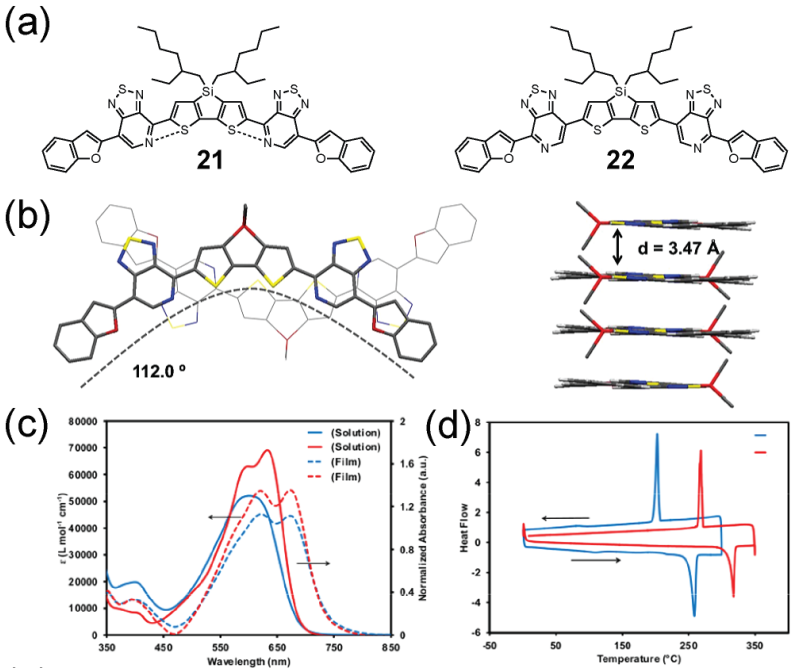

Figure 10. (a) The chemical structures of 21 and 22; (b) single crystal structure and solid-state packing of 21; (c) UV-vis absorption and (d) differential scanning calorimetric traces of 21 (in red) and 22(in blue).

The S…N interaction has been studied extensively and exists widely in conjugated molecules containing thiophene and nitrogen-embedded heterocycles. Bazan *et al.* developed a series of conjugated oligomers composed of thiophene-derived

electron-rich units and electron-deficient pyridalthiadiazole units (**Figure 10a**).[84] In the single-crystal structure of **21**, the distance between sulfur and nitrogen was measured to be 2.89 Å (**Figure 10b**), much smaller than the sum of the van der Waals radii of sulfur and nitrogen (≈3.5 Å), indicating the presence of noncovalent bonding interactions.[84] The coplanar conformation of **21** was, as a result, greatly stabilized, leading to a red-shifted absorption spectrum (**Figure 10c**), compared to a control molecule without an S…N interaction (**22**). The coplanar conformation of **21** further enhanced the aggregation interaction in the solid state, as evidenced by the short π-π stacking distance (**Figure 10b**) and an elevated melting temperature (**Figure 10d**).[84]

Later on, the employment of intramolecular S…F interactions was proved to be an effective strategy to improve the performance of conjugated polymers in organic electronic devices by enhancing the backbone coplanarity. For instance, Heeney and co-workers functionalized poly(thiophene) with fluorine atoms and applied the polymeric materials as the semiconducting layer in FETs.[85] During the synthesis of **23** (**Figure 11**), it was found that fluorinated precursors significantly increased the regioselectivity of the Grignard reaction. Furthermore, according to the DFT optimized geometry, the presence of fluorine resulted in a high energy barrier for torsional motion due to the S…F interaction, affording a coplanar backbone of polymer **23**. In comparison with its non-fluorinated analogue, **23** demonstrated a decreased solubility, an increased melting temperature and a higher crystallization enthalpy, which were consistent with the stronger aggregation induced by the enhanced backbone coplanarity and rigidity.[85]

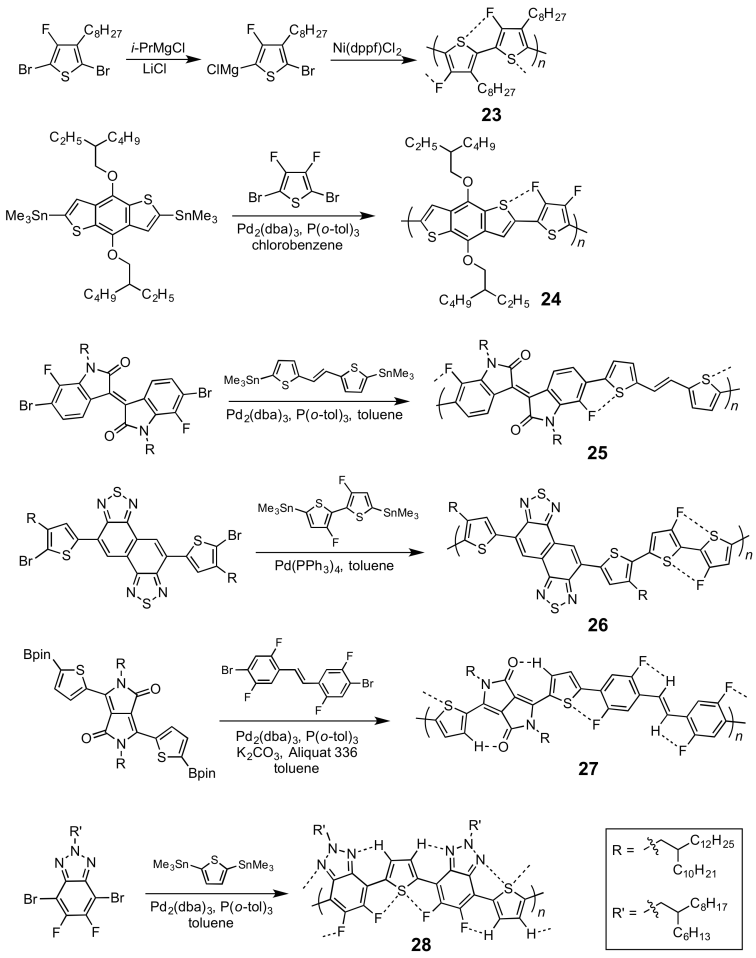

Figure 11. Synthesis of π-conjugated polymers 23, 24,25, 26, 27, and 28 with conformation controlled by S…F electrostatic interaction.

In terms of device performance, **23** gave a significantly increased hole mobility in FETs (0.70 $cm^2 V^{-1} s^{-1}$) owing to its coplanar backbone. In 2015, Beaujuge et al. reported the synthesis of **24**, followed by a systematic study on its coplanar conformation (**Figure 11**).[86] Both theoretical computation and solid-state ^1H-^1H NMR analysis revealed a coplanar conformation and the S…F interaction in **24**. The enhanced backbone coplanarity of **24** contributed to its high hole mobility measured from the space-charge limited current experiments. More recently, fluorinated π-conjugated

monomer were incorporated into donor–acceptor alternating copolymers (**25**,[87] **26**,[88] **27,**[58] and **28**[89]), taking advantage of of its ability to induce a coplanar conformation by forming S…F interactions or C−H…F hydrogen bonds (**Figure 11**). With a partially or fully coplanar conformation induced by these noncovalent interactions, these polymeric materials showed high FET mobilities,[87,89] and PCE[88] in organic electronic devices.

In the past few years, installing alkoxyl chains has been employed as an effective strategy to coplanarize the backbone conformation by forming S…O interactions in thiophene-containing π-conjugated molecules or polymers.[18,46,90] In this context, a series of high-performance organic semiconducting polymers (**29**, **30**, and **31**) were developed based on S…O conformational lock (**Figure 12a**).[57,58,90-93] In one of the pioneering reports, Huang, Marks, et al. identified the noncovalent S…O interactions clearly and unambiguously characterized the resulting coplanar conformation through single-crystal X-ray diffraction of **32** (**Figure 12b**).[91] Such a coplanar and regioregular segment in the polymer backbone afforded the well-defined solid-state packing and a high electronic device performance. Recently, Bo et al. Demonstrated [18]that with a fully coplanar conformation locked by S…O interactions and hydrogen bonds, a small conjugated molecule **33** (**Figure 12c**) possessed an extended effective conjugation length and an increased quantum yield. Therefore, the absorption spectrum was broadened and the nonradiative energy loss was suppressed, leading to a boosted PCE value up to 9.60%, when compound **33** was used as the acceptor material in a solar cell device.

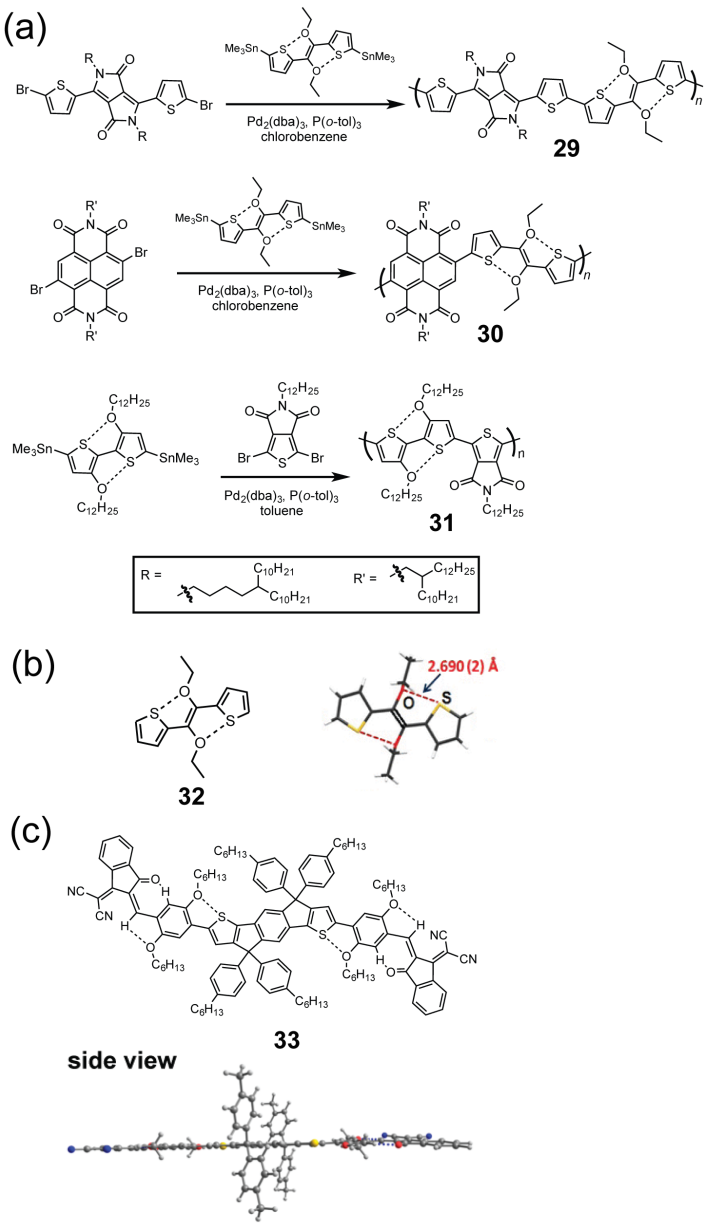

Figure 12. (a) Synthesis of 29, 30, and 31 featuring a partially coplanar conformation promoted by S…O electrostatic interactions; (b) the chemical and single crystal structure of 32; (c) the chemical structure and DFT optimized geometry of 33 featuring a fully coplanar conformation promoted by S…O electrostatic interactions and hydrogen bonds.

1.3 Challenges and Outlook

The employment of dynamic noncovalent bonds serves as a ubiquitous and promising strategy to control the conformation of π-conjugated systems. With a coplanar conformation promoted by noncovalent bonds, π-conjugated molecules and polymers have controllable properties and great potential in materials application. Previous sections summarize important developments on the employment of noncovalent bonds to achieve control on coplanar conformation of π-conjugated molecules. A number of examples are listed to demonstrate the structure–property relationships of torsional motion in π-conjugated systems. Controlling conformation of a π-conjugated backbone with dynamic noncovalent bonds represents a promising strategy to access desirable physical properties and high performance in materials applications. In order to fulfill the potential of these noncovalent-bond-bridged conjugated materials, however, challenges in the molecular design, synthesis, characterization, and processing need to be addressed.

One of the major advantages of using noncovalent bonds is the possibility to achieve an active control over conformation so that an accurate structure–property relationship can be established. Following this principle, the desirable properties can be accessed by controlling the conformation precisely. Only a few examples[41,64,73] demonstrated tunable properties and materials performance through conformational control. To achieve such a goal, a thorough molecular design is required, in which two major factors should be taken into consideration: (i) the tunability of noncovalent bond strength and (ii) the building units of π-conjugated backbone. In terms of noncovalent bond strength, a strong and robust noncovalent bond can significantly stabilize the

desired conformation even in some extreme conditions,[94] while a weak noncovalent bond will be highly sensitive to the external stimuli[95] that triggers the dissociation to induce the conformational change. For instance, the bulky mesityl groups in **16** significantly weakened the originally strong N→B coordinative interaction.[73] Therefore, the reversible formation/dissociation of N→B coordination can be activated, giving rise to the thermochromic behavior of this compound. The other important design principle involves the selection of proper building units to pursue the desired properties and application. In the examples of using traditional hydrogen bonds to achieve the coplanarity, a band gap smaller than 1.8 eV (with $\lambda > 650$ nm) has not yet been achieved due to the lack of intrinsic mechanism for band gap narrowing and effective orbital overlapping on available hydrogen bonding units.[41,50] From a synthetic perspective, these issues can be resolved by the development of novel building blocks that integrates noncovalent bonds with structural features already exhibited promising materials performances. In this scenario, the additional coplanar character induced by noncovalent bonds is expected to further improve the performance of π-conjugated systems. Moreover, as demonstrated in **1**[41] and **15**,[72] the steric hindrance between the conjugated backbone units can still twist the molecular conformation even in the presence of intramolecular noncovalent binding. To avoid such steric effects, heterocyclic building units lacking such steric repulsion, such as thiazole and pyrazine, can be introduced.[96]

An accurate characterization is essential to correlate the backbone conformation with properties and materials performance. For noncovalent bond bridged π-conjugated

molecules, the characterization includes three major aspects: monitoring noncovalent binding events, determining molecular conformation, and characterizing solid-state properties. In the past decade, momentous progress on the characterization of noncovalent binding events has been made.[42,54,84,97] The noncovalent interactions can be monitored in both solution phase and in the solid state using experimental and theoretical tools, such as ^{1}H NMR for hydrogen bonds,[41,61] ^{11}B NMR for N→B coordinative bonds,[42,70,73] FT-IR,[41] DFT calculations, etc.[53] In addition, UV-vis, fluorescence spectroscopy, and cyclic voltammetry can be used to investigate the opto-electronic properties of π-conjugated systems to indirectly probe the molecular conformations.[48,64,73] For the solid-state properties, AFM and SEM were applied to characterize the thin film morphology.[46,98] Meanwhile, the employment of GIWAXS and powder X-ray diffraction can determine crystallinity and solid-state packing.[54,91] Methods to directly determine molecular conformation are still rather limited, despite that a number of physical organic methods can be employed to determine molecular conformation indirectly. Single crystal X-ray diffraction analysis[42,84,96] and computational study [53]are still the primary tools for conformational characterization. The crystallographic method often only demonstrates the static conformation in the solid state while the dynamic motion in the solution phase cannot be represented in crystal structures. Computational methods, meanwhile, are often precise only for small π-conjugated systems. Therefore, it is still an elusive task to determine the molecular conformation precisely, particularly for polymers. Last but not least, active control of the conformation using external stimuli, such as temperature change or competing chemical

reagents are interesting means to induce the formation or dissociation of noncovalent interactions during the characterization. It would be ideal if the molecular properties of π-conjugated molecules could be monitored in a real-time manner in the presence of external stimuli to correlate the conformation with molecular properties.

The enhanced coplanarity of π-conjugated backbones often promotes intermolecular π–π stacking interactions, usually resulting in limited solubility, particularly for conjugated polymers. For example, the poor solubility of **6** prevented the molecular weight determination in solution phase.[63] Such a poor solubility hinders the further development on this type of conjugated molecule in the aspects of synthesis, characterization, and application. The dynamic nature of noncovalent bridging bonds, however, provides a promising solution to this problem, because the dissociation of these noncovalent bonds can lead to a less rigid and more soluble conjugated backbone. In this context, using competing chemical reagents as solvents can serve as an effective strategy to increase the solubility. After solution processing these organic conjugated materials into the solid state, the competing reagents can be removed so that the coplanar conformation and rigid structures will be restored by turning on the noncovalent bonds.

Despite these challenges, more thrilling discoveries in this field will be achieved in the future through integrated efforts made by chemists, materials scientists, and engineers.

CHAPTER II

MOLECULAR COPLANARITY AND SELF-ASSEMBLY PROMOTED BY INTRAMOLECULAR HYDROGEN BONDS*

2.1 Introduction

Molecular conformation represents one of the most important structural features for organic molecules. In a π-conjugated compound, the conformation not only shapes the properties of individual molecules but also plays an essential role in determining intermolecular interactions and selfassembly behaviors. Generally, a coplanar backbone of a conjugated molecule facilitates extended π-delocalization,[99,100] consequently inducing enhanced intramolecular charge transfer and a narrowed band gap.[43,44,48] Moreover, coplanarity of conjugated skeletons promotes strong intermolecular π-π interactions and electronic coupling,[54] leading to self-assembly in solution,[9,10,101] formation of well-defined nano/microstructures,[12,102] and condensed packing modes in the solid state.[103,104] Therefore, pursuing coplanar conformations becomes an important strategy in the development of functional π-conjugated organic materials.

The prevailing strategy to achieve such a goal is the construction of fused-ring constitutions by forming additional strands of covalent bonds so that a coplanar conformation is enforced. On one hand, this method is efficient in affording excellent optoelectronic properties of individual molecules[36,37] and endorses strong intermolecular

*Reprinted with permission from "Molecular Coplanarity and Self-Assembly Promoted by Intramolecular Hydrogen Bonds" Zhu, C.; Mu, A. U.; Lin, Y.-H.; Guo, Z.-H.; Yuan, T.; Wheeler, S. E.; Fang, L. *Org. Lett.* **2016**, *18*, 6332. Copyright 2016 American Chemical Society.

interactions, which can be further translated into the formation of nano-/microscale assemblies in the solid state.[12,38,39,105,106] On the other hand, the covalently fused constitution often leads to synthetic and processing challenges and does not allow active control over the torsional conformation of these conjugated molecules.

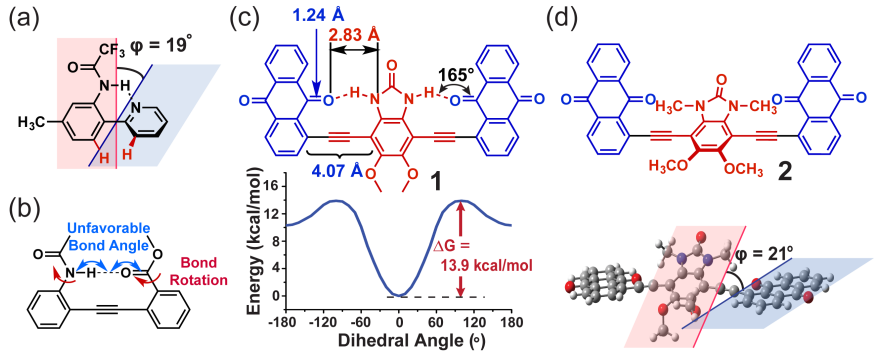

Figure 13. (a) An intramolecular hydrogen bonded 2-phenylpyridine derivative with a dihedral angle measured from the single crystal structure.[110] (b) A *p*-phenylene ethynylene derivative with a parallel linear hydrogen bond.[111] (c) The structural formula of 34 and the potential energy surface scan [B97D/6-31G(d,p)] of 34 by changing the dihedral angle between the hydrogen bond donating units and accepting units. (d) The structural formula and DFT optimized conformation [B3LYP/6-311G(d,p)] of 35.

Alternatively, the employment of intramolecular noncovalent bonds, such as hydrogen bonds,[10,40,41,48,54,64,107,108] B−N Lewis acid−base pairing,[42,43,109] metal coordination,[44] and van der Waals forces,[46,53,90] could serve as a promising approach to induce the desired conformation in a π-conjugated molecule while enabling dynamic conformational control. Unlike covalent bonds, the thermodynamically driven formation of noncovalent bonds is reversible,[41,42,48] enabling on-demand control of molecular conformation and therefore active manipulation over molecular/supermolecular properties.[41]

Among various types of noncovalent forces, hydrogen bonds stand out as ideal candidates because of their tunable strength and directionality,[49] allowing for precise control of molecular conformation. The introduction of conjugated coplanarity by intramolecular hydrogen bonds, however, is still a challenging task. For example, in a 2-phenylpyridine-based system (**Figure 13a**), the coplanarity is distorted by 2,2′-H,H repulsion even in the presence of an intramolecular hydrogen bond.[110] Such steric repulsion can be avoided in a 1,2-diphenylethyne derived model compound, in which linear intramolecular hydrogen bonds are installed in parallel (**Figure 13b**).[48,107,108,112,113] Modern theoretical calculations, however, suggested that the linear hydrogen bond was not as favorable as a bent hydrogen bond in terms of the strength.[114] Moreover, most hydrogen bond donating and accepting moieties were connected to conjugated backbones through rotatable single bonds, which could lead to increased flexibility and hence a greater entropy penalty when adopting the coplanar conformation. In addition, although some promising molecular properties have been reported,[41,48] the expected self-assembly and favorable solid-state packing have not been clearly demonstrated yet. Herein, we report the achievement of unambiguous molecular coplanarity, controllable self-assembly, and solid-state fiber formations of a large model π-system **34** (**Figure 13c**), in which well-defined intramolecular hydrogen bonds play a crucial role in governing these characters.

2.2 Molecular Design

In compound **34**, 1,4-bis(phenylethynyl)benzene was selected as the backbone to avoid the aforementioned 2,2′-H,H steric repulsion.[48,107,108,112,113] The hydrogen bonding moieties were incorporated into the backbone through a fused-ring constitution. This strategy decreases the entropy penalty when the molecule adopts the desired coplanar conformation and, therefore, enhances the strength of the intramolecular hydrogen bonds and the molecular rigidity. Meanwhile, these preorganized hydrogen bonds adopted a bent structure ($\angle$N− H···O ≈ 165° measured from optimized geometry) and a favorable binding orientation at oxygen.[114,115] Using the reported bond lengths from crystal structures of related building blocks,[116,117] the distance between hydrogen bonding nitrogen and oxygen was estimated to be ∼2.84 Å (**Figure 13c**), falling into the range where hydrogen bonds can be formed effectively.[95] In addition, condensed solid-state packing,[54,103] aggregation in solution, and self-assembly into well-defined nano/microstructures[12,102] were expected once the strong hydrogen bonds and high molecular rigidity were achieved. To validate this molecular design, density functional theory (DFT) was employed to examine the torsional energy landscape of **34**. By fixing the anthraquinone units into the same plane, the torsional potential energy was computed by changing the dihedral angle between the hydrogen bond donor and the anthraquinone plane. The lowest energy was found in the coplanar conformer. The 13.9 kcal/mol potential well suggested that this coplanar conformation was strongly stabilized by the hydrogen bonds (**Figure 13c**). In parallel, a control molecule (**35**) was designed by inhibiting the hydrogen bonds by methylation. Geometry optimization of this molecule

revealed a twisted backbone due to the steric interaction between methly groups and the anthraquinone units (**Figure 13d**).

2.3 Synthesis and Characterization

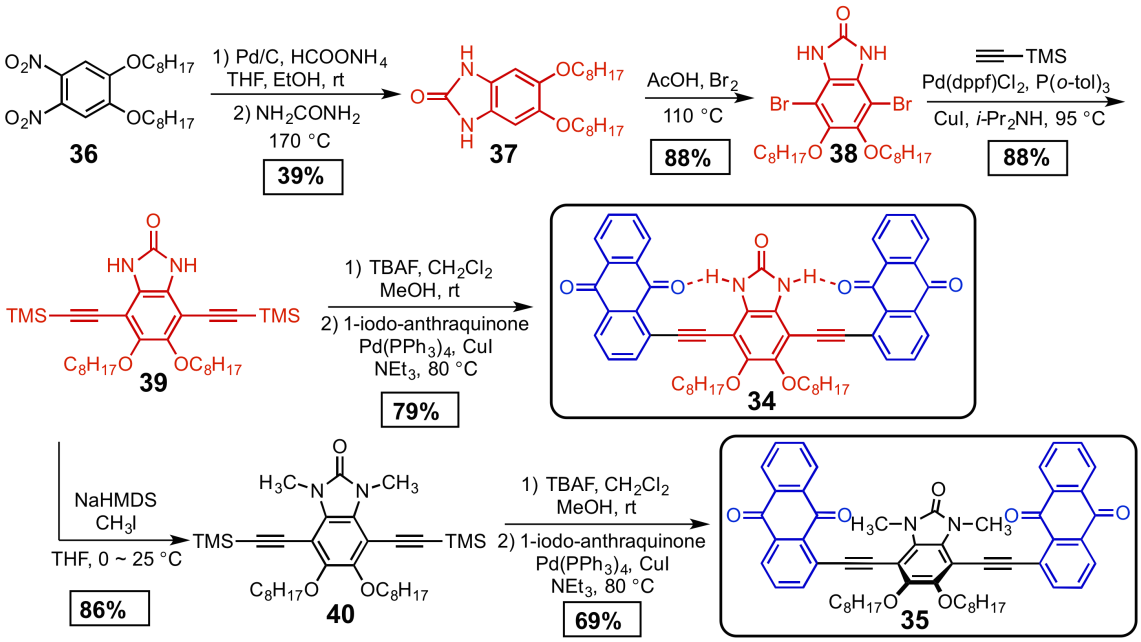

Figure 14. Synthesis of the coplanar model compound 34 and its non-coplanar counterpart 35

The synthesis toward **34** started with compound **36** prepared according to a literature report (**Figure 14**).[118] The linear n-octyl chains were installed to increase the solubility of **34** without perturbing the potentially strong π–π stacking between the coplanar backbones.[38,119] After reducing the nitro groups in **36** into amine functionalities, the intermediate was treated directly with molten urea, affording the hydrogen bond donating intermediate (**37**). After bromination, Sonogashira coupling of **38** gave

intermediate **39**. The final product **34** was obtained after deprotection of **39** followed by another Sonogashira coupling with 1-iodo-anthraquinone. Compound **35** was prepared from **39** as well. After methylation, the intermediate **40** was converted into **35** using a similar tandem procedure.

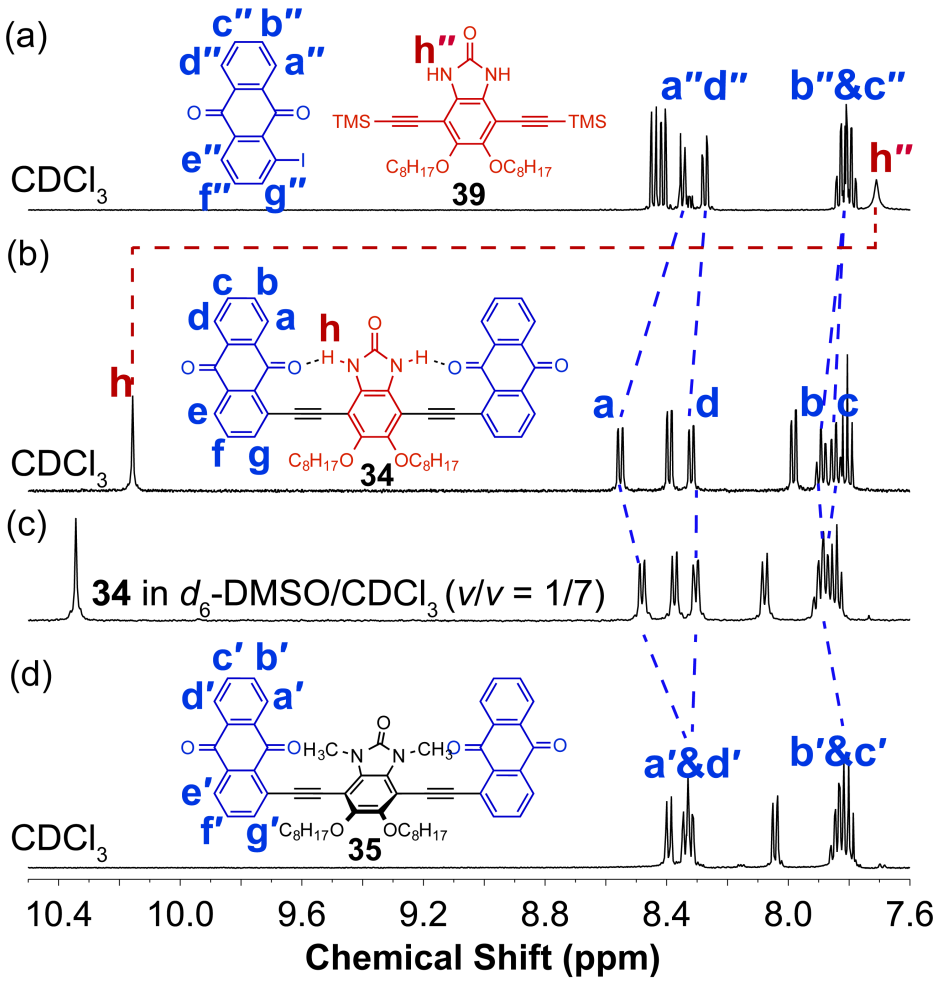

Figure 15. ^{1}H NMR spctra (500 MHz, 295 K) of (a) a mixture of 1-iodoanthraquinone and 39 in $CDCl_3$; (b) 34 in $CDCl_3$; (c) 34 in d_6-DMSO/$CDCl_3$ (v/v =1/7) and (d) 35 in $CDCl_3$.

For compound **34**, a remarkable downfield shift of the N−H proton signal (10.15 ppm) was observed in $CDCl_3$ at room temperature, in contrast to that in its precursor **39** (7.72 ppm), corroborating the formation of hydrogen bonds in solution at room temperature (**Figure 15**). Because of the preorganized geometry and rigid nature of the hydrogen bonding moiety, the hydrogen bonds in **34** were expected to be strong and robust in solution and in the solid state. Although variable-temperature ^1H NMR experiments revealed a slight dissociation of these hydrogen bonds at high temperatures, the chemical shift of the N−H proton remained in the downfield region at 9.99 ppm at 65 °C in $CDCl_3$ and 10.27 ppm at 80 °C in d_6-benzene, respectively (**Figure 16**). This result indicated that intramolecular hydrogen bonds maintained control over the coplanar molecular conformation even in these boiling solutions.

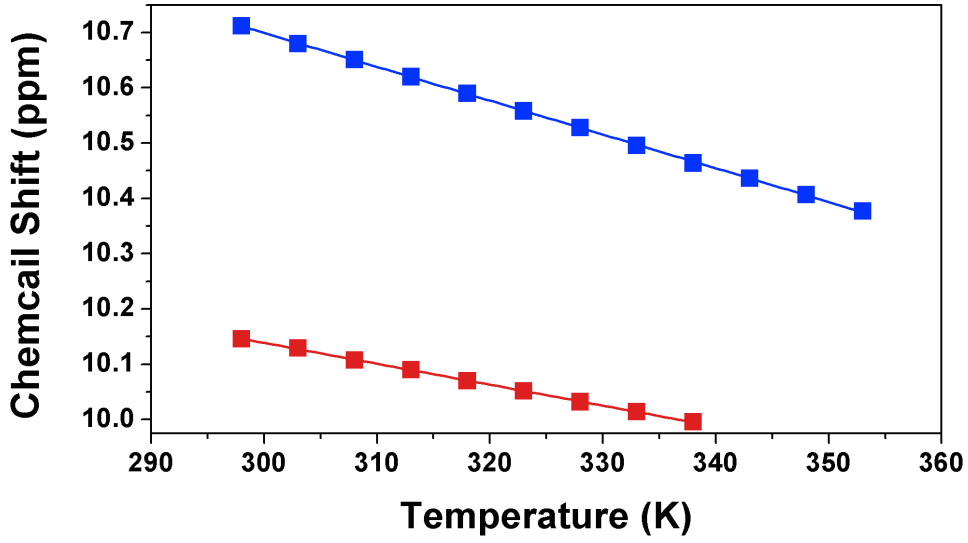

Figure 16. The plot of the chemical shifts of Proton h in 34 in $CDCl_3$ (red) and d_6-benzene (blue) against temperature according to ^1H NMR (500 MHz) experiement results. The temeperature coefficients were calculated to be −3.7 ppb/K and −6.0 ppb/K, respectively.

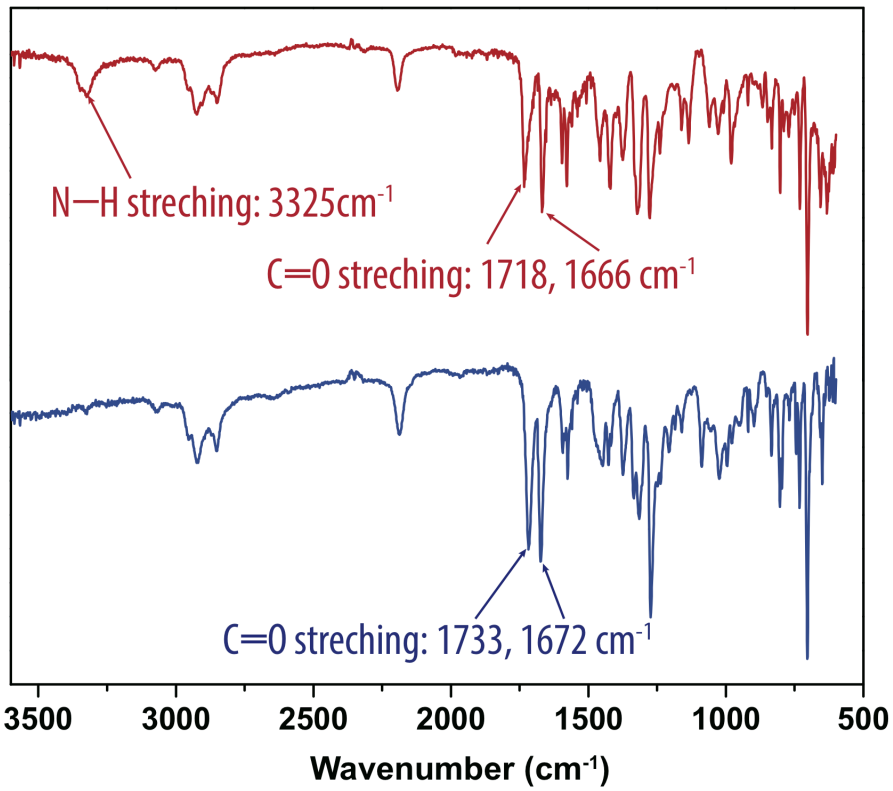

Figure 17. FT-IR spectra of 34 (in red) and 35 (in blue) in the solid state at room temperature.

The Fourier transform infrared spectra (**Figure 17**) showed significantly weakened N−H stretching in **34** (3325 cm^{-1}) compared to a non-hydrogen bonded amide N−H stretching (3450−3460 cm^{-1}),[115] confirming these robust hydrogen bonds in the solid state.

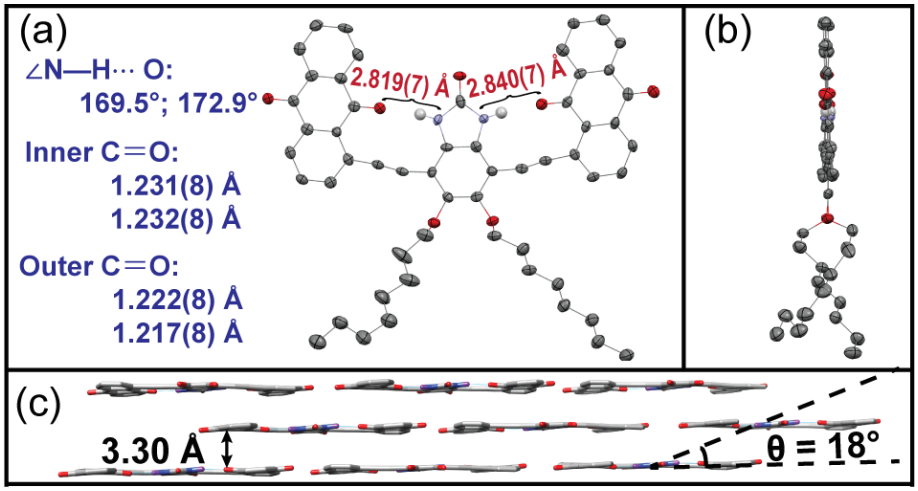

Figure 18. (a) Front view and (b) side view of single crystal structure of 34. The thermal ellipsoids were scaled to the 50% probability level. (c) A side view of the packing mode of 34 in single crystal. The octyl chains and $C_2H_2Cl_4$ solvent molecules are omitted for clarity.

The solid-state structure of **34** was elucidated unambiguously using single crystal X-ray diffraction. The distances between the hydrogen-bond-donating nitrogen atom and the hydrogenbond-accepting oxygen atom were 2.819(7) Å and 2.840(7) Å on each side respectively (**Figure 18a**), close to the predicted values, falling into a strong-hydrogen-bond-forming distance.[95] The bond lengths of the inner C=O were longer than those of the outer C=O, in agreement with the decreased carbonyl stretching frequency after accepting hydrogen bonds (**Figure 17**). An almost coplanar backbone of **34** was observed (dihedral angles less than 4° between the planes of the hydrogen bond donor and acceptors) (**Figure 18b**). The ethynylene linker was slightly bentin the crystal structure due to the formation of hydrogen bonds. The extended coplanar backbone allows for the condensed packing with a π–π stacking distance of 3.30 Å (**Figure 18c**), which is even shorter than the interlayer distance of graphite (3.35 Å).[120]

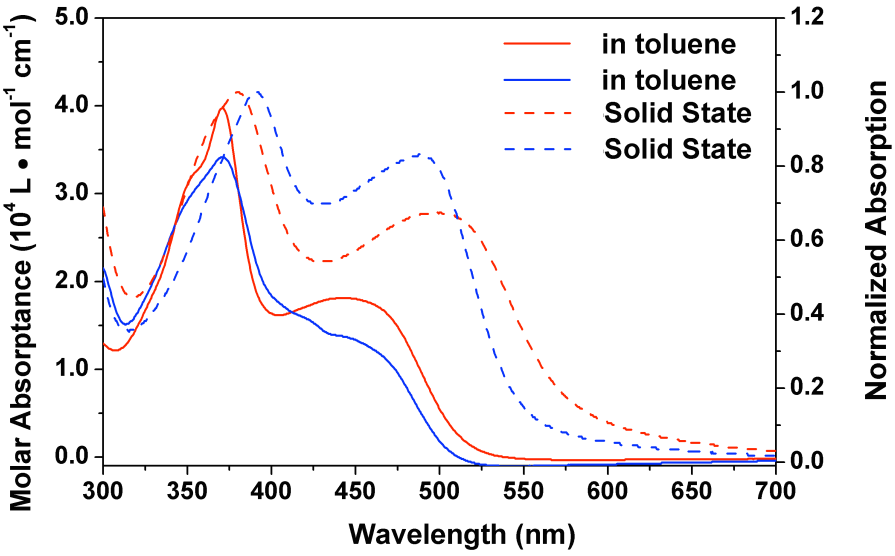

Figure 19. UV-vis absorption spectra of 34 (in red) and 35 (in blue) in toluene solution (1.0×10^{-5} mol/L) and in the solid state (spin-cast thin films on quartz substrates).

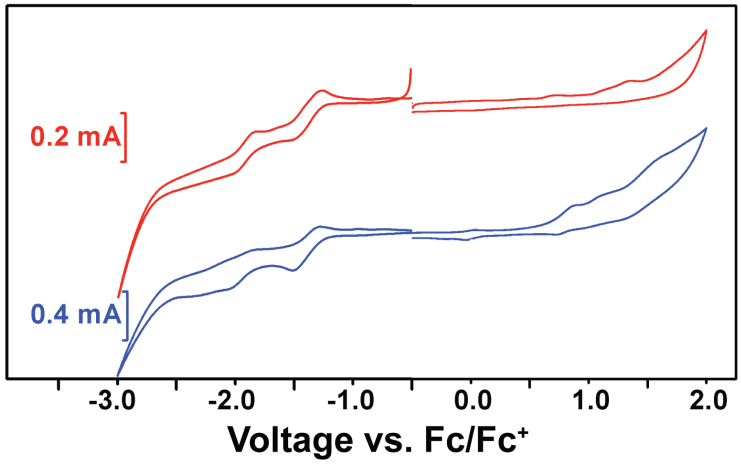

Figure 20. Cyclic voltammetry traces of 34 (in red) and 35 (in blue) in CH_2Cl_2 (concentration: 1.0×10^{-3} mol/L; scan rate: 100 mV/s).

In comparison to the control compound **35**, the hydrogen bond formation and the conformational coplanarity of **34** impacted its electronic structure by facilitating a more coherent electronic conjugation of the backbone.[43,48,107] Despite the very similar

constitutional structures of **34** and **35**, the absorption onset of **34** was 20 nm red-shifted compared to that of **35** (**Figure 19**). Furthermore, cyclic and differential pulse voltammetry (**Figures 20**, **21**) revealed a lowered LUMO level (−3.44 eV) and a smaller band gap (1.98 eV) of **34** compared to that of **35** (2.04 eV).

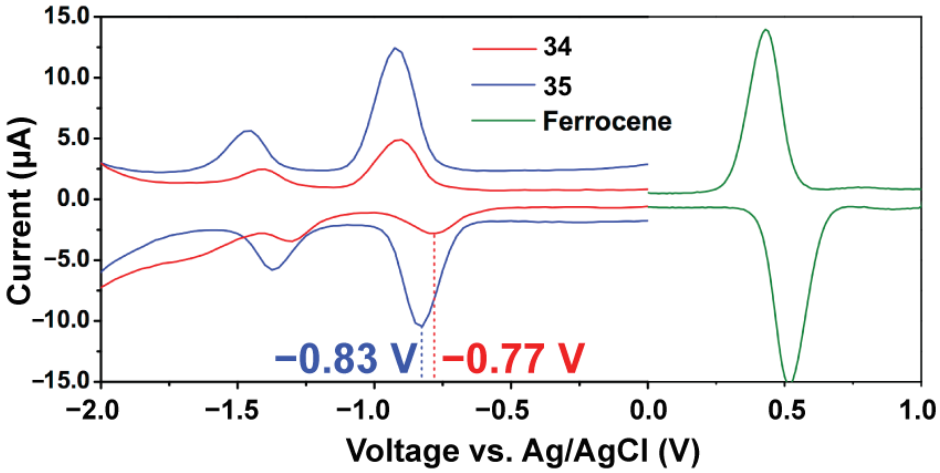

Figure 21. DPV traces of 34 and 35 (1.0×10^{-4} mol/L) in CH_2Cl_2 with $TBAPF_6$ as the electrolyte. The scan period, width, and height were 100 ms, 10 ms, and 50 mV, respectively, with a potential increment of 10 mV.

2.4 Controllable Aggregation and Self-Assembly

The robust coplanar conformation and tight intermolecular π−π stacking of **34** were expected to lead to aggregation/selfassembly of the molecule.[121-123] To study this character, variableconcentration ^{1}H NMR investigations of **34** and **35** were performed in $CDCl_3$. At 295 K, as the concentration of **34** increased, the chemical shifts of the aromatic protons were shifted upfield by ~20 ppb (**Figure 22**), indicating an aggregation process.[119,124] In contrast, the spectra of **35** did not show any significant upfield shift even at a much higher concentration (**Figure 22**). Such a drastic difference was

attributed to the hydrogen bond induced coplanarity of **34**, which enhanced π–π stacking in solution and promoted the aggregation, while the twisted backbone and active torsional motion of **35** prevented efficient aggregation.

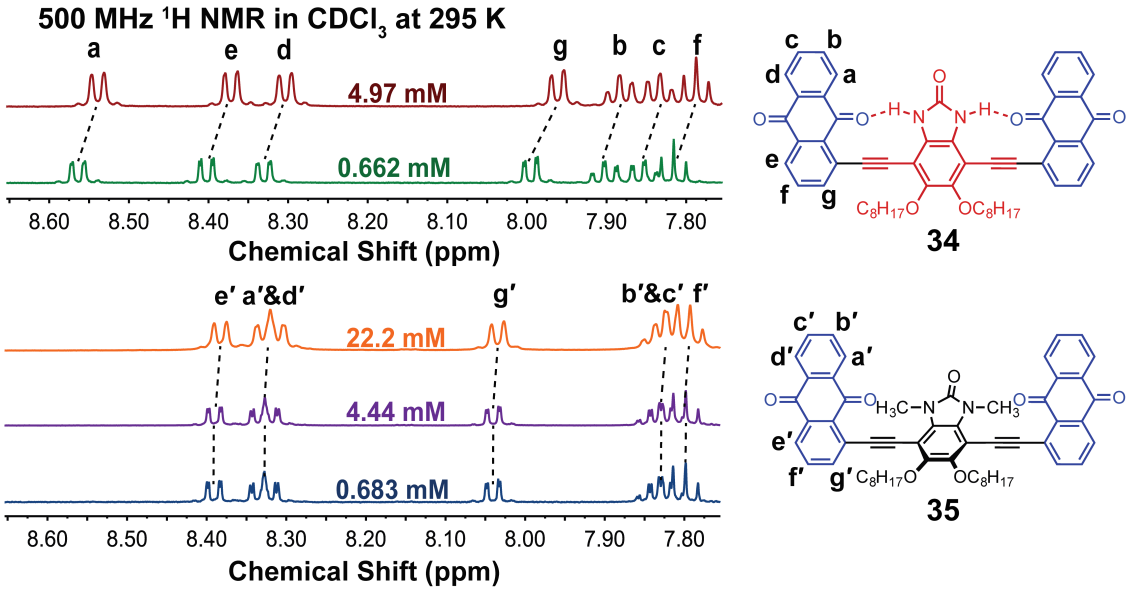

Figure 22. The aromatic region of ^{1}H NMR spectra of 34 and 35 in $CDCl_3$ in different concentrations

The selfassociation constant of **34** in $CDCl_3$ was calculated to be 83 M^{-1} at 295 K, assuming an isodesmic aggregation model. Such a large association constant was comparable with literature reported rigid macrocyclic molecules.[121] To further quantify the thermodynamic parameters of this aggregation process, selfassociation constants were measured at different temperatures (**Figure 23a**). The van't Hoff plot revealed the aggregation enthalpy change of **34** to be −8.86 ± 0.43 kcal/mol and the entropy change to be −21.4 ± 1.4 cal/(mol K), demonstrating a strongly enthalpy-driven process.

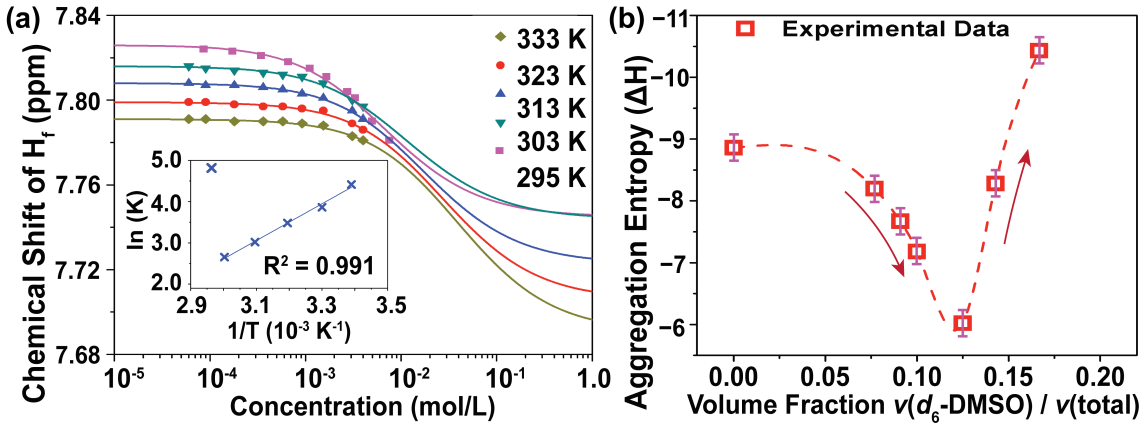

Figure 23. (a) Temperature- and concentration-dependent ^{1}H NMR chemical shifts of proton *f* of 34, fitted with the isodesmic model; the inset is a van't Hoff plot of aggregation constants at different temperatures. (b) Aggregation enthalpy of 34 in $CDCl_3$/d_6-DMSO mixed solvents while increasing the volume fraction of d_6-DMSO.

To confirm the mechanism of the intramolecular hydrogen bond-promoted self-assembly, the aggregation properties of **34** were investigated with the addition of DMSO, a hydrogen bond competing solvent. In general, the addition of a hydrophilic solvent, such as DMSO, to a solution of nonpolar compounds is expected to increase the aggregation because of the enhanced hydrophobic interaction in between the solute molecules.[121-123] For compound **34**, however, it was expected that DMSO should decrease the association constant because of the disruption of intramolecular hydrogen bonds. Indeed, by adding up to 14% (volume fraction) of DMSO to a $CDCl_3$ solution of **34**, the aggregation enthalpy became less negative and the association constant decreased (**Figure 23b**). The hydrophobic aggregation was not observed until the fraction of d_6-DMSO was increased over 17%, where the hydrophilic nature of DMSO started to predominate. This observation confirmed that the intramolecular hydrogen

bond was playing a crucial role to affect the aggregation behavior of **34** by keeping the coplanar conformation and locking the torsional motion. Such controllable aggregation behavior of **34** demonstrated the advantage of the intrinsic dynamic nature of noncovalent bonds when used for conformational control.

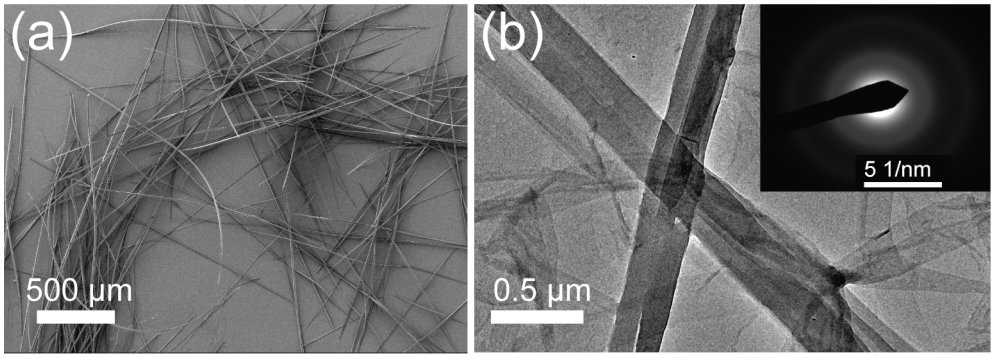

Figure 24. (a) SEM images of nano-/microfibers of 34 grown from slow evaporation of CH_2Cl_2 solutions. (b) TEM images of these fibers with the SAED pattern.

The coplanar backbone, strong anisotropic π–π interactions, negative aggregation enthalpy, and the linear peripheral octyl chains distinguished **34** as an ideal candidate for the growth of one-dimensional organic nano-/microstructures.[119] From a CH_2Cl_2 solution of **34**, one-dimensional fibers with a high aspect ratio (over 500) were obtained feasibly by slow evaporation (**Figure 24a**) and vapor diffusion. Under SEM, these fibers showed diameters ranging from 0.3 to 8 μm with the lengths reaching several millimeters (**Figure 24a**). Under transmission eletron microscopy (TEM), a series of ring-like diffraction patterns were observed on SAED images (**Figure 24b**), suggesting a certain extent of ordered arrangements in these fibers, consistent with the powder X-ray diffraction measurement (**Figure 25**).[125]

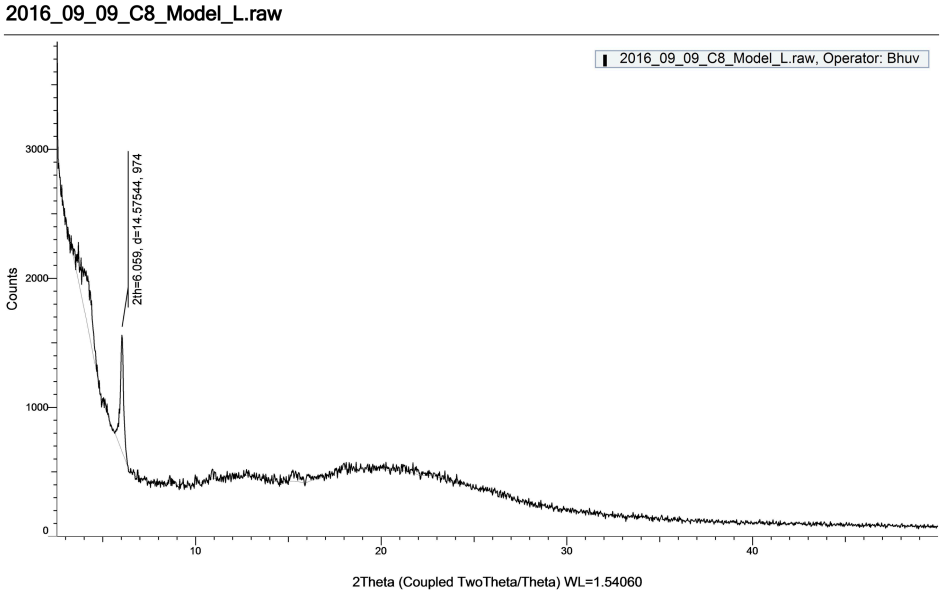

Figure 25. Powder X-ray diffraction map of fibers of 34 grown by slow evaporation in CH_2Cl_2.

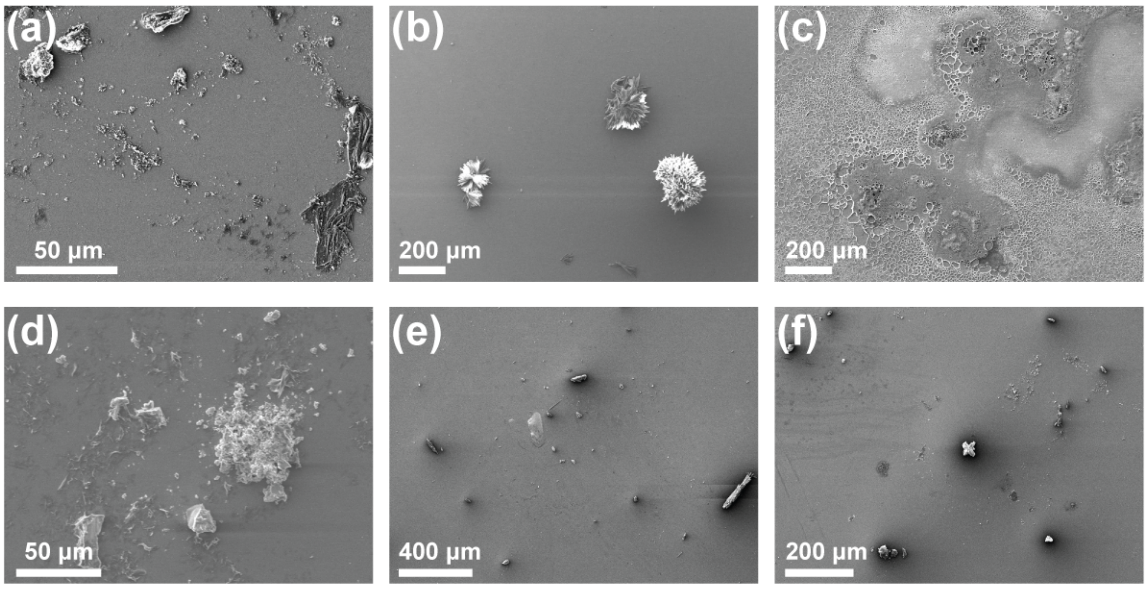

Figure 26. SEM images showing aggregates of 35 grown by slow evaporation using (a) CH_2Cl_2 and by vapor diffusion using (b) CH_2Cl_2/diethyl ether, (c) $CHCl_3$/pentane, (d) THF/pentane, (e) toluene/hexane and (f) DMF/ethanol.

In contrast, compound **35** did not exhibit any self-assembled fibers due to the lack of the intermolecular aggregation enthalpy as the driving force (**Figure 26**). Such a distinctive difference between **34** and **35** indicated the significance of using intramolecular noncovalent bonds in promoting the self-assembly of molecules into well-defined solid-state structures.

2.5 Conclusion

In conclusion, the investigation of model compound **34** and its non-hydrogen bonded analogue **35** clearly demonstrated the significant impact of preorganized intramolecular hydrogen bonds on molecular conformation and intermolecular selfassembly. These hydrogen bonds were designed to force the molecules to adopt a thermodynamically stable coplanar conformation. This robust coplanarity induced strong intermolecular aggregation and preferential self-assembly into one-dimensional fibers in the solid state. Overall, this work not only establishes a fundamental correlation between intramolecular noncovalentbonds and molecular/supramolecular properties but also enables practical strategies for tailoring material properties of conjugated organic species through noncovalent conformational control.

2.6 Experimental Section

2.6.1 General Methods

Starting materials and reagents were purchased from Sigma Aldrich, Acrons Organics, Alfa Aesar or Oakwood and used as received. THF were dried using IT pure

solvent system (PureSolv-MD-5) and used without further treatment. ^{1}H, ^{13}C NMR were recorded on the Varian Inova 500 MHz spectrometer. ^{1}H and ^{13}C chemical shifts were reported in ppm relative to the signals corresponding to the residual non-deuterated solvents ($CDCl_3$: ^{1}H 7.26 ppm, ^{13}C 77.16 ppm) or the internal standard (tetramethylsilane: ^{1}H 0.00 ppm). The broad singlet at ~1.55 ppm on ^{1}H NMR spectra represents the resonance signal of H_2O in $CDCl_3$. High resolution electrospray ionization (ESI) mass spectra were measured on Applied Biosystems PE SCIEX QSTAR. Column chromatography was carried out using Biotage® IsoleraTM Prime instrument with various size of SiO2 Biotage ZIP® cartridge. Preparative gel permeation chromatography (GPC) was performed in chloroform solution at room temperature using JAI recycling preparative HPLC (LC-92XXII NEXT SERIES). UV-vis absorption spectra were recorded on Shimadzu UV-2600 Spectrophotometer. Fourier transform infrared (FT-IR) spectra were recorded with ZnSe ATR using Shimadzu IRAffinity-1S. Surface coating was carried with a Cressington Sputter Coater and the coating thickness was monitored by Cressington Thickness Controller. Scanning electron microscopy (SEM) images were recorded with JEOL JSM-7500F field emission scanning electron microscope. Transmission electron microscopy (TEM) images were recorded with JEOL JEM-2010 transmission electron microscope.

2.6.2 Synthesis

37: Compound **36** (2.4 g, 5.5 mmol) was dissolved in a mixture of THF (40 mL) and EtOH (80 mL). To the solution, 10% Pd/C (0.60 g) and HCO_2NH_4 (60 g) were

added. The mixture was stirred at room temperature overnight. Then the mixture was filtered and the filtrate was transferred to another flask under N_2. The solvents were removed under vacuum. Urea (40 g) was added to the residue and the temperature was increased to 170 °C. The mixture was stirred for 4 h. After cooling to room temperature, water and ethyl acetate were added into the mixture. The organic layer was washed with brine and dried with $MgSO_4$. After purification through column chromatography (SiO_2, hexane/EtOAc 3:1 to 1:3), the product (0.83 g, 39%) was isolated as pale yellow powder. m.p. 98 ~ 100 °C. ^{1}H NMR (500 MHz, $CDCl_3$) δ 9.20 (s, 2H), 6.72 (s, 2H), 3.93 (t, *J* = 6.5 Hz, 4H), 1.78 (m, *J* = 6.5 Hz, 4H), 1.46 (m, *J* = 6.5 Hz, 4H), 1.37~1.23 (m, 16H), 0.88 (t, *J* = 6.5 Hz, 6H); ^{13}C NMR (125 Hz, $CDCl_3$) δ 157.65, 145.49, 122.42, 98.35, 70.50, 31.78, 29.44, 29.39, 29.24, 26.03, 22.61, 14.04. HRMS (ESI-TOF): *m/z* $[M+H]^+$ Calcd for $C_{23}H_{39}N_2O_3$ 391.2961; Found 391.2965. IR Absorption (cm^{-1}): 3290 (br), 3100 ~ 2820, 1686, 1520 ~ 1450, 1288, 1238, 1188, 1138.

38: Compound **37** (0.78 g, 2.0 mmol) was dissolved in acetic acid (4 mL). The solution was stirred at 70 °C. Then a solution of liquid bromine (0.94 g, 6.0 mmol) in acetic acid (4 mL) was added into the mixture over 10 min. The mixture was stirred under refluxing for 4 h. After cooling to room temperature, the mixture was extracted with CH_2Cl_2 and washed with brine, 1M NaOH solution, water and dried with $MgSO_4$. After purification through column chromatography (SiO_2, hexane/EtOAc 5:1 to 2:1), the product (0.96 g, 88%) was isolated as white powders. m.p. 137 ~ 140 °C. ^{1}H NMR (500 MHz, $CDCl_3$) δ 8.99 (s, 2H), 4.16 (t, *J* = 6.5 Hz, 4H), 1.88 (m, *J* = 6.5 Hz, 4H), 1.34-1.26 (m, 10H), 0.90 (t, *J* = 6.5 Hz, 6H); ^{13}C NMR (125 Hz, $CDCl_3$) δ 156.69, 146.44,

124.85, 98.39, 74.91, 32.00, 30.33, 29.58, 29.45, 26.20, 22.82, 14.26. HRMS (ESI-TOF): *m/z* $[M+H]^+$ Calcd for $C_{23}H_{37}N_2O_3Br_2$ 549.1146; Found 549.1133. IR Absorption (cm^{-1}): 3106 (br), 2970 ~ 2820, 1693, 1490 ~ 1440, 1320, 1269, 1204, 1142.

39: Compound **38** (654 mg, 1.2 mmol) and trimethylsilyl acetylene (3 mL) were dissolved in diisopropylamine (12 mL). The solution was degassed before $Pd(dppf)Cl_2 \bullet CH_2Cl_2$ (49 mg, 0.06 mmol) and P(*o*-tol)$_3$ (36.5 mg, 0.12 mmol) were added to the solution under N_2. The reaction tube was sealed firmly and the mixture was stirred at 110 °C for 5 days. After cooling to room temperature, the mixture was extracted with CH_2Cl_2 and filtered through celite. The organic layer was washed with 1 M HCl solution and dried with $MgSO_4$. After purification by column chromatography (SiO_2, hexane/EtOAc 9:1 to 3:1), the product (627 mg, 88%) was purified was isolated as brown powders. m.p. 89 ~ 92 °C. ^{1}H NMR (500 MHz, $CDCl_3$) δ 7.62 (s, 2H), 4.03 (t, *J* = 6.5 Hz, 4H), 1.77 (m, *J* = 6.5 Hz, 4H), 1.50 (m, *J* = 7 Hz, 4H), 1.36-1.25 (m, 8H), 0.88 (t, *J* = 7 Hz, 6H), 0.28 (s, 18H); ^{13}C NMR (125 Hz, $CDCl_3$) δ 148.69, 126.04, 105.37, 101.91, 95.52, 76.62, 75.06, 32.02, 30.47, 29.67, 29.44, 26.28, 22.83, 14.25, 0.15. HRMS (ESI-TOF): *m/z* $[M+H]^+$ Calcd for $C_{33}H_{55}N_2O_3Si_2$ 583.3751; Found 583.3762. IR Absorption (cm^{-1}): 3180 (br), 2980 ~ 2750, 2163, 1685, 1525 ~ 1410, 1338, 1271, 1246, 1190, 1137.

40: Compound **39** (175 mg, 0.30 mmol) was dissolved in anhydrous THF (4 mL) at 0 °C under N_2. NaHMDS (0.6 mL, 2 M in THF) solution was added dropwise. After stirring at 0 °C for 1 h, CH_3I (213 mg, 1.5 mmol) was added in one portion. The mixture was stirred at room temperature overnight. The mixture was extracted with CH_2Cl_2 and

the organic layer was washed with brine. After purification through column chromatography (SiO_2, hexane/EtOAc 19:1 to 9:1), the product (157 mg, 86%) was isolated as yellow oil. ^{1}H NMR (500 MHz, $CDCl_3$) δ 4.00 (t, J = 6.5 Hz, 4H), 3.71 (s, 6H), 1.79 (m, J = 6.5 Hz, 4H), 1.48 (m, J = 7 Hz, 4H), 1.34-1.25 (m, 8H), 0.88 (t, J = 7 Hz, 6H), 0.26 (s, 18H); ^{13}C NMR (125 Hz, $CDCl_3$) δ 155.34, 148.95, 126.62, 104.73, 102.07, 97.15, 74.84, 32.02, 30.55, 29.73, 29.46, 26.33, 22.83, 14.25, −0.24. HRMS (ESI-TOF): *m/z* $[M+H]^+$ Calcd for $C_{35}H_{59}N_2O_3Si_2$ 611.4064; Found 611.4022. IR Absorption (cm^{-1}): 2900 ~ 2750, 2164, 1733, 1672, 1490 ~ 1410, 1316, 1272, 1136.

34: Compound **39** (175 mg, 0.30 mmol) was dissolved in a mixture of MeOH (4 mL) and CH_2Cl_2 (4 mL). Then a solution of tetra-*n*-butylammonium fluoride in THF (1.0 M, 1.2 mL) was added into the solution. The mixture was stirred at room temperature overnight. The mixture was then extracted with ethyl acetate. The organic layer was washed with brine, water and dried with $MgSO_4$. After removing organic solvents, the crude deprotected product was added together with 1-iodoanthraquione (302 mg, 0.90 mmol) to a Schlenk tube filled with 8 mL Et_3N. The mixture was degassed and taken into an oxygen and water free glovebox, where $Pd(Ph_3)_4$ (34.6 mg, 0.03 mmol) and CuI (11.5 mg, 0.06 mmol) were added. The mixture was stirred at 80 °C for 3 days. After cooling to room temperature, the mixture was extracted with $CHCl_3$ and washed with 1 M HCl solution. The organic layer was dried with $MgSO_4$. After purification by preparative GPC using $CHCl_3$ as the eluent (retention time: 30 min, flow rate: 14 mL/min), the product (200 mg, 79%) was isolated as red powders. M.p.>240 °C. ^{1}H NMR (500 MHz, $CDCl_3$) δ 10.16 (s, 2H), 8.55 (dd, J_1 = 7.5 Hz, J_2 = 1.0 Hz, 2H),

8.39 (dd, J_1 = 7.5 Hz, J_2 = 1.5 Hz, 2H), 8.32 (dd, J_1 = 7.5 Hz, J_2 = 1.0 Hz, 2H), 7.98 (dd, J_1 = 7.5 Hz, J_2 = 1.0 Hz, 2H), 7.89 (td, J_1 = 7.5 Hz, J_2 = 1.0 Hz, 2H), 7.84 (td, J_1 = 7.5 Hz, J_2 = 1.0 Hz, 2H), 7.81 (t, J = 7.5 Hz, 2H), 4.23 (t, J = 6.5 Hz, 4H), 1.90 (m, J = 6.5 Hz, 4H), 1.64 (m, J = 7 Hz, 4H), 1.45-1.26 (m, 16H), 0.88 (t, J = 7 Hz, 6H); ^{13}C NMR (125 Hz, $CDCl_3$) δ 182.70, 182.61, 155.26, 147.49, 139.20, 134.97, 134.55, 133.98, 133.46, 133.13, 132.94, 128.88, 128.49, 127.97, 127.16, 123.48, 102.13, 99.28, 88.85, 75.46, 32.07, 30.63, 29.754, 29.60, 26.59, 22.87, 14.27. MS (ESI-TOF): *m/z* $[M+H]^+$ Calcd for $C_{55}H_{51}N_2O_7$ 851.37; Found 851.44. Elemental Analysis: Calcd for $C_{55}H_{50}N_2O_7$: C, 77.63; H, 5.92; N, 3.29; Found C, 77.19; H, 5.61; N, 3.80. IR Absorption (cm^{-1}): 3325, 3100 ~ 2810, 2192, 1718, 1666, 1600 ~ 1550, 1480 ~ 1400, 1321, 1276, 1136.

35: Compound **40** (122 mg, 0.20 mmol) was dissolved in a mixture of MeOH (3 mL) and CH_2Cl_2 (3 mL). Then a solution of tetra-*n*-butylammonium fluoride in THF (1.0 M, 0.8 mL) was added into the solution. The mixture was stirred at room temperature overnight. The mixture was extracted with ethyl acetate. The organic layer was washed with brine, water and dried with $MgSO_4$. After removing organic solvents, the crude deprotected product was added together with 1-iodoanthraquione (202 mg, 0.60 mmol) to a Schlenk tube filled with Et_3N (6 mL). The mixture was degassed and taken into a oxygen and water free glovebox, where $Pd(Ph_3)_4$ (23.6 mg, 0.02 mmol) and CuI (7.4 mg, 0.04mmol) were added. The mixture was stirred at 80 °C for 3 days. After cooling to room temperature, the mixture was extracted with chloroform and washed with 1 M HCl solution. The organic layer was dried with $MgSO_4$. After purification by preparative GPC using $CHCl_3$ as the eluent (retention time: 30 min, flow rate: 14

mL/min), the product (120 mg, 79%) was isolated as red powders. m.p. 228 ~ 231 °C. ^{1}H NMR (500 MHz, $CDCl_3$) δ 8.39 (dd, J_1 = 7.5 Hz, J_2 = 1.0 Hz, 2H), 8.32 (m, 4H), 8.00 (dd, J_1 = 7.5 Hz, J_2 = 1.0 Hz, 2H), 7.82 (m, 4H), 7.80 (t, J = 7.5 Hz, 2H), 4.24 (t, J = 6.5 Hz, 4H), 3.98 (s, 6H), 1.90 (m, J = 6.5 Hz, 4H), 1.50 (m, J = 7 Hz, 4H), 1.34-1.12 (m, 16H), 0.81 (t, J = 7 Hz, 6H). ^{13}C NMR (125 Hz, $CDCl_3$) δ 182.88, 181.92, 155.38, 149.11, 140.27, 134.73, 134.66, 134.133, 134.11, 133.15, 133.10, 132.88, 127.86, 127.68, 127.14, 126.84, 123.47, 102.41, 97.81, 88.77, 75.28, 32.00, 30.644, 29.80, 29.75, 29.52, 26.43, 22.81, 14.22. MS (ESI-TOF): *m/z* $[M+H]^+$ Calcd for $C_{57}H_{55}N_2O_7$ 879.40; Found 879.45. Elemental Analysis: Calcd for $C_{57}H_{54}N_2O_7$: C, 77.80; H, 6.19; N, 3.21; Found C, 77.20; H, 5.77; N, 3.21. IR Absorption (cm^{-1}): 3100 ~ 2750, 2189, 1733, 1672, 1605 ~ 1555, 1480 ~ 1400, 1316, 1276, 1085.

2.6.3 NMR Spectra

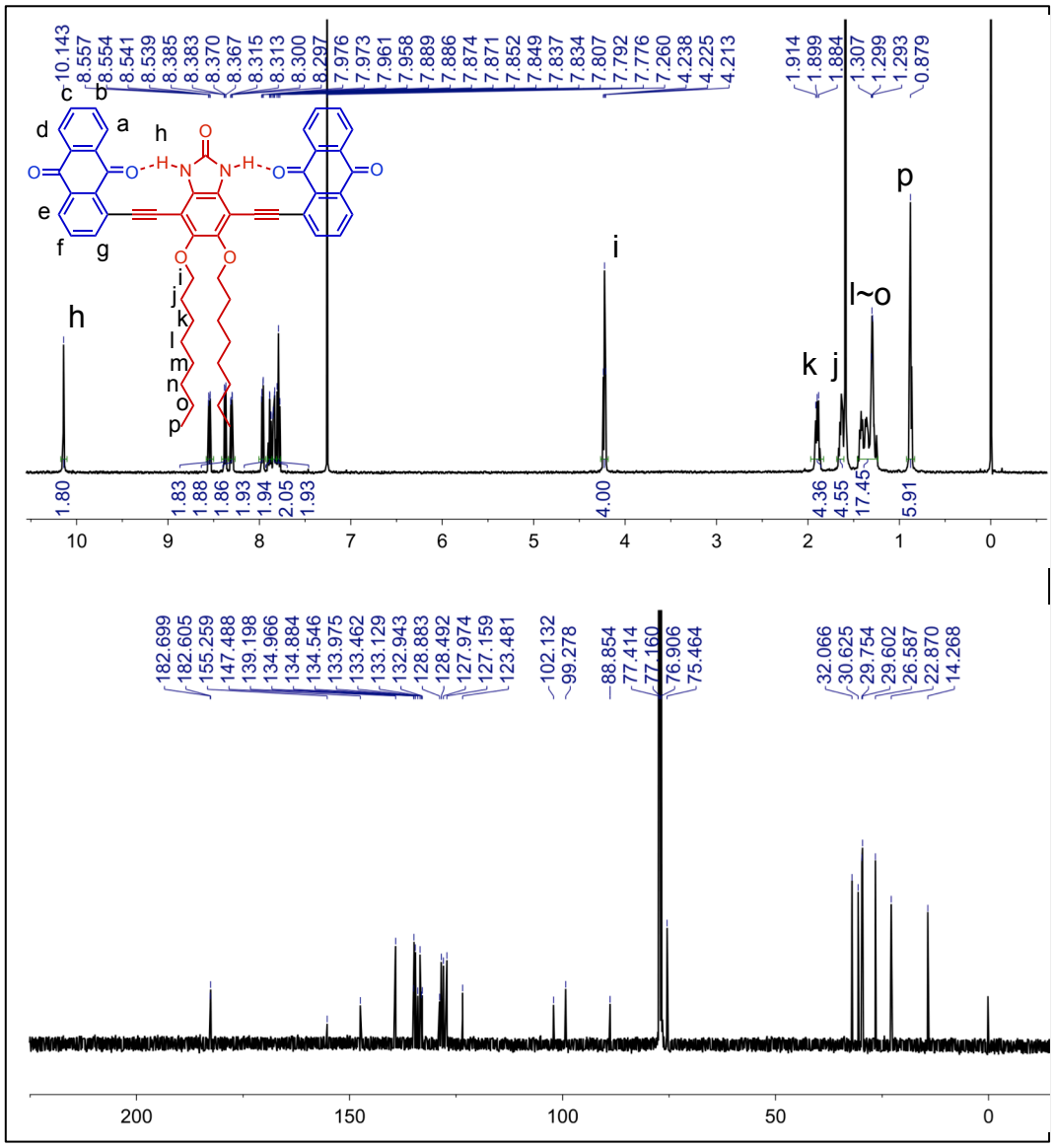

Figure 27. ^{1}H (500 MHz), ^{13}C NMR (125 MHz) spectra of 34 in $CDCl_3$ at room temperature.

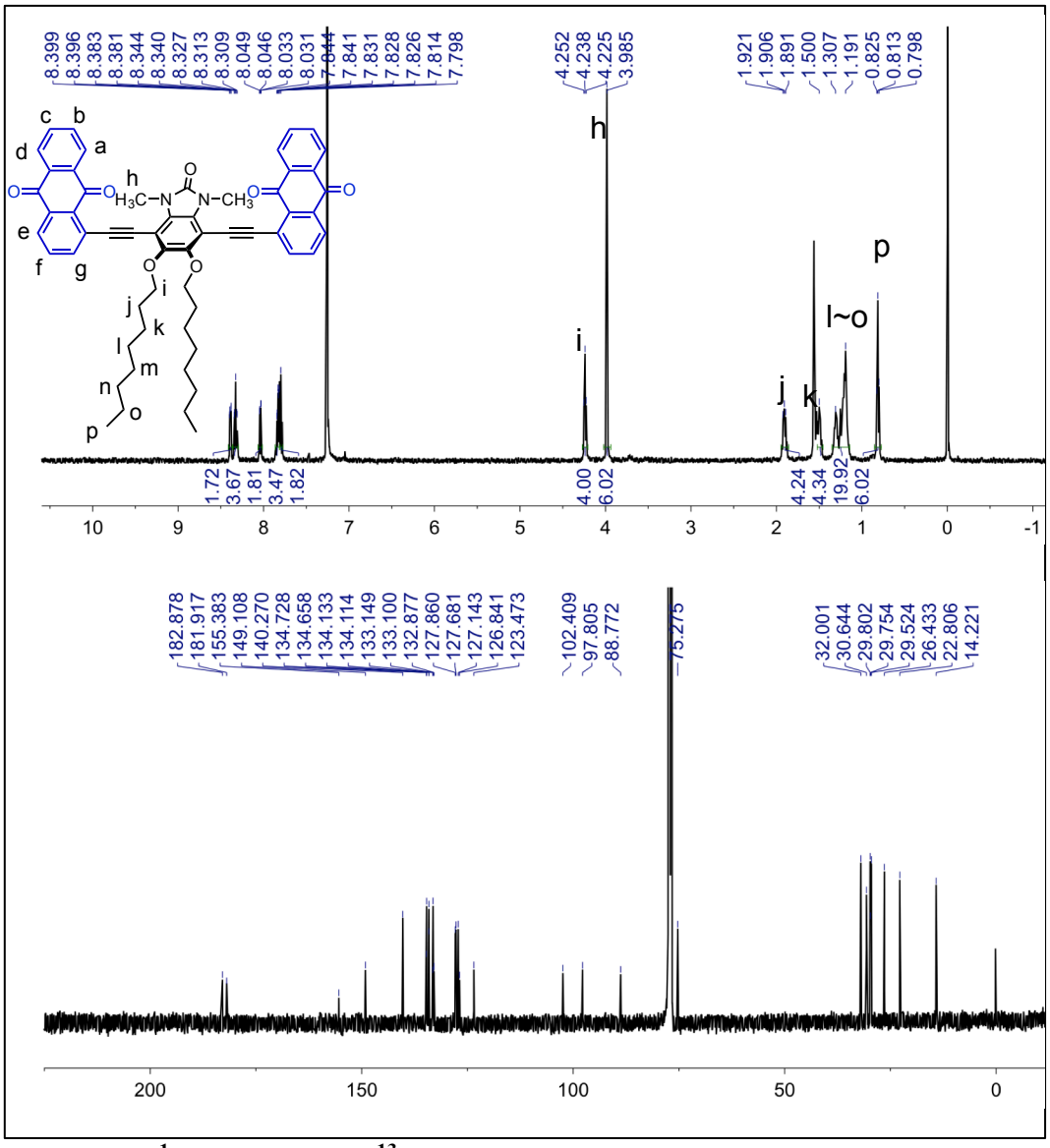

Figure 28. ^{1}H (500 MHz), ^{13}C NMR (125 MHz) spectra of 35 in $CDCl_3$ at room temperature.

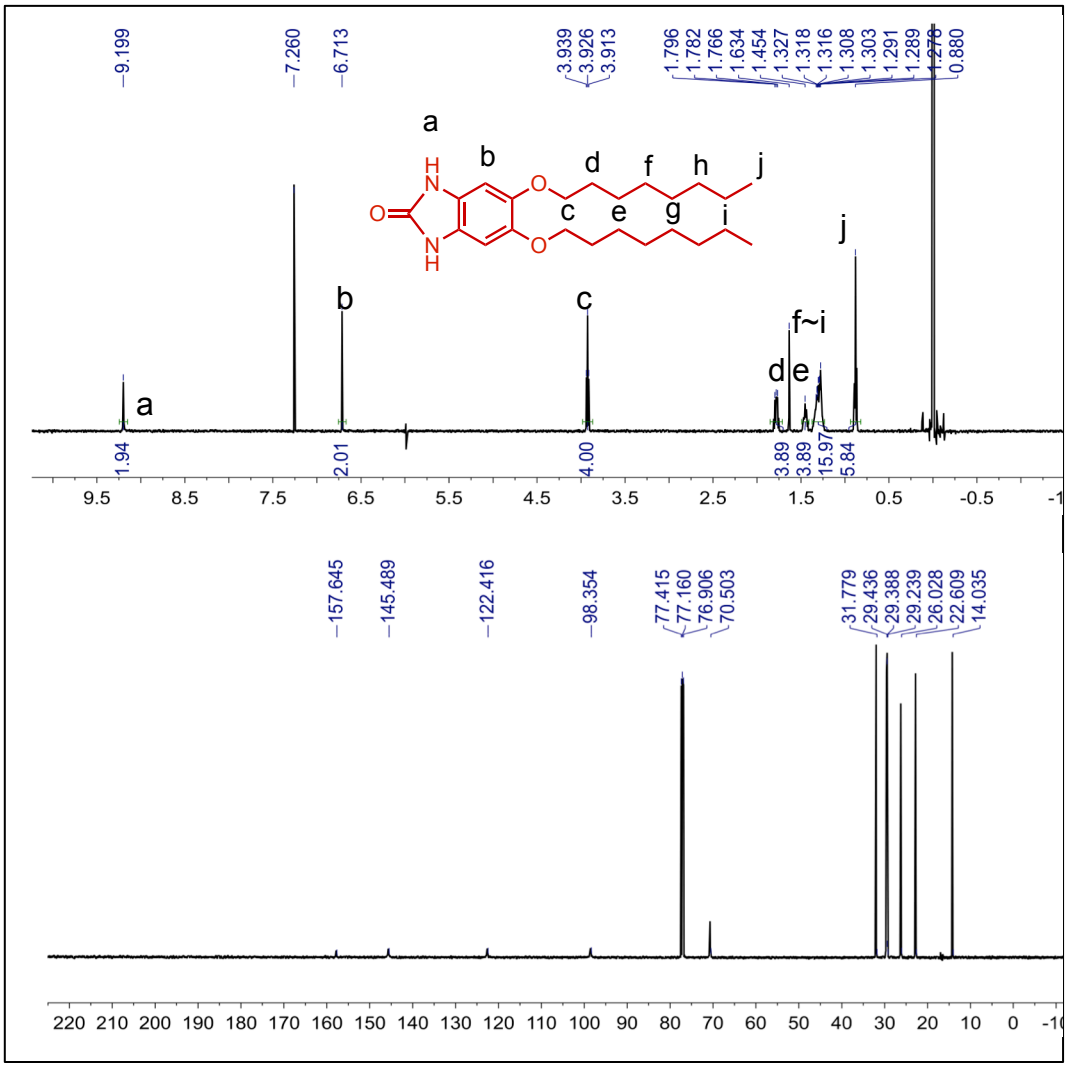

Figure 29. ^{1}H (500 MHz), ^{13}C NMR (125 MHz) spectra of 37 in $CDCl_3$ at room temperature.

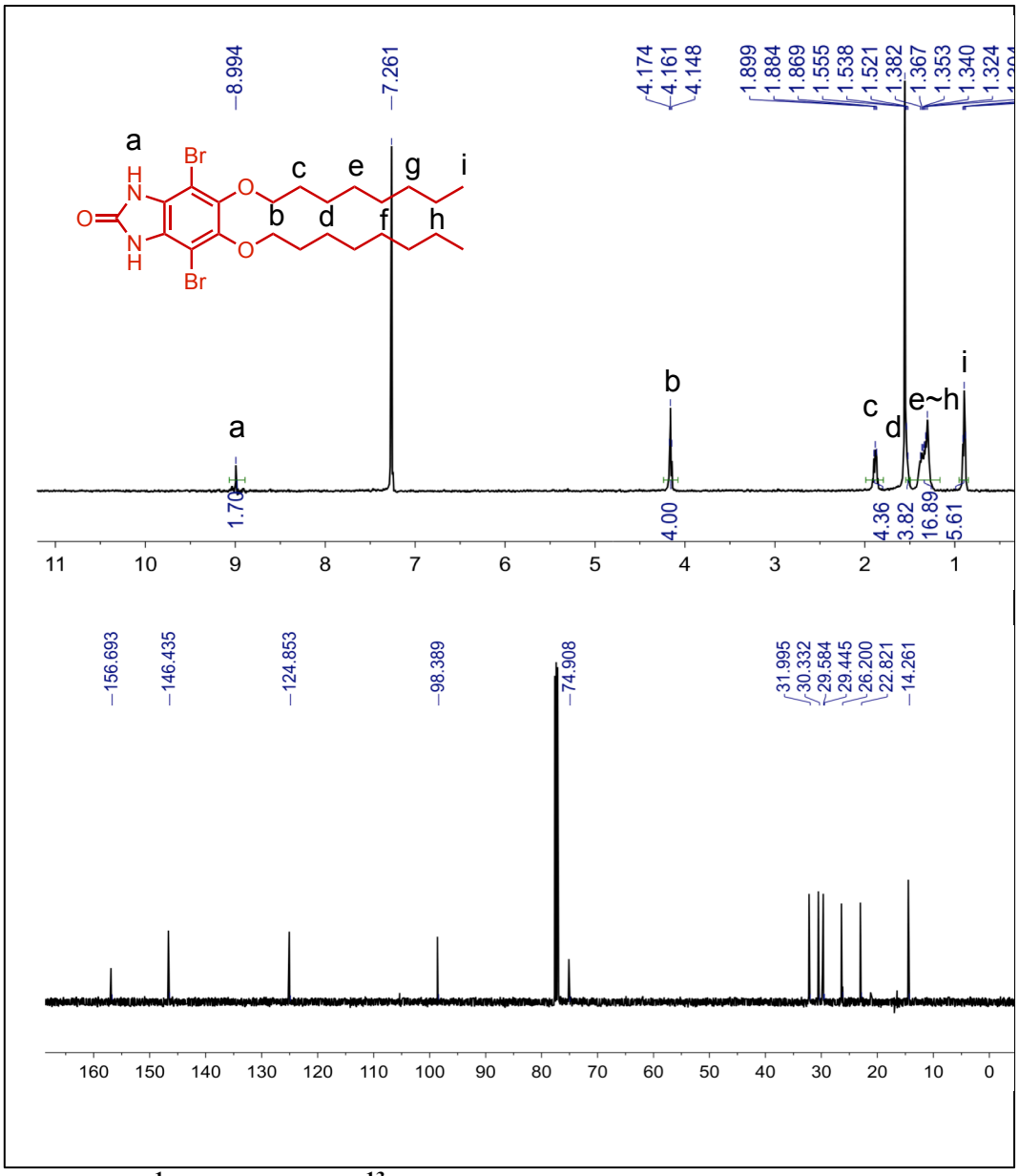

Figure 30. ^{1}H (500 MHz), ^{13}C NMR (125 MHz) spectra of 38 in $CDCl_3$ at room temperature. Proton *d* is overlapping with H_2O.

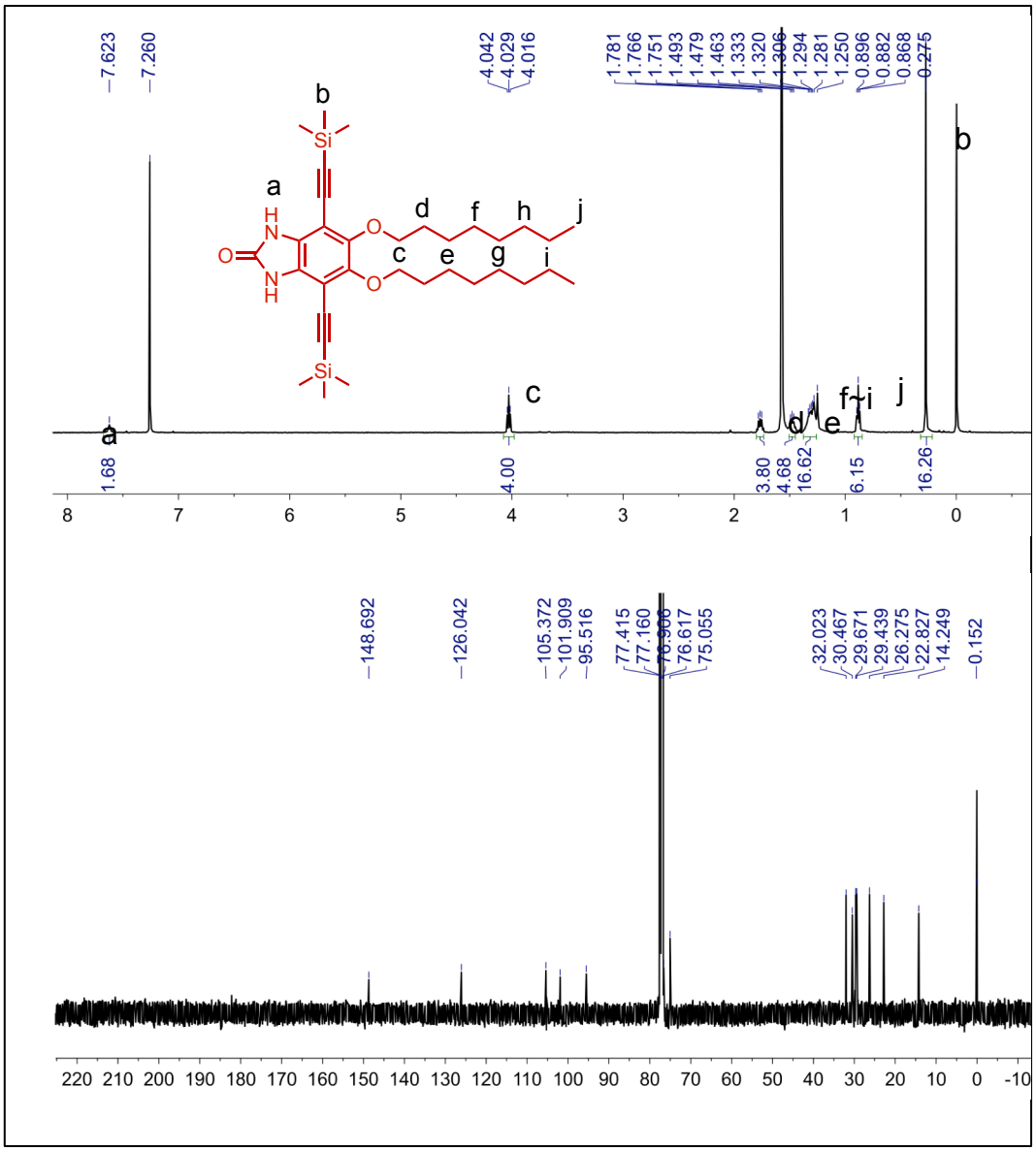

Figure 31. ^{1}H (500 MHz), ^{13}C NMR (125 MHz) spectra of 39 in $CDCl_3$ at room temperature.

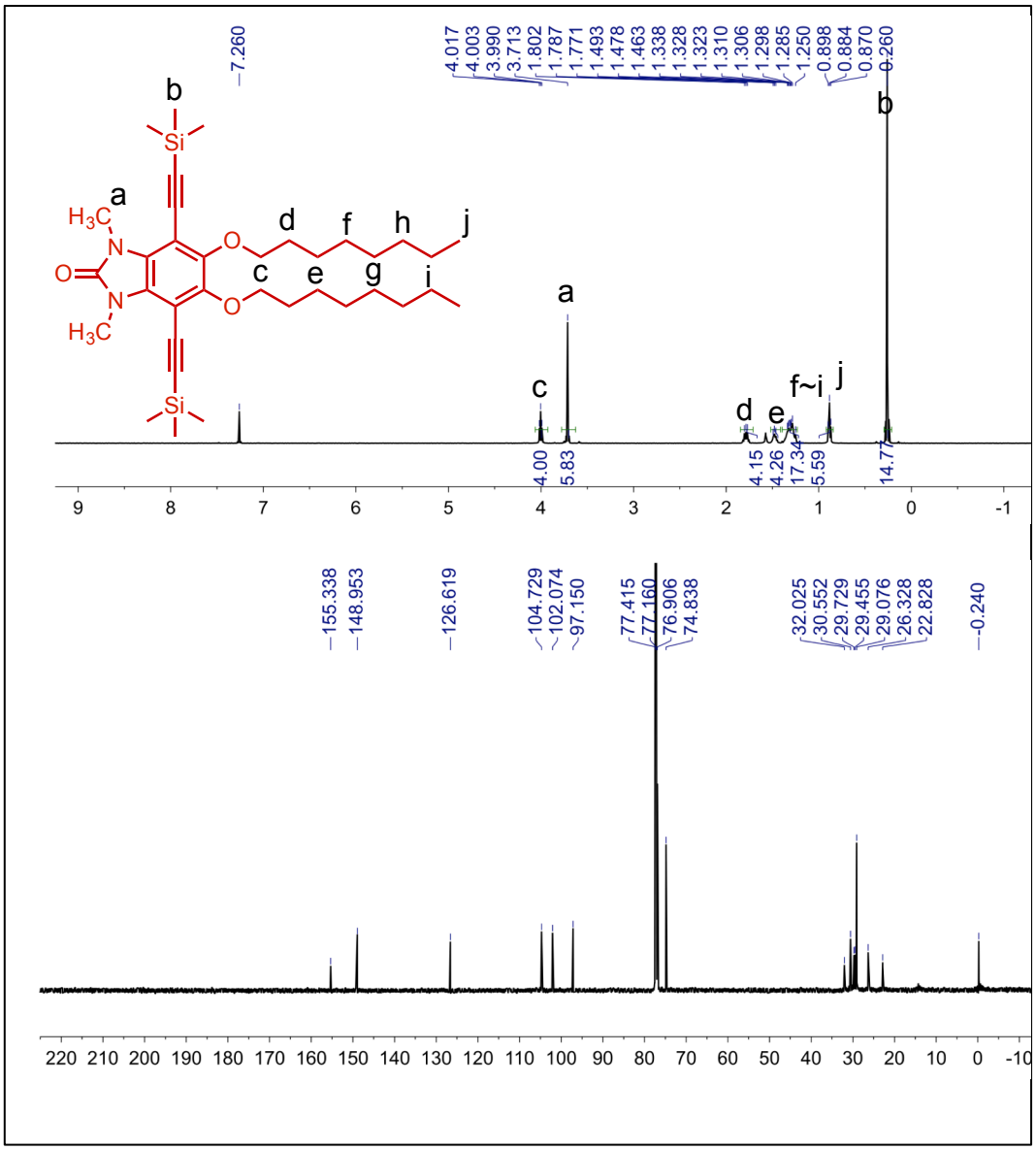

Figure 32. ^{1}H (500 MHz), ^{13}C NMR (125 MHz) spectra of 40 in $CDCl_3$ at room temperature.

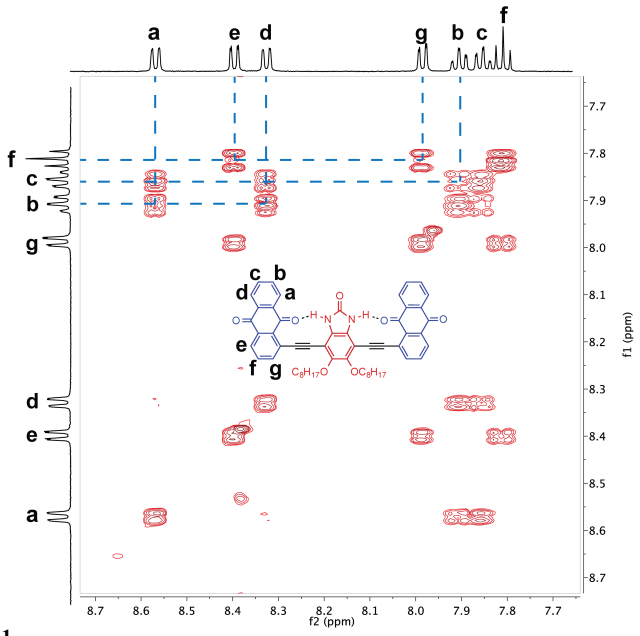

Figure 33. ^{1}H-^{1}H COSY NMR (500 MHz) spectra of 34 in $CDCl_3$ at room temperature.

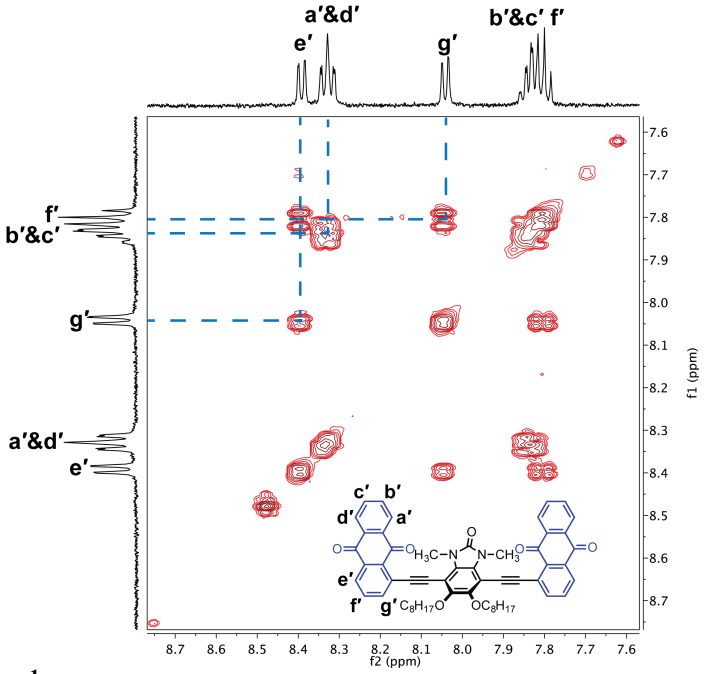

Figure 34. ^{1}H-^{1}H COSY NMR (500 MHz) spectra of 35 in $CDCl_3$ at room temperature.

CHAPTER III

SYNTHESIS AND SOLUTION PROCESSING OF A RIGID POLYMER ENABLED BY ACTIVE MANIPULATION OF INTRAMOLECULAR HYDROGEN BONDS*

3.1 Introduction

Intramolecular hydrogen bonds are ubiquitous in biomacromolecules and synthetic polymers, playing a pivotal role in shaping macromolecular conformations and governing macroscopic properties of these polymers. For example, they induce and stabilize the secondary structures of polypeptides (**Figure 35a**) and proteins.[126-128] They are also important in determining the properties and functions of polysaccharides,[129] poly(vinyl alcohol),[130] polyacrylamide,[131,132] polyhydroxyalkanoates,[133,134] poly(*p*-sulfophenylene terephthalamide),[135] a variety of copolymers, etc.[136] Inspired by these natural and synthetic examples, chemists designed and incorporated intramolecular hydrogen bonds into artificial polymers to tailor their conformations and functions. These noncovalent interactions were employed to lock molecular conformations of a variety of synthetic polymers, to construct helical architectures,[137-140] to access desired optical behaviors,[41,51,52] and to achieve favorable charge transport properties.[1,54] However, after locking the global conformation, specifically to a coplanar geometry, decreased solubilities of the polymers were often encountered,[2,41,52,63] leading to low

*Reprinted with permission from "Synthesis and Solution Processing of a Rigid Polymer Enabled by Active Manipulation of Intramolecular Hydrogen Bonds" Zhu, C.; Mu, A. U.; Wang, C.; Ji, X.; Fang, L. *ACS Macro Lett.*, **2018**, *7*, 801. Copyright 2018 American Chemical Society

molecular weights and poor solution processability that prohibit the urgently demanded wide application of this promising strategy for desired properties.

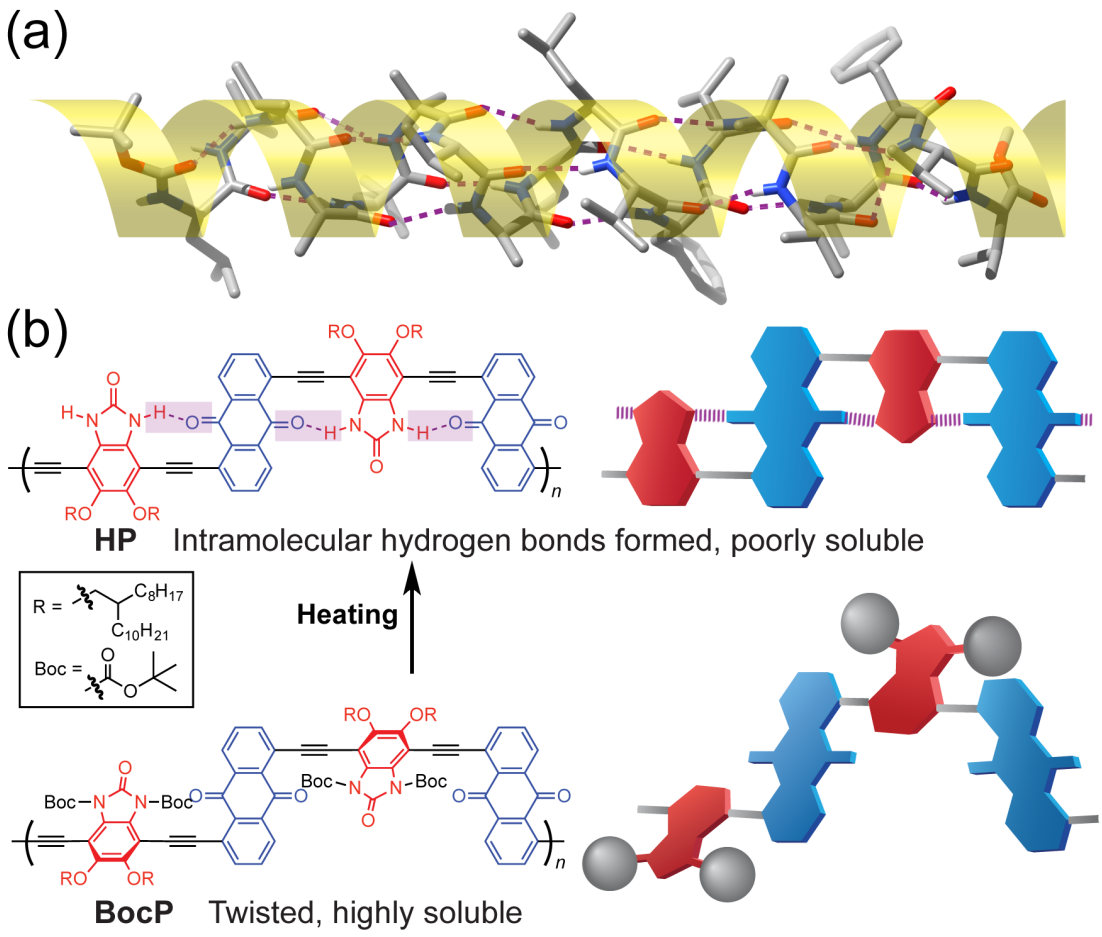

Figure 35. (a) Example of intramolecular hydrogen bonds: crystal structure of a polypeptide with helical conformation induced by intramolecular hydrogen bonds[141] and (b) chemical structures and graphical representations of HP and BocP.

We envisioned that the critical challenges associated with the poor solubility and processability of these rigid polymers can be addressed by manipulating the intramolecular noncovalent interactions. In fact, the modulation of intramolecular hydrogen bonds represents one of the fundamental mechanisms for biomacromolecules

to adopt different conformations to perform diverse functions in many essential life processes.[142] For artificial polymers, it is still formidably challenging to actively control these intramolecular hydrogen bonds to achieve tunable properties, specifically those relating to synthesis and processing. In this context, global intramolecular hydrogen bonds (ubiquitously formed between each two adjacent building units throughout the backbone) need to be accurately arranged and efficiently manipulated in macromolecular backbones. Meanwhile, the typical high degrees of freedom of these hydrogen bonding moieties and the flexible macromolecular chains increase the complexity in controlling the conformations.[143] Herein, we report a molecular engineering strategy to address this long-standing issue by chemically inhibiting and regenerating global intramolecular hydrogen bonds that are preorganized in a model polymer (**HP**). By inhibiting hydrogen bonds, a well-soluble precursor **BocP** was synthesized with a high molecular weight (**Figure 35b**) and good solution processability. Regenerating these global hydrogen bonds in the solid state afforded the polymer **HP** with a rigidified backbone, leading to excellent solvent resistance while enabling multilayer processing.

3.2 Molecular Design

The hydrogen-bonded polymer model system (**HP**, **Figure 35b**) was designed upon a poly(phenylene acetylene) backbone and composed of alternating hydrogen bond donating 2*H*-benzimidazol-2-one units and hydrogen bond accepting anthracene-9,10-dione units. These hydrogen bond donors and acceptors were fused to the polymer backbone so that the degree of freedom of these functional groups was significantly reduced compared to single bonded moieties,[64] leading to a much smaller entropy

penalty for the formation of intramolecular hydrogen bonds.[11] Therefore, the hydrogen bond strength was expected to be enhanced, and the rigid backbone conformation can be precisely predicted. Meanwhile, the length of the ethynylene spacer allowed for the formation of a strong hydrogen bond with a favorable distance.[95] These design principles were validated by a single-crystal structure of a small molecular model system.[11] Furthermore, DFT calculations on a representative structural segment of the **HP** backbone demonstrated torsional angles of 0.2° and 3.2° in the ground state (**Figure 36**). In this context, the conformation of **HP** was expected to be constrained by these intramolecular hydrogen bonds, giving torsional angles smaller than 5° between the alternating units. Such a constrained and rigidified molecular conformation, however, could lead to poor solubility as a result of strong intermolecular π–π interactions,[11] bringing difficulties in characterization and processing. More importantly, this rigid polymer is likely to precipitate during the solution-phase synthesis, terminating the polymerization prematurely and resulting in a low molecular weight of the product. In this context, **HP** could serve as a model system to test the hydrogen bond manipulation strategy to address the aforementioned challenges.

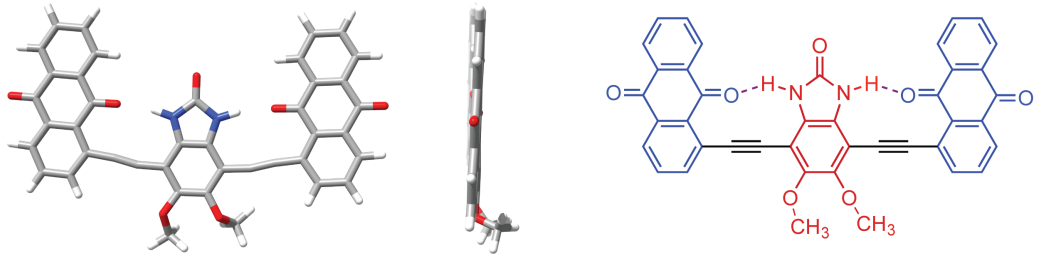

Figure 36. Structural formula and molecular geometry of a representative structural segment of HP backbone.

It was envisioned that a hydrogen bond "masking" strategy can be implemented in the synthesis and processing of **HP** (**Figure 35b**). The 2*H*-benzimidazol-2-one units were functionalized with *t*-butyloxycarbonyl (Boc) groups so that the hydrogen bond donating ability was "masked". Once the corresponding polymer **BocP** was formed, the lack of intramolecular hydrogen bonds and the presence of bulky Boc groups twisted the molecule into a conformation with a torsional angle over 40°, as revealed by DFT calculation (**Figure 37**). Such a highly twisted backbone was expected to prevent the interchain aggregation and consequently increase the solubility and processability. It would also allow for the achievement of high molecular weight polymers without precipitation during the solution-phase synthesis. More importantly, because Boc groups are thermally cleavable in a quantitative manner without leaving behind nonvolatile residues,[32,144,145] the intramolecular hydrogen bonds can be regenerated in the solid state by simple heating, converting **BocP** into **HP**. In other words, the processing and solid-phase synthesis of **HP** can be achieved on the basis of highly soluble precursor **BocP**, followed by unmasking intramolecular hydrogen bonds through thermal treatment.

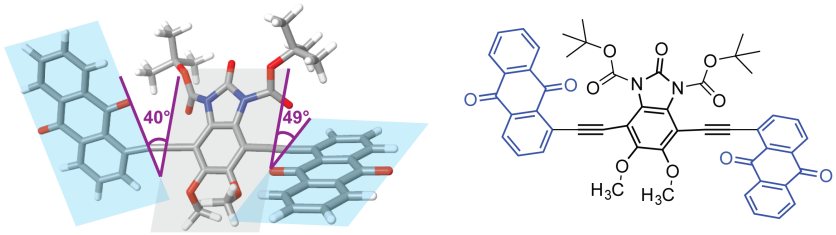

Figure 37. Structural formula and molecular geometry of a representative structural segment of BocP backbone.

3.3 Synthesis and Characterization

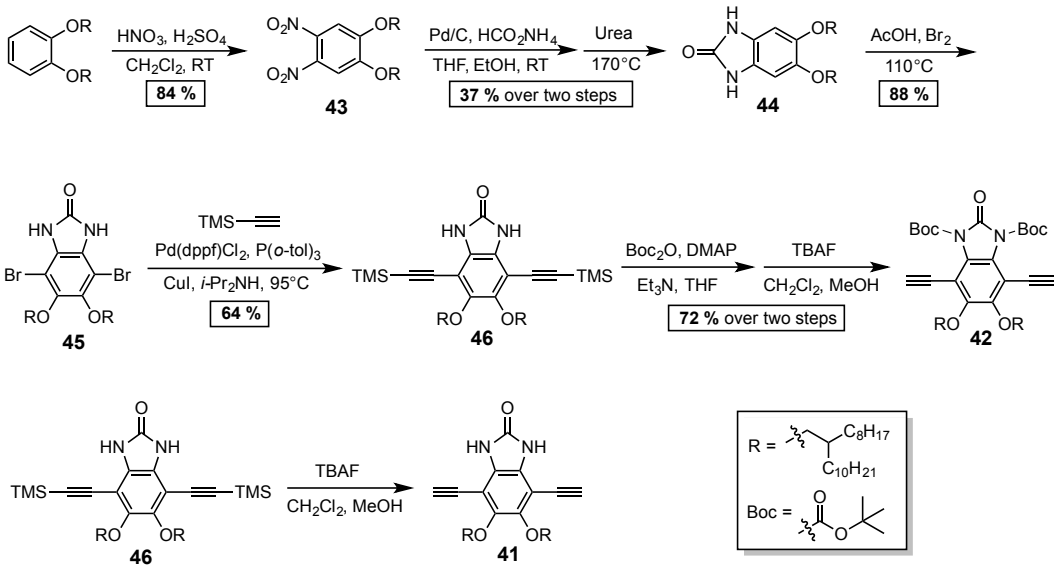

Figure 38. Synthetic route to monomers 41 and 42.

To test the aforementioned hypothesis, we first attempted the synthesis of the target polymer **HP** *without* Boc protection. The monomer, compound 4**1**, was prepared according to a literature report (**Figure 38**).[11] The polymerization was conducted through a Sonogashira coupling reaction between 4**1** and 1,5-diiodoanthracene-9,10-dione in a mixed solvent of toluene and diisopropylamine (Route A, **Figure 39**). During

this solution-phase step-growth polymerization, a large amount of precipitates were observed. These precipitates, labeled as "batch A" (**HP-A**), were only partially soluble in organic solvents (8% dissolved in 2-methyltetrahydrofuran, 17% dissolved in chlorobenzene). After extracting with hot tetrahydrofuran, analytical size exclusion chromatography (SEC) of the soluble fraction revealed (**Figure 40a**) a low number-average molecular weight (M_n) of 5.2 kg/mol, which is similar to an intramolecular hydrogen bond rigidified model study reported in the literature.[41] Most of the polymer sample, however, remained insoluble likely due to the high rigidity and strong interchain aggregations. Therefore, extensive characterization and solution processing of **HP-A** were not feasible.

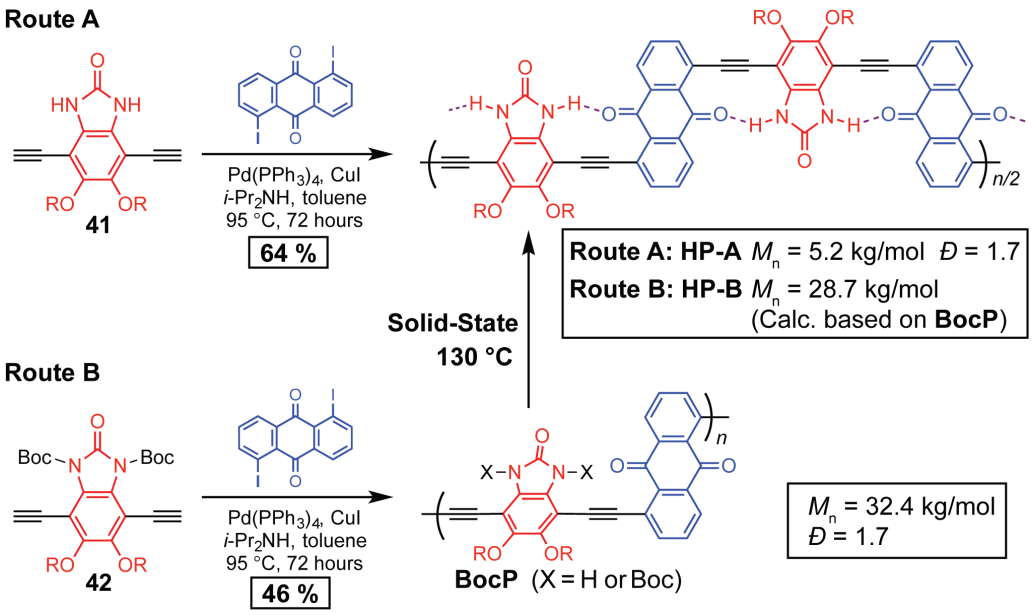

Figure 39. Two Synthetic Routes to HP: Route A: direct polymerization of monomer 41 without masking the hydrogen bonds. Route B: polymerization of Boc-protected monomer 42 followed by solid-state unmasking of the hydrogen bonds.

To implement the hydrogen-bond masking strategy, the synthesis of precursor **BocP** was performed, followed by solid-state conversion of **BocP** into a higher molecular weight batch **HP-B** (Route B, **Figure 39**). The synthesis started from the polymerization of 1,5-diiodoanthracene-9,10-dione and monomer **2**, in which the hydrogen bond donating urea groups were protected by Boc groups. The polymerization did not result in any precipitate. After workup and purification by preparative SEC to remove oligomers, **BocP** was isolated as a readily soluble material not only in conventional organic solvents like dichloromethane, chloroform, and toluene but also in environmentally friendly solvents such as 2-methyltetrahydrofuran (>10 mg/mL) (**Figure 40a**).[146]

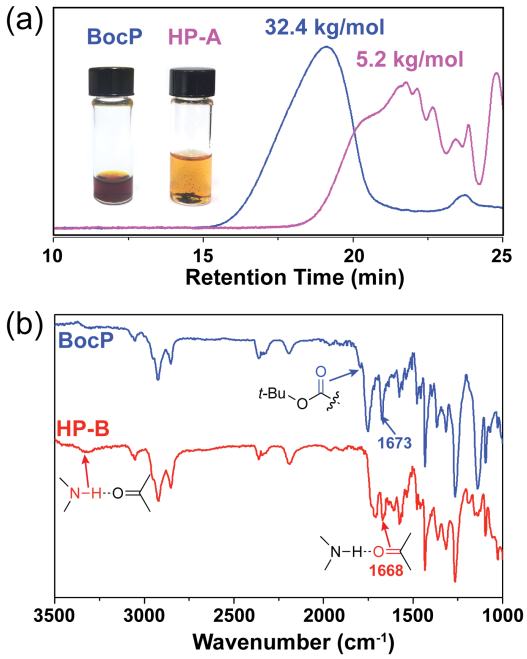

Figure 40. (a) Size exclusion chromatogram of BocP and the soluble fraction of HP-A. Inset is a photograph of HP-A and BocP (5 mg/mL) in 2-methyltetrahydrofuran at room temperature. (b) FT-IR spectra of BocP and HP-B.

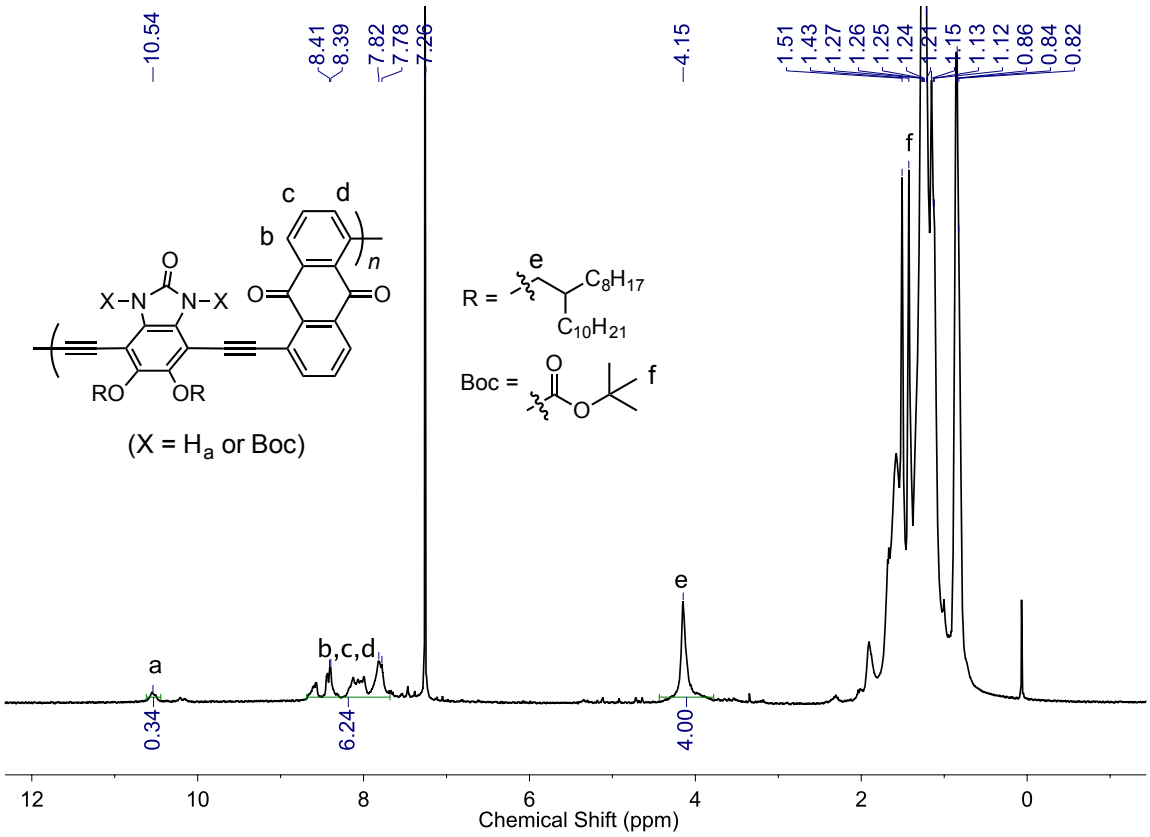

Figure 41. ^{1}H (500 MHz) NMR spectrum of BocP in $CDCl_3$ at room temperature.

BocP was first characterized by analytical SEC, showing a much higher molecular weight (32.4 kg/mol) than the soluble fraction of **HP-A** and a polydispersity index of 1.7. In the ^{1}H NMR spectrum of **BocP** (**Figure 41**), all resonance signals were assigned based on the spectra of the monomers. An unexpected small resonance peak at 10.55 ppm,[11,95] indicated that some of the Boc groups were cleaved during the polymerization. Apparently, this partial Boc group cleavage did not lower the solubility of the polymer significantly to impact the solution-phase synthesis. It was also noticed that the resonance peak of the Boc groups was upfield shifted for 0.21 ppm after the polymerization, a result of the shielding effect of the ring current coming from the

neighboring aromatic units. This observation also corroborated the twisted molecular geometry calculated by DFT, in which the Boc groups were in close proximity with the π-face of anthracene–dione units.

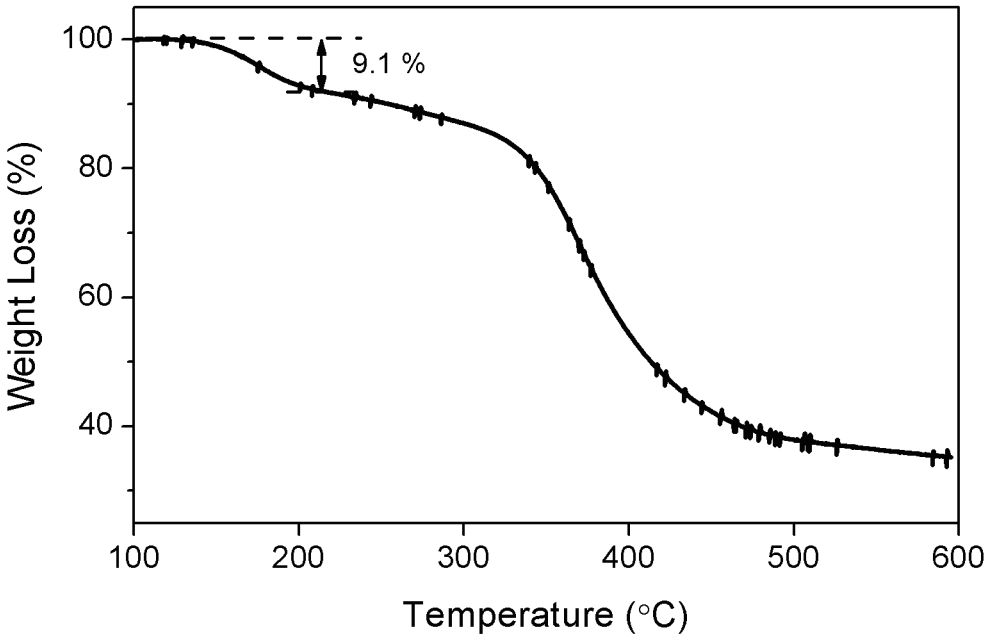

Figure 42. The TGA trace of BocP. Boc cleavage started at 130 °C. A weight loss of 9.1% was observed from 130 °C to 210 °C. The polymer further decomposed at 270 °C with an additional weight loss of 5%.

In thermal gravimetric analysis, an expected weight loss of 9.1% from 130 to 160 °C was observed (**Figure 42**), corresponding to the thermal cleavage of Boc groups.[32,144,145] This weight loss was smaller than the theoretical calculated value (16.8%), further confirming the preceding partial cleavage of Boc groups during the solution-phase polymerization. This well-soluble polymer **BocP** was converted into **HP-B**, by heating at 130 °C for 1 h. Intramolecular hydrogen bonds were unmasked, and

consequently, **HP-B** became insoluble in organic solvents (**Figure 43**) due to its rigid backbone, strong intermolecular interactions, and higher molecular weight (compared to **HP-A**). This process represents an example of switching the macromolecular properties of this rigid model polymer through the manipulation of intramolecular hydrogen bonds.

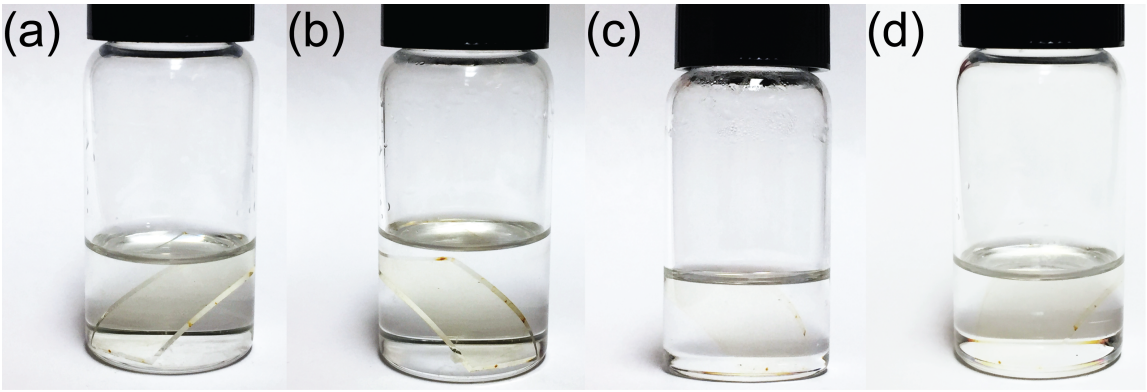

Figure 43. Thin films of HP-B on glass substrates at room temperature soaked in different organic solvents: (a) chloroform, (b) THF, (c) chlorobenzene, (d) chlorobenzene after heating at 120 °C for 2 hours.

FT-IR spectroscopy was employed to further investigate the Boc cleavage process. The IR spectrum **(Figure 40b**) of **BocP** showed three peaks at 1796, 1751, and 1673 cm^{-1}, corresponding to C═O stretching in the Boc groups, benzimidazol-2-one, and anthracene-9,10-dione units, respectively. In addition, a weak peak at 3318 cm^{-1} was observed, which was attributed to stretching of the partially deprotected N–H groups, consistent with that of a reported small molecular analogue.[11] After the sample was treated by heating, the C═O stretching peak of Boc groups at 1796 cm^{-1} disappeared. Meanwhile, the intensity of the N–H stretching peak increased (**Figure 40b**), suggesting

the increased amount of hydrogen bonded N–H groups after the cleavage of Boc groups. It was also noticed that the C═O stretching energy in anthracene-9,10-dione units decreased to 1668 cm^{-1} as a result of accepting intramolecular hydrogen bonds.[11] Moreover, the characteristic IR peaks of **HP-B** were identical to those of directly synthesized **HP-A** (**Figure 44**), further corroborating the successful regeneration of functional groups in **HP-B** after the thermal treatment of **BocP**.

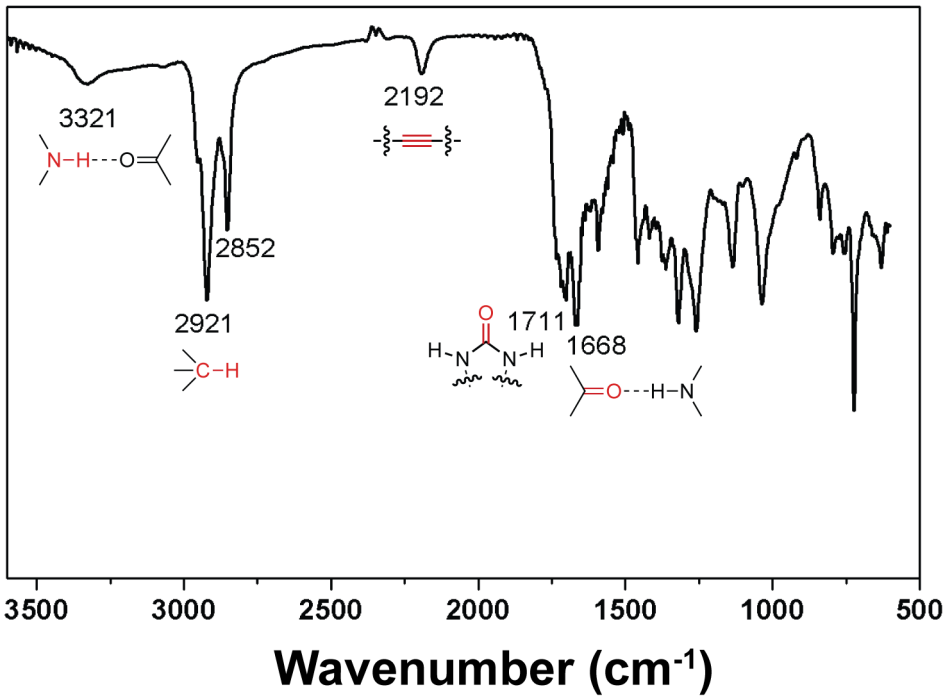

Figure 44. Fourier transform infrared spectrum of HP-A in the solid state at room temperature.

3.4 Active Manipulation of Hydrogen Bonds and Solution Processing

Thin-film processability of polymeric materials is essential for many important applications and is often a prerequisite for their solid-state characterization.[147-149] The

directly synthesized batch, **HP-A**, was difficult to solution process due to the low solubility. Melt processing was not feasible due to either its rigid nature or lack of glass transition. Therefore, its solid-state properties, such as photophysics, energy levels, morphology, and packing, cannot be comprehensively characterized. In contrast, the switched-on solubility of **BocP** and feasible regeneration of intramolecular hydrogen bonds allowed for solution processing of **HP-B** into thin films despite its insoluble nature. This strategy of manipulating intramolecular hydrogen bonds enabled characterization of **HP-B** in the thin film state. UV–vis absorption and cyclic voltammetry measurements of **HP-B** and **BocP**thin films were conducted. Both polymers possessed two major absorption bands at around 500 and 370 nm (**Figure 45**). Compared to **BocP**, **HP-B** showed a slightly red-shifted absorption, indicating a narrowed optical band gap due to its constrained conformation and enhanced intermolecular electronic coupling.

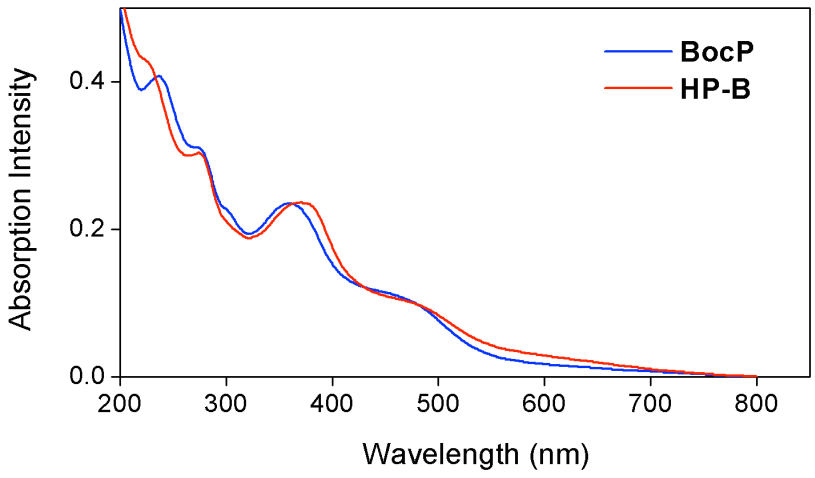

Figure 45. UV-vis absorption of thin films (spin coated from a solution of 2 mg/mL BocP in chloroform at 1000 rpm) of BocP and HP-B on glass substrates.

The cyclic voltammetry trace (**Figure 46**) of the film of **BocP**on indium tin oxide showed a reduction potential of −1.26 V and an oxidation potential of 0.83 V [vs ferrocene/ferrocenium]. After the *in situ* formation of **HP-B** by heating, the oxidation potential decreased to 0.75 V. Meanwhile, the reduction potential shifted positively to −1.22 V, which can be attributed to the more electron-deficient anthracene-9,10-dione units induced by the intramolecular hydrogen bonds in **HP-B**.[11] Overall, due to the formation of intramolecular hydrogen bonds and its coplanar conformation, **HP-B** possessed a narrowed frontier orbital band gap compared to the twisted polymer **BocP**.

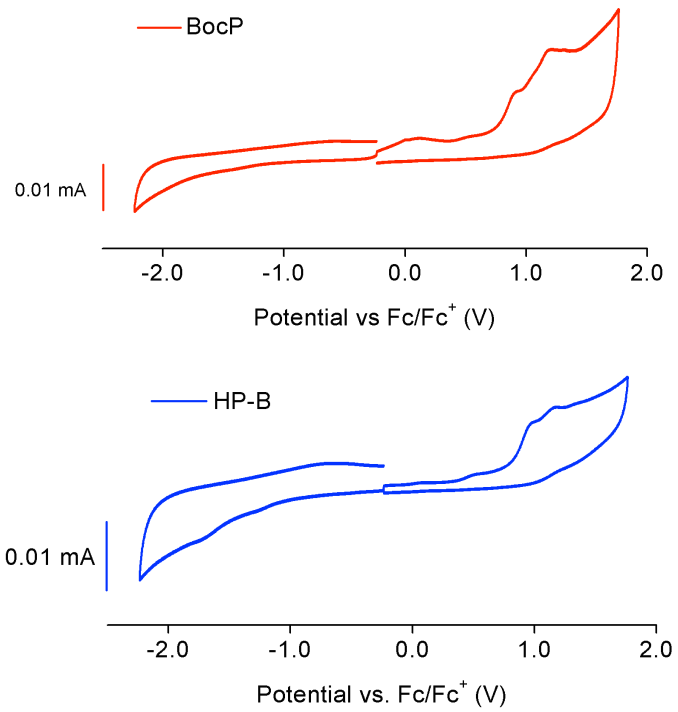

Figure 46. Cyclic voltammogram of BocP and HP-B in the solid state.

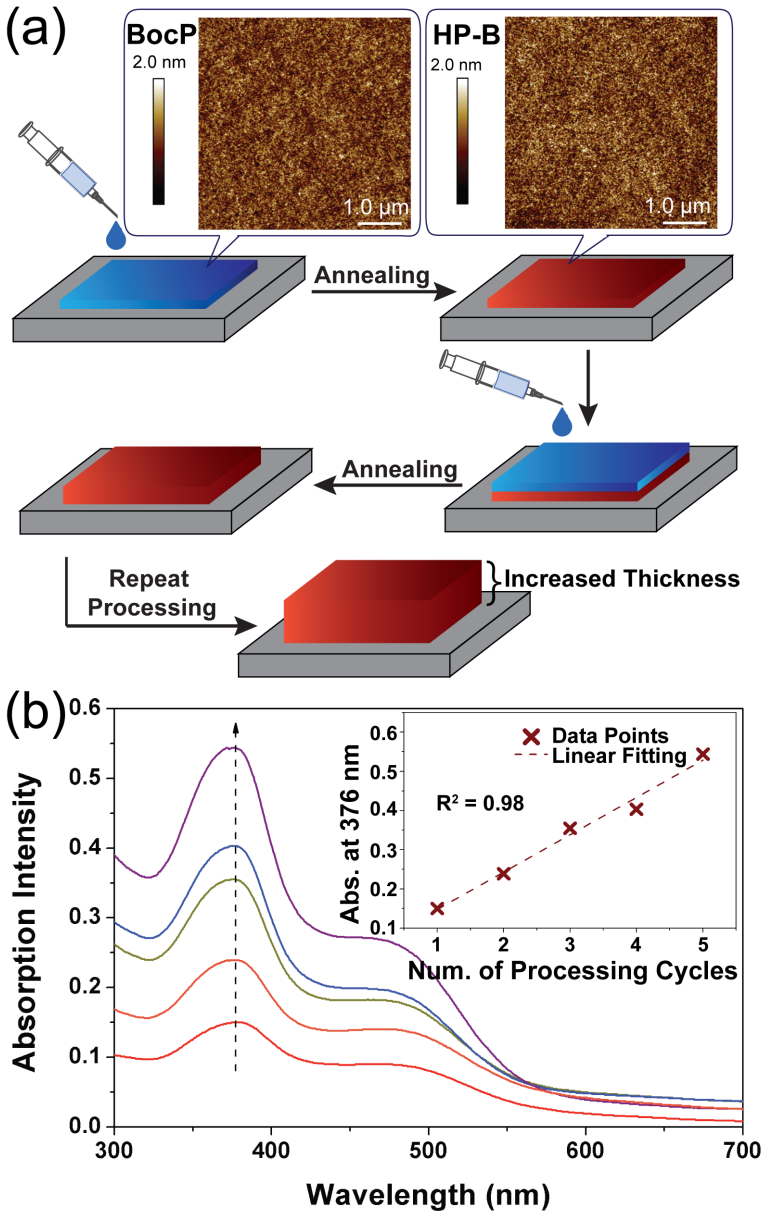

Figure 47. (a) AFM images of thin films of BocP and HP-B; graphic representation of multilayer-film processing of solvent-resistant film of HP-B. (b) UV–vis spectra of the HP-B films after different numbers of processing cycles. Inset is the plot between the processing cycle numbers and absorption intensities at 376 nm.

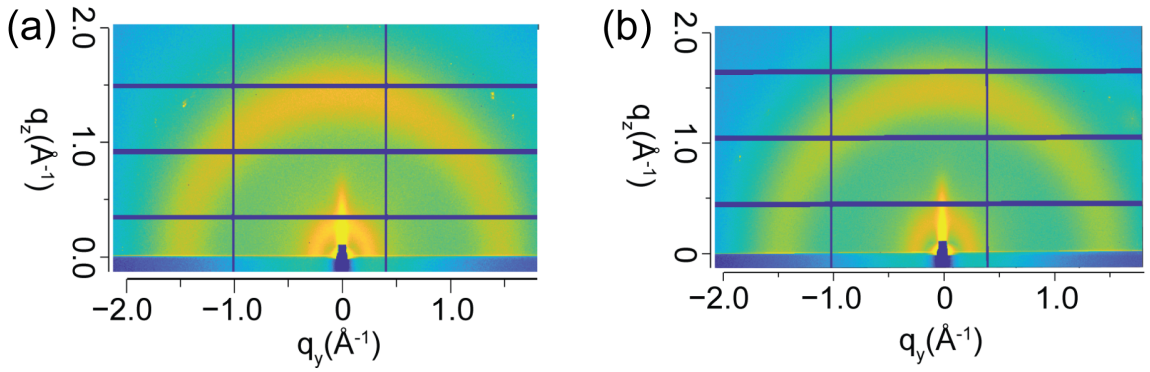

Figure 48. GIWAXS patterns of (a) a BocP (as casted) thin film and (b) a HP-B (annealed) thin film. The thin film of BocP was prepared by spin coating a BocP solution (2.0 mg/mL in chlorobenzene) at a spinning rate of 1000 rpm on silica wafer substrates. The thin film of HP-B was prepared by thermal annealing another thin film of BocP at 130 °C for 1 hour in a N_2-filled glovebox.

The atomic force microscopy (AFM) image of the **BocP** thin film [spin-casted from a solution of chlorobenzene (2 mg/mL)] showed an amorphous morphology and a smooth surface with root-mean-square roughness of 0.28 nm (**Figure 47**), suggesting an excellent film-forming ability. GIWAXS of this sample showed no significant features (**Figure 48**), further confirming the amorphous nature of the film. After the thermal treatment at 130 °C, the AFM image of the **HP-B** film demonstrated a similar morphology with only a slightly increased root-mean-square roughness (0.30 nm). Meanwhile, the GIWAXS pattern remained featureless, indicating that the Boc cleavage process did not alter the morphology of the film significantly. This retained morphology was likely a result of the low chain mobility of **HP-B** due to the strong π–π interactions between the rigid and coplanar polymer backbones.

After thermal cleavage of Boc groups, the resulting film of **HP-B** became resistant to common organic solvents (**Figure 43**). For most reported solution-processed

thin films of polymers, if not further cross-linked, additional contact with organic solvents would often lead to redissolution or solvent damages of the original films. This problem represents a major challenge for multilayer film fabrication using solution-processing techniques.[145,150] The demonstrated *in situ* formation of intramolecular hydrogen bonds in **HP-B** offered an ideal strategy to address this issue. In our model test, several cycles of the solution casting and thermal cleavage were performed (**Figure 47a**) to deposit multiple layers of **HP-B** in a cumulative manner. In these cycles, solution casting an additional **BocP** layer did not impact the **HP-B** layer on the substrate, due to the switched off solubility of **HP-B** after the regeneration of intramolecular hydrogen bonds. This well-controlled multilayering process led to a linear correlation between the absorption intensities and the number of processing cycles (**Figure 47b**). This method sets the foundation for future developments of polymeric materials suitable for multilayer solution processing and 3D printing by manipulating intramolecular noncovalent bonds and the backbone conformation. [150-152]

3.5 Conclusion

In conclusion, we present here a molecular engineering strategy to manipulate intramolecular hydrogen bonds of rigid macromolecules, offering an innovative fundamental method to accomplish the challenging synthesis and processing of this important class of polymeric materials. After masking intramolecular hydrogen bonds with Boc groups, the synthesis of a high molecular weight batch of **BocP** with an excellent solubility was accomplished. Thermal cleavage of these Boc groups unmasked

the preorganized intramolecular hydrogen bonds in **HP-B** in the solid state. As a result, the rigidified backbones of **HP-B** amplified the interchain interactions, leading to good resistance toward organic solvents. This approach was employed to demonstrate the multilayer solution casting of **HP-B**, providing a practical method for multilayer processing and 3D printing of such materials without the concern of solvent orthogonality. This strategy can be feasibly applied to other monomers containing amide, amino, or urea groups as hydrogen bond donors to access diverse structures and properties of this class of rigid polymers.

3.6 Experimental Section

3.6.1 General Methods

Starting materials and reagents were purchased from Sigma Aldrich, Acrons Organics, Alfa Aesar or Oakwood and used as received. THF was dried and distilled under nitrogen from sodium using benzophenone as the indicator. CH_2Cl_2, DMF, and toluene were dried using a IT pure solvent system (PureSolv-MD-5) and used without further treatment. 1,2-Bis[(2-octyldodecyl)oxy]benzene was synthesized according to a reported literature procedure.[153] ^{1}H and ^{13}C NMR spectra were recorded on Varian Inova 300 MHz or 500 MHz spectrometers. The NMR chemical shifts were reported in ppm relative to the signals corresponding to the residual non-deuterated solvents ($CDCl_3$: ^{1}H 7.26 ppm, ^{13}C 77.16 ppm) or the internal standard (tetramethylsilane: ^{1}H 0.00 ppm). Abbreviations for reported signal multiplicities are as follows: s, singlet; d, doublet; t, triplet; q, quartet; m, multiplet; br, broad. The broad singlet at ~1.55 ppm on ^{1}H NMR

spectra represents the resonance signal of H_2O in $CDCl_3$. High resolution electrospray ionization (ESI) mass spectra were recorded on Applied Biosystems PE SCIEX QSTAR. Column chromatography was carried out using Biotage® IsoleraTM Prime instrument with various size of SiO_2 Biotage ZIP® cartridge. Analytical size exclusion chromatography (SEC) measurements were performed on a TOSOH EcoSEC (HLC-8320GPC) in THF solution at 40 °C temperature through TSKgel SuperHM-M and TSKgel SuperH-RC columns. The molecular weights were calculated using a calibration curve based on polystyrene standards. Preparative SEC was performed in chloroform solution at room temperature using a JAI recycling preparative HPLC (LC-92XXII NEXT SERIES) through a JAIGEL-2H-40 column. UV-vis absorption spectra were recorded on a Shimadzu UV-2600 Spectrophotometer. Fourier transform infrared spectra were recorded in attenuated total reflection mode using ZnSe on a Shimadzu IRAffinity-1S spectrometer. Thermal gravimetric analysis (TGA) was recorded under nitrogen atmosphere with heating rate of 10 °C min^{-1} from 40 °C to 600 °C using TA Q500. Silicon wafers were cleaned by UV-ozone treatment for 15 minutes. Atomic force microscopy (AFM) images were recorded with Bruker Dimension Icon AFM in a tapping mode and processed using NanoScope Analysis. Grazing incidence wide angle X- ray scattering (GIWAXS) was conducted at Beamline 7.3.3 at the Advanced Light Source (ALS), Lawrence Berkeley National Laboratory, using an approximately 0.5 mm wide 10 keV X-ray beam. Using the GIXSGUI package for Matlab, data are corrected using silver behenate as the standard sample.[154] DFT calculation were performed with the Gaussian 09 package.[155] The molecular conformation was optimized by DFT

calculation using B3LYP/6-31g(d,p). For the computational simplicity, 2-octyldodecyl chains were replaced by methyl groups. Cyclic voltammetry in the solid state was carried out at room temperature in nitrogen-purged acetonitrile with a CHI voltammetric analyzer. Tetrabutylammonium hexafluorophosphate (0.1 M in acetonitrile) was used as the supporting electrolyte. The conventional three-electrode configuration consisted of an indium tin oxide (ITO) working electrode, a platinum wire anxiliary electrode, and a Ag/AgCl electrode with ferrocene/ferrocenium as the standard. Cyclic voltammograms were obtained at a scan rate of 100 mV/s. The thin film of **BocP** was prepared by drop-casting the 2-methyltetrahydrofuran solution of **BocP** (5 mg/mL) on an ITO coated glass substrate. The thin film of **HP-B** was generated by heating the aforementioned BocP thin film on an ITO coated glass substrate at 130 °C for 1 hour under nitrogen. The thin film of **BocP** was prepared by spin coating a **BocP** solution (2.0 mg/mL in chlorobenzene) at a spinning rate of 1000 rpm on silica wafer substrates. The thin film of **HP-B** was prepared by thermal annealing another thin film of **BocP** at 130 °C for 1 hour in a N_2-filled glovebox.

3.6.2 Synthesis

Compound **43**: To a stirred concentrated HNO_3 (35 mL), a solution of 1,2-bis[(2-octyldodecyl)oxy]benzene (9.13 g, 13.0 mmol) in dichloromethane (80 mL) was added dropwise over 30 min at room temperature. After the addition, 13 mL concentrated H_2SO_4 was added in one portion. The mixture was stirred for 90 min at room temperature, before poured onto crushed ice. After phase separating, the organic layer

was washed with 1 M NaOH twice, brine twice and dried with $MgSO_4$. The product was purified through column chromatography (SiO_2, hexane/ dichloromethane 4:1) and isolated as a yellow oil (8.24 g, 84%). ^{1}H NMR (300 MHz, $CDCl_3$) δ = 7.28 (s, 2H), 3.95 (d, *J* = 5.4 Hz, 4H), 1.83 (m, *J* = 6.0 Hz, 2H), 1.41-1.26 (m, 64H), 0.88 (t, *J* = 6.6 Hz, 12H); ^{13}C NMR (75 Hz, $CDCl_3$) δ 152.24, 136.51, 107.62, 72.63, 38.08, 32.15, 32.14, 31.81, 31.43, 30.23, 29.94, 29.89, 29.86, 29.81, 29.60, 29.59, 27.04, 22.89, 14.22. ESI-MS: *m/z* $[M+Cl]^-$ Calcd for $C_{46}H_{84}N_2O_6Cl$ 795.6018; Found 795.6009.

Compound **44**: Compound **43** (4.0 g, 5.3 mmol) was dissolved in a mixed solvent of THF (60 mL) and EtOH (120 mL). To the solution, 10% Pd/C (1.2 g) and HCO_2NH_4 (60 g) were added at room temperature. After stirring at room temperature overnight, the reaction mixture was filtered and the filtrate was collected under N_2. The solvent was removed under reduced pressure and dried under vacuum. Urea (40 g) was subsequently added to the residue and the temperature was increased to 170 °C. The molten mixture was stirred for 4 h. After cooling down to room temperature, water and ethyl acetate were added into the mixture. After phase separating, the organic layer was washed with brine twice and dried with $MgSO_4$. The crude product was purified through column chromatography (SiO_2, hexane/ ethyl acetate 4:1 to 1:3) and was isolated as a brown oil (1.50 g, 39%). ^{1}H NMR (300 MHz, $CDCl_3$) δ = 10.20 (s, 2H), 6.73 (s, 2H), 3.78 (d, *J* = 5.7 Hz, 4H), 1.76 (m, *J* = 5.7 Hz, 2H), 1.38-1.24 (m, 64H), 0.87 (t, *J* = 6.0 Hz, 12H); ^{13}C NMR (75 Hz, $CDCl_3$) δ 157.37, 146.37, 122.52, 98.58, 73.72, 38.51, 32.18, 31.57, 30.32, 29.93, 29.90, 29.86, 29.57, 29.55, 27.13, 22.85, 14.23. ESI-MS: *m/z* $[M+H]^+$ Calcd for $C_{47}H_{87}N_2O_3$ 727.6717; Found 727.6695.

Compound **45**: Compound **44** (2.10 g, 2.77 mmol) was dissolved in acetic acid (6 mL) and heated up to 70 °C. Then a solution of liquid bromine (1.36 g, 8.67 mmol) in acetic acid (6 mL) was added over 10 min. The reaction mixture was stirred under reflux for 4 h. After cooling to room temperature, the mixture was extracted with CH_2Cl_2 and washed with brine twice, 1M NaOH twice, water once and dried with $MgSO_4$. The crude product was purified through column chromatography (SiO_2, hexane/ ethyl acetate 4:1 to 2:1) to give **45** as a brown oil (2.23 g, 88%). ^{1}H NMR (300 MHz, $CDCl_3$) δ = 10.20 (s, 2H), 3.85 (d, *J* = 6.0 Hz, 4H), 1.81 (m, *J* = 6.0 Hz, 2H), 1.34-1.26 (m, 64H), 0.87 (t, *J* = 6.6 Hz, 12H); ^{13}C NMR (125 Hz, $CDCl_3$) δ 155.87, 146.45, 125.05, 124.93, 98.06, 78.24, 39.30, 32.16, 32.12, 31.34, 30.38, 30.17, 29.98, 29.96, 29.92, 29.63, 29.62, 27.15, 22.93, 14.35. ESI-MS: *m/z* $[M-H]^-$ Calcd for $C_{47}H_{83}N_2O_3Br_2$ 883.4750; Found 883.4819.

Compound **46**: Compound **45** (900 mg, 0.983 mmol) and trimethylsilyl acetylene (1.93 g, 19.66 mmol) were dissolved in diisopropylamine (11 mL) at room temperature. The solution was degassed by three freeze-pump-thaw cycles before $Pd(dppf)Cl_2CH_2Cl_2$ (48.3 mg, 0.05 mmol), CuI (19.1 mg, 0.10 mmol) and P(*o*-tol)$_3$ (61.8 mg, 0.20 mmol) were added under N_2. The mixture was stirred at 95 °C for 7 days. After cooling to room temperature, the mixture was extracted with CH_2Cl_2 and filtered through celite. The organic phase was dried with $MgSO_4$. The crude product was purified through column chromatography (SiO_2, hexane/ ethyl acetate 8:1 to 3:1) to give **46** as a light yellow oil (623 mg, 69%). ^{1}H NMR (500 MHz, $CDCl_3$) δ = 7.93 (s, 2H), 3.90 (d, *J* = 6.0 Hz, 4H), 1.79 (m, *J* = 6.9 Hz, 2H), 1.52-1.25(m, 64H), 0.88 (t, *J* = 6.3 Hz, 12H), 0.28 (s, 18H); ^{13}C NMR (125 Hz, $CDCl_3$) δ 148.89, 126.27, 105.38, 101.81, 95.74, 78.54, 45.20, 39.37,

32.18, 32.15, 31.40, 30.40, 30.06, 29.98, 29.96, 29.94, 29.90, 29.62, 27.28, 27.24, 22.94, 22.92, 14.34, 0.15. ESI-MS: *m/z* $[M+H]^+$ Calcd for $C_{57}H_{103}N_2O_3Si_2$ 919.7507; Found 919.7472.

Compound **41**: A solution of compound **46** (437 mg, 0.475 mmol) in a mixed solvent of MeOH (30 mL) and THF (30 mL) was added a solution of tetra-n-butylammonium fluoride in THF (1.0 M, 1.9 mL). The mixture was stirred at room temperature overnight and subsequently extracted with ethyl acetate. The organic layer was washed with brine twice, water once, and dried with $MgSO_4$. The crude product was purified through column chromatography (SiO_2, hexane/ ethyl acetate 4:1) to afford monomer 4**1** as a light yellow oil (320 mg, 87%). ^{1}H NMR (500 MHz, $CDCl_3$) δ = 8.39 (s, 2H), 3.91 (d, *J* = 5.7 Hz, 4H), 3.54 (s, 2H), 1.77 (m, *J* = 6.0 Hz, 2H), 1.51 (m, *J* = 6.0 Hz, 4H), 1.38-1.26 (m, 60H), 0.88 (t, *J* = 6.6 Hz, 12H); ^{13}C NMR (125 Hz, $CDCl_3$) δ 155.05, 149.34, 126.68, 101.10, 87.15, 78.39, 75.15, 39.28, 32.16, 31.36, 30.38, 30.04, 29.98, 29.93, 29.92, 29.64, 29.61, 27.16, 27.12, 22.95, 22.93, 14.36. ESI-MS: *m/z* $[M+H]^+$ Calcd for $C_{51}H_{87}N_2O_3$ 775.6717; Found 775.6701.

Compound **42**: Compound **46** (184 mg, 0.2 mmol) was dissolved in anhydrous THF (5 mL) at 0 °C under N_2. Trimethylamine (2 mL) and a few crystals of DMAP were added dropwise. Di-*tert*-butyl dicarbonate (0.2 mL) was added in one portion subsequently. The reaction mixture was warmed up to room temperature and stirred overnight. The mixture was extracted with CH_2Cl_2, and the organic layer was washed with brine. After removing the solvent under reduced pressure, the residue was re-dissolved in a mixed solvent of CH_2Cl_2 (5 mL) and methanol (1 mL) at room

temperature. A solution of tetra-n-butylammonium fluoride in THF (1.0 M, 1.0 mL) was added. The mixture was stirred at room temperature overnight and subsequently extracted with CH_2Cl_2. The organic phase was washed with brine twice, water twice and dried with $MgSO_4$. The crude product was purified through column chromatography (SiO_2, hexane/ ethyl acetate 9:1 to 4:1) to afford monomer **42** as a light yellow oil (141 mg, 72%). ^{1}H NMR (500 MHz, $CDCl_3$) δ = 3.92 (d, *J* = 6.0 Hz, 2H), 3.57 (s, 2H), 1.79 (m, *J* = 6.0 Hz, 2H), 1.64 (s, 18H) 1.52-1.25(m, 64H), 0.88 (t, *J* = 6.5 Hz, 12H); ^{13}C NMR (125 Hz, $CDCl_3$) δ = 154.98, 149.27, 126.61, 101.03, 87.08, 78.32, 75.15, 39.28, 32.16, 31.36, 30.38, 30.04, 29.98, 29.93, 29.92, 29.64, 29.61, 27.16, 27.12, 22.95, 22.93, 14.36. ESI-MS: *m/z* $[M+K]^+$ Calcd for $C_{61}H_{102}N_2O_7K$ 1013.7325; Found 1013.7396.

HP-A: Monomer **41** (38.3 mg, 0.0494 mmol) and 1,5-diiodoanthracene-9,10-dione (22.7 mg, 0.0494 mmol) were added into mixed solvents of toluene (5 mL) and diisopropylamine (2.5 mL). The suspension was degassed by three freeze-pump-thaw cycles before $Pd(PPh_3)_4$ (2.8 mg, 2.5 μmol) and CuI (0.5 mg, 2.5 μmol) were added under N_2. The mixture was stirred at 95 °C for 3 days. After cooling to room temperature, the reaction mixture was added into methanol (100 mL). The polymer suspension was stirred at room temperature over night. The resulting solids were filtered, washed with methanol twice, and dried under vacuum to afford **HP-A** as dark brown solids (31.0 mg, 64%, M_n = 5.2 kg/mol, PDI = 1.7 determined by SEC).

BocP: Monomer **42** (28.4 mg, 0.0291 mmol) and 1,5-diiodoanthracene-9,10-dione (13.4 mg, 0.0291 mmol) were added into mixed solvents of toluene (4 mL) and diisopropylamine (2 mL). The suspension was degassed by three freeze-pump-thaw

cycles before $Pd(PPh_3)_4$ (1.7 mg, 1.46 μmol) and CuI (0.3 mg, 1.46 μmol) were added under N_2. The mixture was stirred at 95 °C for 3 days. After cooling to room temperature, the solvents were removed under reduced pressure. The residue was extracted with CH_2Cl_2, washed with brine three times and dried over $MgSO_4$. After removal of CH_2Cl_2 and dried under vacuum, the crude polymer products were isolated as dark brown solids (26 mg, 74%, M_n = 15.4 kg/mol, PDI = 2.2 determined by SEC). These crude products were further purified by the preparative SEC using chloroform as the eluent with an eluting rate of 14 mL/min to remove low molecular weight oligomers. Further removal of chloroform under reduced pressure afforded **BocP** as dark brown solids (16 mg, 46%, M_n = 32.5 kg/mol, PDI = 1.7 determined by SEC). ^{1}H NMR (500 MHz, $CDCl_3$) δ = 10.54 (broad, 0.34H), 8.60 ~ 7.70 (m, broad, 6H), 4.15 (broad, 4H). Due to the significant overlapping with signals of H_2O and HDO, the integration of aliphatic protons in **BocP** was not accurate.

HP-B: To a 20 mL vial, **BocP** (5.1 mg, M_n = 32.5 kg/mol, PDI = 1.7 determined by SEC) was added. The vial containing **BocP** was capped with a black phenolic cap with PTFE liner, further transferred into a N_2-filled glovebox, and heated up to 130 °C on a hot plate for 1 hour. After cooling down to room temperature, **HP-B** (4.5 mg, M_n = 28.7 kg/mol, calculated based on **BocP**) was collected as dark brown solids.

3.6.3 NMR Spectra

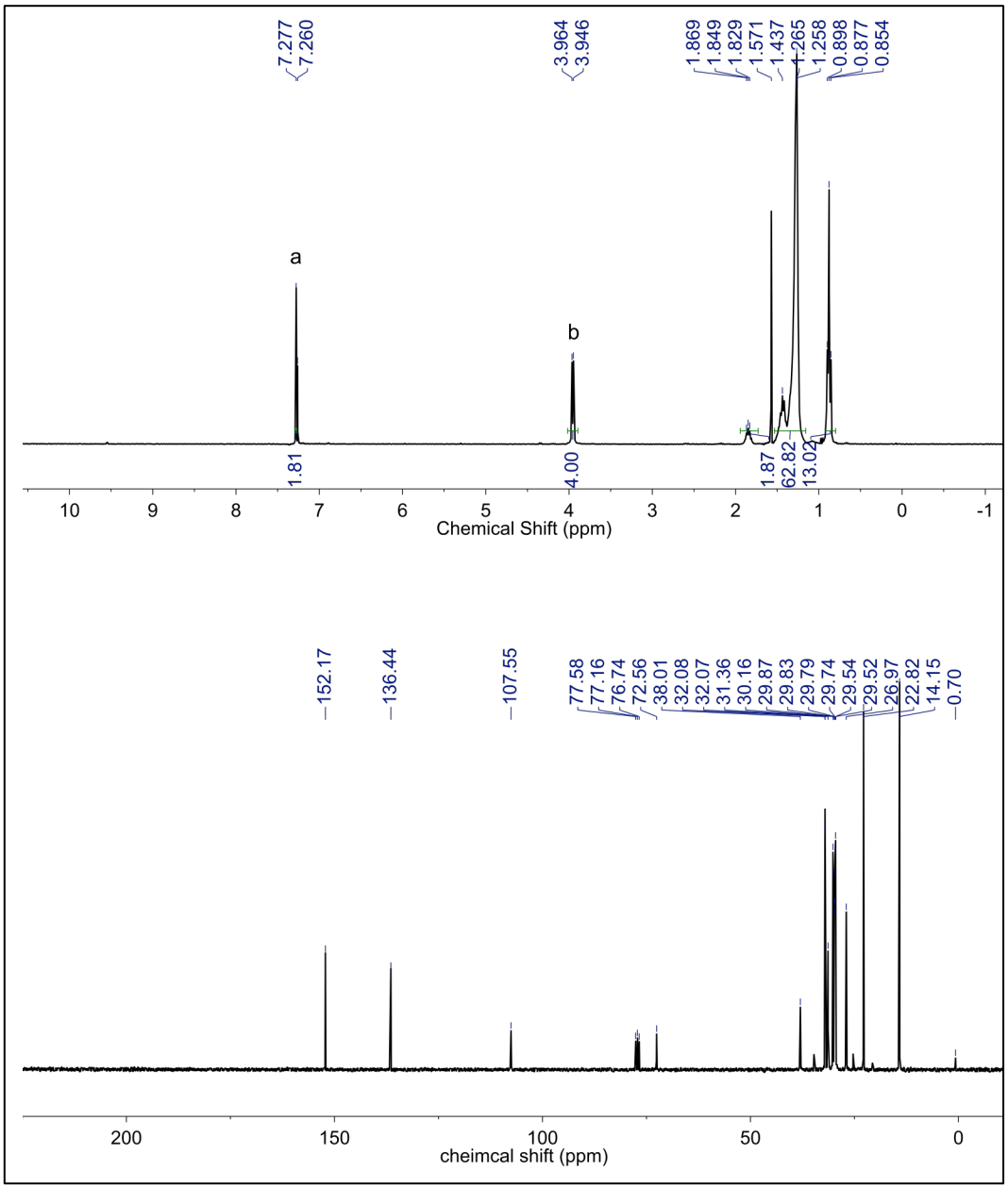

Figure 49. ^{1}H (300 MHz), ^{13}C (75 MHz) NMR spectra of 43 in $CDCl_3$ at room temperature.

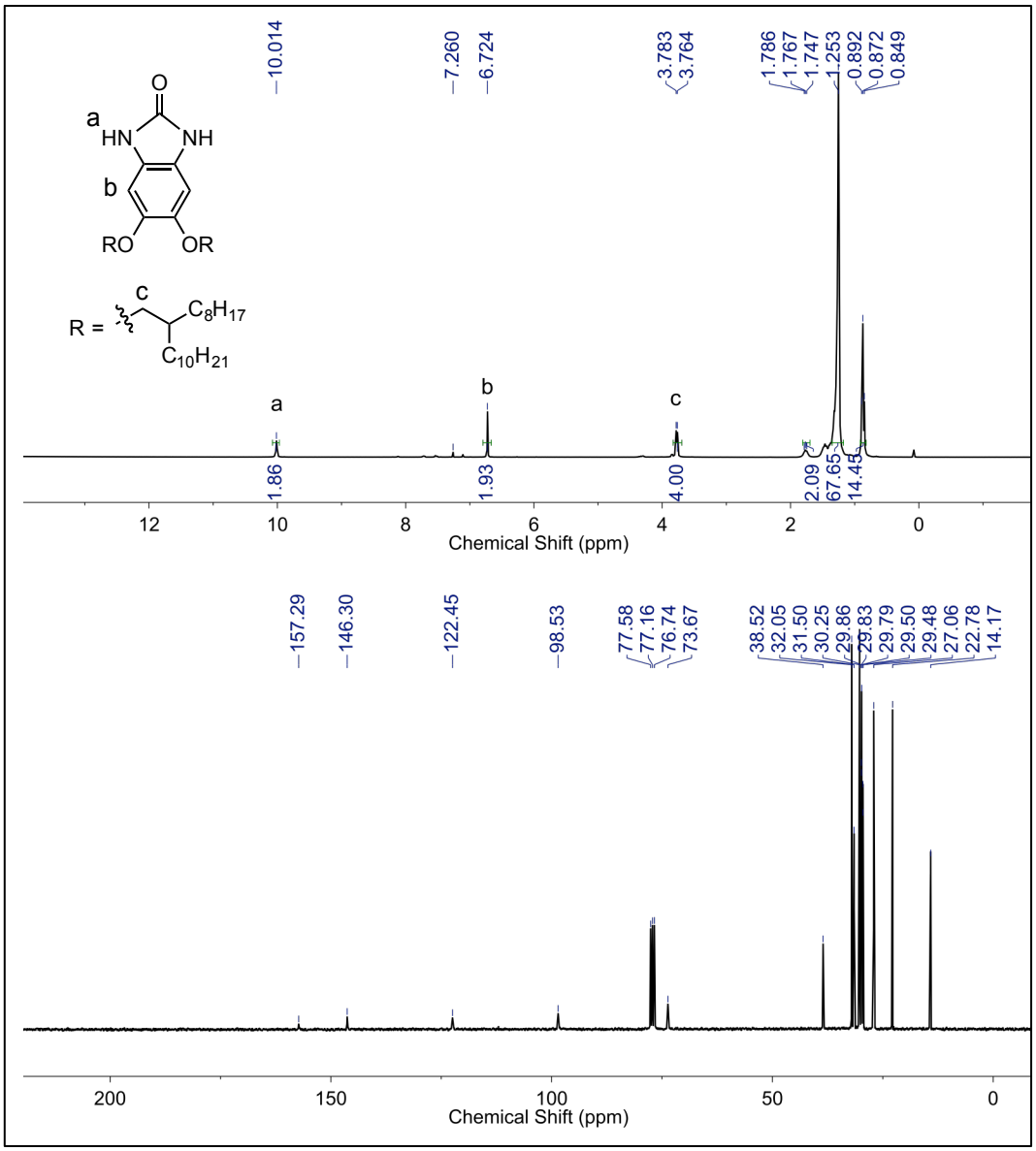

Figure 50. ^{1}H (300 MHz), ^{13}C (75 MHz) NMR spectra of 44 in $CDCl_3$ at room temperature.

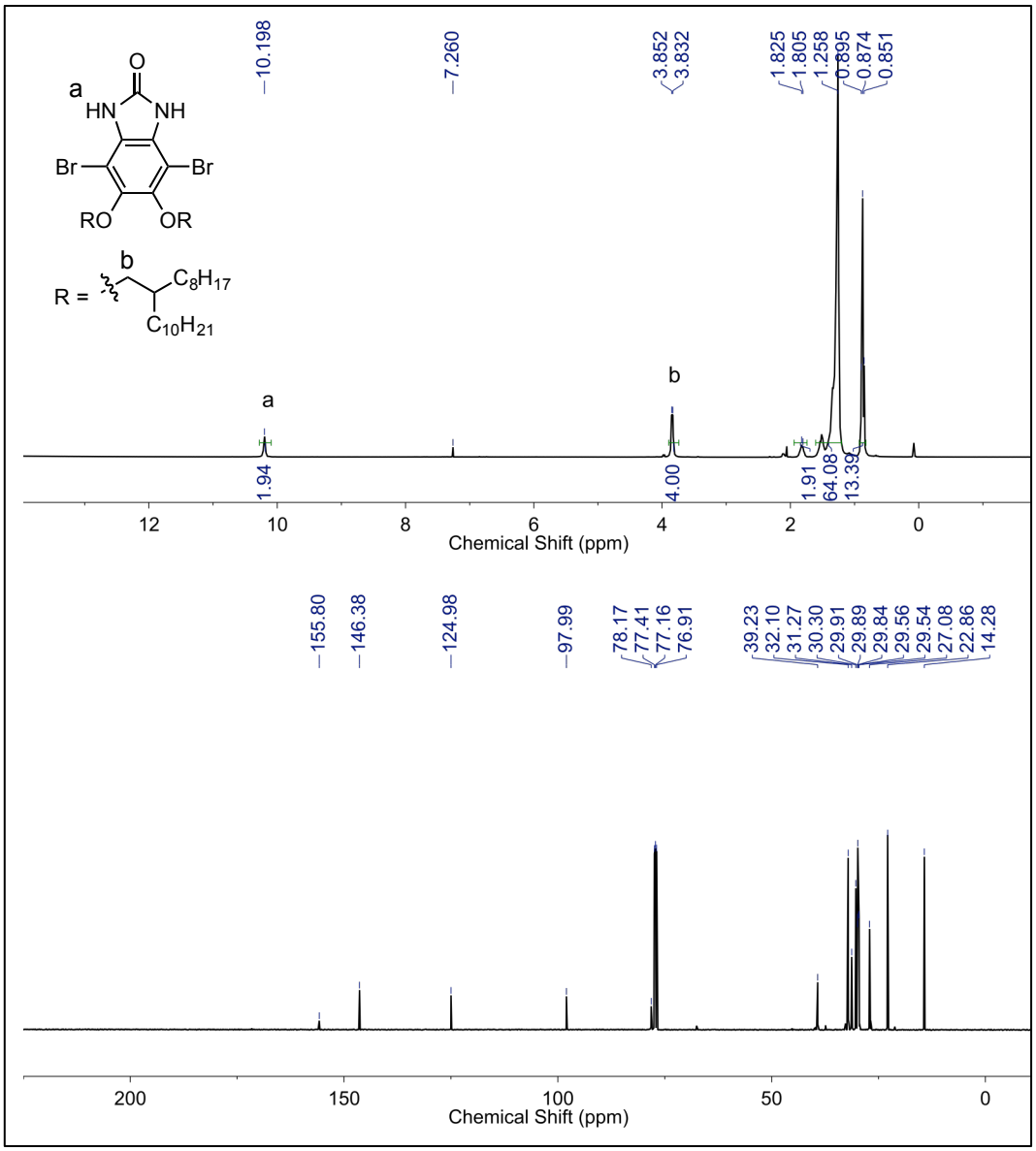

Figure 51. ^{1}H (300 MHz), ^{13}C (125 MHz) NMR spectra of 45 in $CDCl_3$ at room temperature.

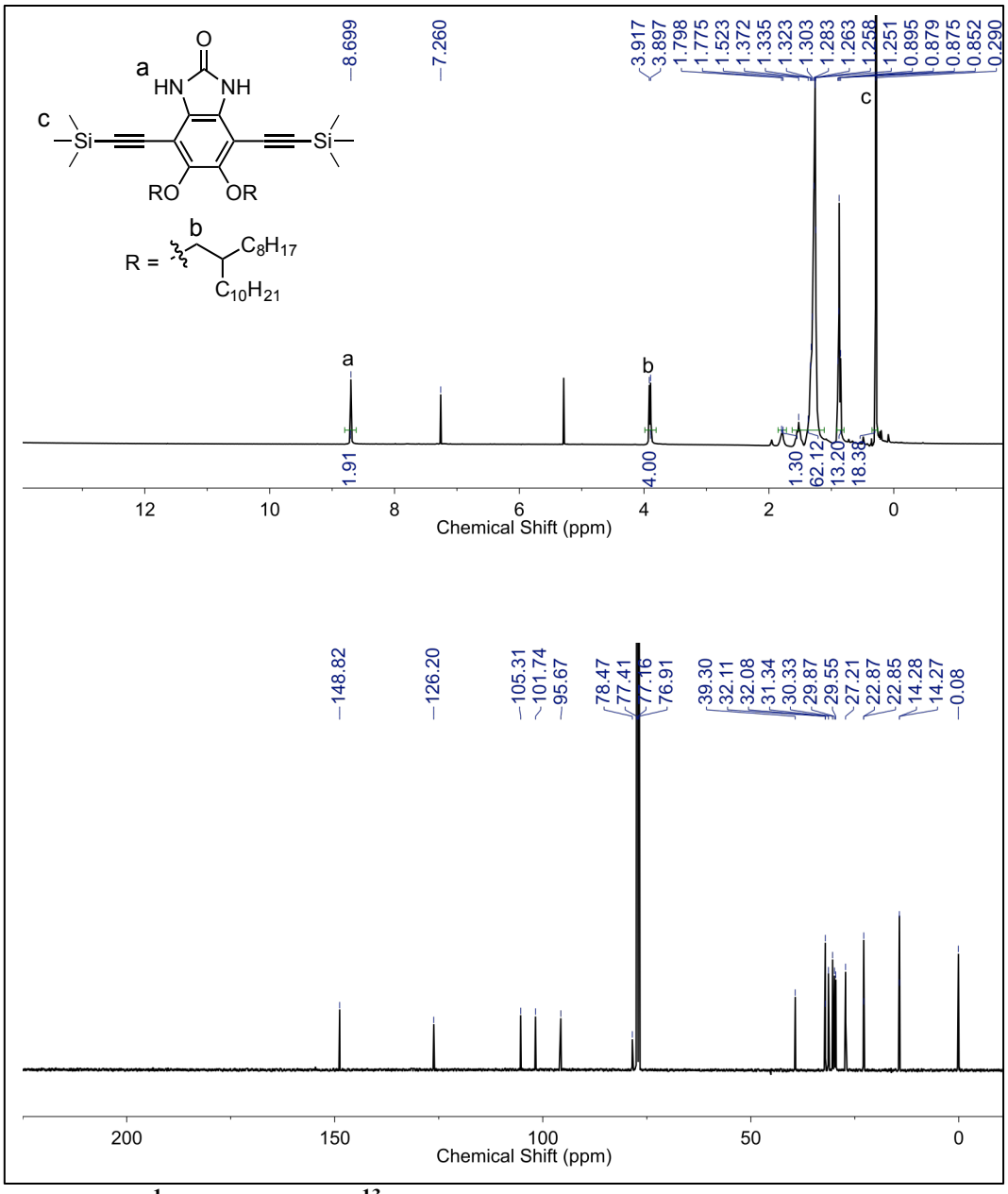

Figure 52. ^{1}H (300 MHz), ^{13}C (125 MHz) NMR spectra of 46 in $CDCl_3$ at room temperature.

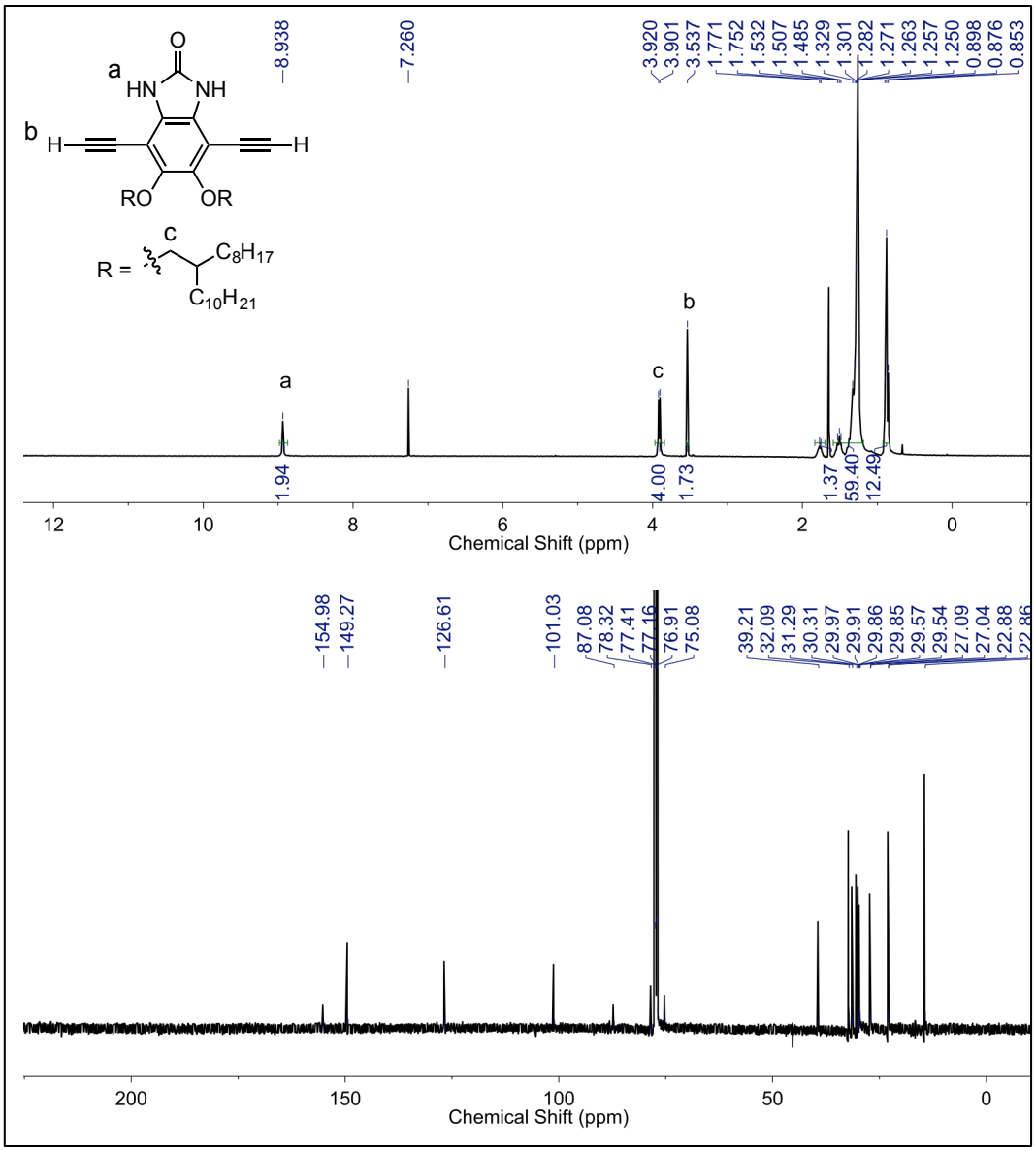

Figure 53. ^{1}H (300 MHz), ^{13}C (125 MHz) NMR spectra of monomer 41 in $CDCl_3$ at room temperature.

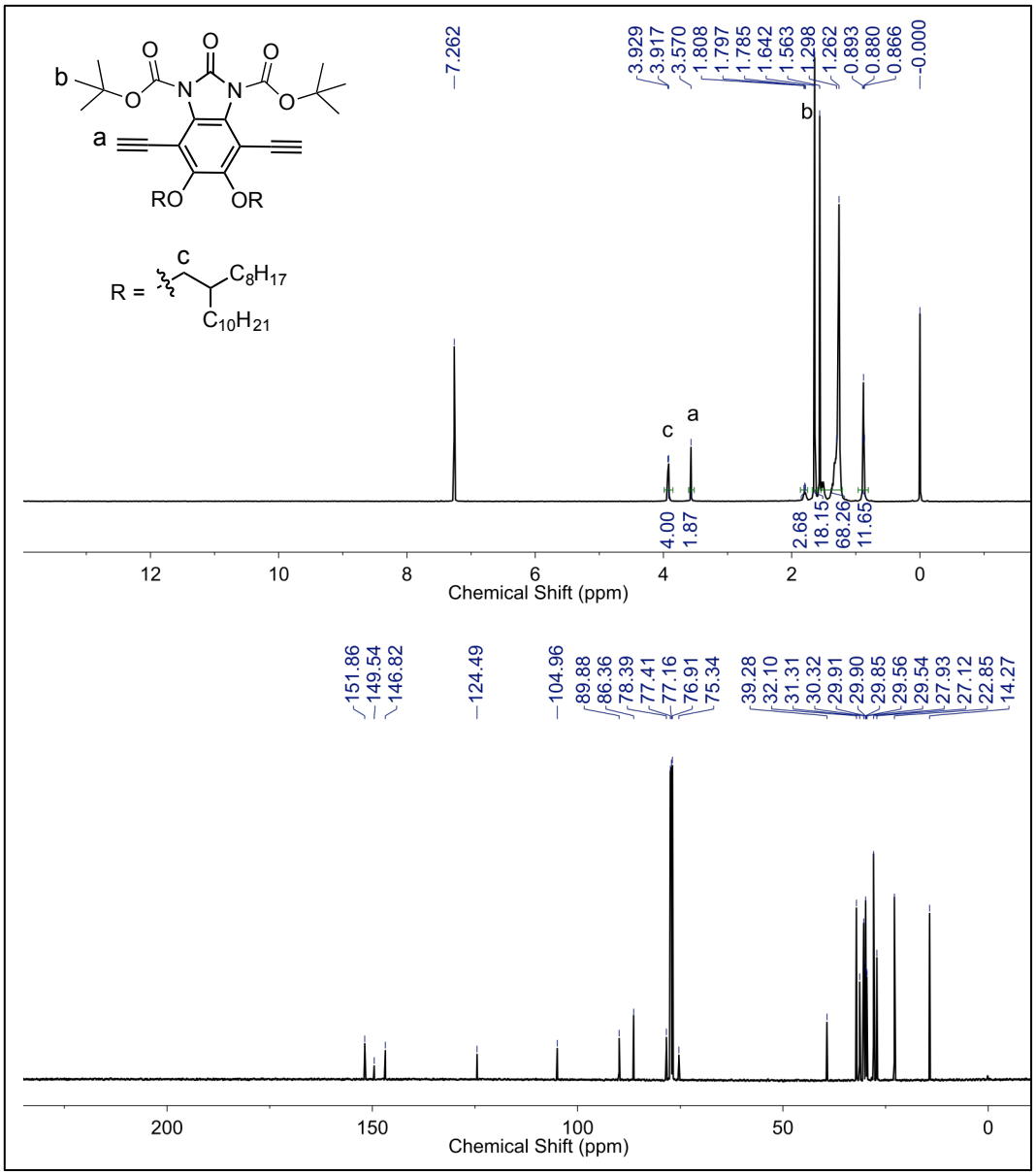

Figure 54. ^{1}H (500 MHz), ^{13}C (125 MHz) NMR spectra of monomer 42 in $CDCl_3$ at room temperature.

3.6.4 Size Exclusion Chromatography

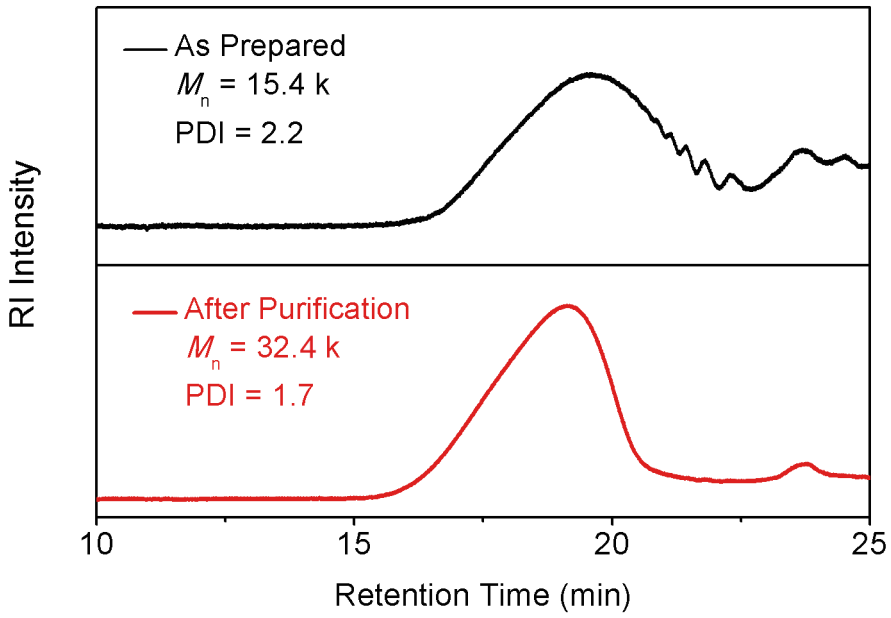

Figure 55. Size exclusion chromatogram of BocP (top: as prepared; bottom: purified after preparative SEC).

CHAPTER IV

LOW BAND GAP COPLANAR CONJUGATED MOLECULES FEATURING DYNAMIC INTRAMOLECULAR LEWIS ACID-BASE COORDINATION*

4.1 Introduction

Low band gap materials are pivotally important in applications associated with photovoltaic devices and near-infrared (NIR) absorbing materials.[22,156-159] Among them, π-conjugated organic materials are particularly captivating on account of their composition of earth-abundant elementals, high photoabsorptivity through direct band gaps, and facile yet controllable solution processability.[160] Two practical strategies are often invoked in the design and synthesis of low band gap π-conjugated organic compounds: (1) Incorporation of conjugated electron-donating and -accepting units in an alternating manner[161-163] and (2) extension of the coherent π-electron delocalization.[164-167]

The first strategy relies on the recombination of the highest occupied molecular orbitals (HOMO) and the lowest unoccupied molecular orbitals (LUMO) of the alternating electron-donating and -accepting units to afford a higher HOMO and a lower LUMO, hence, a narrowed band gap.[168] In order to achieve an extremely low band gap, an electron-rich donor unit is often employed. This approach, however, can lead to the resulting product with a high lying HOMO, which can be easily oxidized and hence

*Reprinted with permission from "Low Band Gap Coplanar Conjugated Molecules Featuring Dynamic Intramolecular Lewis Acid–Base Coordination" Zhu, C.; Guo, Z.-H.; Mu, A. U.; Liu, Y.; Wheeler, S. E.; Fang, L. *J. Org. Chem.*, **2016**, *81*, 4347. Copyright 2016 American Chemical Society.

suffer from stability issues in an ambient environment.[165] In this context, a more viable strategy for the development of stable low band gap molecules should lower the LUMO level while maintaining the HOMO level. Additionally, lower LUMO energies can lead to *n*-type materials with high electron affinities that are generally less accessible compared to the more widely investigated *p*-type organic materials.[169-171]

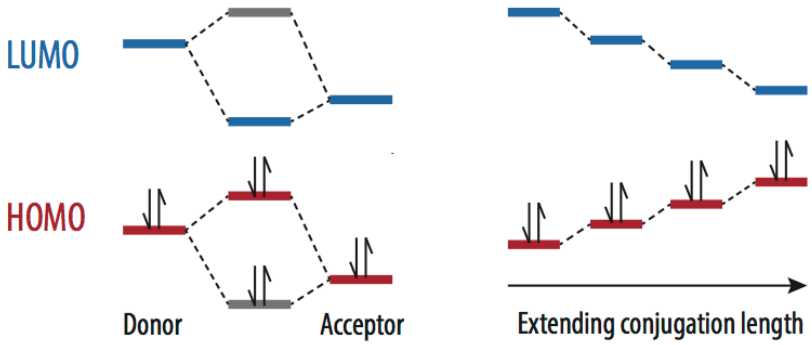

Figure 56. Two general strategies that are often invoked in the design and synthesis of low band gap π-conjugated organic compounds: incorporation of conjugated electron-donating and -accepting units in an alternating manner (left) and extension of the coherent π-electron delocalization (right).

In order to apply the second strategy, namely, extension of π-electron delocalization, conjugated polymers are preferable compared to small molecules because of their longer possible conjugation.[172] The effective coherent conjugation length of conventional single-strand polymers, however, is severely limited by the torsional motion in between the aromatic units.[28] A coplanar π-system with restricted torsional disorder, in contrast, is expected to enjoy a much longer coherent conjugation along the backbone.[13,46,167,173-176] Thus, locking the entire π-system into a coplanar conformation

through a second strand of bonds emerged as an important method toward the development of materials with lower band gaps.[3]

In 2006, Yamaguchi et al. demonstrated[42] the use of noncovalent B←N coordination between a boryl-thienyl unit and an adjacent thiazole unit, which led to a partially coplanar molecule and a lower band gap. Since then, several examples of B←N bond promoted, stepladder-type conjugated small molecules, oligomers, and polymers have been reported.[68,69,109,169,177-182] It is still a challenge, however, to achieve coplanarity of an entirely π-conjugated molecule with more than two aromatic units through B←N bonds. Recently, acceptor–donor–acceptor type conjugated ladder molecules featuring B–N bridging bonds were synthesizied.[69] Analogous donor–acceptor–donor type coplanar molecules, however, have not been achieved yet due to significant deactivation of the nitrogen centers in the central acceptor unit. Herein, we report a new strategy of using B←N coordination to simultaneously achieve (1) coplanarity through the entire π-backbones and (2) low lying LUMO levels in small donor–acceptor–donor molecules. By taking advantage of the dynamic nature of B←N coordination, rational control over the optical activities has been achieved by using competitive Lewis basic solvents. Furthermore, the electronic and optical properties of these molecules featuring dynamic bonds were studied in detail through a combination of experimental and theoretical tools.

4.2 Molecular Design, Synthesis and Characterization

The target model compounds **48** and **50** were designed such that the formation of B←N bonds not only fixes the torsional conformation of the entire π-conjugated system

but also strengthens the electron-withdrawing characteristics of the central electron-poor units. The combination of these two effects should lower the LUMO energy levels and band gaps significantly. In these systems, a pyrazine unit was selected as the central electron-accepting unit because it can donate two pairs of electrons in two directions in a central symmetric manner.[180] On the other hand, flanking electron-donating thiophene or thienothiophene units were installed in **48** and **50**, respectively. Because the two nitrogen atoms of the central ring are *para*- to one another, the mutual deactivation effect on their Lewis basicity was relatively weak.

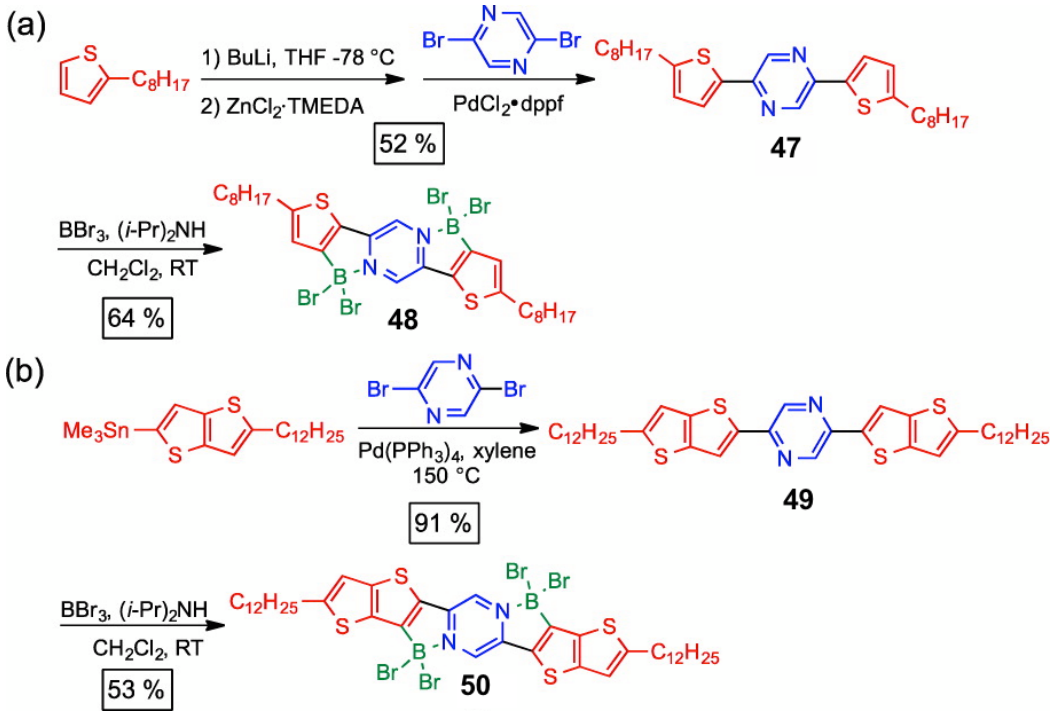

Figure 57. Synthesis of B←N bridged donor–acceptor–donor ladder-type molecules 48 and 50.

The synthesis of **48** started with Negishi coupling between 2-octylthiophene and dibromopyrazine, which afforded the linear conjugated molecule **47** (**Figure 57**). The second step involved *N*-directed electrophilic aromatic substitution of the electron-rich thiophene with BBr_3 (1.0 M solution in CH_2Cl_2).[68,69] Owing to its strong Lewis acidity, BBr_3 was first coordinated with the Lewis basic nitrogen atom on pyrazine. This process made the C_3 position of the thiophene unit spatially favorable for the subsequent electrophilic aromatic substitution. In the presence of diisopropylamine, one-pot formation of two B←N coordination bonds and two C–B covalent bonds was accomplished to construct two stable five-membered rings in the product **48**. These rings fused the two thiophene units and the central pyrazine unit together and confined the conformation of the entire π-system into a coplanar geometry. A similar strategy was adopted to synthesize thienothiophene-derived analogue **50**, which possessed a further extended conjugation backbone with seven fused rings. By treating the precursor **49** with neat BBr_3 as a stronger borylation reagent in the presence of an excess amount of diisopropylamine, **50** was formed and isolated in 53% yield. In either case, the electron-rich nature of the thiophene or thienothiophene promoted the electrophilic substitution reaction in which two C–B covalent bonds and two B←N coordination bonds formed in one pot. ^{11}B NMR spectra corroborated the chemical environment and the sp^3 hybridized nature of the boron center:[179,183-185] the lone pair donated from the nitrogen center shields the boron nuclei, leading to a significant downfield chemical shift on the spectra (Compound **48**: −4.26 ppm; Compound **50**: −4.12 ppm).

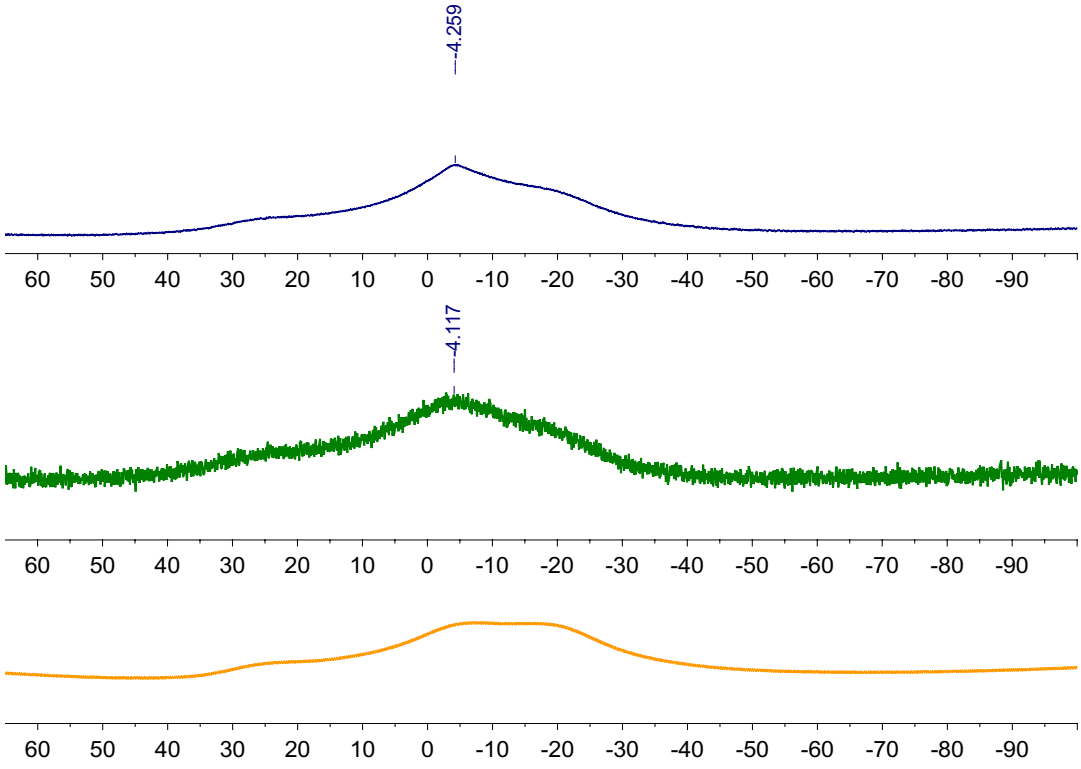

Figure 58. ^{11}B NMR spectra of 48 (blue) and 50 (green) in $CDCl_3$, and a background ^{11}B NMR of D_2O (orange). The broad signal between 25 pm and -20 ppm is a result of glassy NMR probe containing boron.

Compared to their precursors **47** and **49,** the absorption spectra of **48** and **50** in $CHCl_3$ (~9.8×10^{-6} M) were dramatically red-shifted to the NIR region (**Figure 59**), corresponding to low optical band gaps of 1.59 and 1.34 eV, respectively. This drastic red shift can be attributed to planarization effects and the resulting positive overlap between frontier orbitals.[157,186,187] **50** demonstrated an even lower band gap on account of the extended conjugation and the more electron-rich nature of thienothiophene. Time-dependent density function theory (TD-DFT) was employed to simulate the energy

transition and oscillator strength of individual molecules of both **2** and **4** (**Figure 59**). These computed transitions match well with the experimental spectra. Such good agreement can be attributed to the limited conformational variation in these rigid molecules, thanks to the strong bridging intramolecular B←N bonds. The low energy absorption bands at 700 nm for **48** and at 820 nm for **50** were attributed to the transition from HOMO to LUMO. The transitions from HOMO to LUMO+1 mainly contributed to the absorption below 450 nm with high intensities. The noticeable vibrational progressions presented in the spectra of **48** and **50** in chloroform, even for the low energy HOMO—LUMO bands, further corroborated their rigid conformation in solution.[31,188]

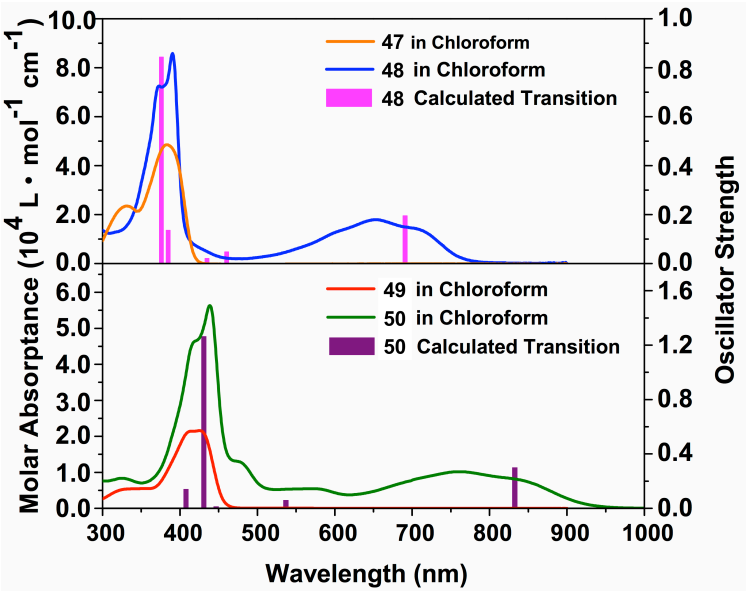

Figure 59. Solution phase UV–vis–NIR spectra and calculated oscillator strength [B3LYP/6-311G(d,p)] of 48 (top) and 50 (bottom), in comparison to their precursors 47 and 49.

In addition, the thin film of **48** demonstrated an almost identical solid-state absorption spectrum compared to that in $CHCl_3$ solution (**Figure 60**). This observation indicated that there was no significant conformational change from solution phase to solid state, further corroborating the coplanar and rigid backbone of this B←N ladder type molecule.[31]

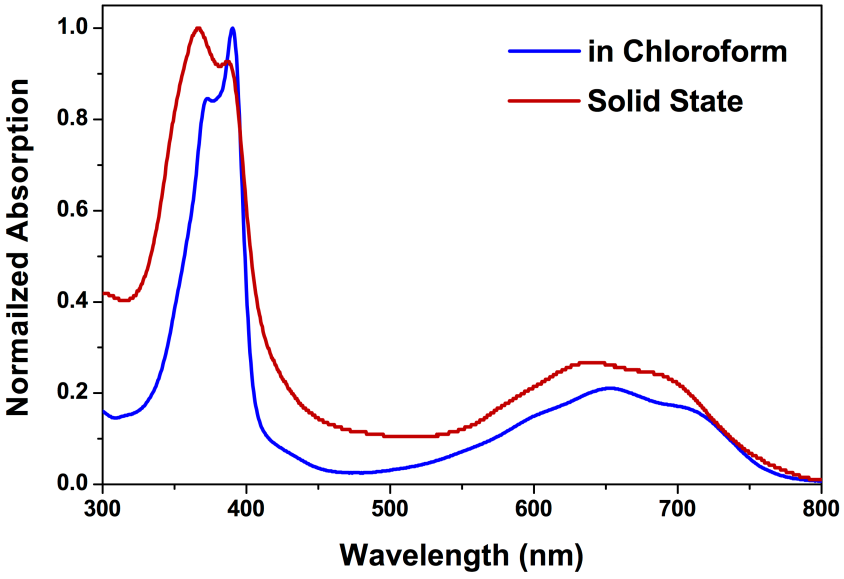

Figure 60. Normailzed UV-vis absorption spectra of 48 in chloroform (9.9×10^{-6} M) and in solid state.

4.3 Dynamic Nature of B←N Coordination

It is expected that the intrinsically dynamic B←N coordination[189-191] should be controllable in the presence of certain external stimuli. For example, the addition of a Lewis base should weaken this bond by competing for the boron center, shifting the thermodynamic equilibrium toward a less planar conformation. As a result, the electronic structure and optical property of these compounds can be controlled actively:

in a Lewis basic solvent, the B←N bond should be more labile and the molecular conformation should be less rigid, leading to a blue-shifted absorption spectrum, and *vice versa*.

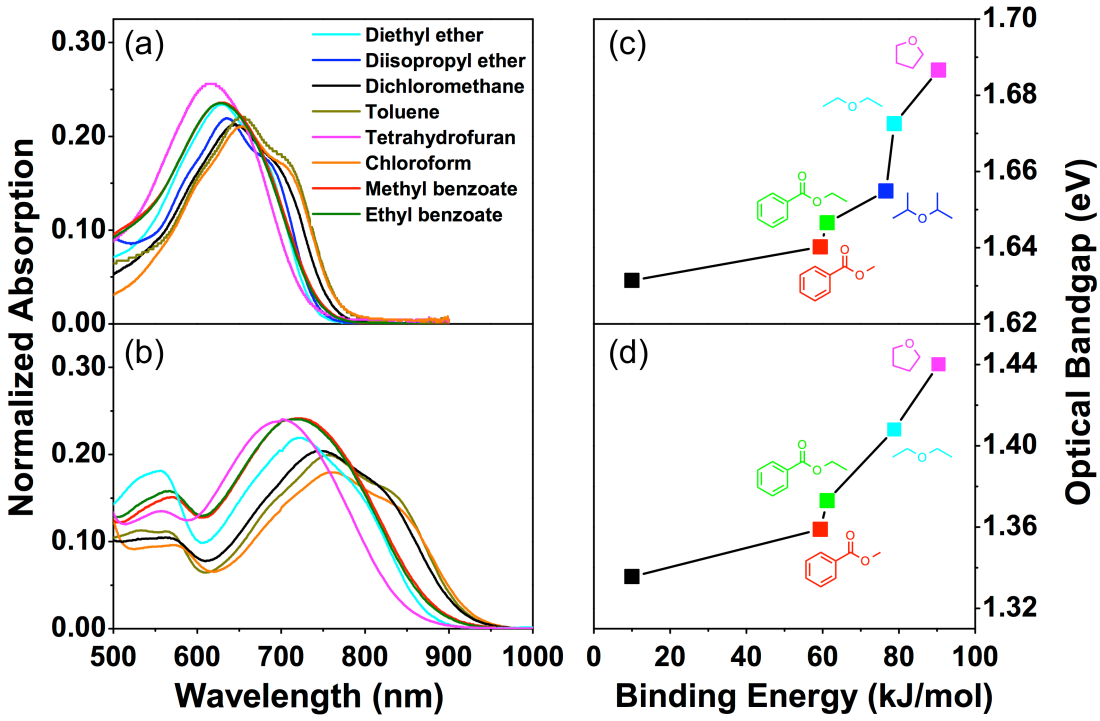

Figure 61. Charge transfer absorption of 48 (a) and 50 (b) in a variety of organic solvents and the correlation between optical band gaps of 48 (c) and 50 (d) with the Lewis basicities of organic solvents (enthalpies from complex formation with BF_3).

In this context, UV–vis–NIR spectra of **48** and **50** were examined in various solvents with varying Lewis basicity. However, it is well-known that solvation effects, such as dipole interaction[192] and electronic polarization,[193,194] can also affect the absorption and optical band gap. In order to minimize these solvation effects, organic solvents were carefully selected with small and similar dielectric constants (dielectric

constants range from 3.8 to 9.2).[195] In general, the low energy absorption peaks were blue-shifted in Lewis basic solvents (**Figure 61**). The optical HOMO—LUMO band gaps measured in these solvents were plotted against the enthalpies from the complex formation between the solvent and BF_3, which provides a measure of the Lewis basicity of the solvent.[196] The band gap increased monotonically as the Lewis basicity increased (**Figure 61**), consistent with the weakening of the intramolecular B←N coordination bonds. Moreover, as the Lewis basicity increased, the vibrational progressions gradually disappeared because **48** and **50** were less rigid.

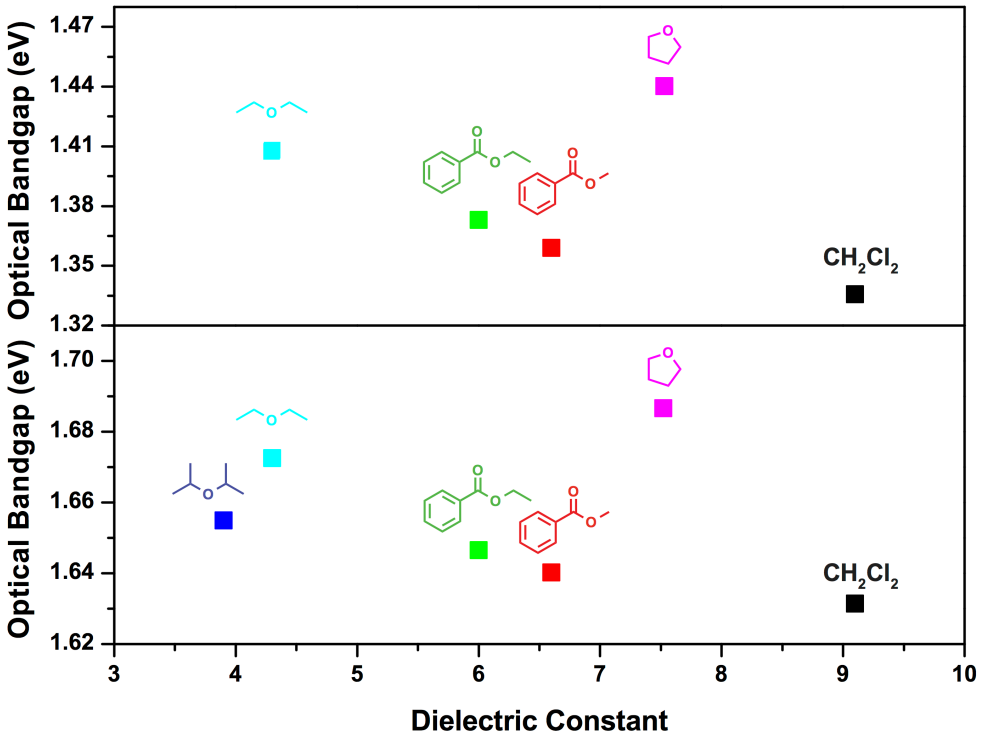

Figure 62. Plots of optical bandgaps of 48 (bottom) and 50 (top) against dielectric constants of organic solvents.

Furthermore, to rule out the aforementioned solvation effects, the optical band gaps were also plotted against the dielectric constants of these solvents (**Figure 62**), showing no significant correlation.

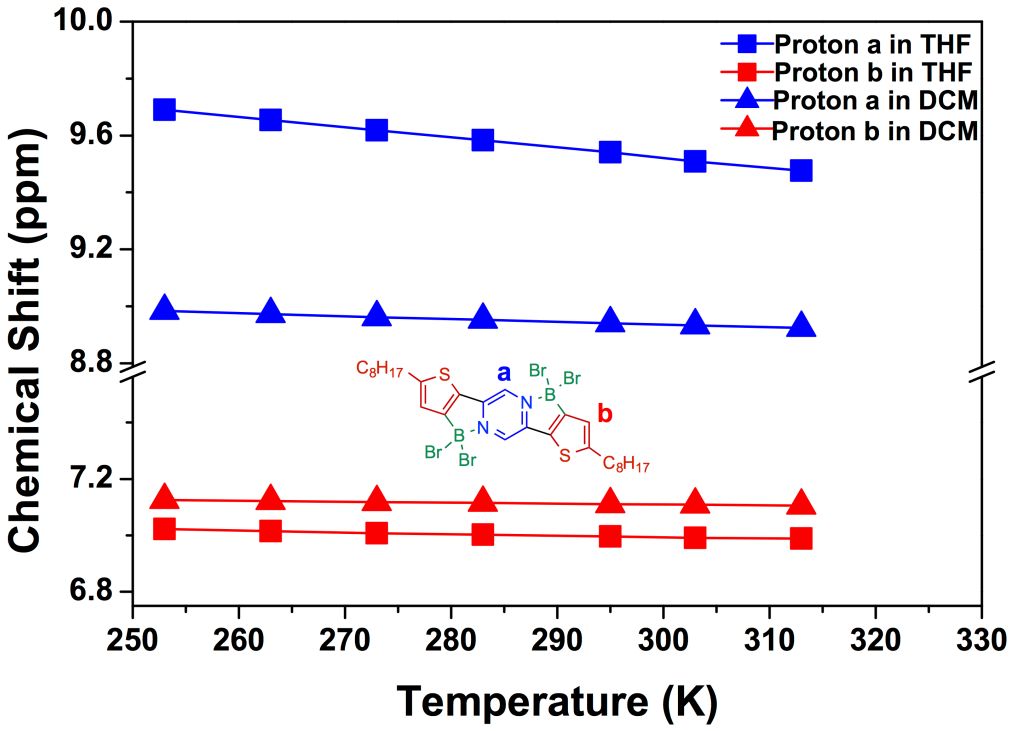

Figure 63. Chemical shift change of protons in the aromatic region of 48 in CD_2Cl_2 and d_8-THF against the temperature.

To further characterize such Lewis acid–base competition with solvent molecules, variable-temperature NMR analysis of **48** was conducted in weak (CD_2Cl_2) and strong (d_8-THF) Lewis basic solvents, respectively. In d_8-THF, the resonance signal of the central pyrazine proton was found shifted downfield by 0.2 ppm while cooling down from 40 °C to −20 °C (**Figure 63**), as a result of the more favorable intramolecular B←N coordination interaction and less competitive solvent effect at a lower

temperature.[115,197] In contrast, the chemical shift change in CD_2Cl_2 was only 0.06 ppm in this temperature range, because the weaker Lewis base CD_2Cl_2 exerted much weaker solvent competition. Thus, the employment of Lewis basic solvents provides the ability to control the optical band gaps of these dynamic B←N bridged molecules in the NIR region through competitive coordination interactions.

4.4 Electronic Properties

Be sure that all figures and tables fit within the document's regular margins. Frontier orbital energy levels of molecules **1–4** were investigated by using a combination of experimental and theoretical techniques.

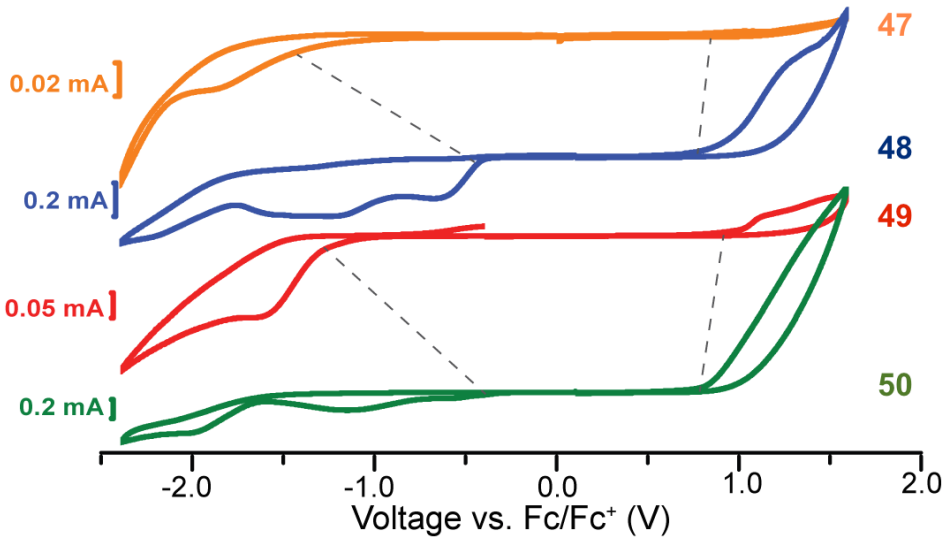

Figure 64. Cyclic voltammetry of 47–50, 0.10 M $TBAPF_6$ in CH_3CN. (The comparison of reduction onsets and oxidation onsets for 48, 50 and their precursors were shown in dotted lines.)

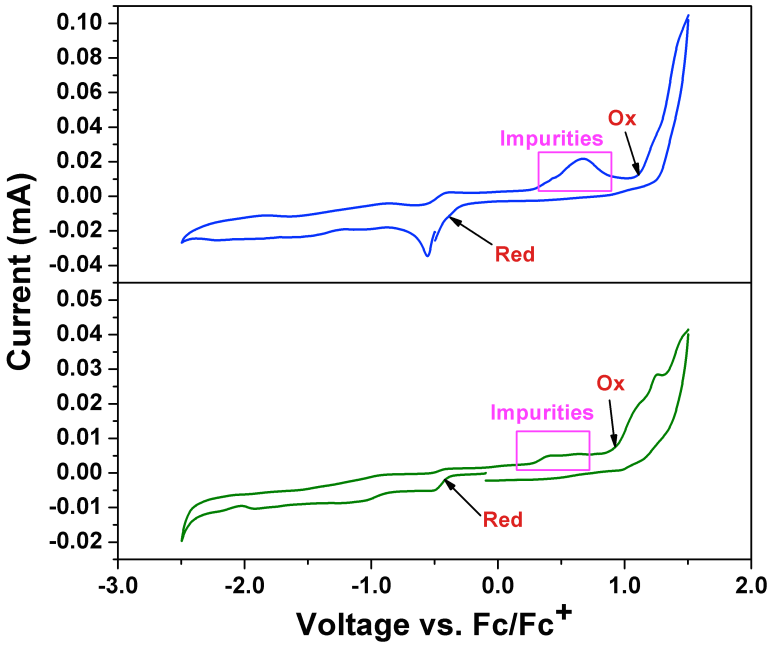

Figure 65. Cyclic voltammetry of 48 and 50, 0.10 M $TBAPF_6$ in CH_2Cl_2.

Cyclic voltammetry traces (**Figure 64**) of **47**–**50** were recorded in solid state after drop-casting the solution of each compound on the working electrode[145] in order to eliminate the impact induced by the Lewis basicity of the electrolyte solution and avoid possible decomposition in solution (**Figure 65**). Cyclic voltammetry traces of **48** and **50** showed irreversible reduction peaks around −0.4 V versus Fc/Fc^+, which was about 1 V lower than their precursors **1** and **3**, respectively. The oxidation onsets for **47**–**50** were all similar around 0.8 V versus Fc/Fc^+. These values suggested that the B–N bond formation lowered the LUMO level but not the HOMO level, as expected. These experimental data were further corroborated by DFT computations (**Figure 66**). Compared to **47** and **49**, both **48** and **50** exhibit dramatically decreased LUMO levels below −4.0 eV, in contrast to the almost unchanged HOMO levels, in agreement with the

values from the electrochemical experiments. The coordination between boron and nitrogen significantly lowers the LUMO energy levels for **48** and **50**, with no significant impact on the HOMO levels. As mentioned above, this represents an ideal approach to achieving a low band gap without increasing the HOMO level and reducing stability.

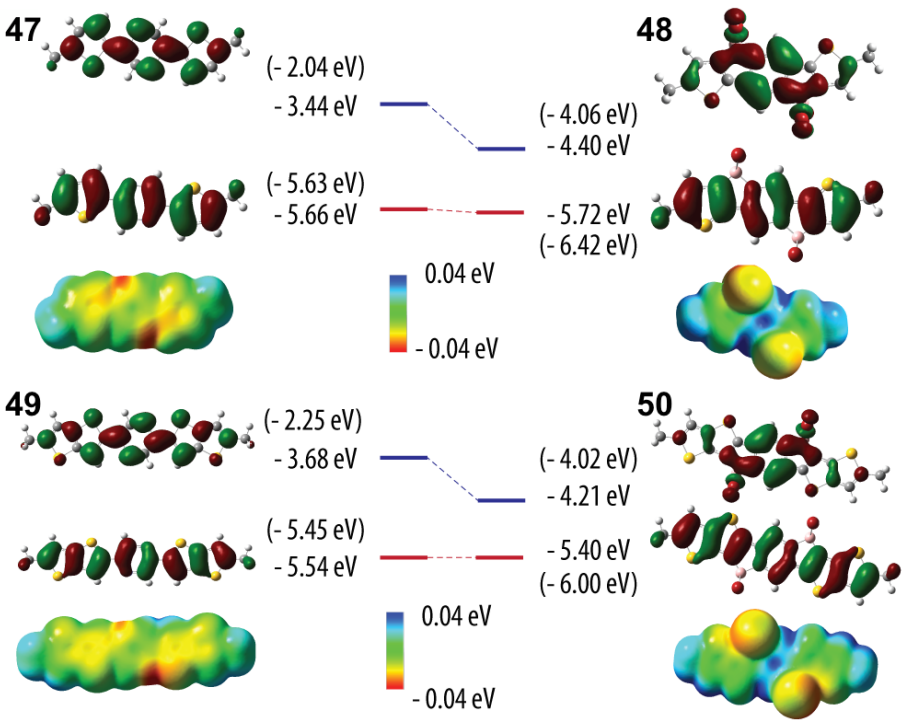

Figure 66. HOMO, LUMO energy levels [experimental data and calculated values (in parentheses)], calculated molecular orbitals, and electrostatic potential map for 47–50 [B3LYP/6-311G(d,p)].

In order to understand how the B←N coordination bond impacts the electronic structure and optical activities of **48** and **50**, HOMO, LUMO energy levels and transitions energies were computed for different molecular conformations by changing the dihedral angles between the pyrazine unit and the flanking electron-rich units (**Table**

1 and **Table 2**). When the dihedral angles were larger than 40°, the distance between boron and nitrogen (3.15 Å) was too large to form B←N coordination bonds.[42,159,198,199] As a result, the LUMO energy levels were drastically lifted and the calculated band gaps for **48** and **50** and their precursors were increased. Meanwhile, the calculated HOMO—LUMO optical transition was greatly blue-shifted. Furthermore, the distance between boron and nitrogen was manipulated to see the correlation between the coordination bond length and energy levels.

Dihedral Angle (°)	0	10	20	30	40	50
LUMO (eV)	-4.064	-4.063	-4.058	-4.048	-2.663	-2.656
HOMO (eV)	-6.417	-6.417	-6.418	-6.421	-6.368	-6.523
Bandgap (eV)	2.353	2.354	2.360	2.373	3.705	3.867
HOMO—LUMO (eV)	1.8368	1.8371	1.8350	1.8352	3.0986	3.2175

Table 1. Calculated energy levels and HOMO—LUMO transition energies of 48 at different dihedral angles [B3LYP/6-311g(d,p)].

Dihedral Angle (°)	0	10	20	30	40	50
LUMO (eV)	-4.019	-4.017	-4.011	-4.001	-2.622	-2.674
HOMO (eV)	-5.999	-6.001	-6.007	-6.019	-5.952	-6.085
Bandgap (eV)	1.980	1.984	1.996	2.018	3.330	3.411
HOMO->LUMO (eV)	1.5348	1.5364	1.5384	1.5434	2.7902	2.8252

Table 2. Calculated energy levels and HOMO—LUMO transition energies of 50 at different dihedral angles [B3LYP/6-311g(d,p)].

As the distance increased, the B←N coordination was weakened, leading to gradually increased LUMO energy levels and wider band gaps. The electrostatic potential maps for **47**–**50** were further computed. As shown in **Figure 66**, the electrostatic potential of the thiophene or thienothiophene units increased after the formation of B←N bonds, which is consistent with a depletion of electron density.[182,200-202] The observed upfield shifts of the ^{1}H NMR chemical shifts of the protons of the thiophene or thienothiophene units also provide indirect evidence of this relative depletion of electron density.[203] Additionally, the positive electrostatic potential on pyrazine also increased dramatically after the coordination event, which is again consistent with an increase in partial positive charge.

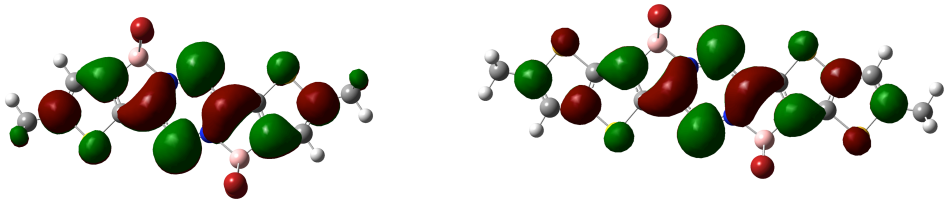

Figure 67. Calculated LUMO+1 orbitals of 48 (left) and 50 (right) [B3LYP/6-311g(d,p)].

According to the DFT computations, while the HOMOs remain delocalized throughout the molecules, the LUMOs of **48** and **50** were more localized on pyrazine compared to precursors **47** and **49**. This result suggests that the LUMOs of **48** and **50** mainly comprise the π* orbital of the positively charged pyrazine. Meanwhile, the LUMO+1 levels of **48** and **50** were still delocalized throughout the molecules, which can be assigned as the π* orbital of the entire conjugated systems (**Figure 67**). In other words, the B←N coordination inserted a new energy level (LUMO) between the

delocalized π (HOMO) and π* (LUMO+1) orbitals of the entire conjugated molecules. Overall, the comprehensive electron-withdrawing effect and the coordination behavior gave rise to the low-lying LUMO levels and the unchanged HOMO levels of **48** and **50**.

4.5 Conclusion

In conclusion, an integrated strategy for creating low band gap coplanar organic materials was developed on the basis of intramolecular Lewis acid–base coordination. Facile synthesis of the model compounds was achieved through an *N*-directed borylation reaction on donor–acceptor–donor precursors. The low-lying LUMOs of the resulting small molecules lead to a band gap as low as 1.3 eV. More interestingly, on account of the dynamic nature of the Lewis acid–base coordination, the band gaps of these systems can be actively modulated by external competing reagents, such as Lewis basic solvents. With a low-lying LUMO and coplanar conformation achieved simultaneously, this work provides a promising model for the future design and development of low band gap *n*-type materials.

4.6 Experimental Section

4.6.1 General Methods

Starting materials and reagents were purchased from commercial sources and used as received. THF was dried using an IT pure solvent system and used without further treatment. 2-Octylthiophene[204] and (5-dodecylthieno[3,2-*b*]thiophen-2-yl)trimethylstannane[205] were synthesized according to procedures reported in literature.

All the reactions were performed under nitrogen and in dry solvents. ^{1}H, ^{13}C NMR spectra were recorded on a 300 or 500 MHz spectrometer, and ^{11}B NMR were recorded on a 400 Hz spectrometer. Variable-temperature NMR spectra were recorded on 500 MHz spectrometers. ^{1}H and ^{13}C chemical shifts were reported in ppm relative to the signals corresponding to the residual nondeuterated solvents ($CDCl_3$: ^{1}H 7.26 ppm, ^{13}C 77.23 ppm). ^{11}B chemical shifts were reported in ppm relative to the signal of $BF_3 \cdot OEt_2$ (0.00 ppm). High resolution electrospray ionization mass spectra data were obtained via ESI or MALDI mode with a TOF analyzer. UV–vis and UV–vis–NIR absorption sepectra were were performed in a 1.0 cm path-length cuvette, and the neat solvent was used as baseline. Cyclic voltammetry in the solid state and solution phase was carried out at room temperature in nitrogen-purged acetonitrile and dichloromethane respectively with a CHI voltammetric analyzer. $TBAPF_6$ (0.1 M) was used as the supporting electrolyte. The conventional three-electrode configuration consists of an ITO (solid state)/glassy carbon (solution phase) working electrode, a platinum wire anxiliary electrode, and a Ag/AgCl electrode with ferrocenium/ferrocene as the standard. Cyclic voltammograms were obtained at a scan rate of 100 mV/s.

4.6.2 Synthesis

Compound **47**: 2-Octylthiophene (864 mg, 4.40 mmol) was dissolved in anhydrous THF (4 mL) at −78 °C under nitrogen. BuLi (2.8 mL, 1.6 M in hexane) was added into the solution dropwise over 15 min. The mixture was stirred at −78 °C for 1 h. $ZnCl_2 \cdot$TMEDA (404 mg, 1.60 mmol) was added into the mixture, and the mixture was

warmed up to room temperature slowly over 1 h. A suspension of 2,5-dibromopyrazine (476 mg, 2.00 mmol) and Pd(dppf)Cl_2·CH_2Cl_2 (0.08 mmol, 65.4 mg) in THF (1.5 mL) was added into the reaction mixture. The resulting mixture was stirred at 50 °C overnight. After being cooled to room temperature, the reaction mixture was washed with 1 M HCl, and EtOAc was added to extract the product. The organic layer was washed with 1 M HCl and H_2O (20 mL × 2). After drying with $MgSO_4$, the organic solution was dried on a rotary evaporator. The product was further purified by column chromatography on SiO_2 [Hexane/CH_2Cl_2 (2:1)]. The product was isolated as a yellow solid (490 mg, yield: 52%). ^{1}H NMR ($CDCl_3$, 300 MHz, 25 °C): δ = 0.88 (t, *J* = 7.0 Hz, 6H), 1.40–1.25 (m, 20H), 1.72 (m, *J* = 7.5 Hz, 4H), 2.85 (t, *J* = 7.5 Hz, 4H), 6.82 (d, *J* = 4.0 Hz, 2H), 7.46 (d, *J* = 4 Hz, 2H), 8.77 (s, 2H). ^{13}C NMR ($CDCl_3$, 500 MHz, 25 °C): δ = 14.3, 22.6, 28.9, 29.2, 29.4, 29.7, 31.6, 32.8, 105.2, 125.8, 138.9, 139.2, 146.0, 150.0. HRMS (MALDI-TOF) *m*/*z* $[M + H]^+$ Calcd for $C_{28}H_{41}N_2S_2$ 469.2705; Found 469.2728.

Compound **48**: **47** (188 mg, 0.40 mmol) and *i*-Pr_2NH (0.112 mL, 0.80 mmol) were dissolved in anhydrous CH_2Cl_2(2 mL) under nitrogen at 0 °C. BBr_3 (2.4 mL, 1 M in CH_2Cl_2) was added into the solution dropwise. After the addition, the reaction mixture was warmed up to room temperature and stirred overnight. The organic solvent was removed under vacuum. The resulting blue solids were washed with H_2O (10 mL × 2) and filtered. After drying, those solids were washed with hexane (10 mL × 3) and dried under vacuum to give the final product as a blue powder (207 mg, yield: 64%). ^{1}H NMR ($CDCl_3$, 500 MHz, 25 °C): δ = 0.89 (t, *J* = 6.9 Hz, 6H), 1.40–1.30 (m, 20H), 1.77 (m, *J* = 7.2 Hz, 4H), 2.97 (t, *J* = 7.5 Hz, 4H), 7.12 (s, 2H), 8.84 (s, 2H). ^{11}B NMR ($CDCl_3$, 128

MHz, 25 °C): −4.26. ^{13}C NMR ($CDCl_3$, 75 MHz, 25 °C): δ = 14.3, 22.9, 29.2, 29.3, 29.4, 30.2, 31.4, 31.6, 127.0, 130.0, 134.9, 143.7, 163.5, 165.2. HRMS (ESI-TOF) *m*/*z* [M – H]$^-$ Calcd for $C_{28}H_{37}B_2Br_4N_2S_2$ 806.9295; Found 806.9263.

Compound **49**: (5-Dodecylthieno[3,2-*b*]thiophen-2-yl)trimethylstannane (729 mg, 1.55 mmol) and 2,5-dibromo-pyrazine (147 mg, 0.62 mmol) were dissolved in anhydrous xylene (5 mL). The solution was degassed, and $Pd(PPh_3)_4$ (89.3 mg, 0.077 mmol) was added. The tube was sealed, and the mixture was stirred at 150 °C for 40 h. After the mixture cooled to room temperature, hexane was added. The dispension was filtered, and the solids were washed with hexane, MeOH, and acetone. After drying under vacuum, the product was isolated as a yellow solid (381 mg, yield: 91%). ^{1}H NMR ($CDCl_3$ and TFA-*d*, 500 MHz, 25 °C): δ = 0.88 (t, *J* = 7.0 Hz, 6H), 1.40–1.25 (m, 20H), 1.75 (m, *J* = 7.5 Hz, 4H), 2.93 (t, *J* = 7.5 Hz, 4H), 7.05 (s, 2H), 8.08 (s, 2H), 9.02 (s, 2H). ^{13}C NMR ($CDCl_3$ and *d*-TFA, 125 MHz, 25 °C): δ = 14.2, 23.0, 29.4, 29.5, 29.6, 29.7, 29.8, 29.9, 31.4, 31.9, 117.1, 123.5, 132.3, 137.0, 140.0, 142.9, 145.4, 157.2. HRMS (ESI-TOF) *m*/*z* [M – H]$^-$ Calcd for $C_{40}H_{55}N_2S_4$ 691.3248; Found 691.3288.

Compound **50**: **49** (67.7 mg, 0.10 mmol) and *i*-Pr_2NH (0.15 mL, 1.27 mmol) were dissolved in anhydrous CH_2Cl_2 (5 mL) under nitrogen at 0 °C. BBr_3 (0.5 mL) was added into the solution dropwise. After the addition, the reaction mixture was warmed up to room temperature and stirred overnight. The organic solvent was removed under vacuum. The resulting green solids were washed with H_2O (10 mL × 2) and filtered. After drying, those solids were washed with hexane (10 mL × 3) and dried under vacuum to give the final product as a deep green powder (54 mg, 53%). ^{1}H NMR

($CDCl_3$, 500 MHz, 25 °C): δ = 0.89 (t, *J* = 6.9 Hz, 6H), 1.20–1.50 (m, 36H), 1.77 (m, *J* = 7.2 Hz, 4H), 2.97 (t, *J* = 7.5 Hz, 4H), 7.12 (s, 2H), 8.84 (s, 2H). ^{11}B NMR (CDCl3, 128 MHz, 25 °C): −4.12. ^{13}C NMR ($CDCl_3$, 300 MHz, 25 °C): δ = 14.1, 22.7, 29.1, 29.1, 29.2, 31.2, 31.4, 31.8, 117.4, 131.38, 134.6, 138.7, 144.0, 150.1, 158.6. HRMS (ESI-TOF) *m*/*z* $[M - H]^-$ Calcd for $C_{40}H_{53}B_2Br_4N_2S_4$1030.9970; Found 1031.0008.

4.6.3 UV-vis-NIR Sepctra

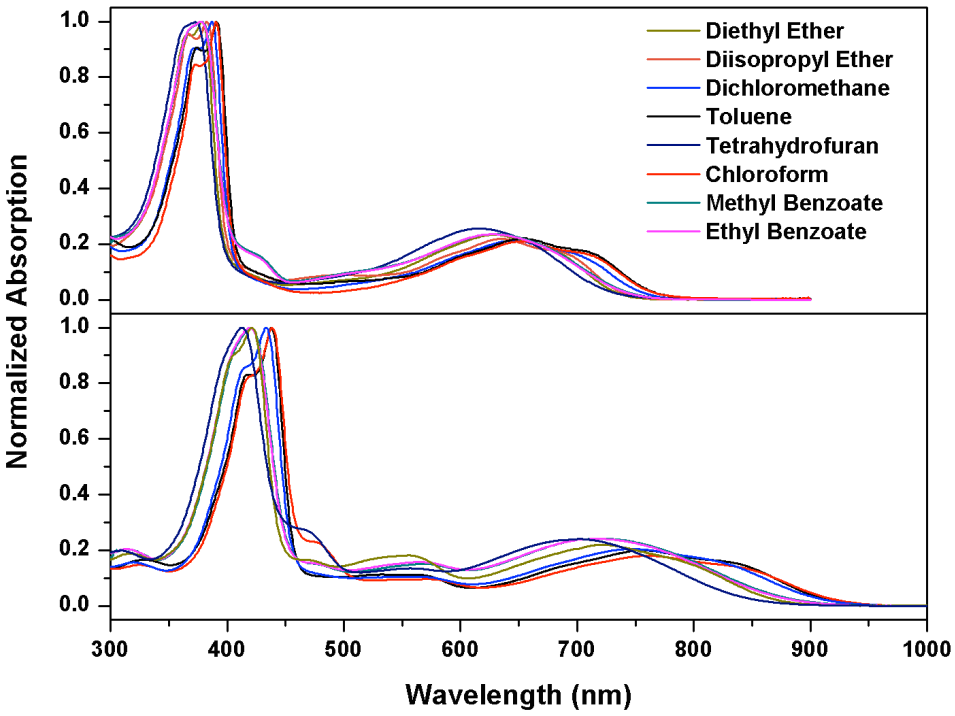

Figure 68. Normalized absorption spectra of Compound 48 (top, concentration: 9.9×10^{-6} M) and Compound 50 (bottom, concentration: 9.7×10^{-6} M) in a series of organic solvents at room temperature.

4.6.4 NMR Spectra

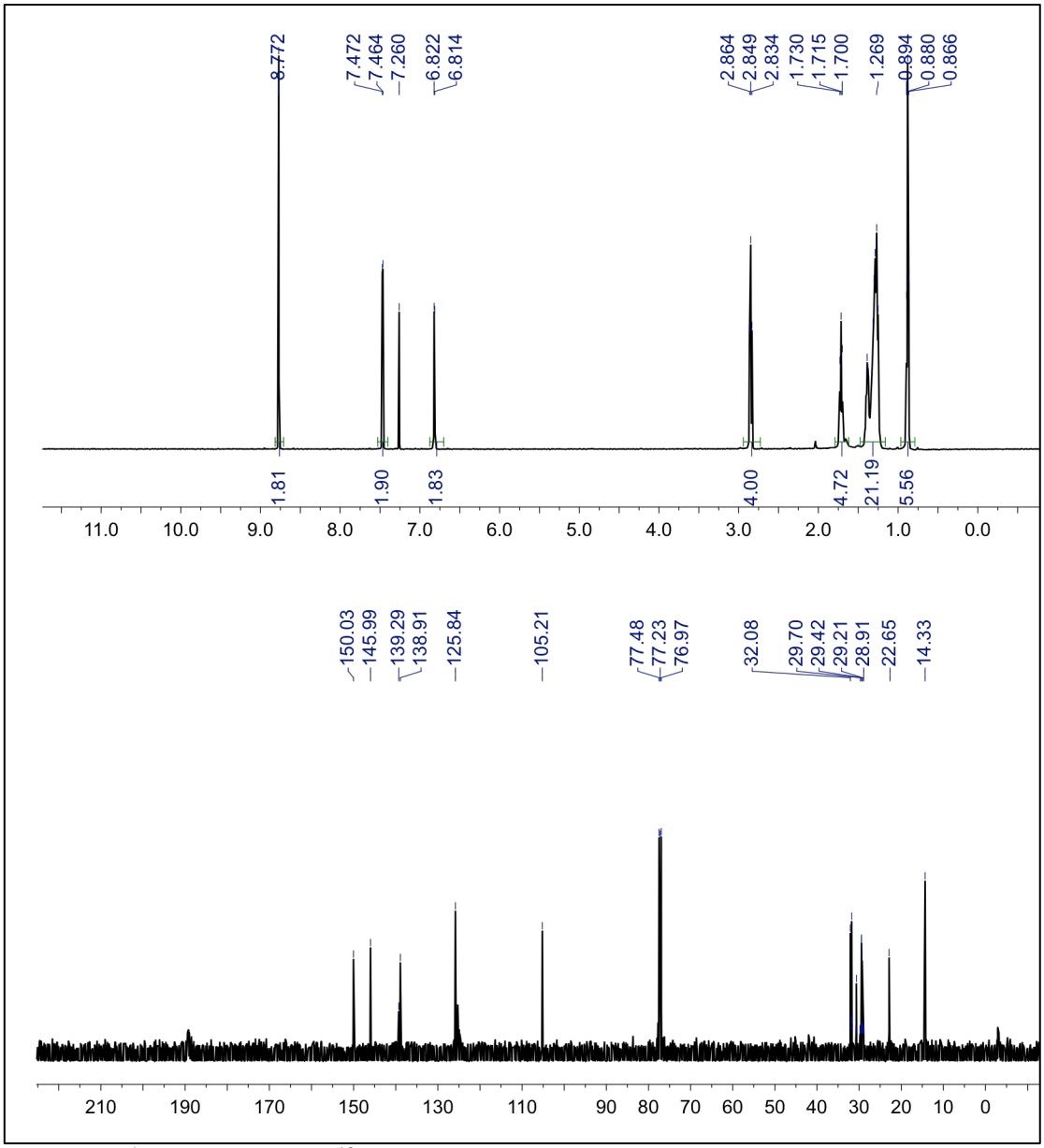

Figure 69. ^{1}H (500 MHz), ^{13}C NMR (125 MHz) spectra of 47 in $CDCl_3$ at room temperature.

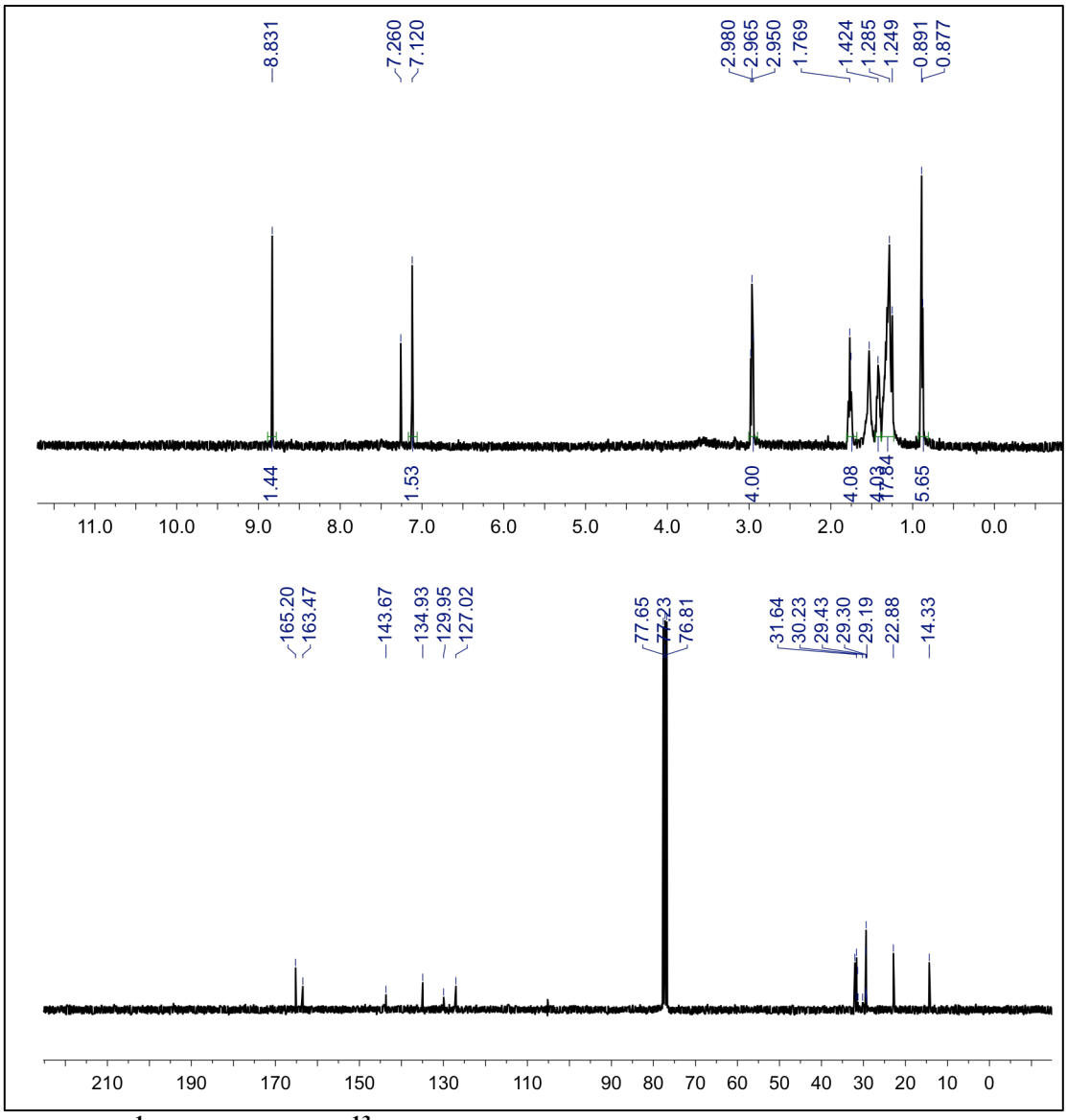

Figure 70. ^{1}H (500 MHz), ^{13}C NMR (75 MHz) spectra of 48 in $CDCl_3$ at room temperature.

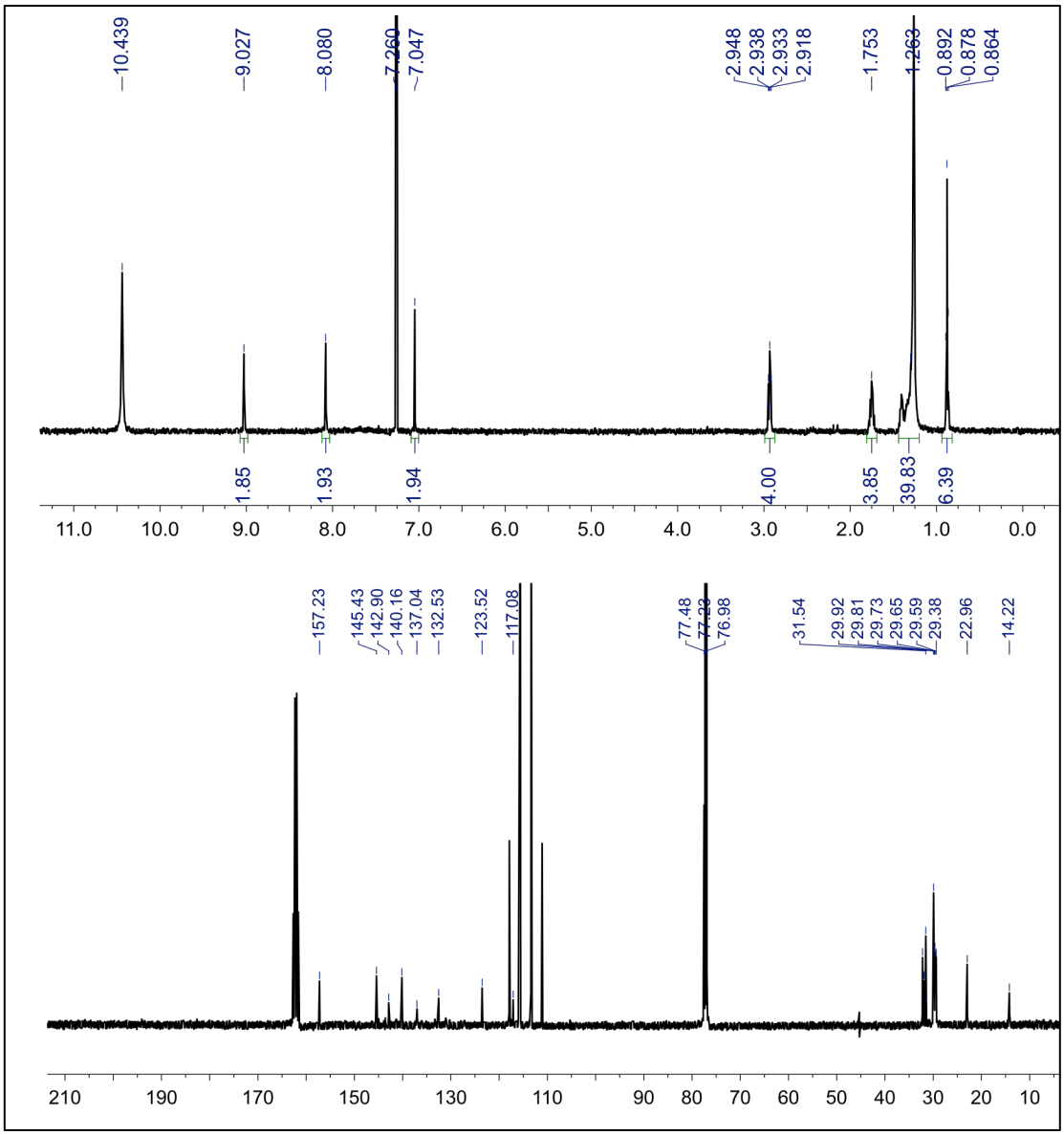

Figure 71. ^{1}H (500 MHz), ^{13}C NMR (125 MHz) spectra of 49 in $CDCl_3$ and TFA at room temperature.

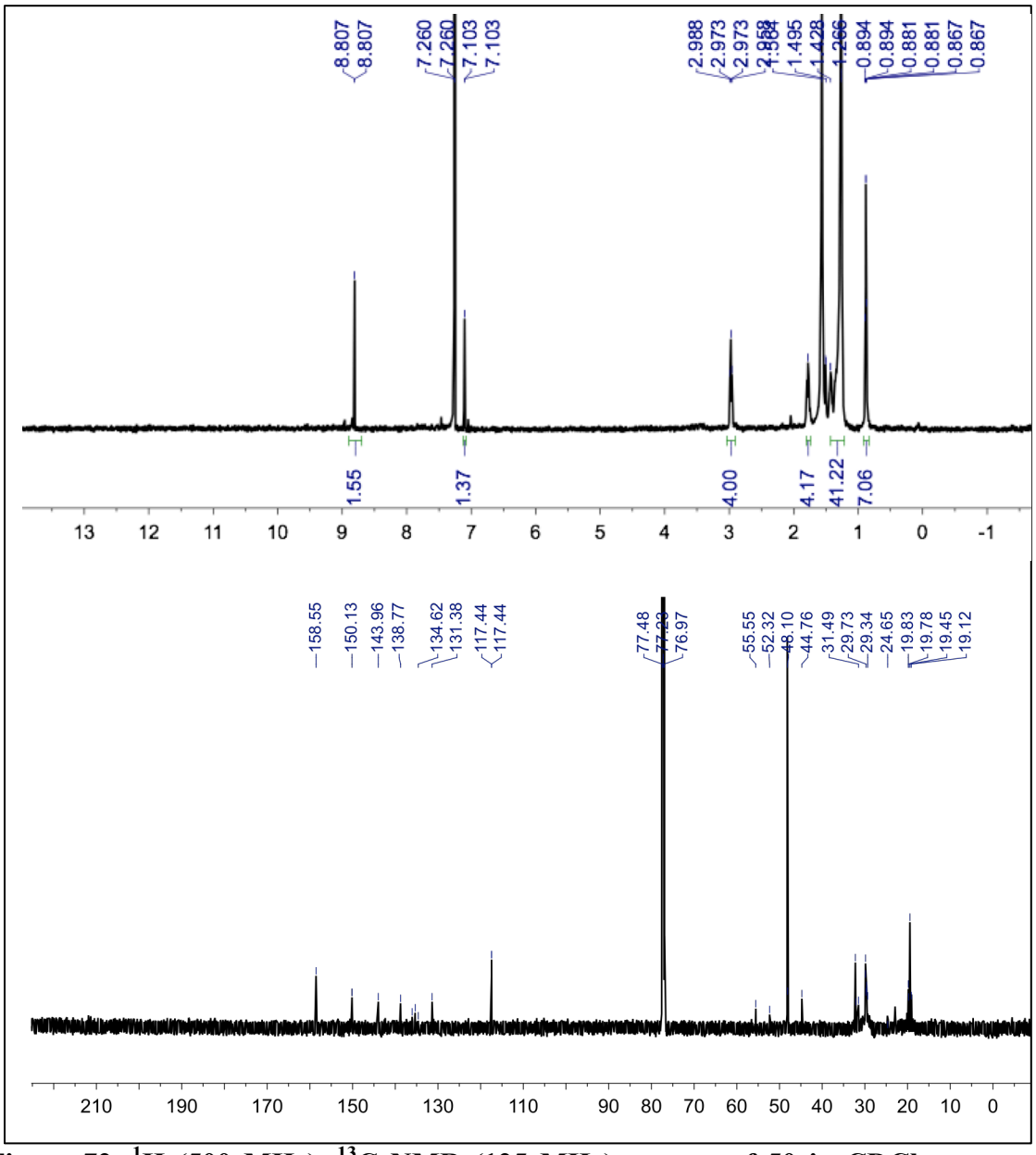

Figure 72. ^{1}H (500 MHz), ^{13}C NMR (125 MHz) spectra of 50 in $CDCl_3$ at room temperature.

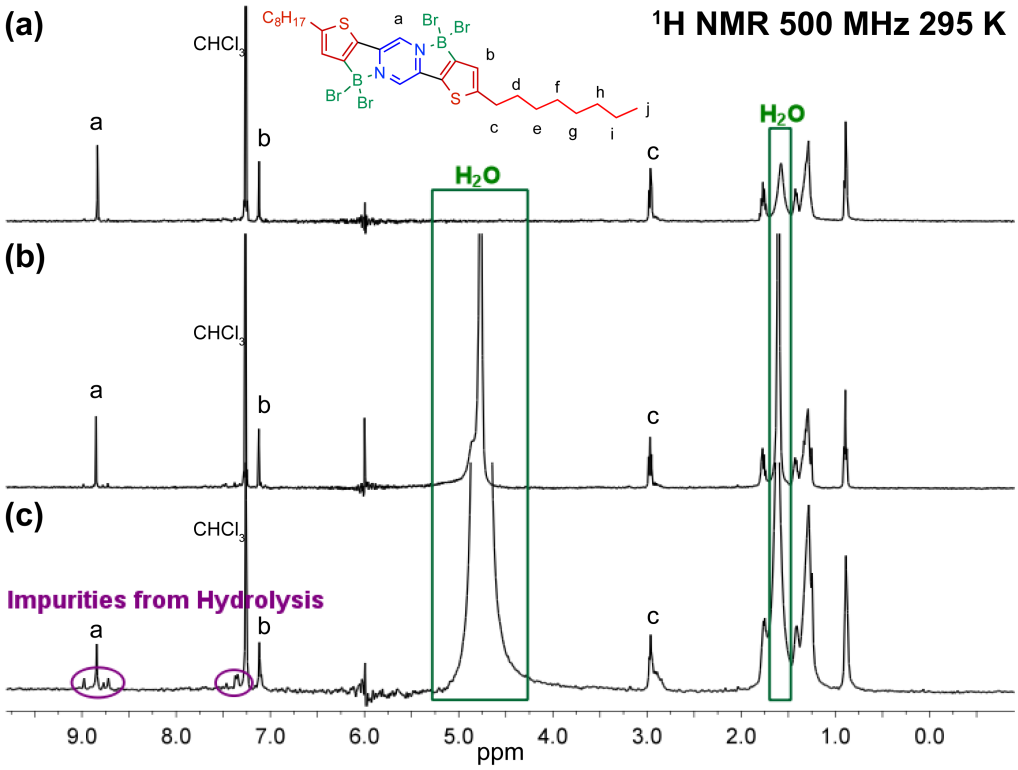

Figure 73. ^{1}H NMR spectra of (a) freshly prepared $CDCl_3$ solution of 48; (b) $CDCl_3$ solution of 48, 10 min after adding water; (c) $CDCl_3$ solution of 48, 2hrs after adding water.

CHAPTER V

EXTRAORDINARY REDOX ACTIVITIES IN LADDER-TYPE CONJUGATED MOLECULES ENABLED BY B←N COORDINATION-PROMOTED DELOCALIZATION AND HYPERCONJUGATION*

5.1 Introduction

Ladder-type conjugated molecules, constituted with an uninterrupted sequence of fused adjacent rings that share two or more atoms with one another, have shown great promise for applications on multiple fronts that demand superior optical, electronic, or mechanical properties.[32,33,174,175,206-211] Stemming from the strong intramolecular electronic couplings throughout fused conjugated backbones, ladder-type conjugated compounds also demonstrate intriguing electrochemical behaviors, such as the capability of undergoing multiple electron transfers.[206,212] The extended conjugation and rigid backbones can greatly stabilize the highly reactive radical and ionic intermediates that are generated during the redox processes. For instance, ladder-type oligothiophene exhibited stepwise oxidations.[206,213] A recently reported series of ladder-type conjugated polycyclic hydrocarbons, featuring extensive graphitic constitutions, demonstrated four distinct reversible redox processes.[214] In this context, ladder-type molecular design

*Reprinted with permission from "Extraordinary Redox Activities in Ladder-Type Conjugated Molecules Enabled by BN Coordination-Promoted Delocalization and Hyperconjugation" Zhu, C.; Ji, X.; You, D.; Chen, T. L.; Mu, A. U.; Baker, K. P.; Klivansky, L. M.; Liu, Y.; Fang, L. *J. Am. Chem. Soc.*, **2018**, *140*, 18173. Copyright 2018 American Chemical Society.

represents an important strategy to achieve exotic molecular materials desirable for sophisticated electrochemical applications.[212,215,216]

To date, redox-active ladder-type compounds are mostly fused with entirely covalent bonds.[33,209,210] Alternatively, intramolecular noncovalent B←N coordination[42,43,69,71] has been exploited to serve as a bridge to construct ladder-type conjugated molecules while imparting modification to the aromatic character.[1,2] Compared to the isoelectronic and isosteric C–C single bond, intramolecular B←N coordination in a conjugated molecule not only extends the π-delocalization but also dramatically changes the electronic structures, electronic and optical properties,[42,43,65,70,71,73,75,176,179,217-221] and reactivities,[222,223] because of the intrinsically different valence electron configurations and electronegativities of boron and nitrogen compared to carbon. For instance, the incorporation of B←N coordination into conjugated molecules deepens the lowest unoccupied molecular orbital (LUMO) energy levels, which facilitates reductive electron-transfer processes.[69-71,74,179,221] Additionally, a boron atom can couple with a neighboring unpaired spin, providing additional stabilization effects for radical intermediates during redox processes.[74,224-226] Therefore, the employment of B ← N coordination represents a powerful strategy to develop novel conjugated molecules and macromolecules with new redox properties that were not accessible before.

Despite the great potential of this noncovalent approach, it is still challenging to achieve robust redox activities in B ← N bridged ladder-type molecules, especially oxidation processes, because of the electron-deficient nature of boron moieties and the

resulting low stability of the corresponding oxidized states. Meanwhile, the underlying mechanism of the redox processes of B ← N bridged ladder-type molecules remains unclear, especially on the impacts of tetracoordinated boron centers on the electronic structures and optical characteristics of these molecules. Herein, we report a molecular design strategy that allowed for the access to five redox states, both reduced and oxidized, of B ← N bridged ladder-type molecules, as well as the corresponding mechanistic investigations.

5.2 Molecular Design

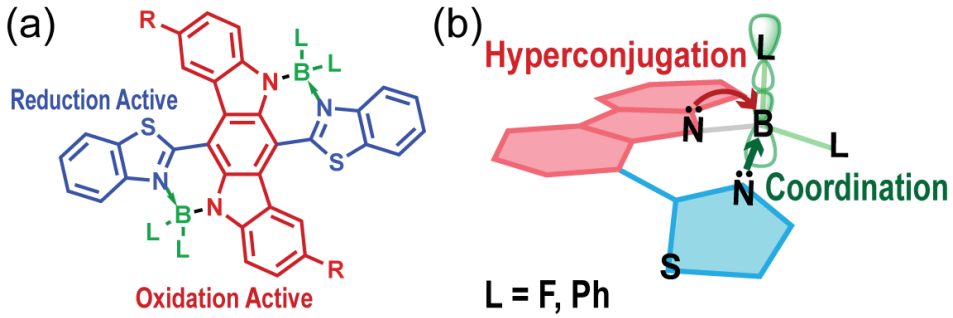

Figure 74. (a) Designed ladder-type molecule featuring cruciform arrangement of redox-active units (reduction-active in blue and oxidation-active in red) and B ← N coordination that can rigidify and coplanarize the entire molecule; (b) representative orbital interactions of the boron center in the designed conjugated molecules.

To pursue both robust reductive and oxidative electron-transfer processes in B ← N bridged ladder-type molecules, we envisioned that the molecular design should first integrate multiple redox-active components in an orthogonal and compact manner, so that multiple electron-transfer processes can be enabled in a small molecule without

interfering with each other. Second, B ← N coordination needs to be installed to rigidify the π-system to facilitate the desired delocalization of charges and spins, therefore stabilizing the reduced or oxidized species. On the basis of these principles, we designed a ladder-type molecule composed of an oxidation-active indolo[3,2-*b*]carbazole (ICBZ) unit and two reduction-active benzo[*d*]thiazole (BTH) units (**Figure 74**). The ICBZ unit is covalently linked to the BTH units at the 6 and 12 positions, leading to a cruciform-like geometry, generating two distinctive delocalization regions for oxidation and reduction, respectively. On one hand, ICBZ is known to undergo two-electron oxidation processes into a relatively stable quinonoid structure.[227,228] The two N–H functionalities on ICBZ provided the point to covalently attach the boron centers.[229-231] Indeed, B ← N bridged ladder-type ICBZ derivatives reported by Curiel et al.[231] showed the expected reversible electrochemical oxidation behavior. In our design, tertiary butyl groups are installed at the 2 and 8 positions of ICBZ to ensure the solubility of this rigid compound. On the other hand, BTH was selected as the reduction-active unit.[232] The Lewis basic nitrogen atoms on the thiazole rings were employed to form the B ← N coordination.

The B ← N coordination in this molecular design was formed in a geometrically favored six-membered heterocycle architecture, which fused the ICBZ and BTH units into a ladder-type structure. The "N–B ← N" constitution was expected to be stable not only in ambient condition but also during redox processes, similar to the known stability of BODIPY dyes.[233,234] The strong B ← N coordination significantly withdrew the electron density from BTH units, resulting in an enhanced electron affinity.[43,69,70] Consequently, the reduction of such a molecule could fall into an

accessible potential range. Moreover, this boron-containing six-membered heterocycle architecture reassembles the structure of cyclohexa-1,3-diene, in which a series of hyperconjugative interactions were previously observed to significantly impact the molecular conformation, properties, and stability.[235,236] In this design, the sp^3 hybridized boron atom carried two ligands that were expected to undergo hyperconjugative interactions similar to those existing in cyclohexa-1,3-diene (**Figure 74b**). We hypothesized that these hyperconjugative interactions could further stabilize the radical intermediates upon reduction/oxidation, by assisting the charge and spin delocalization. Consequently, the low-energy singly occupied molecular orbital (SOMO) to LUMO transition of these stabilized organic radicals could be utilized to achieve electrochromism in the near-infrared (NIR) region,[237] which is highly desired for various applications including data storage, smart windows, and sensing.[212,238-240]

5.3 Synthesis and Optical Properties

On the basis of these design principles, two molecular candidates, **BN-F** and **BN-Ph**, with fluoride and phenyl groups attached to the boron center as ligands, respectively, were synthesized. The syntheses were accomplished (**Figure 57**) in three steps starting from 2,8-di-*tert*-butyl-5,11-dihydroindolo[3,2-*b*]carbazole (compound **51**). First of all, treatment of **51** with 2.0 equiv of *N*-bromosuccinimide (NBS) selectively brominated the 6- and 12-positions to give a dibromo derivative, **52**. Compound **52** was subsequently subjected to Stille coupling reaction with 2-(tributylstannyl)benzo[*d*]thiazole. CuI and CsF were used to facilitate the transmetalation step[241] during the Stille reaction to give

intermediate **53**. In this step, temperature control was crucial to achieve a high yield. Significant side reactions were found above 130 °C, which was likely a result of undesired copper-catalyzed reactions, such as Ullmann coupling.[242] Finally, borylation of **53** with BF_3 or BPh_2Cl in the presence of non-nucleophilic bases afforded the desired products in excellent isolated yields (96% and 72%, respectively). Notably, the isolation yield of **BN-Ph** was significantly improved compared to a previously reported reaction using BPh_3 to introduce B ← N coordinate bonds into a similar ICBZ backbone,[231] likely due to the higher electrophilicity and smaller steric hindrance of BPh_2Cl. **BN-F** and **BN-Ph** showed good stabilities in ambient conditions. For example, **BN-Ph** was purified by normal-phase silica gel chromatography.

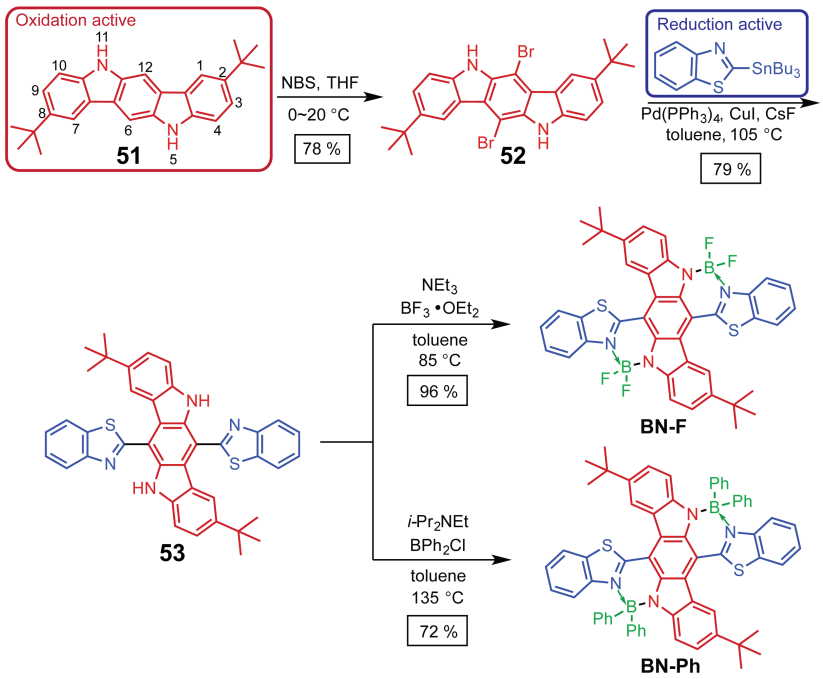

Figure 75. Synthesis of BN-F and BN-Ph.

Both final products were fully characterized by NMR spectroscopy and mass spectrometry. In addition, **BN-Ph** was characterized unambiguously by single-crystal X-ray diffraction analysis. Single crystals of **BN-Ph** suitable for X-ray diffraction analysis were obtained by vapor diffusion of pentane into a chloroform solution. Tetrahedral geometry of the boron centers was revealed, with a short B ← N coordinate bond length of 1.643 Å. The anticipated rigid conformation of **BN-Ph** bridged by the B ← N coordination was validated in the solid-state crystal structure. The dihedral angles between ICBZ units and BTH units were measured to be 20.0° in **BN-Ph**, significantly smaller than that observed in the density functional theory (DFT) computed, energy-minimized geometry of the precursor **53** (**Figure 76**).

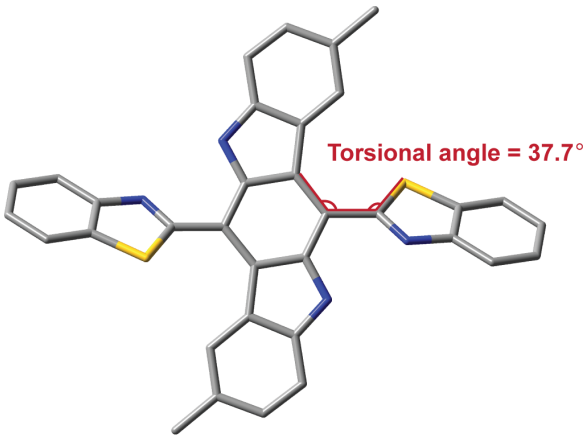

Figure 76. DFT calculation optimized geometry of compound 53. Methyl groups were used to replace *t*-butyl groups for the simplicity of calculation. Hydrogen atoms were omitted for clarity.

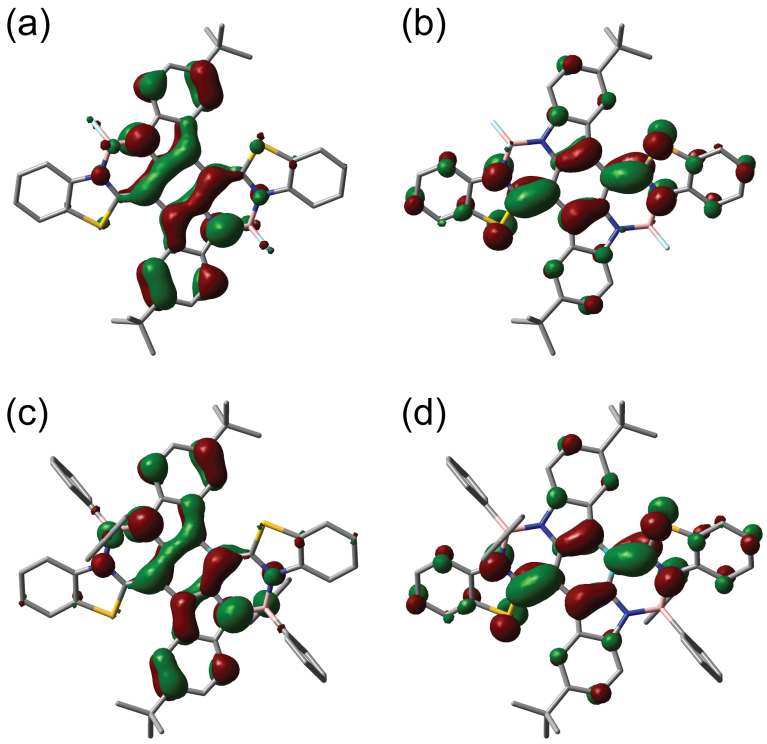

Figure 77. Computed (a) HOMO, (b) LUMO of BN-F, and (c) HOMO, (d) LUMO of BN-Ph (isovalue = 0.03). Hydrogen atoms were omitted for clarity.

DFT calculations on the π-conjugated backbone revealed extended π-delocalization on **BN-F** and **BN-Ph**. The visualized highest occupied molecular orbitals (HOMOs) of both molecules were delocalized over the entire conjugated backbones with non-negligible contributions from the boron centers and the ligands (**Figure 77**). The majority of LUMOs were on the electron-deficient BTH units and the boron centers. Time-dependent DFT calculations afforded multiple optical transitions with significant intensities, including the lowest band gap HOMO → LUMO transitions, and the higher-energy HOMO–1 → LUMO transitions. These transitions matched well with experimental spectra. Both **BN-F** and **BN-Ph** possessed low band gap NIR absorptions and fluorescent emissions. For example, the UV–vis–NIR spectrum of a dilute solution

of **BN-F** in CH_2Cl_2 showed the low-energy HOMO → LUMO absorption peak at 695 nm ($\varepsilon = 1.17 \times 10^4\ M^{-1}\cdot cm^{-1}$) (**Figure 78**). For **BN-Ph** with phenyl ligands on the boron center, such HOMO → LUMO band red-shifted into the NIR region (λ_{max} = 768 nm, $\varepsilon = 1.80 \times 10^4\ M^{-1}\cdot cm^{-1}$) (**Figure 78**).

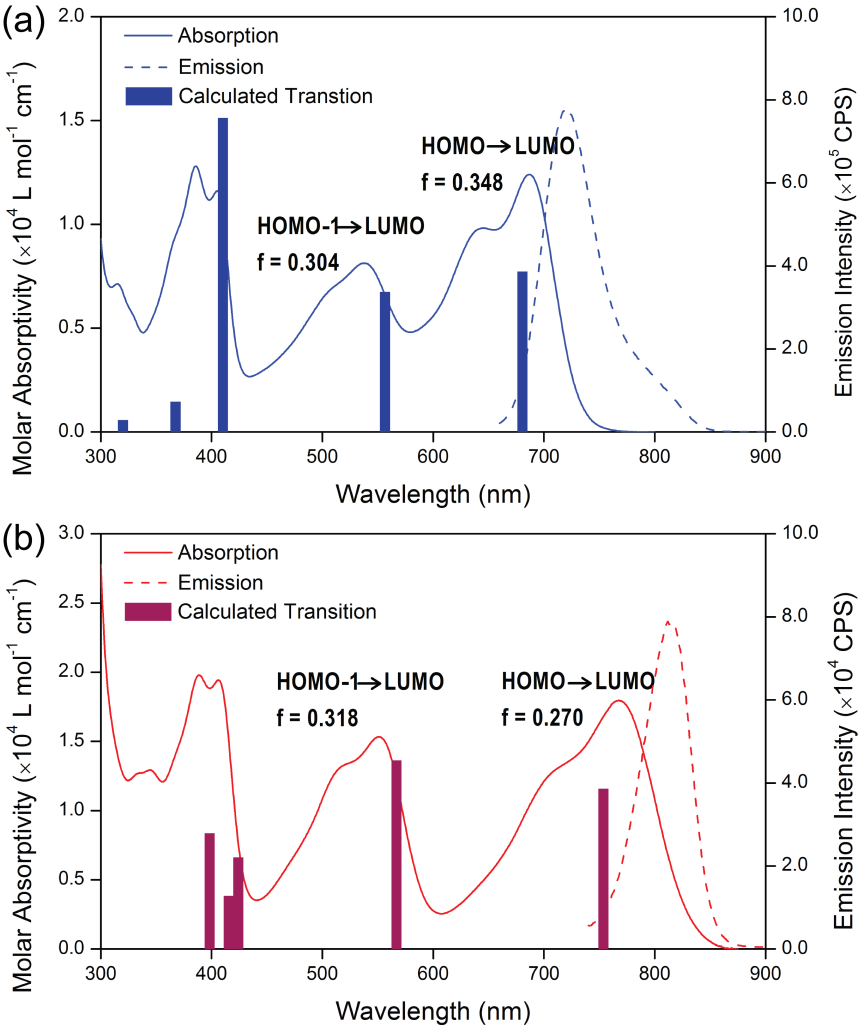

Figure 78. UV–vis–NIR absorption (solid lines) and emission (dashed lines) of (a) BN-F and (b) BN-Ph in CH_2Cl_2 with transition energies calculated by time-dependent DFT using B3LYP/6-311g(d,p) with CH_2Cl_2 CPCM solvation.

The presence of vibrational progression in both spectra indicated the rigid nature of **BN-F** and **BN-Ph**.[31,32] Fluorescence emission of **BN-F** and **BN-Ph** appeared in the NIR region with λ_{max} at 720 and 812 nm in CH_2Cl_2, respectively (**Figure 78**). Small Stokes shifts (576 cm^{-1} for **BN-F** and 705 cm^{-1} for **BN-Ph**) also implied their backbone rigidity, due to the lack of energy loss associated with conformational changes during the excitation–emission processes. The fluorescence quantum yields of **BN-F** and **BN-Ph** were measured using reference standards (zinc phthalocyanine for **BN-F** and indocyanine green for **BN-Ph**) to be 2.8% and 1.2% in CH_2Cl_2, respectively.

5.4 Redox and Electrochromic Properties

On the basis of the molecular design, **BN-F** and **BN-Ph** were expected to undergo multistage electron-transfer processes. Indeed, cyclic voltammograms (CVs) unveiled four well-separated, reversible electron-transfer processes in both **BN-F** and **BN-Ph** (**Figure 79a, b**), indicating five accessible redox states for both compounds. The excellent reversibility of these processes indicated the high stability of all the states including radical anions (−1), dianions (−2), radical cations (+1), and dications (+2). The measured electrochemical band gaps of **BN-F** and **BN-Ph** (1.81 and 1.62 eV, respectively) matched well with the optical band gaps (1.78 and 1.60 eV, respectively). Among these two voltammograms, the redox processes of **BN-Ph** appeared cathodically shifted (**Figure 79b**) compared to those of **BN-F**, likely due to the more electron-rich nature of the phenyl ligand compared to fluoride. Such an effect

was more significant on the oxidation processes, leading to a narrower band gap of **BN-Ph** than that of **BN-F**.

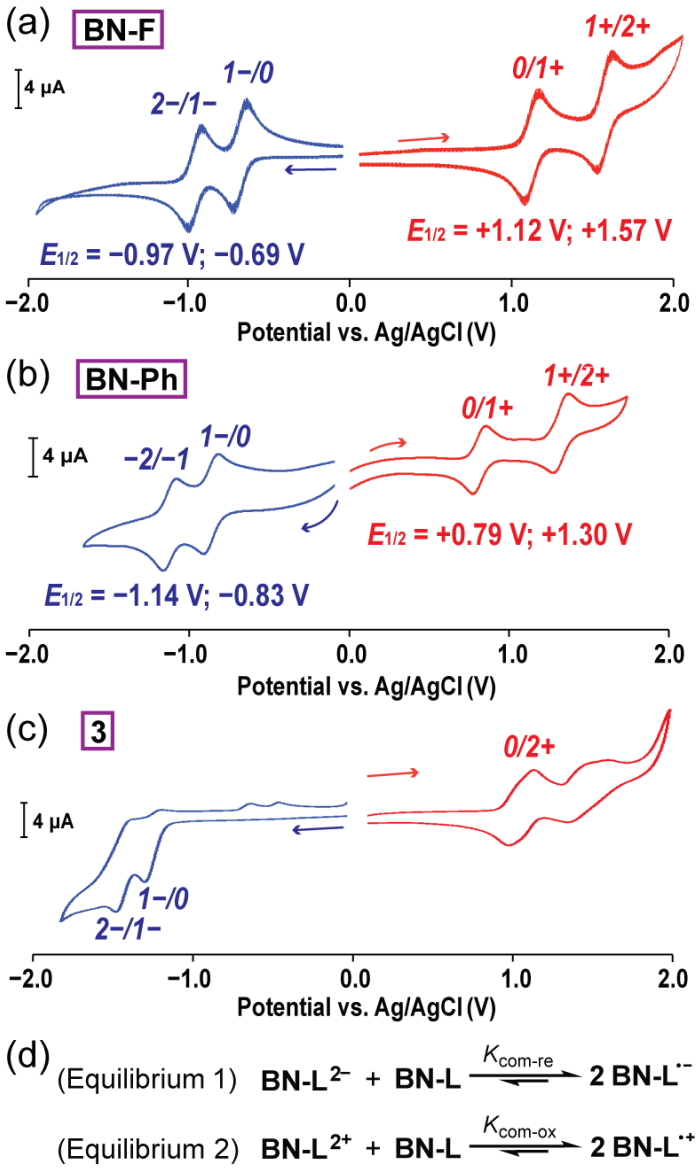

Figure 79. CV curves of (a) BN-F, (b) BN-Ph, and (c) 53 in CH_2Cl_2 [0.10 M $TBAPF_6$ as the electrolyte; Ag/AgCl as the reference electrode; scan rate = 100 mV/s]. The half-wave potentials of each redox process were noted in (a) BN-F and (b) BN-Ph. (d) Comproportionation equilibriums of radical cations and radical anions.

All the anodic and cathodic peaks of **BN-F** and **BN-Ph** during both oxidation and reduction sweeps were well-separated, suggesting the good stabilities of the radical anion and radical cation intermediates toward disproportionation. For example, the potential gaps between the two reduction waves for both **BN-F** and **BN-Ph** were ~0.3 V (**Figure 79a**, **b**). These values corresponded to large radical comproportionation constants of the reduced forms ($K_{com\text{-}re}$) of 5.41×10^4 for **BN-F** and 1.74×10^5 for **BN-Ph** at 25 °C (equilibrium 1 in **Figure 79d**), indicating a highly stable radical anion. On the oxidation side, the potential gaps between the two oxidative processes were even larger (0.45 V for **BN-F** and 0.51 V for **BN-Ph**), corresponding to remarkably high radical comproportionation constants ($K_{com\text{-}ox}$) of 4.04×10^7 and 4.17×10^8 at 25 °C, respectively (equilibrium 2 in **Figure 79d**). Such high stabilities of the radicals were attributed to the strong spin-delocalization on the rigid backbones of **BN-F** and **BN-Ph** as designed. In contrast, precursor **3** without B ← N coordination, as a control, showed overlapping two-electron oxidation processes (**Figure 79c**) and irreversible reduction processes. Such a drastic difference on the redox behaviors between **BN-F**/**BN-Ph** and **53** demonstrated profound changes in the electronic structures after the installment of the B ← N coordination. These electrochemical data demonstrated the highly efficient stabilization effect of the B ← N coordination on the oxidized/reduced states through extending charge/spin delocalization.

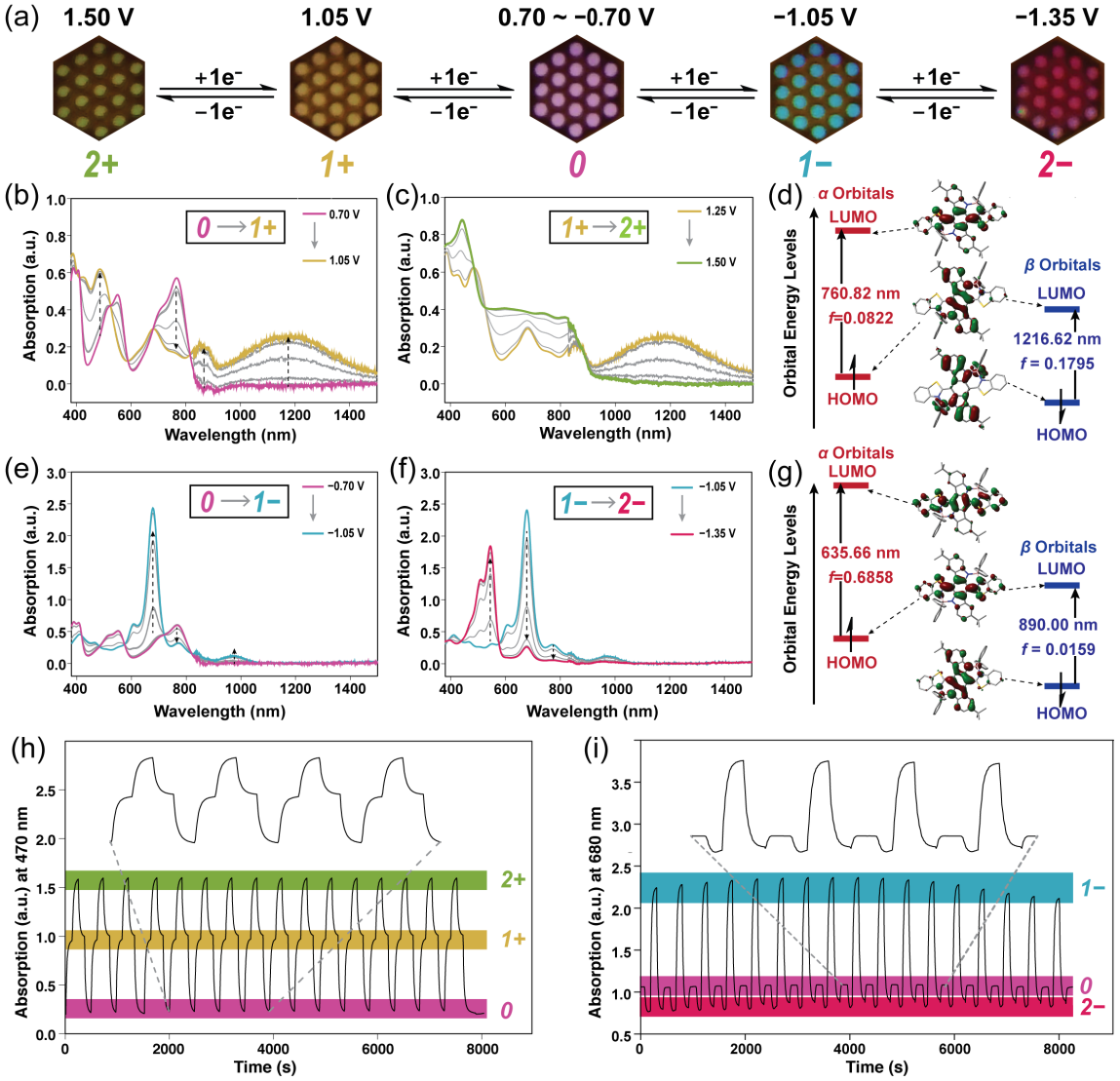

Figure 80. (a) Photographs of the BN-Ph solutions at different redox states in the presence of a honeycomb working electrode in a spectroelectrochemical cell (in CH_2Cl_2 with 0.10 M $TBAPF_6$). UV–vis–NIR absorption changes of the BN-Ph solutions upon stepwise applications of potentials on the honeycomb working electrode (step height = 0.05 V, vs Ag/AgCl) from (b) +0.70 to +1.05 V, (c) +1.25 to +1.50 V, (e) −0.70 to −1.05 V, and (f) −1.05 to −1.35 V. Molecular frontier orbitals and calculated transition energies with oscillator strengths of (d) BN-Ph$^{\bullet+}$ and (g) BN-Ph$^{\bullet-}$ [UB3LYP/6-311g(d,p) with CH_2Cl_2 CPCM solvation]. Multiple cycles of absorption changes of the BN-Ph solutions when the potential was switching between (h) 0.20, 1.10, and 1.50 V and (i) −0.30, −1.05, and −1.40 V.

	BN-Ph$^{\bullet+}$	**BN-Ph^{2+}**
Transition	1216.62	1154.28
Oscillator	0.1795	0.0821
Main	HOMO-β→LUMO-β	HOMO→LUMO
Transition	817.79	1129.83
Oscillator	0.0098	0.0118
Main	HOMO−3-β→LUMO-β	HOMO−2→LUMO
Transition	787.95	1067.26
Oscillator	0.0058	0.0141
Main	HOMO−5-β→LUMO-β	HOMO−5→LUMO
Transition	760.82	881.20
Oscillator	0.0822	0.2855
Main	HOMO-α→LUMO-α	HOMO−9→LUMO

Table 3. Calculated transition energies [B3LYP/6-311g(d,p)] of BN-Ph$^{\bullet+}$ and BN-Ph^{2+} based on the molecular geometries obtained at the level of B3LYP/6-311g(d,p).

The excellent redox reversibility allowed spectroelectrochemical measurements on **BN-Ph**, i.e., UV–vis–NIR absorption spectra recorded during each of the electrochemical redox processes, which gave highly reversible multicolor electrochromism (**Figure 80a**). According to time-dependent DFT calculations, these drastic color changes were attributed to the substantial differences on the transition energy diagrams of the different redox states (**Table 3** and **Table 4**).When the applied

potential swept from 0.70 to 1.05 V (vs Ag/AgCl), **BN-Ph** was gradually oxidized into the radical cation form **BN-Ph**$^{\bullet+}$. During this process, the HOMO→LUMO transition of the neutral **BN-Ph** at 768 nm diminished, while a new NIR absorption at 1180 nm emerged (**Figure 80b**). This low-energy absorption band corresponded to the transition of HOMO-β → LUMO-β of the delocalized radical cation (**Figure 80d**), according to DFT calculation. On the basis of the cutoff shape of this NIR absorption peak, **BN-Ph**$^{\bullet+}$ can be categorized as a class III mixed valence system,[243] in which the two nitrogen-centered redox moieties in ICBZ were strongly coupled with one another. The absorption spectra exhibited no significant change from 1.05 to 1.25 V, indicating the good stability of **BN-Ph**$^{\bullet+}$ over a wide range of potentials. When **BN-Ph**$^{\bullet+}$ was oxidized into the dication form **BN-Ph**$^{2+}$ by increasing the potential from 1.30 to 1.50 V, the characteristic radical cation absorption peak at 1180 nm gradually diminished, while multiple absorption bands covering a broad visible light region emerged (**Figure 80c**). To test the reversibility of these oxidation processes, iterative potential sweepings were conducted between +0.20, +1.10, and +1.50 V for >15 cycles (**Figure 80h**). Excellent reversibility was demonstrated without notable degradation of the absorption intensity (monitored at 470 nm).

Similarly, the radical anion and dianion of **BN-Ph** were investigated by spectroelectrochemistry study. Upon the application of a negative potential of −0.75 V, **BN-Ph** started to be reduced as the absorption intensity at 768 nm decreased (**Figure 80e**) while a highly intensive peak at 677 nm and a weak absorption peak at ~940 nm emerged, corresponding to the optical transitions, HOMO–1-α → LUMO-α and HOMO-

β → LUMO-β of radical anion **BN-Ph$^{\bullet-}$** (**Figure 80g**). The Gaussian shape of this low energy peak indicated that **BN-Ph$^{\bullet-}$** was a class II mixed valence system, in which the two reduced BTH moieties were coupled in a weaker manner.[243,244]

	BN-Ph$^{\bullet-}$	**BN-Ph^{2-}**
Transition	890.00	529.61
Oscillator	0.0159	1.1407
Main	HOMO-β→LUMO-β	HOMO→LUMO
Transition	659.08	494.81
Oscillator	0.2646	0.0662
Main	HOMO−1-β→LUMO-β	HOMO→LUMO+2
Transition	635.66	464.19
Oscillator	0.6858	0.0126
Main	HOMO-α→LUMO-α	HOMO→LUMO+4
Transition	446.89	439.19
Oscillator	0.2161	0.0713
Main	HOMO−3-β→LUMO-β	HOMO→LUMO+6

Table 4. Calculated transition energies [B3LYP/6-311g(d,p)] of BN-Ph$^{\bullet-}$ and BN-Ph^{2-} based on the molecular geometries obtained at the level of B3LYP/6-311g(d,p).

Further decrease of the potential from −1.05 to −1.35 V resulted in the second step of reduction into the dianion, **BN-Ph^{2-}**, accompanied by the diminishing of all the

peaks in the long-wavelength region and the emerging of a higher-energy peak centered at 544 nm as the new HOMO → LUMO transition (**Figure 80f**). Again, excellent reversibility of the reduction processes was confirmed by monitoring the absorption intensity at 680 nm while sweeping the potential iteratively between −0.30, −1.05, and −1.40 V (**Figure 80i**) for >15 cycles.

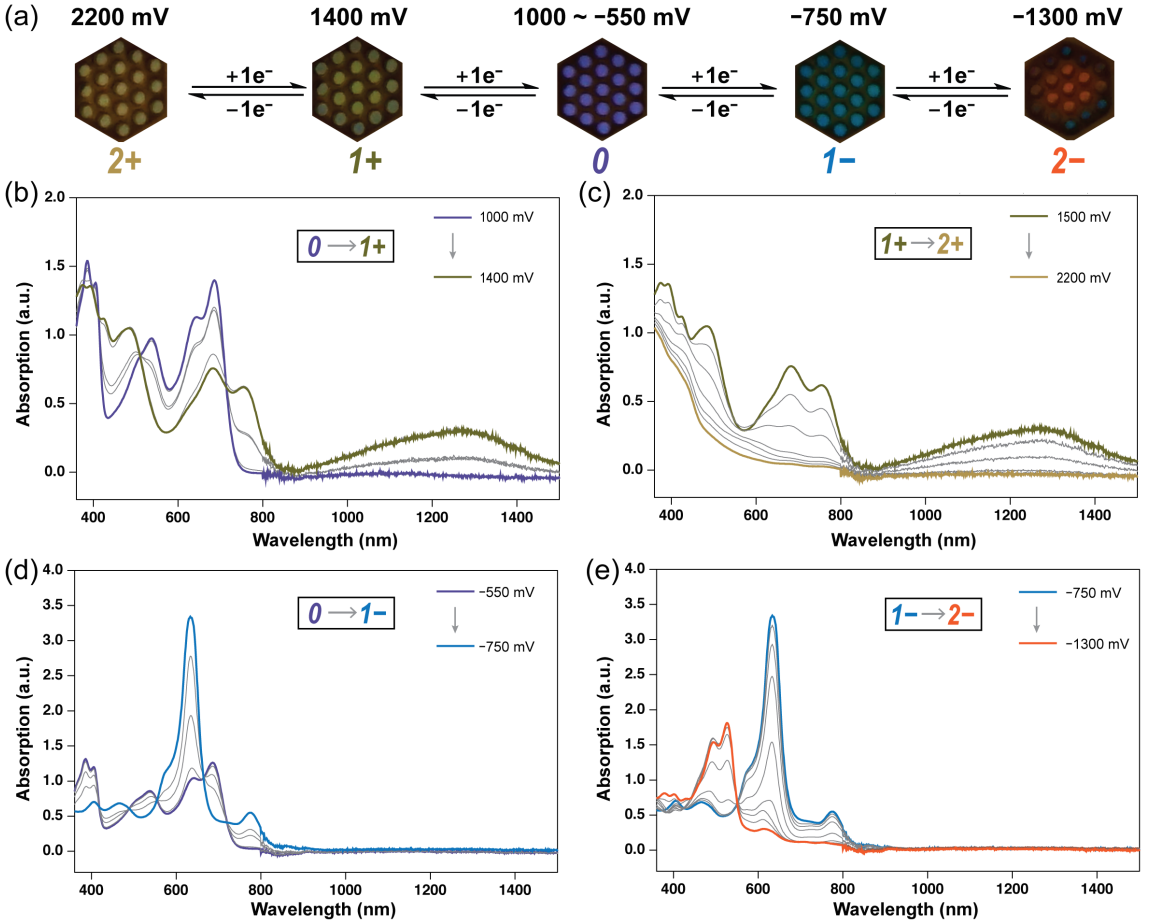

Figure 81. (a) Photographs of the honeycomb electrode in CH_2Cl_2 with 0.10 M $TBAPF_6$ as the electrolyte for different redox states of BN-F. UV-vis absorption changes of BN-F in CH_2Cl_2 upon stepwise application of potentials from (b) +1000 mV to +1400 mV (step heigh: 100 mV), (c) +1500 mV to +2200 mV (step heigh: 100 mV), (d) −550 mV to −750 mV (step heigh: 50 mV) and (e) −750 mV to −1300 mV (step heigh: 100 mV) vs. Ag/AgCl.

Spectroelectrochemical measurements were also conducted in a CH_2Cl_2 solution of **BN-F**, which showed a similar reversible multistage electrochromism over a wide range of electric potentials (**Figure 81**).

5.5 Mechanistic Investigation

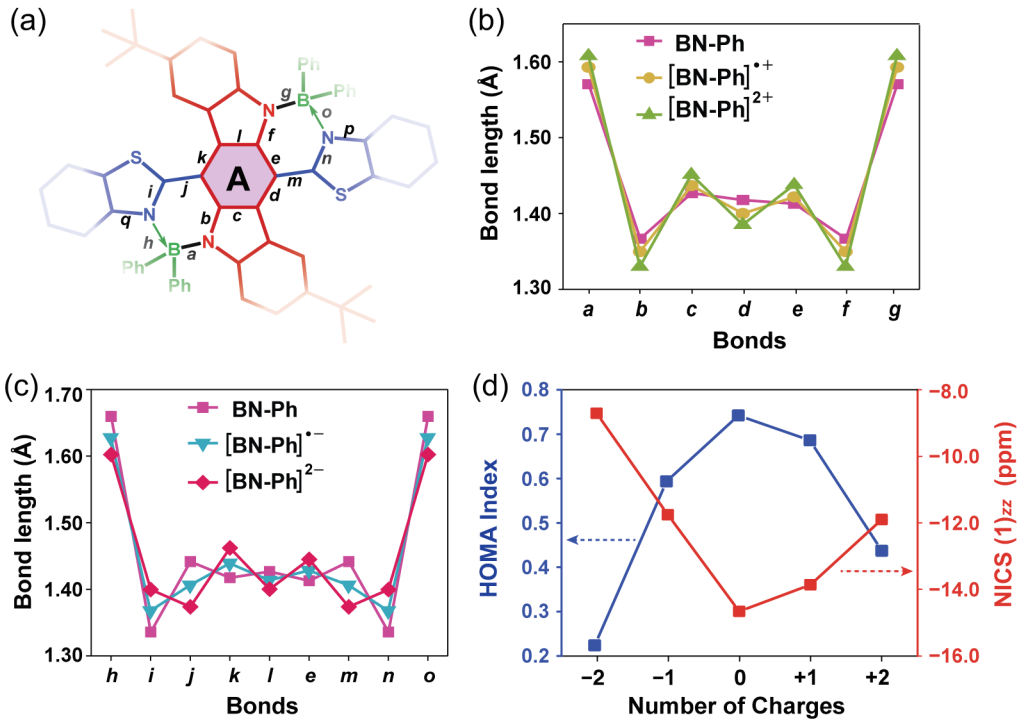

Figure 82. (a) The redox-active core structure of BN-Ph labeled with bond indices from *a* to *q*; (b) DFT calculated lengths of the bonds *a*–*g* before and after oxidation; (c) DFT calculated lengths of the bonds *e* and *h*–*o* before and after reduction [B3LYP/6-311g(d,p)]; (d) calculated HOMA and NICS(1)$_{zz}$ values for the central ring "A" of BN-Ph in different redox states.

To shed light on the mechanism of these remarkable redox and electrochromic activities of **BN-Ph** and **BN-F**, DFT computations were performed starting with

geometry optimization [B3LYP/6-311g(d,p)] for all five redox states of **BN-Ph** in the gas phase. At the neutral state of **BN-Ph**, the lengths of bonds *c*, *d*, and *e* in the central ring "A" (1.412–1.427 Å) were close to that in a benzene ring (**Figure 82a**). Upon oxidation into the radical cation **BN-Ph**$^{\bullet+}$, DFT calculation showed that the bond length alternation (BLA) between these three bonds increased, indicating a decrease of aromaticity. The BLA increased further in the diradical form **BN-Ph**$^{2+}$ (**Figure 82b**), so that bonds *c*and *e* were elongated to 1.451 and 1.438 Å, respectively, while bond *d* was shortened to 1.388 Å, close to the length of a typical C═C double bond. Additionally, the C–N bonds *b* and *f* were shortened from 1.366 Å in **BN-Ph** to 1.330 Å in **BN-Ph**$^{2+}$. This computational study revealed a tendency toward the quinonoid character of the ICBZ unit after oxidation (**Figure 83**).

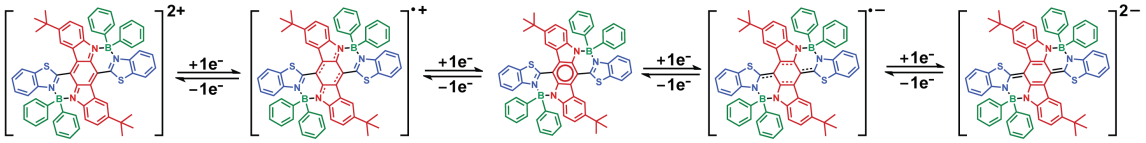

Figure 83. Constitutional structures of the five different redox states of BN-Ph.

In contrast, optimized geometries of the reduced forms exhibited that a different quinonoid structure was formed in between the two BTH units involving bonds *j*, *k*, *l*, *e*, and *m* (**Figure 82c**). In this case, bonds *j*, *l*, and *m* were shortened, accompanied by increased lengths of bonds *e* and *k*, during the transformation into **BN-Ph**$^{\bullet-}$ and **BN-Ph**$^{2-}$. These computational results suggested that, in the B ← N bridged molecule, two different yet orthogonal pathways of BLA changes were accessible to two different

quinonoid constitutions during the oxidation and reduction (**Figure 83**), respectively, contributing to the excellent stability in all the oxidized and reduced forms of **BN-Ph**. Considering the noncovalent nature of B ← N coordinate bonds, the molecular geometries were also optimized at the level of B3LYP/TZVP with D3 version of Grimme's dispersion correction, which revealed similar structural transformations (**Figure 85**). Similar BLA changes and structural transformations were also observed in the optimized molecular geometries for different redox states of **BN-F**. In addition, the aromaticity of ring "A" was calculated using the harmonic oscillator model of aromaticity (HOMA) and the nucleus-independent chemical shift (NICS) values (**Figure 83d**).[245-247] Both calculations confirmed a strong aromaticity of ring "A" in the neutral state and decreased aromaticity upon oxidation or reduction.

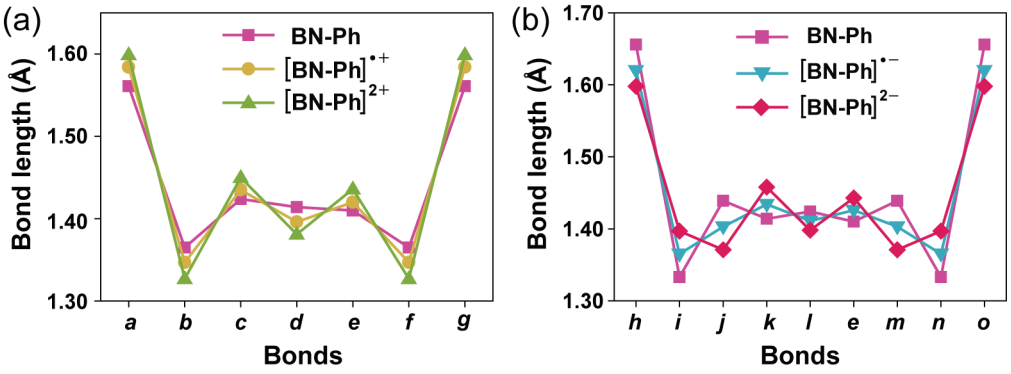

Figure 84. (a) DFT calculated lengths of the bonds *a*~*g* in BN-Ph before and after oxidation; (b) DFT calculated lengths of the bonds *e* and *h*~*o* in BN-Ph before and after reduction (B3LYP/TZVP with D3 version of Grimme's dispersion correction). Bond indices were shown in Figure 82a.

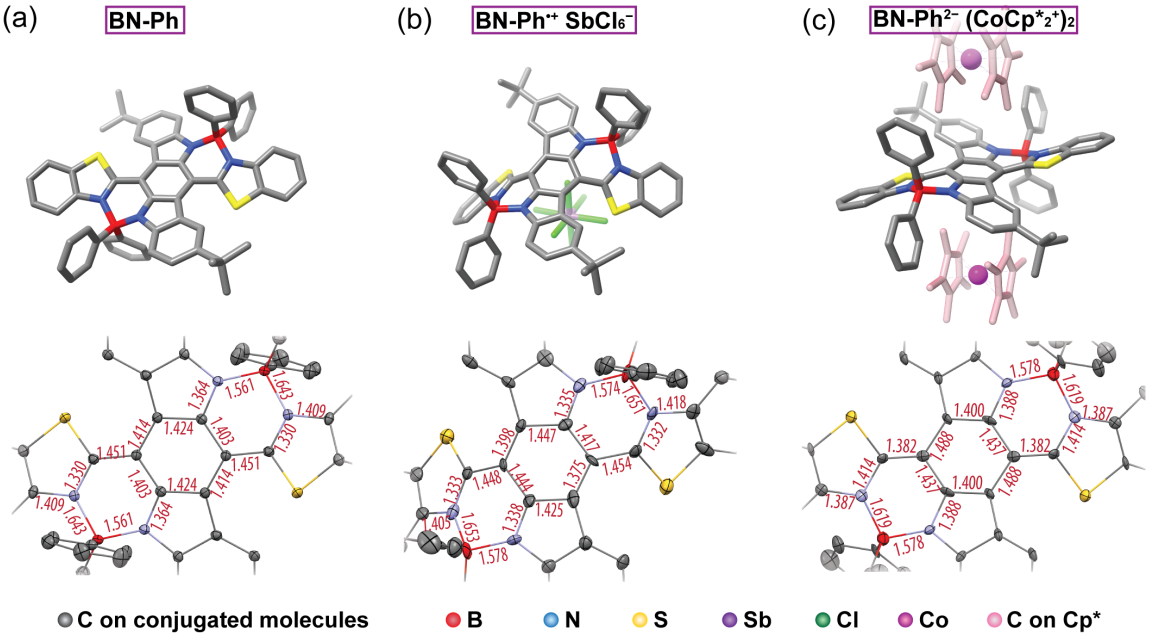

Figure 85. Single-crystal X-ray structures of (a) BN-Ph, (b) BN-Ph$^{\bullet+}$SbCl$_6^-$, and (c) BN-Ph^{2-}[CoCp*$_2^+$]$_2$ and bond lengths of the area around the central ring "A". Hydrogen atoms and solvent molecules were omitted for clarity. Thermal ellipsoids are scaled to the 50% probability level.

To validate these DFT computational results, the bond lengths and molecular geometries were examined by using experimental data from single-crystal X-ray diffraction of the neutral **BN-Ph**, the radical cation salt **BN-Ph$^{\bullet+}$SbCl$_6^-$**, and the dianion salt **BN-Ph^{2-}[CoCp*$_2^+$]$_2$** (**Figure 85**). The radical cation was chemically accessed by one-electron oxidation of **BN-Ph** with 1.2 equiv of tris(4-bromophenyl)ammoniumyl hexachloroantimonate (Magic Blue) in a CH_2Cl_2 solution. The single crystals suitable for X-ray diffraction were grown by slow vapor diffusion of pentane into a CH_2Cl_2 solution of **BN-Ph$^{\bullet+}$SbCl$_6^-$**. The dianion, on the other hand, was chemically prepared after two-electron reduction of **BN-Ph** by the addition of 3.0 equiv of decamethylcobaltocene (CoCp*$_2$). Vapor diffusion of diethyl ether into a concentrated

solution of **BN-Ph**$^{2-}$ in acetonitrile yielded single crystals suitable for X-ray diffraction analysis. Bond lengths measured from the single-crystal structures of **BN-Ph**, **BN-Ph**$^{\bullet+}$**SbCl**$_6^-$, and **BN-Ph**$^{2-}$**[CoCp*$_2^+$]$_2$** matched well with the DFT calculated bond lengths, further confirming the mechanism of the orthogonal quinonoid transformations upon oxidation and reduction, respectively. The average difference between the bond lengths calculated at the level of B3LYP/6-311g(d,p) and experimentally measured bond lengths was only 0.010 Å. Such an average difference obtained from calculation at the level of B3LYP/TZVP with D3 version of Grimme's dispersion correction was also ~0.010 Å, suggesting highly reliable computation results. The only exception was bond *d*, which was longer in the neutral state (1.444 Å) from the experimental result than that from the calculation, likely because of the steric strain between ICBZ and BTH units. In both **BN-Ph**$^{\bullet+}$ and **BN-Ph**$^{2-}$, the B ← N coordinate bonds retained their strength so that the rigid backbone scaffolds were maintained. In fact, the B ← N coordinate bond was even shorter in **BN-Ph**$^{2-}$ (1.619 Å) as a result of the stronger Lewis basicity of the nitrogen center on BTH after reduction. Moreover, the backbone of **BN-Ph**$^{2-}$ was more coplanar compared to that of **BN-Ph** (dihedral angles between ICBZ and BTH units reduced to 6.3°), due to an enhanced double-bond character of bonds *j* and *m*.

Additional characterizations were performed on the reduced and oxidized states of **BN-Ph** in order to further understand their electronic structures during the redox processes. Electron paramagnetic resonance (EPR) spectroscopy of the **BN-Ph**$^{\bullet+}$**SbCl**$_6^-$ solution showed a broad resonance signal (**Figure 86a**). The spin concentration (7.8×10^{17} spin/mL) was close to the theoretical value (8.9×10^{17} spin/mL) when assuming the

formation of an organic monoradical (S= 1/2) on each molecule, indicative of a high conversion from **BN-Ph** to **BN-Ph**$^{\bullet+}$. The lack of hyperfine splitting in the EPR spectrum was attributed to the delocalized spin that experienced multiple couplings with a number of nuclei in this molecule,[224] in accordance with DFT computed substantial delocalization of the unpaired spin density (**Figure 86b** and **Figure 87**). The reduced radical anion, **BN-Ph**$^{\bullet-}$, demonstrated similar EPR signal and spin delocalization (**Figure 86c**, **d**).

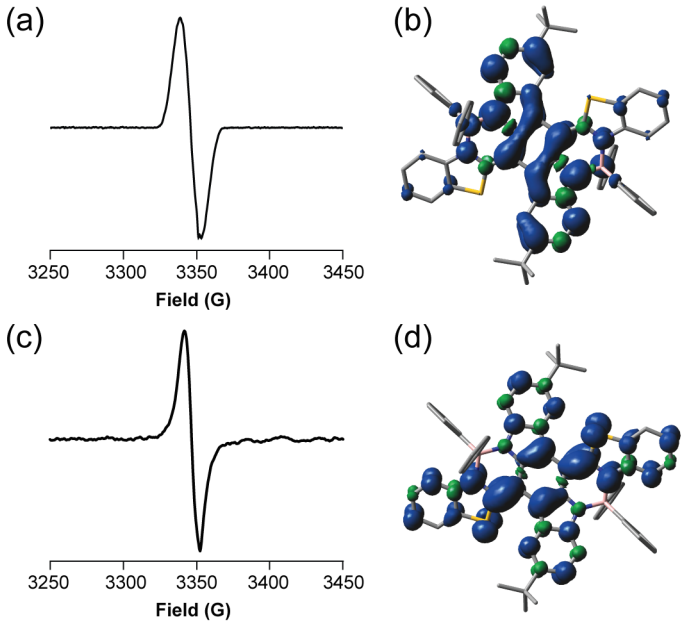

Figure 86. EPR spectra of (a) BN-Ph$^{\bullet+}$ in CH_2Cl_2 (0.13 mM) and (c) BN-Ph$^{\bullet-}$ in acetonitrile (0.03 mM) at 288 K. DFT computed spin density maps (isovalue = 0.0008) of (b) BN-Ph$^{\bullet+}$ and (d) BN-Ph$^{\bullet-}$[UB3LYP/6-311g++(d,p)].

Overall, experimental investigations together with computational studies clearly revealed the underlying mechanism of the unique redox processes of ladder-type **BN-Ph** molecules, which involved two distinct pathways of constitutional changes from a

benzenoid structure into two types of quinonoid structures upon oxidation and reduction, respectively. The oxidation-active moiety and reduction-active moiety were orthogonally compacted into a single molecular scaffold, giving rise to the reversible multistage redox processes. In addition, B ← N coordination promoted the rigid ladder-type structure in which separated redox centers were strongly coupled with each other, and the unpaired electron of radicals was stabilized by extensive delocalization.

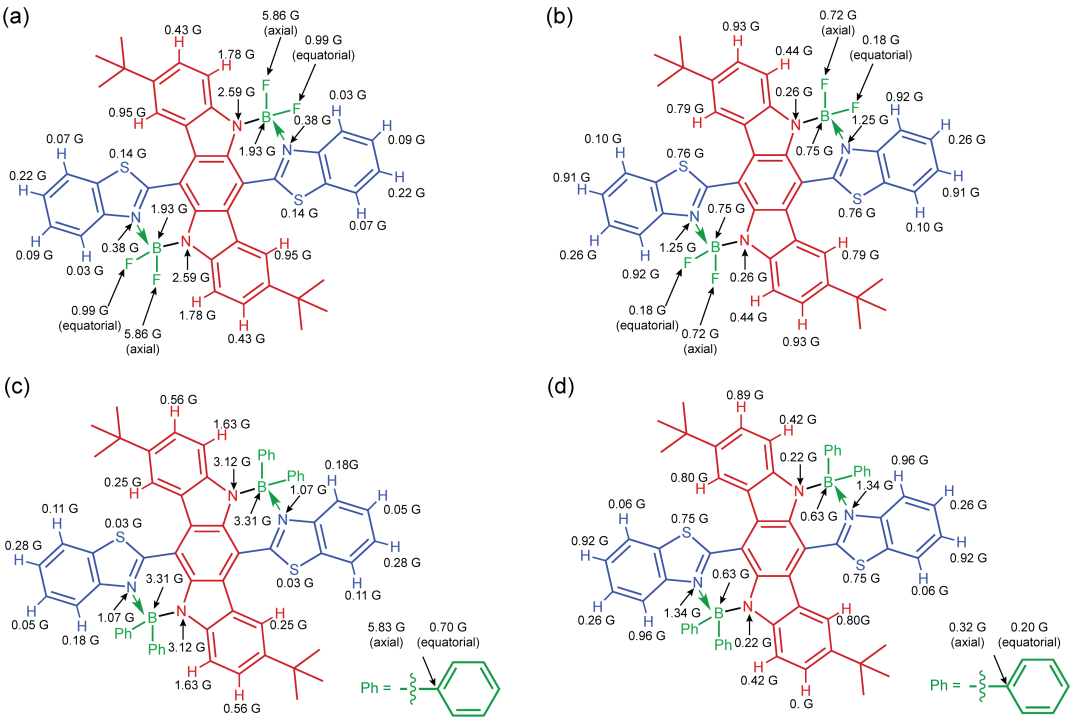

Figure 87. Calculated isotropic Fermi coupling constants of (a) BN-F$^{\bullet+}$, (b) BN-F$^{\bullet-}$, (c) BN-Ph$^{\bullet+}$, (d) BN-Ph$^{\bullet-}$.

5.6 Hyperconjugation

In **BN-Ph** and **BN-F**, the boron centers stabilized the redox states through a number of different mechanisms, including spin coupling, extending π-delocalization,

and modulating electron densities. It was also hypothesized that the boron-ligand moieties impacted the electronic structures of these molecules through hyperconjugation similar to that existing in cyclohexa-1,3-diene (**Figure 74b**), providing additional stabilization effects. According to the crystal structures of **BN-Ph**, **BN-Ph**$^{\bullet+}$, and **BN-Ph**$^{2-}$, the two phenyl ligands on the boron center adopted different bonding orientations: one of the B–C σ-bonds was almost perpendicular to the conjugated backbone (denoted as the "axial" bond), while the other one was almost in the plane of the backbone (denoted as the "equatorial" bond). Such an unsymmetrical geometry of the boron ligand (B—L, L = Ph or F) bonds was also predicted by DFT optimized structures of both **BN-Ph** and **BN-F**. The nonequivalent bonding orientations suggested hyperconjugative interactions between the axial bonds and the conjugated backbone in these ladder-type molecules. To unveil the hyperconjugations of these axial B−L σ/σ* orbitals, natural bond orbital (NBO) analysis was performed on **BN-Ph**, **BN-F**, and their dianionic and dicationic forms.[236,248] The strengths of these interactions can be correlated with second-order perturbation energies [$E^{(2)}$] computed from NBO analysis.[249,250] In the neutral state of **BN-Ph**, a hyperconjugative donor–acceptor interaction [$E^{(2)}$ = 4.18 kcal/mol] was identified from the lone pair [*lp*(N)] on the ICBZ unit to the antibonding [σ*(B–C)] orbital on the axial position (**Figure 88a**).[249] After the two-electron oxidation, the quinonoid ICBZ unit of **BN-Ph**$^{2+}$ lost the lone pair on the nitrogen center and had a lower electron density. Despite a weaker electron-donating ability, the π(C–N) orbital of the quinonoid ICBZ still interacted hyperconjugatively [$E^{(2)}$ = 2.05 kcal/mol] with the axial σ*(B–C) orbital (**Figure 88b**). More interestingly, a unique back-donating

interaction [$E^{(2)}$ = 2.70 kcal/mol] was observed from the σ(B–C) orbital to the π*(C–N) orbital of the electron-deficient, quinonoid ICBZ unit (**Figure 88c**), reinforcing the hyperconjugative stabilization effect by diluting the positive charges on the dicationic backbone of **BN-Ph^{2+}**. In the reduced form of dianionic **BN-Ph^{2-}**, the NBO analysis showed that the σ*(B–C) orbital also served as an acceptor to stabilize the negative charges on the reduced BTH units. In **BN-Ph^{2-}**, bonds *p* and *q* (**Figure 82a**) possessed a partial double-bond character (1.387 Å in the crystal structure) so that their π orbitals participated in a hyperconjugation [$E^{(2)}$ = 3.27 kcal/mol] with the σ*(B–C) orbital (**Figure 88d**). In this case, the hyperconjugation further delocalized the negative charges and, therefore, enhanced the stability of the highly charged dianion. In **BN-F** with the fluoride ligands, NBO analysis at different redox states demonstrated similar but even stronger hyperconjugative interactions between the axial σ*(B–F) orbital and the conjugated backbone, as a result of the high electronegativity of fluorine atoms (**Figure 88e–h**). In the optimized structure of **BN-F**, the axial σ*(B–F) orbitals withdrew the electron density through hyperconjugation [$E^{(2)}$ = 7.36 kcal/mol] from the electron lone pair of the nitrogen atom on the ICBZ unit (**Figure 88e**). Meanwhile, another donor–acceptor interaction of 2.84 kcal/mol was found in **BN-F** between the π(C–N) bond in the BTH unit and the axial σ*(B–F) orbital (**Figure 88f**). Therefore, these profound hyperconjugative effects in **BN-F**, together with the inductive effect from fluorine atoms, contributed to its low-lying HOMO and LUMO levels compared to **BN-Ph**.

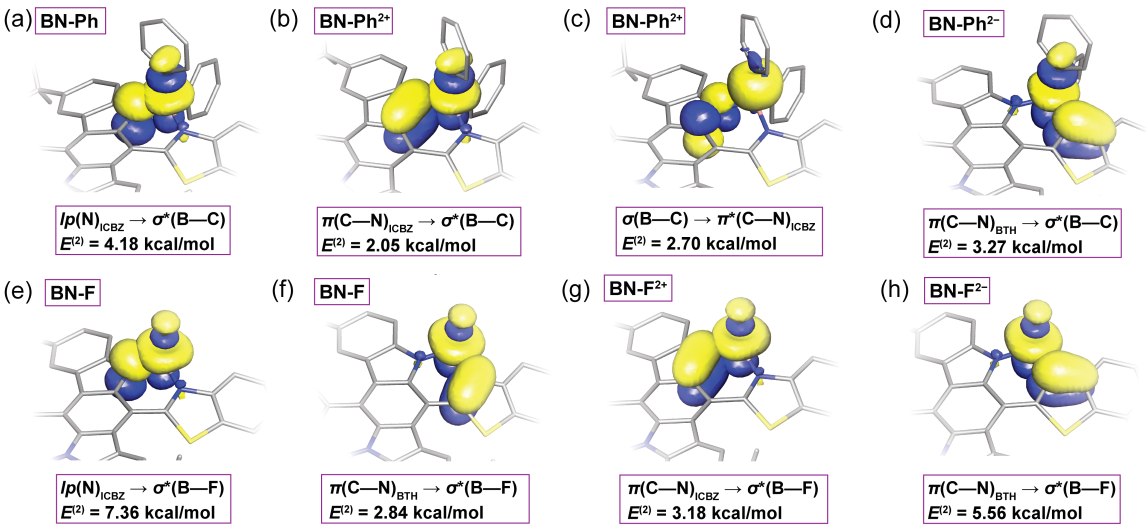

Figure 88. NBO plots of hyperconjugative interactions in different redox states of BN-Ph (a, b, c, d) and BN-F (e, f, g, h).

According to DFT calculation, these hyperconjugative interactions were also present in the paramagnetic radical cations and radical anions. Isotropic Fermi couplings of the axial ligands with the already delocalized spin were much higher than those of the equatorial ligands, indicating strong interactions between the axial bond with the backbone through hyperconjugation. Overall, the hyperconjugative stabilization effect further assisted the desirable charge and spin delocalization during the redox processes. Meanwhile, such orbital interactions provided an additional mechanism to impact the electronic structures and properties of the entire ladder-type molecules.

5.7 Conclusion

In conclusion, we demonstrated herein a molecular design strategy to achieve highly reversible, multistage redox activities and multicolor electrochromism in compact

ladder-type molecules bridged with B ← N coordination. The structural transformations from a benzenoid constitution into two distinct types of quinonoid constitutions during both reduction and oxidation processes were elucidated, giving a clear mechanistic picture of these robust multistage electron-transfer processes. Combined theoretical and experimental investigations demonstrated that the B ← N coordination played a pivotal role in rendering the remarkable redox properties of these molecules by extending the charge and spin delocalization and by enforcing the rigid conformation. We systematically established a hyperconjugation mechanism that impacted the electronic structures and further stabilized the different redox states. These results advanced fundamental knowledge of sp^3 boron-containing π-systems, providing practical design principles for the development of *p*-block element-derived molecules and macromolecules with exotic optical, electronic, and spin properties, such as fully fused ladder polymers bridged by these B ← N coordinate bonds.

5.8 Experimental Section

5.8.1 General Methods

Starting materials and reagents were purchased from Sigma Aldrich, Acros Organics, Alfa Aesar or Oakwood and used as received. Anhydrous CH_2Cl_2 and pentane were purchased from EMD Milipore and used without further purification. THF was dried and distilled under nitrogen from sodium using benzophenone as the indicator. Diethyl ether was dried and distilled under nitrogen from sodium-potassium alloy using benzophenone as the indicator. Acetonitrile was dried and distilled under nitrogen from

CaH_2. Diethyl ether and acetonitrile were degassed by three cycles of freeze-pump-thaw before use. Toluene was dried using an IT pure solvent system (PureSolv-MD-5) and used without further treatment. Chlorodiphenylborane was synthesized according to a reported literature procedure. ^{1}H and ^{13}C NMR spectra were recorded on Varian Inova 500 MHz spectrometers. The NMR chemical shifts were reported in ppm relative to the signals corresponding to the residual non-deuterated solvents ($CDCl_3$: ^{1}H 7.26 ppm, ^{13}C 77.16 ppm; CD_3CN: ^{1}H 1.94 ppm) or the internal standard (tetramethylsilane: ^{1}H 0.00 ppm). Abbreviations for reported signal multiplicities are as follows: s, singlet; d, doublet; t, triplet; q, quartet; m, multiplet; br, broad. The broad singlet at ~1.55 ppm on ^{1}H NMR spectra represents the resonance signal of H_2O in $CDCl_3$. High resolution electrospray ionization (ESI) mass spectra were recorded on Applied Biosystems PE SCIEX QSTAR. Column chromatography was carried out using Biotage® IsoleraTM Prime instrument with various size of SiO_2 Biotage ZIP® cartridge. UV-vis absorption spectra were recorded on a Shimadzu UV-2600 Spectrophotometer. Absorption spectra data shown in Table 1 and Figure 5 were obtained from the measurement of diluted dichloromethane solutions (around 1×10^{-5} mol/L). Emission spectra data shown in Table 1 were obtained from the measurement of diluted dichloromethane solutions (~1.0×10^{-6} mol/L). Spectroelectrochemical measurements were conducted with a Shimadzu UV3600 UV−vis-NIR spectrophotometer and a 273A potentiostat (Princeton Applied Research). The measurement was carried out in a honeycomb spectroelectrochemical cell (Pine Research Instrumentation, Inc.) composed of a quartz UV-vis cell (path length = 1.7 mm), a gold electrode chip and a mini Ag/AgCl reference electrode. Electron

paramagnetic resonance spectra were recorded in a continuous wave X-band EleXsys EPR spectrometer at 288 K. Cyclic voltammetry was carried out at room temperature in nitrogen-purged CH_2Cl_2 with a CHI voltammetric analyzer. Tetrabutylammonium hexafluorophosphate (0.1 M in acetonitrile) was used as the supporting electrolyte. The conventional three-electrode configuration consisted of a glassy carbon working electrode, a platinum wire anxiliary electrode, and a Ag/AgCl electrode. Cyclic voltammograms were obtained at a scan rate of 100 mV/s. The energy levels were calculated using ferrocene/ferrocenium (Fc/Fc^+) as the standard reference. Fc/Fc^+ vs Ag/AgCl = 0.45 V.

5.8.2 Synthesis

Compound **51**: (4-*tert*-Butylphenyl)hydrazine monohydrochloride (4.40 g, 21.92 mmol) was suspended in ethanol (32 mL) at room temperature. A solution of sodium acetate (5.39 g, 65.76 mmol) in water (16 mL) was added. The mixture was stirred at room temperature of 15 minutes. To this mixture, a solution of cyclohexane-1,4-dione (1.23 g, 10.96 mmol) in ethanol (10 mL) was added dropwise over 5 minutes. After the addition, acetic acid (8 mL) was added in one portion. The mixture was stirred for 1 hour at 50 °C and 1 hour at 0 °C. Subseuqently, the reaction mixture was filtered to yield a pale yellow solid. The solid was collected and further dried under vacuum for 2 hours, before it was added portionwise over 10 minutes to a mixture of acetic acid (12 mL) and sulfuric acid (98%, 3 mL) at 10 °C. The mixture was warmed up to room temperature and stirred for another 10 minutes. The temperature was then further increased to 65 °C

and maintained for 30 minutes. Subsequently, the mixture was cooled down to room temperature and poured into water (100 mL) at 0 °C. The resulting precipitate was filtered and washed extensively with methanol to give the pure product as a gray solid (810 mg, 19%). In addition, the methanol filtrate was concentrated under reduced pressure. The residue was purified through column chromatography (SiO_2, hexane/ethyl acetate 4:1) to give additional product as a gray solid (91 mg, 3%). The combined yield of **51** was 22%. ^{1}H NMR (500 MHz, $CDCl_3$) δ = 8.12 (d, *J* = 1.5 Hz, 2H), 8.04 (s, 2H), 7.50 (dd, *J* = 8.5 Hz, 2.0 Hz, 2H), 7.38 (d, *J* = 8.5 Hz, 2H), 1.46 (s, 18H), the signals of NH protons were not observed; ^{13}C NMR (125 MHz, $CDCl_3$) δ = 142.10, 139.25, 135.93, 126.65, 124.00, 116.47, 114.94, 110.14, 100.68, 34.91, 32.27. ESI-MS: *m/z* $[M+H]^+$ Calcd for $C_{26}H_{29}N_2$ 369.2331; Found 369.2290.

Compound **52**: Compound **51** (921 mg, 2.5 mmol) was dissolved in anhydrous THF (30 mL) at 0 °C. To this mixture, a freshly prepared solution of NBS (445 mg, 2.5 mmol) in THF (15 mL) was added dropwise. The mixture was stirred at 0 °C for 10 minutes. Subsequently, another freshly prepared solution of NBS (445 mg, 2.5 mmol) in THF (15 mL) was added dropwise. The mixture was warmed up slowly and stirred at room temperature overnight. The solvent was removed under reduced pressure. The residue was dissolved in CH_2Cl_2. The organic solution was washed by water twice and dried with $MgSO_4$. The crude product was purified through column chromatography (SiO_2, hexane/ethyl acetate 19:1 to 7:1), to give **52** as a pale yellow crystalline solid (1.025 g, 78%). ^{1}H NMR (500 MHz, $CDCl_3$) δ = 8.80 (d, *J* = 2.0 Hz, 2H), 8.22 (s, 2H), 7.60 (dd, *J* = 8.5 Hz, 2.0 Hz, 2H), 7.46 (d, *J* = 8.5 Hz, 2H), 1.48 (s, 18H). ^{13}C NMR (125

MHz, $CDCl_3$) δ = 142.72, 138.74, 135.20, 125.12, 123.50, 121.36, 118.64, 110.36, 96.21, 35.03, 32.17. ESI-MS: *m/z* $[M-H]^-$ Calcd for $C_{26}H_{25}N_2Br_2$ 525.0364; Found 525.0366.

Compound **53**: Compound **52** (105.0 mg, 0.20 mmol) and 2-(tributylstannyl)benzo[d]thiazole (340.0 mg, 0.80 mmol) were added into toluene (6 mL). The suspension was degassed by three cycles of freeze-pump-thaw before $Pd(PPh_3)_4$ (23.2 mg, 0.020 mmol), CuI (7.6 mg, 0.040 mmol) and CsF (304.0 mg, 2.0 mmol) were added under N_2. The reaction mixture was stirred at 105 °C for 48 hours. After cooling to room temperature, the mixture was extracted with CH_2Cl_2 and washed with 1M HCl once, brine twice, water once and dried with $MgSO_4$. The crude product was purified through column chromatography (SiO_2, hexane/CH_2Cl_2 1:1 to 1:9) to give **53** as an orange solid (96.2 mg, 76%). ^1H NMR (500 MHz, $CDCl_3$) δ = 9.73 (s, 2H), 8.34 ~ 8.33 (m, 4H), 8.05 (d, *J* = 8.0 Hz, 2H), 7.65 (td, *J* = 7.8 Hz, 1.0 Hz, 2H), 7.54 (td, *J* = 7.8 Hz, 1.0 Hz, 2H), 7.49 (dd, *J* = 8.5 Hz, 1.5 Hz, 2H), 7.40 (d, *J* = 8.5 Hz, 2H), 1.30 (s, 18H). ^{13}C NMR (125 MHz, $CDCl_3$) δ = 164.63, 153.64, 141.91, 139.56, 135.77, 135.74, 126.75, 125.93, 125.09, 123.65, 121.88, 121.69, 121.11, 120.02, 111.81, 110.66, 34.98, 32.08. ESI-MS: *m/z* $[M+H]^+$ Calcd for $C_{40}H_{35}N_4S_2$ 635.2303; Found 635.2282.

BN-F: Compound **53** (95.1 mg, 0.15 mmol) was added into a thick-wall reaction vessel equipped with a PTFE cap. The reaction vessel was transferred into a N_2-filled glovebox, where anhydrous toluene (10 mL), triethylamine (0.3 mL) and $BF_3 \cdot OEt_2$ (0.45 mL, 3.6 mmol) were added. The vessel was taken out from the glovebox with the cap firmly closed. The reaction mixture was stirred at 85 °C for 48 hours. After cooling to the room temperature, the reaction mixture was added into 200 mL methanol

dropwise. The resulting precipitates were filtered and washed with water and methanol to afford **BN-F** as a dark purple solid (105.2 mg, 96%). ^{1}H NMR (500 MHz, $CDCl_3$) δ = 9.11 (d, *J* = 1.5 Hz, 2H), 8.80 (d, *J* = 8.5 Hz, 2H), 8.12 (d, *J* = 8.5 Hz, 2H), 8.08 (d, *J* = 8.5 Hz, 2H), 7.83 (td, *J* = 8.0, 1.5 Hz, 2H), 7.77 (dd, *J* = 8.5 Hz, 1.5 Hz, 2H), 7.70 (td, *J* = 8.0, 1.5 Hz, 2H). The resonance peak of *t*-butyl groups overlapped with the peak of H_2O in $CDCl_3$. ^{13}C NMR was not obtained for **BN-F**, due to its very limited solubility. MALDI-MS: *m/z* $[M-F]^+$ Calcd for $C_{40}H_{32}B_2F_3N_4S_2$ 711.221, Found 711.304; $[M+Na]^+$ Calcd for $C_{40}H_{32}B_2F_3N_4S_2Na$ 753.209, Found 753.304; $[M+K]^+$ Calcd for $C_{40}H_{32}B_2F_4N_4S_2K$ 769.183, Found 769.294.

BN-Ph: Compound **53** (44.4 mg, 0.07 mmol) was added into a thick-wall reaction vessel equipped with a PTFE cap. The reaction vessel was transferred into a N_2-filled glovebox, where anhydrous toluene (5 mL), diisopropylethylamine (0.3 mL) and BPh_2Cl (281 mg, 1.4 mmol) were added. The vessel was taken out from the glovebox with the cap firmly closed.The reaction mixture was stirred at 135 °C for 48 hours. After cooling to room temperature, toluene was removed under reduced pressure. The resulting mixture was extracted with CH_2Cl_2 and washed with 1M HCl once, brine twice, water once and dried with $MgSO_4$. Purification through column chromatography (SiO_2, hexane/CH_2Cl_2 9:1 to 1:9) gave the crude product, which was further purified by preparative size exclusion chromatography using chloroform as the eluent. The final product, **BN-Ph**, was isolated as a purple solid (48.5 mg, 72%). ^{1}H NMR (500 MHz, CD_2Cl_2) δ = 8.93 (d, *J* = 2.0 Hz, 2H), 7.98 (d, *J* = 8.5 Hz, 2H), 7.58 (d, *J* = 9.0 Hz, 2H), 7.47 (td, *J* = 8.0, 1.0 Hz, 2H), 7.35 (dd, *J* = 8.0, 2.0 Hz, 8H), 7.31 (td, *J* = 8.0, 1.0 Hz,

2H), 7.23 ~ 7.21 (m, 12H), 6.66 (d, J = 9.0 Hz, 2H), 1.42 (s, 18H). ^{13}C NMR (125 MHz, $CDCl_3$) δ = 165.62, 146.26, 145.06, 140.84, 140.63, 133.97, 130.95, 127.99, 127.63, 127.01, 126.40, 125.53, 123.07, 121.90, 121.57, 119.87, 119.39, 115.16, 111.03, 35.15, 32.18. The resonance signals for carbon atoms that covalently bonded to boron atoms were not observed due to the quadrupolar nature of boron. ESI-MS: *m/z* $[M+H]^+$ Calcd for $C_{64}H_{53}B_2N_4S_2$ 963.3898; Found 963.3930.

5.8.3 Redox Reactions

All the reactions were performed in a N_2 filled glovebox.

BN-Ph$^{\bullet+}$ SbCl$_6^-$: To a solution of **BN-Ph** (1.2 mg, 1.3 μmol) in CH_2Cl_2 (1 mL), tris(4-bromophenyl)-ammoniumyl hexachloroantimonate (1.3 mg, 1.6 μmol) was added. The resulting mixture was stirred at room temperature for 3 hours. The solution was filtered using a syringe filter and used for EPR analysis. The filtered solution was further transferred into a 2 mL vial. This small vial was put into a 20 mL vial filled with pentane for crystal growth. After 3 days, dark brown crystals suitable for X-ray single crystal analysis were formed.

BN-Ph$^{\bullet-}$ CoCp$_2^+$: To a suspension of **BN-Ph** (0.7 mg, 0.8 μmol) in CH_3CN (1 mL), cobaltocene ($CoCp_2$) (0.2 mg, 1.1 μmol) was added. The mixture turned green within one hour and was stirred overnight. Some green precipitates were observed. The mixture was filtered using a syringe filter and used for EPR analysis.

BN-Ph^{2-} [CoCp*$_2^+$]$_2$: To a suspension of **BN-Ph** (1.2 mg, 1.3 μmol) in CH_3CN (1.5 mL), decamethylcobaltocene ($CoCp^*_2$) (1.3 mg, 4.0 μmol) was added. The mixture

turned green within several minutes and further turned red after stirring overnight. The mixture was filtered using a syringe filter. transferred into a 2 mL vial. This small vial was put into a 20 mL vial filled with diethyl ether for crystal growth. After 3 days, dark red crystals suitable for X-ray single crystal analysis were formed. A same experiment was also performed in CD_3CN for NMR analysis. Sharp resonance signals on the ^1H NMR spectrum revealed the diamagnetic nature of this dianionic species, consistent with the quinonoid character of **BN-Ph**$^{2-}$ suggested by the single crystal X-ray analysis and DFT calculation.

BN-F$^{\bullet+}$ **SbCl**$_6^-$: To a solution of **BN-F** (1.1 mg, 1.5 μmol) in CH_2Cl_2 (2 mL), tris(4-bromophenyl)-ammoniumyl hexachloroantimonate (2.5 mg, 3.0 μmol) was added. The resulting mixture was stirred at room temperature overnight. The solution was filtered using a syringe filter and used for EPR analysis.

BN-F$^{\bullet-}$ **CoCp**$_2^+$: To a suspension of **BN-F** (2.0 mg, 2.7 μmol) in CH_2Cl_2 (3 mL), cobaltocene ($CoCp_2$) (0.8 mg, 4.0 μmol) was added. The mixture turned blue within one hour and was stirred overnight. Some blue precipitates were observed. The mixture was filtered using a syringe filter and used for EPR analysis.

5.8.4 NMR Spectra

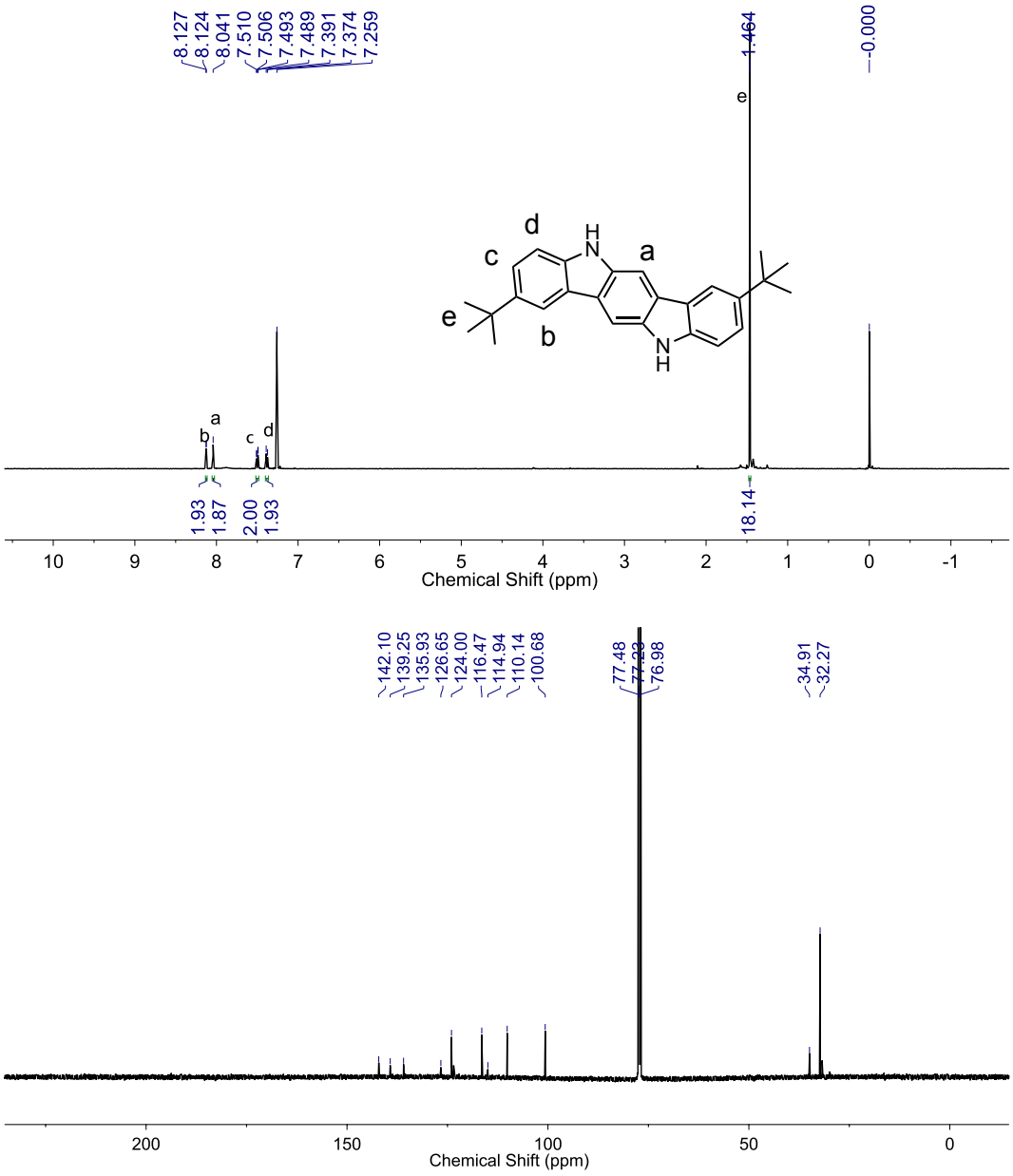

Figure 89. ^{1}H (500 MHz), ^{13}C NMR (125 MHz) of 51 in $CDCl_3$ at 295 K.

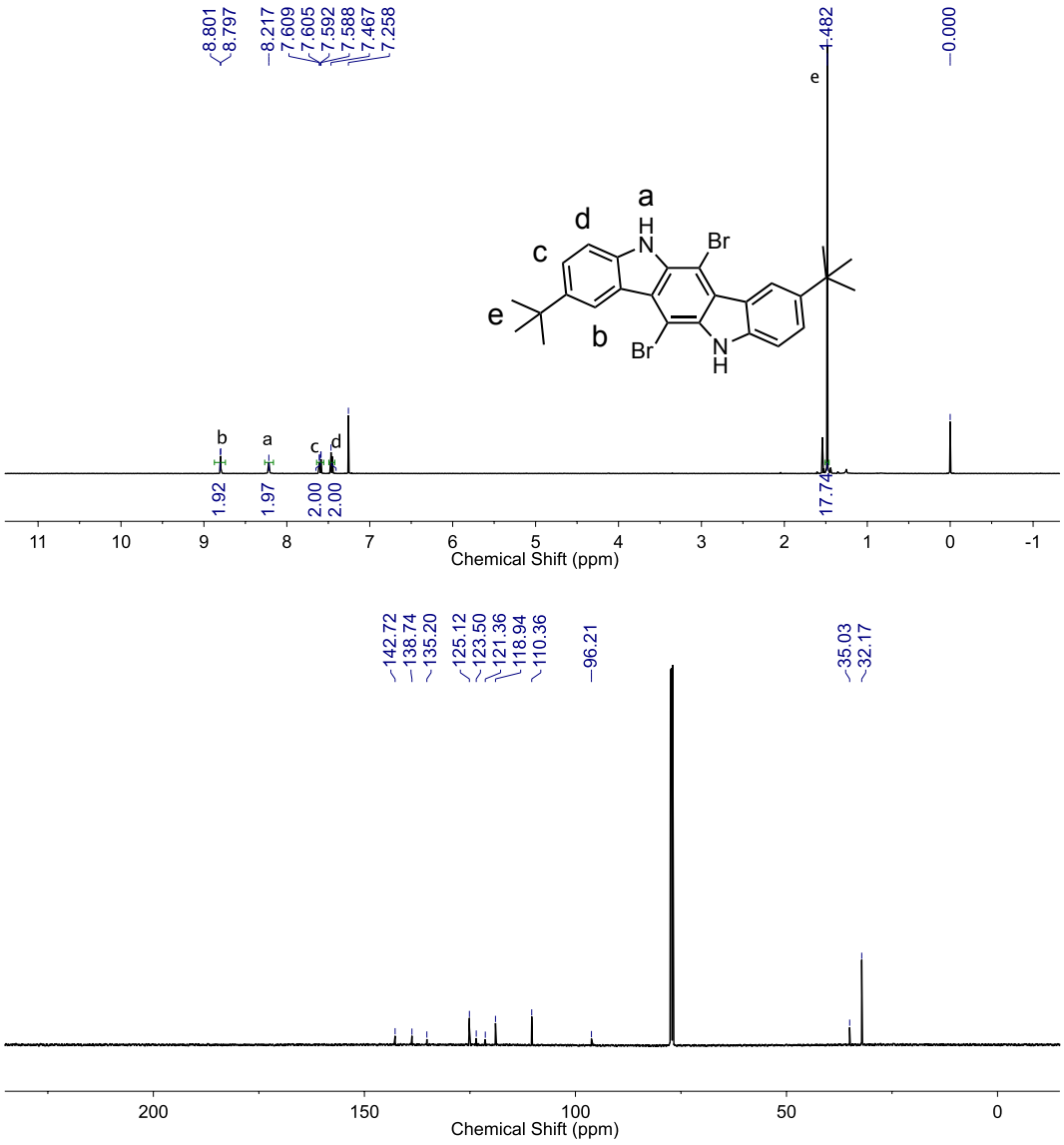

Figure 90. ^{1}H (500 MHz), ^{13}C NMR (125 MHz) of 52 in $CDCl_3$ at 295 K.

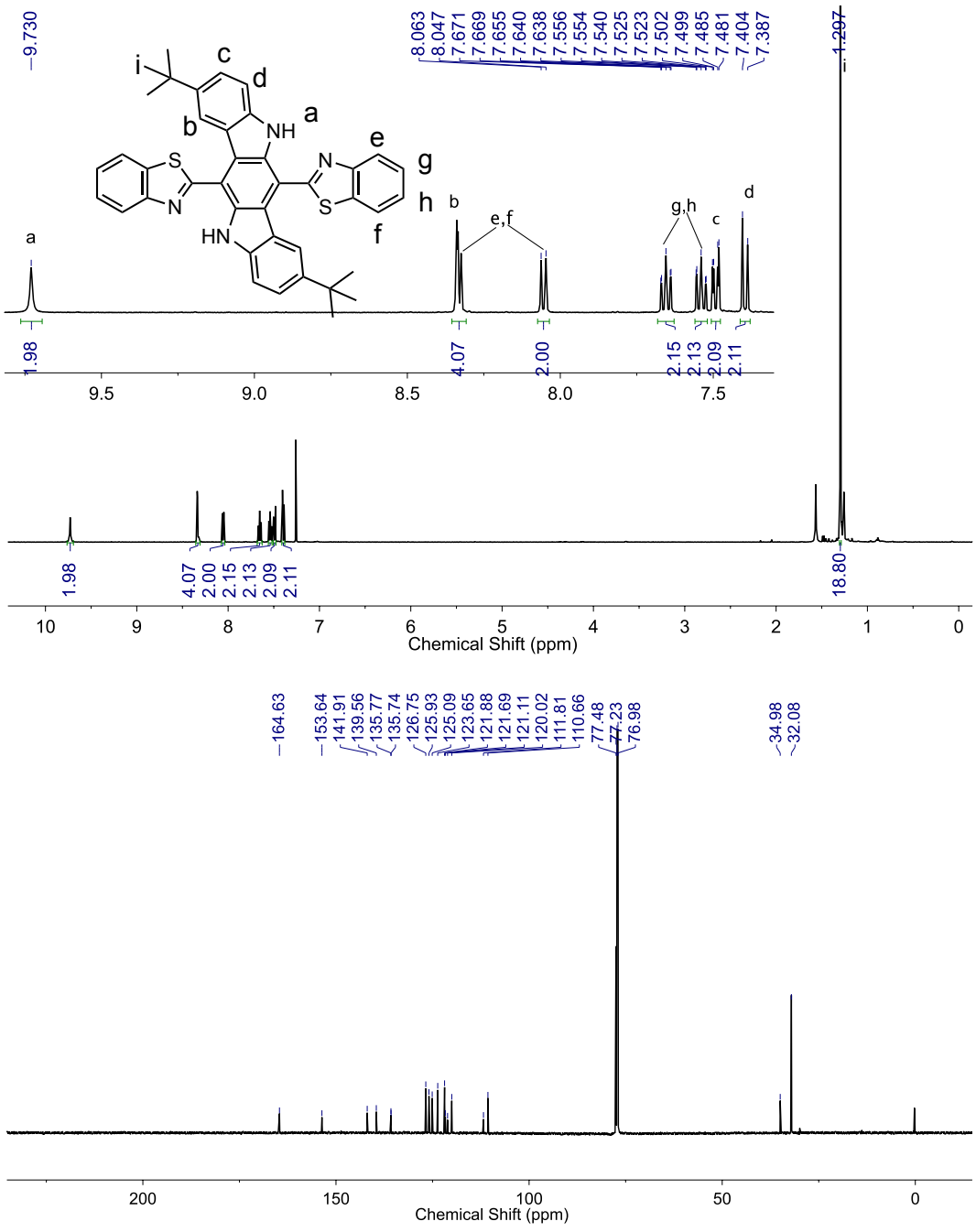

Figure 91. ^{1}H (500 MHz), ^{13}C NMR (125 MHz) of 53 in $CDCl_3$ at 295 K.

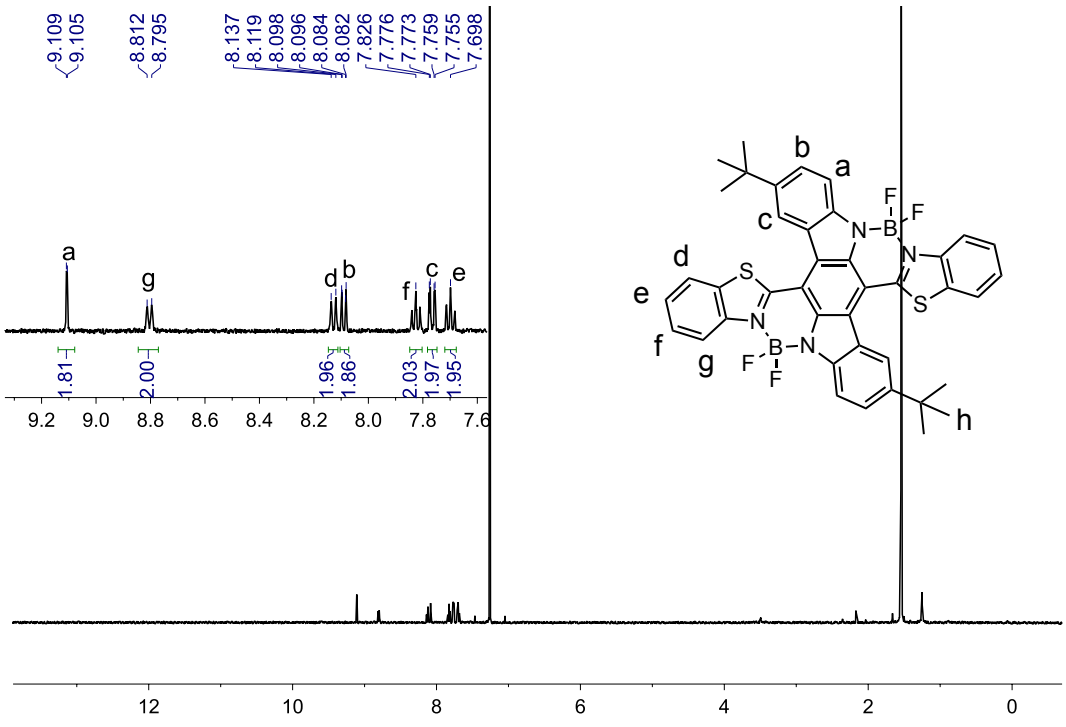

Figure 92. ^{1}H (500 MHz) of BN-F in $CDCl_3$ at 295 K.

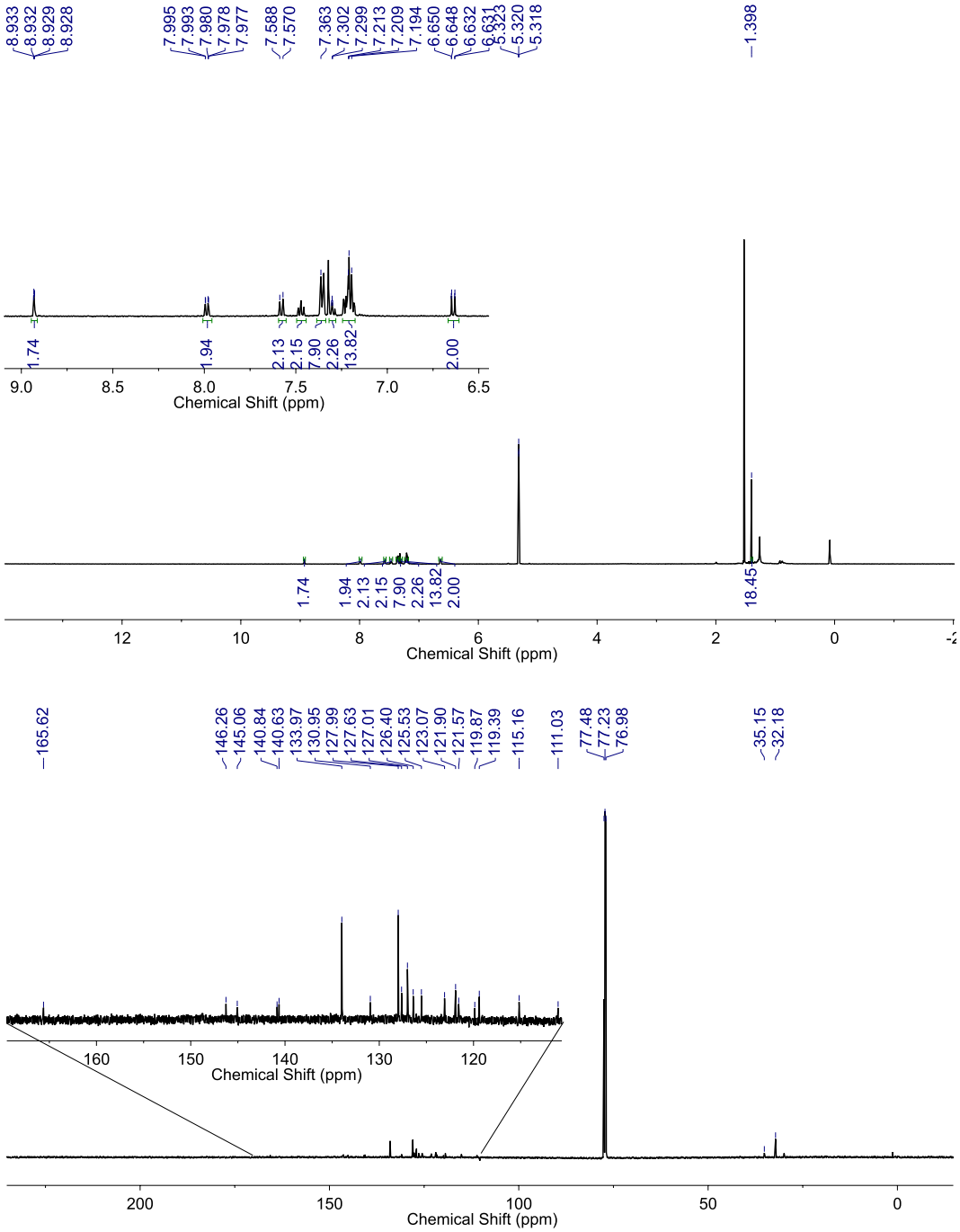

Figure 93. ^{1}H (500 MHz in CD_2Cl_2), ^{13}C NMR (125 MHz in $CDCl_3$) of BN-Ph at 295 K.

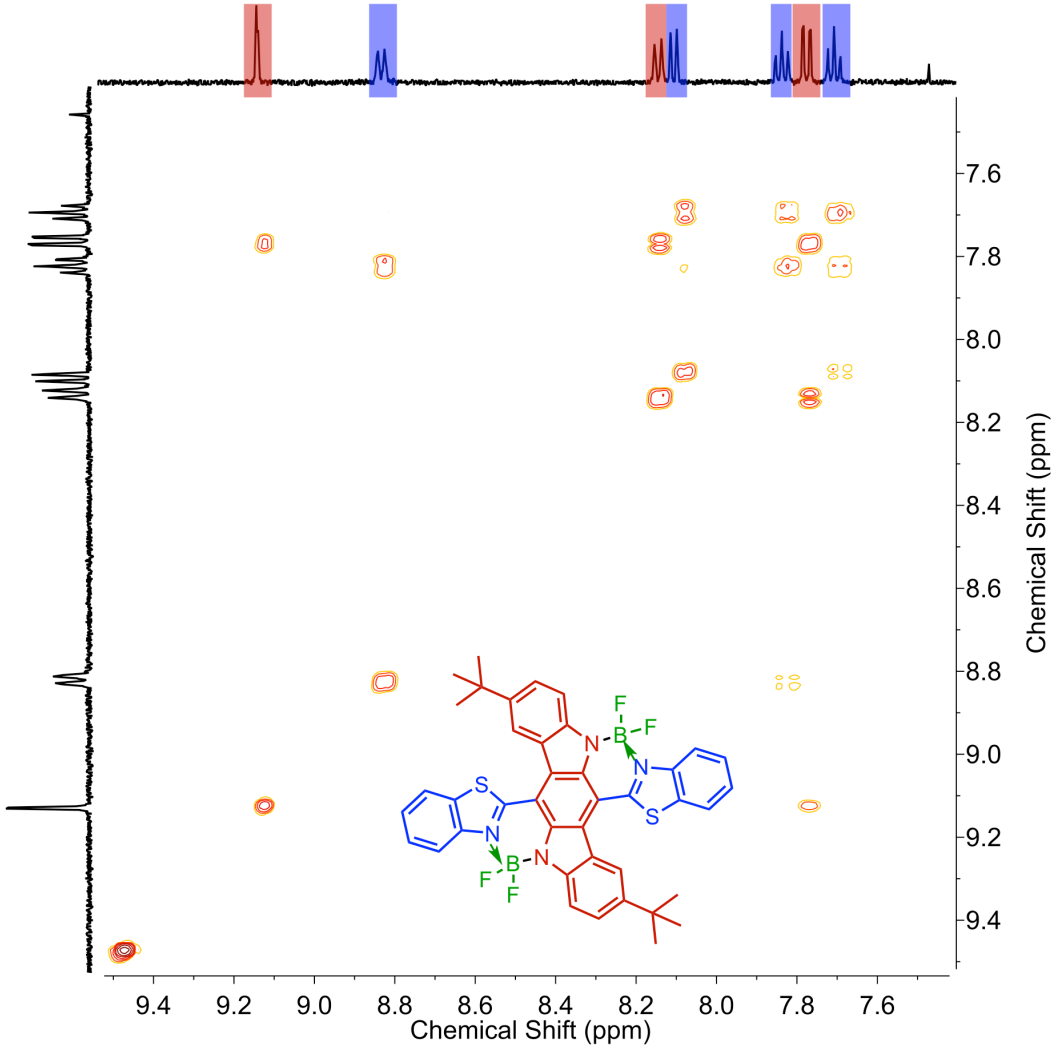

Figure 94. ^{1}H-^{1}H COSY NMR (500 MHz in $CDCl_3$) of BN-F at 323 K.

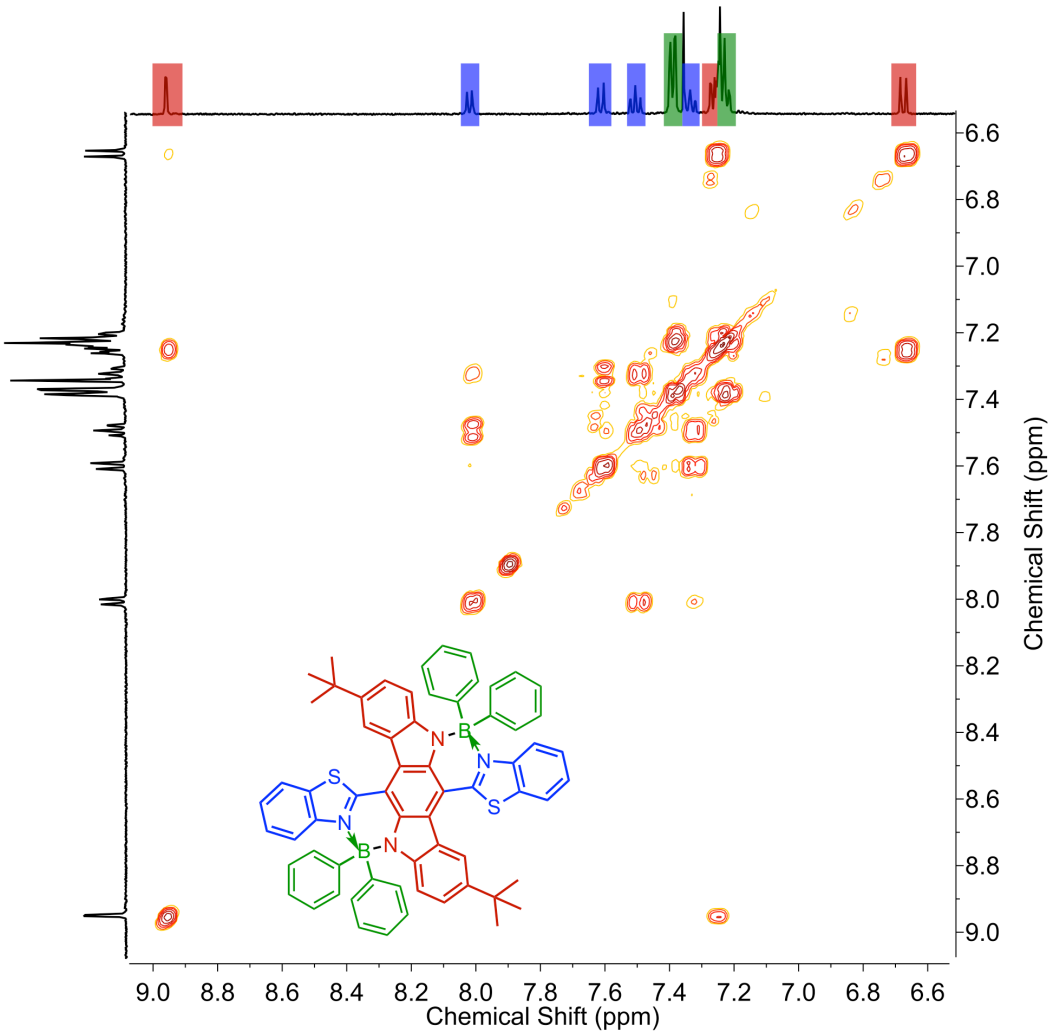

Figure 95. ^{1}H-^{1}H COSY NMR (500 MHz in CD_2Cl_2) of BN-Ph at 295 K.

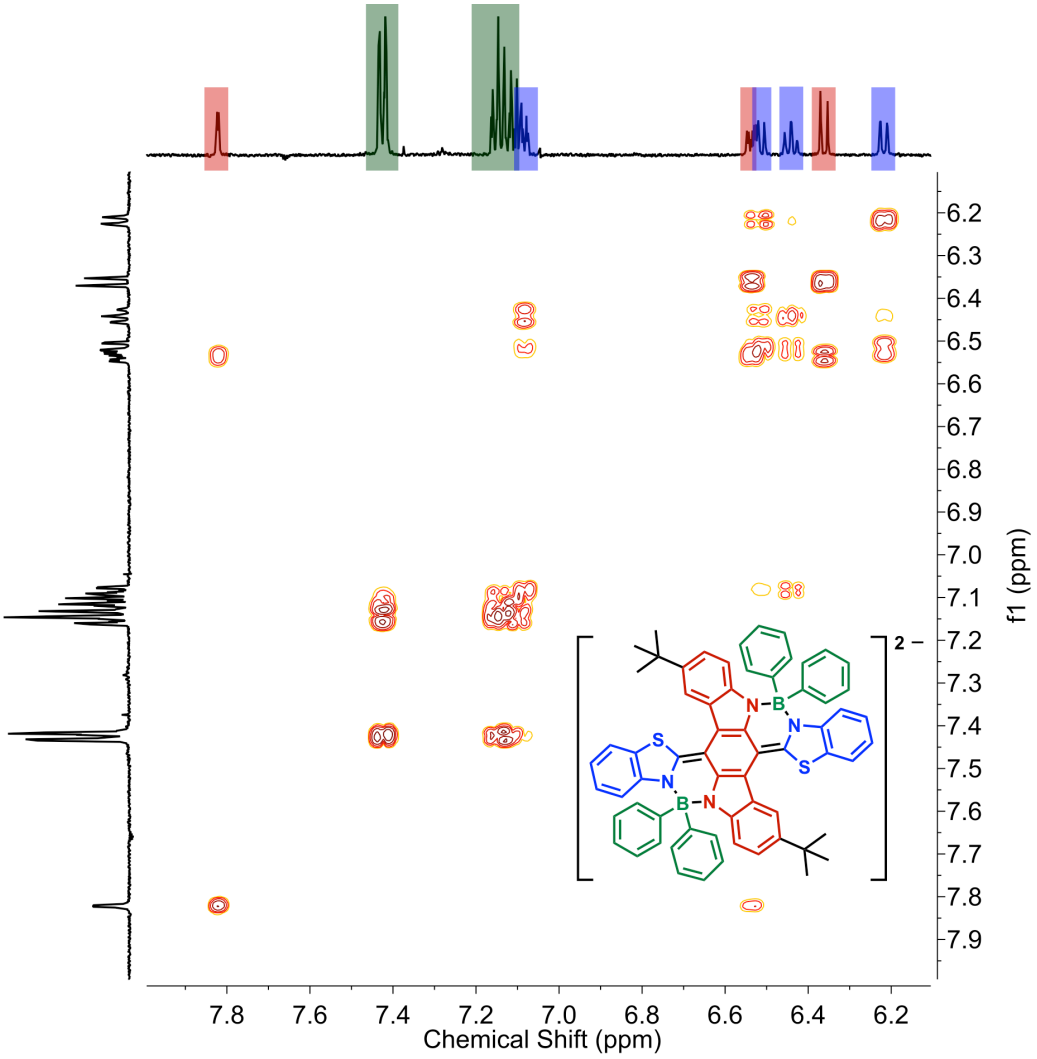

Figure 96. ^{1}H-^{1}H COSY NMR (500 MHz in CD_3CN) of BN-Ph^{2-} at 295 K.

5.8.5 DFT Calculation

The structures of **3**, **BN-F**, **BN-F**$^{2+}$, **BN-F**$^{2-}$, **BN-Ph**, **BN-Ph**$^{2+}$ and **BN-Ph**$^{2-}$ were optimized at the level of B3LYP/6-311g(d,p). The structures of radical species, **BN-F**$^{\bullet+}$, **BN-F**$^{\bullet-}$, **BN-Ph**$^{\bullet+}$ and **BN-Ph**$^{\bullet-}$ were optimized at the level of UB3LYP/6-311g(d,p). Afterwards, single point energy calculation at the level of B3LYP/6-311++g(d,p) were

performed for the computation of molecular orbitals, spin density maps, isotropic Fermi coupling constants and NBO analysis. Based on the optimized structures, transition energies were calculated by Time-Dependent DFT at the level of B3LYP/6-311g(d,p) with CH_2Cl_2 CPCM solvation. We also performed geometry optimization for different redox states of **BN-Ph** using B3LYP/TZVP with D3 version of Grimme's dispersion correction considering the noncovalent nature of B←N coordinate bonds. Furthermore, the transition energies were calculated using CAM-B3LYP/TZVP. Compared to the molecular geometries obtained using B3LYP/6-311g(d,p), these computation results still revealed the same chemical constitution changes during the redox processes. The calculated bond lengths and transition energies were also compared to the single crystal data and spectroelectrochemical measurements. Compared to the molecular geometries optimized at the level of B3LYP/6-311g(d,p), the geometries optimized at the level of B3LYP/TZVP with D3 version of Grimme's dispersion correction afforded more accurate bond lengths in **BN-Ph**, equally accurate bond lengths in **BN-Ph**$^{\bullet+}$, but less accurate bond lengths in **BN-Ph**$^{2-}$, referring to the single crystal data. The time-dependent the calculation at the level of CAM-B3LYP/TZVP based on the geometries obtained at the level of B3LYP/TZVP with D3 version of Grimme's dispersion correction failed to match well with the absorption spectra for different redox states of **BN-Ph**. Overall, our studies together with some recently reported literatures suggested that DFT computations with B3LYP/6-311g(d,p) afford reliable calculation results for this class of rigid ladder-type molecules with intramolecular B←N coordinate bonds.

The NBO analysis was performed using the NBO 6.0 program. Computed orbital interactions were visualized using the Jimp2 software.

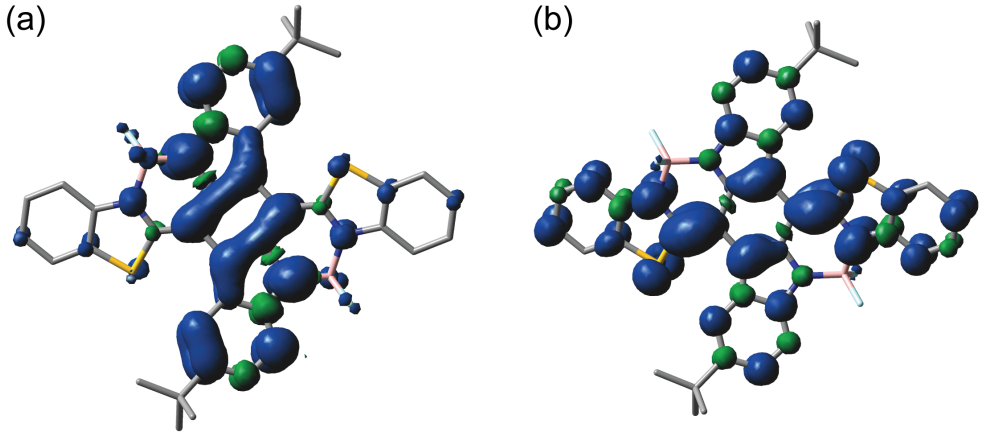

Figure 97. Spin density maps (isovalue = 0.0008) of (b) BN-F$^{\bullet+}$ and (d) BN-F$^{\bullet-}$ calculated at uB3LYP/6-311g++(d,p) level. Hydrogen atoms were omitted for clarity.

5.8.6 Electron Paramagnetic Resonance Spectra

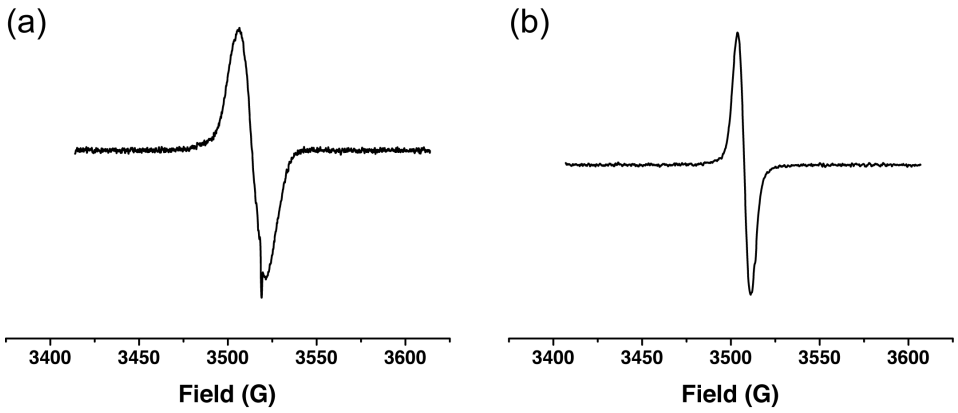

Figure 98. EPR spectra of (a) BN-F$^{\bullet+}$ in CH_2Cl_2 and (b) BN-F$^{\bullet-}$ in CH_2Cl_2 at 288 K.

5.8.7 X-ray Single Crystal Analysis

A BRUKER Venture X-ray (kappa geometry) diffractometer was employed for crystal screening, unit cell determination, and data collection. The goniometer was controlled using the APEX3 software suite.1 The sample was optically centered with the aid of a video camera such that no translations were observed as the crystal was rotated through all positions. The X-ray radiation employed was generated from a Cu-Iμs X-ray tube (Kα = 1.5418Å with a potential of 50 kV and a current of 1.0mA).

45 data frames were taken at widths of 1°. These reflections were used to determine the unit cell. The unit cell was verified by examination of the *h k l* overlays on several frames of data. No super-cell or erroneous reflections were observed. After careful examination of the unit cell, an extended data collection procedure was initiated using omega and phi scans.

Integrated intensity information for each reflection was obtained by reduction of the data frames with the program APEX3. The integration method employed a three dimensional profiling algorithm and all data were corrected for Lorentz and polarization factors, as well as for crystal decay effects. Finally the data was merged and scaled to produce a suitable data set. The absorption correction program SADABS2 was employed to correct the data for absorption effects.

A solution was obtained readily (Z=2; Z'=0.5) using XT/XS in APEX3. Hydrogen atoms were placed in idealized positions and were set riding on the respective parent atoms. All non-hydrogen atoms were refined with anisotropic thermal parameters. Absence of additional symmetry or void were confirmed using PLATON (ADDSYM).

The structure was refined (weighted least squares refinement on F2) to convergence. Olex2 was employed for the final data presentation and structure plots.

CHAPTER VI

CONCLUSION

6.1 Hydrogen Bond Bridged Coplanar Conjugated Molecules and Macromolecules

6.1.1 Summary

Owing to the high directionality and strength tunability, hydrogen bonds stand out as ideal candidates for the purpose of precisely controlling backbone conformation of conjugated molecules and macromolecules. We developed a strategy of fusing hydrogen bond forming moieties into the backbone to enhance the strength of the intramolecular hydrogen bonds and the molecular rigidity of **34**. As a result, the robust coplanar conformation **34** led to strong aggregation in the solution phase and the self-assembly into one-dimensional fibers in the solid state. To further elucidate the mechanism of the intramolecular hydrogen bond-promtoed self-assembly, the aggregation properties of **34** were examined with the addition of DMSO, which distrupted intramolecular hydrogen bonds and resulted in weakened aggregation enthalpies. This work establishes the correlation between intramolecular hydrogen bonds and molecular/supramolecular properties of conjugated molecules.

Futhermore, the intramolecular hydrogen bonds were incoporated into rigid conjugated macromolecules through a similar molecular design strategy. The strong interactions between the rigid coplanar backbone of **HP**, however, led to poor solubility, impeding the synthesis, characterization and processing of such a material. To address this issue, a strategy of masking/unmasking hydrogen bonds with Boc groups was developed. The preinstallaion of Boc groups on the monomers twisted the polymer

backbone during the solution-phase synthesis, rendering the excellent solubility and high molecular weight of **BocP**. Futher thermal cleavage of Boc groups converted **BocP** into **HP-B** with the desired intramolecular hydrogen bonds and coplanarity. Such an Active manipulation of intramolecular hydrogen bonds enabled multilayer solution processing of **HP-B** through several cycles of the solution casting and thermal cleavage in a cumulative manner. This molecular engineering approach represents a practical method for solution processing and 3D printing of such polymeric materials through the manipulation of intramolecular noncovalent bonds.

6.1.2 Perspective

This approach using intramolecular hydrogen bonds to lock the conformation has shown great promise to impact not only the optical and electronic characters of conjugated small molecules and polymers, but also the collective behaviors, such as aggregation and self-assembly of these compounds. To further adopt this strategy to develop the novel organic conjugated materials for application, such as field-effect transistors and organic photovoltaics, it is essential to select the building blocks that have already demonstrated potential for high performance in electronic materials. For instance, thiophene and thiopehene-derived molecules have been widely used as electron-rich units in conjugated polymers. These molecules can be further functionalized with amide groups to serve as hydrogen bond donating moieties, which promote the formation of hydrogen bonds along the polymer chain, and lock the torsional angle between repeating units in the presence of proper hydrogen bond

accepting moieties. In this context, the following synthetic route is proposed (**Figure 99**). The amide group can be generated through a condensation reaction between urea and 3,4-diaminothiophene. Further functionalization with bromide or tributylstannyl groups will afford the monomer applicable for different polymerization. Naphthalene diimide, another widely used building unit, can serve as a hydrogen-accepting moiety utilizing its ketone groups in this molecular design. After coupling reactions, the proposed donor-acceptor alternating polymer **HP-NDI-Th** with intramolecular hydrogen bonds can be synthesized.

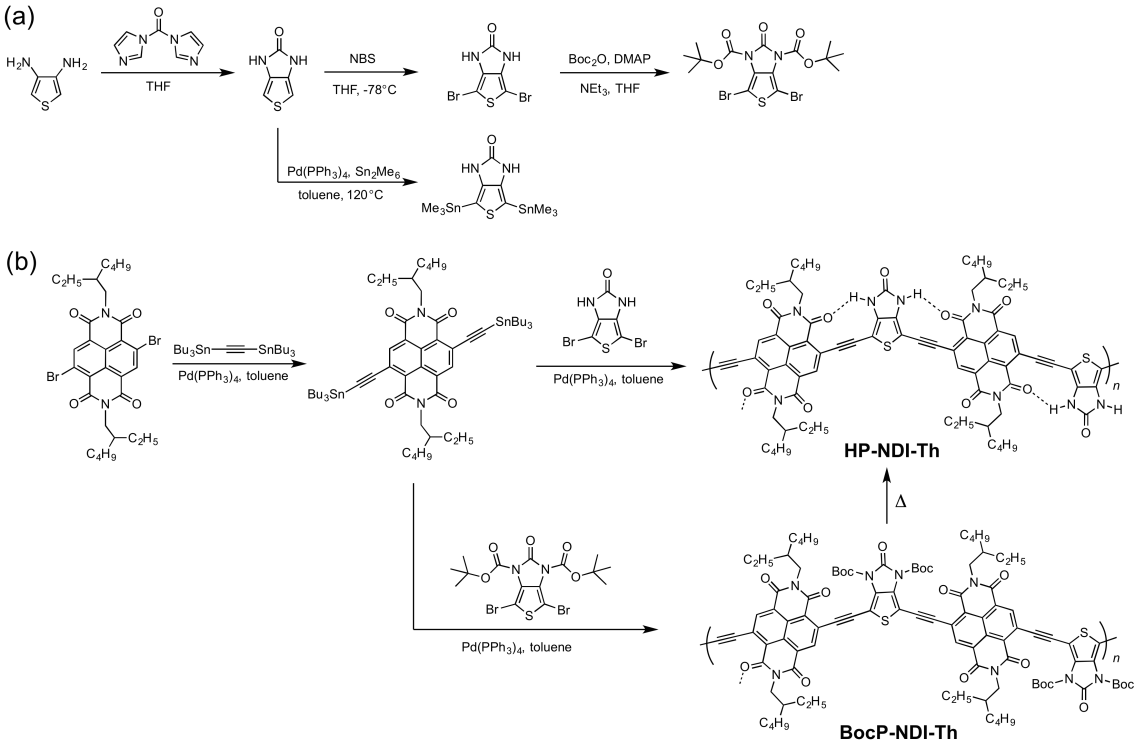

Figure 99. Synthesis routes for (a) thiophene-derived building units with hydrogen bond donating moieties and (b) naphthalene diimide-thiophene copolymers with intramolecular hydrogen bonds.

The coplanar and rigid backbone of **HP-NDI-Th** may lead to strong interchain interactions and poor solubility. This issues can be solved by pre-installing Boc groups on the hydrogen bond donating units to twist the conformation of the resulting polymer **BocP-NDI-Th**. After the solution-phase polymerization, thermal cleavage of Boc groups will afford the desired polymer **HP-NDI-Th** with a coplanar conformation. It is expected that this polymer possesses deep LUMO energy levels and extended π-conjugation length owing to its coplanar conformation.

6.2 B←N Coordinate Bond Bridged Rigid Conjugated Molecules

6.2.1 Summary

As an isoelectronic and isosteric unit of a C–C bond, a B←N coordinate bond was introduced to enforce a rigid and coplanar conformation. *N*-directed electrophilic substitutions were developed to incorporate such intramolecular coordinate bonds into conjugated molecules built upon alternating donor-acceptor constitutions. These molecules enjoyed narrowed band gaps between their frontier molecular orbitals and optical activities in the deep-red and NIR regions. The dynamic nature of B←N coordinate bonds allowed for tunability of their optical band gaps using organic solvents with different Lewis basicity. Strong Lewis basic solvents formed intermolecular coordinate bonds with boron moieties, leading to decreased band gaps.

Moreover, **BN-F** and **BN-Ph** demonstrated robust and reversible multistage redox properties and electrochromism. Combined experimental and theoretical investigations illustrated the structural transformation from a benzenoid consitution into

two distinct quinonoid constitutions during the reduction and oxidation processes, respectively. The intramolecular B←N coordinate bonds extended the charge and spin delocalization, and enforced the rigid molecular structures during the redox processes. We also established a mechanism involving the formation of hyperconjugative interactions between the boron moeities and the conjugated backbones, which further explained the impact from B←N coordinate bonds on the electronic stuctures and spin/charge stablization of these conjugated molecules.

6.2.2 Perspective

The introduction of intramolecular B←N coordinate bonds into conjugated molecules not only rigidify and coplanarize the backbone conformation, but also drastically impact the electronic properties of these molecules, such as decreasing LUMO energy levels. Therefore, this strategy stands out as a promising approach to access novel *n*-type semiconducting materials and acceptors in organic solar cells. To pursue this goal, the following molecules (**Figure 100**) were designed to accommodate multiple intramolecular B←N coordinate bonds and solubilizing groups for the purpose of solution processing. A series of cruciform molecules with solubilizing alkyl chains was proposed (**Figure 100a**). These molecules are expected to possess deep LUMO energy levels and narrowed optical gaps together with enhanced solution processability. Different aryl groups can be incorporated into the ICBZ backbone, which afford tunability over the optical and electronic properties. Several thiazole-derived moieties can be selected as the flanking electron-deficient units and to form intramolecular B←N

coordinate bonds. In the solid state, these flanking units are also expected to form strong intermolecular π-π stacking, therefore promoting intermolecular charge transfer. These molecules can be promising candidates as *n*-type semiconducting materials in FETs.

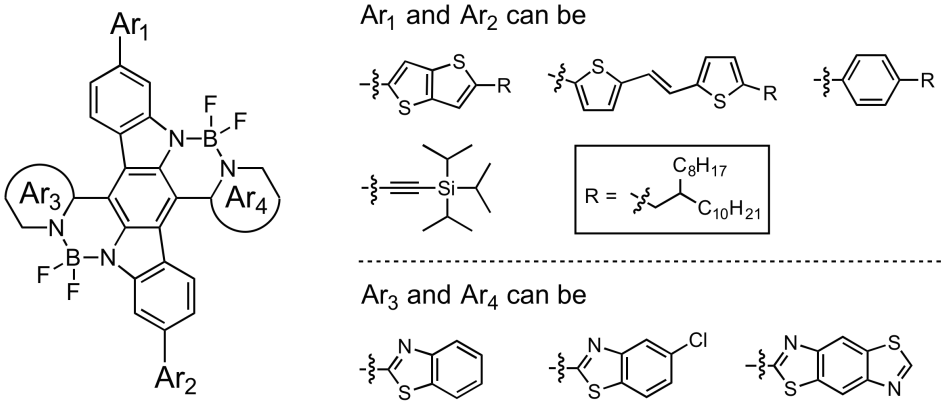

Figure 100. Molecular design of n-type organic semiconducting materials with intramolecular B←N coordinate bonds.

REFERENCES

(1) Huang, H.; Yang, L.; Facchetti, A.; Marks, T. J., Organic and Polymeric Semiconductors Enhanced by Noncovalent Conformational Locks. *Chem. Rev.* **2017,** *117*, 10291-10318.

(2) Zhu, C.; Fang, L., Locking the Coplanar Conformation of π-Conjugated Molecules and Macromolecules Using Dynamic Noncovalent Bonds. *Macromol. Rapid Commun.* **2018,** *39*, 1700241.

(3) Tsuda, A.; Osuka, A., Fully conjugated porphyrin tapes with electronic absorption bands that reach into infrared. *Science* **2001,** *293*, 79-82.

(4) Briseno, A. L.; Mannsfeld, S. C. B.; Shamberger, P. J.; Ohuchi, F. S.; Bao, Z. N.; Jenekhe, S. A.; Xia, Y. N., Self-assembly, molecular packing, and electron transport in n-type polymer semiconductor nanobelts. *Chem. Mater.* **2008,** *20*, 4712-4719.

(5) Samiullah, M.; Moghe, D.; Scherf, U.; Guha, S., Diffusion length of triplet excitons in organic semiconductors. *Phys. Rev. B* **2010,** *82*, 205211.

(6) Venkateshvaran, D.; Nikolka, M.; Sadhanala, A.; Lemaur, V.; Zelazny, M.; Kepa, M.; Hurhangee, M.; Kronemeijer, A. J.; Pecunia, V.; Nasrallah, I.; Romanov, I.; Broch, K.; McCulloch, I.; Emin, D.; Olivier, Y.; Cornil, J.; Beljonne, D.; Sirringhaus, H., Approaching disorder-free transport in high-mobility conjugated polymers. *Nature* **2014,** *515*, 384-388.

(7) Noriega, R.; Rivnay, J.; Vandewal, K.; Koch, F. P. V.; Stingelin, N.; Smith, P.; Toney, M. F.; Salleo, A., A general relationship between disorder, aggregation and charge transport in conjugated polymers. *Nat. Mater.* **2013,** *12*, 1038-1044.

(8) Jackson, N. E.; Kohlstedt, K. L.; Savoie, B. M.; Olvera de la Cruz, M.; Schatz, G. C.; Chen, L. X.; Ratner, M. A., Conformational Order in Aggregates of Conjugated Polymers. *J. Am. Chem. Soc.* **2015,** *137*, 6254-6262.

(9) Wöhrle, T.; Wurzbach, I.; Kirres, J.; Kostidou, A.; Kapernaum, N.; Litterscheidt, J.; Haenle, J. C.; Staffeld, P.; Baro, A.; Giesselmann, F.; Laschat, S., Discotic Liquid Crystals. *Chem. Rev.* **2016,** *116*, 1139-1241.

(10) van Gorp, J. J.; Vekemans, J. A. J. M.; Meijer, E. W., C3-Symmetrical Supramolecular Architectures: Fibers and Organic Gels from Discotic Trisamides and Trisureas. *J. Am. Chem. Soc.* **2002,** *124*, 14759-14769.

(11) Zhu, C.; Mu, A. U.; Lin, Y.-H.; Guo, Z.-H.; Yuan, T.; Wheeler, S. E.; Fang, L., Molecular Coplanarity and Self-Assembly Promoted by Intramolecular Hydrogen Bonds. *Org. Lett.* **2016,** *18*, 6332-6335.

(12) Zang, L.; Che, Y.; Moore, J. S., One-Dimensional Self-Assembly of Planar π-Conjugated Molecules: Adaptable Building Blocks for Organic Nanodevices. *Acc. Chem. Res.* **2008,** *41*, 1596-1608.

(13) Babel, A.; Jenekhe, S. A., High Electron Mobility in Ladder Polymer Field-Effect Transistors. *J. Am. Chem. Soc.* **2003,** *125*, 13656-13657.

(14) Usta, H.; Risko, C.; Wang, Z.; Huang, H.; Deliomeroglu, M. K.; Zhukhovitskiy, A.; Facchetti, A.; Marks, T. J., Design, Synthesis, and Characterization of Ladder-Type Molecules and Polymers. Air-Stable, Solution-Processable n-Channel and Ambipolar Semiconductors for Thin-Film Transistors via Experiment and Theory. *J. Am. Chem. Soc.* **2009,** *131*, 5586-5608.

(15) Durban, M. M.; Kazarinoff, P. D.; Segawa, Y.; Luscombe, C. K., Synthesis and Characterization of Solution-Processable Ladderized n-type Naphthalene Bisimide Copolymers for OFET Applications. *Macromolecules* **2011,** *44*, 4721-4728.

(16) Andersson, L. M.; Hedström, S.; Persson, P., Conformation sensitive charge transport in conjugated polymers. *App. Phys. Lett.* **2013,** *103*, 213303.

(17) Kroon, R.; Lenes, M.; Hummelen, J. C.; Blom, P. W. M.; De Boer, B., Small bandgap polymers for organic solar cells (polymer material development in the last 5 years). *Polym. Rev.* **2008,** *48*, 531-582.

(18) Liu, Y.; Zhang, Z.; Feng, S.; Li, M.; Wu, L.; Hou, R.; Xu, X.; Chen, X.; Bo, Z., Exploiting Noncovalently Conformational Locking as a Design Strategy for High Performance Fused-Ring Electron Acceptor Used in Polymer Solar Cells. *J. Am. Chem. Soc.* **2017,** *139*, 3356-3359.

(19) Qiu, S.; Lu, P.; Liu, X.; Shen, F.; Liu, L.; Ma, Y.; Shen, J., New Ladder-Type Poly(p-phenylene)s Containing Fluorene Unit Exhibiting High Efficient Electroluminescence. *Macromolecules* **2003,** *36*, 9823-9829.

(20) Mishra, A. K.; Graf, M.; Grasse, F.; Jacob, J.; List, E. J. W.; Müllen, K., Blue-Emitting Carbon- and Nitrogen-Bridged Poly(ladder-type tetraphenylene)s. *Chem. Mater.* **2006,** *18*, 2879-2885.

(21) Wu, Y.; Zhang, J.; Fei, Z.; Bo, Z., Spiro-Bridged Ladder-Type Poly(p-phenylene)s: Towards Structurally Perfect Light-Emitting Materials. *J. Am. Chem. Soc.* **2008,** *130*, 7192-7193.

(22) Qian, G.; Wang, Z. Y., Near-infrared organic compounds and emerging applications. *Chem. Asian J.* **2010,** *5*, 1006-1029.

(23) Guo, X.; Kim, F. S.; Seger, M. J.; Jenekhe, S. A.; Watson, M. D., Naphthalene Diimide-Based Polymer Semiconductors: Synthesis, Structure–Property Correlations, and n-Channel and Ambipolar Field-Effect Transistors. *Chem. Mater.* **2012,** *24*, 1434-1442.

(24) Chen, H.; Guo, Y.; Mao, Z.; Yu, G.; Huang, J.; Zhao, Y.; Liu, Y., Naphthalenediimide-Based Copolymers Incorporating Vinyl-Linkages for High-Performance Ambipolar Field-Effect Transistors and Complementary-Like Inverters under Air. *Chem. Mater.* **2013,** *25*, 3589-3596.

(25) Tsai, F.-C.; Chang, C.-C.; Liu, C.-L.; Chen, W.-C.; Jenekhe, S. A., New Thiophene-Linked Conjugated Poly(azomethine)s: Theoretical Electronic Structure, Synthesis, and Properties. *Macromolecules* **2005,** *38*, 1958-1966.

(26) Grein, F., Twist Angles and Rotational Energy Barriers of Biphenyl and Substituted Biphenyls. *J. Phys. Chem. A.* **2002,** *106*, 3823-3827.

(27) Streifel, B. C.; Peart, P. A.; Martínez Hardigree, J. F.; Katz, H. E.; Tovar, J. D., Torsional Influences within Disordered Organic Electronic Materials Based upon Non-Benzenoid 1,6-Methano[10]annulene Rings. *Macromolecules* **2012,** *45*, 7339-7349.

(28) Bjorgaard, J. A.; Köse, M. E., Theoretical Study of Torsional Disorder in Poly(3-alkylthiophene) Single Chains: Intramolecular Charge-Transfer Character and Implications for Photovoltaic Properties. *J. Phys. Chem. A.* **2013,** *117*, 3869-3876.

(29) Bastiansen, O.; Samdal, S., Structure and barrier of internal rotation of biphenyl derivatives in the gaseous state. *J. Mol. Struct.* **1985,** *128*, 115-125.

(30) Zhou, N.; Vegiraju, S.; Yu, X.; Manley, E. F.; Butler, M. R.; Leonardi, M. J.; Guo, P.; Zhao, W.; Hu, Y.; Prabakaran, K.; Chang, R. P. H.; Ratner, M. A.; Chen, L. X.; Facchetti, A.; Chen, M.-C.; Marks, T. J., Diketopyrrolopyrrole (DPP) functionalized tetrathienothiophene (TTA) small molecules for organic thin film transistors and photovoltaic cells. *J. Mater. Chem. C* **2015,** *3*, 8932-8941.

(31) Lee, J.; Rajeeva, B. B.; Yuan, T. Y.; Guo, Z. H.; Lin, Y. H.; Al-Hashimi, M.; Zheng, Y. B.; Fang, L., Thermodynamic synthesis of solution processable ladder polymers. *Chem. Sci.* **2016,** *7*, 881-889.

(32) Zou, Y.; Ji, X.; Cai, J.; Yuan, T.; Stanton, D. J.; Lin, Y.-H.; Naraghi, M.; Fang, L., Synthesis and Solution Processing of a Hydrogen-Bonded Ladder Polymer. *Chem* **2017,** *2*, 139-152.

(33) Lee, J.; Kalin, A. J.; Yuan, T.; Al-Hashimi, M.; Fang, L., Fully conjugated ladder polymers. *Chem. Sci.* **2017,** *8*, 2503-2521.

(34) Yu, L.; Chen, M.; Dalton, L. R., Ladder polymers: recent developments in syntheses, characterization, and potential applications as electronic and optical materials. *Chem. Mater.* **1990,** *2*, 649-659.

(35) Schmidt-Mende, L.; Fechtenkötter, A.; Müllen, K.; Moons, E.; Friend, R. H.; MacKenzie, J. D., Self-Organized Discotic Liquid Crystals for High-Efficiency Organic Photovoltaics. *Science* **2001,** *293*, 1119-1122.

(36) Endres, A. H.; Schaffroth, M.; Paulus, F.; Reiss, H.; Wadepohl, H.; Rominger, F.; Krämer, R.; Bunz, U. H. F., Coronene-Containing N-Heteroarenes: 13 Rings in a Row. *J. Am. Chem. Soc.* **2016,** *138*, 1792-1795.

(37) Zhao, W.; Qian, D.; Zhang, S.; Li, S.; Inganäs, O.; Gao, F.; Hou, J., Fullerene-Free Polymer Solar Cells with over 11% Efficiency and Excellent Thermal Stability. *Adv. Mater.* **2016,** *28*, 4734-4739.

(38) Balakrishnan, K.; Datar, A.; Naddo, T.; Huang, J.; Oitker, R.; Yen, M.; Zhao, J.; Zang, L., Effect of Side-Chain Substituents on Self-Assembly of Perylene Diimide Molecules: Morphology Control. *J. Am. Chem. Soc.* **2006,** *128*, 7390-7398.

(39) Luo, J.; Yan, Q.; Zhou, Y.; Li, T.; Zhu, N.; Bai, C.; Cao, Y.; Wang, J.; Pei, J.; Zhao, D., A photoswitch based on self-assembled single microwire of a phenyleneethynylene macrocycle. *Chem. Commun.* **2010,** *46*, 5725-5727.

(40) Qiao, Y.; Guo, Y.; Yu, C.; Zhang, F.; Xu, W.; Liu, Y.; Zhu, D., Diketopyrrolopyrrole-Containing Quinoidal Small Molecules for High-Performance, Air-Stable, and Solution-Processable n-Channel Organic Field-Effect Transistors. *J. Am. Chem. Soc.* **2012,** *134*, 4084-4087.

(41) Delnoye, D. A. P.; Sijbesma, R. P.; Vekemans, J. A. J. M.; Meijer, E. W., π-Conjugated oligomers and polymers with a self-assembled ladder-like structure. *J. Am. Chem. Soc.* **1996,** *118*, 8717-8718.

(42) Wakamiya, A.; Taniguchi, T.; Yamaguchi, S., Intramolecular B–N Coordination as a Scaffold for Electron-Transporting Materials: Synthesis and Properties of Boryl-Substituted Thienylthiazoles. *Angew. Chem. Int. Ed.* **2006,** *45*, 3170-3173.

(43) Zhu, C.; Guo, Z.-H.; Mu, A. U.; Liu, Y.; Wheeler, S. E.; Fang, L., Low Band Gap Coplanar Conjugated Molecules Featuring Dynamic Intramolecular Lewis Acid–Base Coordination. *J. Org. Chem.* **2016,** *81*, 4347-4352.

(44) Xu, Y. X.; Zhan, T. G.; Zhao, X.; Fang, Q. A.; Jiang, X. K.; Li, Z. T., Oligo(quinoxalineethynylene)s: synthesis, properties, and Ag+-mediated complanation. *Chem. Commun.* **2011,** *47*, 1524-1526.

(45) Coughlin, J. E.; Zhugayevych, A.; Bakus, R. C.; van der Poll, T. S.; Welch, G. C.; Teat, S. J.; Bazan, G. C.; Tretiak, S., A Combined Experimental and Theoretical Study of Conformational Preferences of Molecular Semiconductors. *J. Phys. Chem. C* **2014,** *118*, 15610-15623.

(46) Uddin, M. A.; Lee, T. H.; Xu, S.; Park, S. Y.; Kim, T.; Song, S.; Nguyen, T. L.; Ko, S.-j.; Hwang, S.; Kim, J. Y.; Woo, H. Y., Interplay of Intramolecular Noncovalent Coulomb Interactions for Semicrystalline Photovoltaic Polymers. *Chem. Mater.* **2015,** *27*, 5997-6007.

(47) This class of non-covalent bonds is described as electrostatic interactions, Coulumb interactions and van der Waals interactions in literatures. In this article, we name is by heteroatom non-covalent interactions.

(48) Hu, W.; Zhu, N.; Tang, W.; Zhao, D., Oligo(p-phenyleneethynylene)s with Hydrogen-Bonded Coplanar Conformation. *Org. Lett.* **2008,** *10*, 2669-2672.

(49) Bosman, A. W.; Sijbesma, R. P.; Meijer, E. W., Supramolecular polymers at work. *Mater. Today* **2004,** *7*, 34-39.

(50) Tian, Y.-H.; Kertesz, M., Low-Bandgap Pyrazine Polymers: Ladder-Type Connectivity by Intramolecular S···N(sp2) Interactions and Hydrogen Bonds. *Macromolecules* **2009,** *42*, 2309-2312.

(51) Monkman, A. P.; Pålsson, L.-O.; Higgins, R. W. T.; Wang, C.; Bryce, M. R.; Batsanov, A. S.; Howard, J. A. K., Protonation and Subsequent Intramolecular Hydrogen Bonding as a Method to Control Chain Structure and Tune Luminescence in Heteroatomic Conjugated Polymers. *J. Am. Chem. Soc.* **2002,** *124*, 6049-6055.

(52) Vetrichelvan, M.; Valiyaveettil, S., Intramolecular Hydrogen-Bond-Assisted Planarization of Asymmetrically Functionalized Alternating Phenylene–Pyridinylene Copolymers. *Chem. Eur. J.* **2005,** *11*, 5889-5898.

(53) Jackson, N. E.; Savoie, B. M.; Kohlstedt, K. L.; de la Cruz, M. O.; Schatz, G. C.; Chen, L. X.; Ratner, M. A., Controlling Conformations of Conjugated Polymers and Small Molecules: The Role of Nonbonding Interactions. *J. Am. Chem. Soc.* **2013,** *135*, 10475-10483.

(54) Lei, T.; Xia, X.; Wang, J. Y.; Liu, C. J.; Pei, J., "Conformation locked" strong electron-deficient poly(p-phenylene vinylene) derivatives for ambient-stable n-type field-effect transistors: synthesis, properties, and effects of fluorine substitution position. *J. Am. Chem. Soc.* **2014,** *136*, 2135-2141.

(55) Mukhopadhyay, T.; Puttaraju, B.; Senanayak, S. P.; Sadhanala, A.; Friend, R.; Faber, H. A.; Anthopoulos, T. D.; Salzner, U.; Meyer, A.; Patil, S., Air-Stable n-channel Diketopyrrolopyrrole−Diketopyrrolopyrrole Oligomers for High Performance Ambipolar Organic Transistors. *ACS Appl. Mater. Interfaces.* **2016,** *8*, 25415-25427.

(56) Mueller, C. J.; Gann, E.; Singh, C. R.; Thelakkat, M.; McNeill, C. R., Control of Molecular Orientation in Polydiketopyrrolopyrrole Copolymers via Diffusive Noncovalent Interactions. *Chem. Mater.* **2016,** *28*, 7088-7097.

(57) Zhang, W.; Mao, Z.; Huang, J.; Gao, D.; Yu, G., High-Performance Field-Effect Transistors Fabricated with Donor–Acceptor Copolymers Containing S···O Conformational Locks Supplied by Diethoxydithiophenethenes. *Macromolecules* **2016,** *49*, 6401-6410.

(58) Zhang, W.; Mao, Z.; Zheng, N.; Zou, J.; Wang, L.; Wei, C.; Huang, J.; Gao, D.; Yu, G., Highly planar cross-conjugated alternating polymers with multiple conformational locks: synthesis, characterization and their field-effect properties. *J. Mater. Chem. C* **2016,** *4*, 9266-9275.

(59) Zhang, W.; Mao, Z.; Chen, Z.; Huang, J.; Wei, C.; Gao, D.; Lin, Z.; Li, H.; Wang, L.; Yu, G., Ambipolar tetrafluorodiphenylethene-based donor-acceptor copolymers: synthesis, properties, backbone conformation and fluorine-induced conformational locks. *Polym. Chem.* **2017,** *8*, 879-889.

(60) Wang, C.; Qin, Y.; Sun, Y.; Guan, Y.-S.; Xu, W.; Zhu, D., Thiophene-Diketopyrrolopyrrole-Based Quinoidal Small Molecules as Solution-Processable and Air-Stable Organic Semiconductors: Tuning of the Length and Branching Position of the Alkyl Side Chain toward a High-Performance n-Channel Organic Field-Effect Transistor. *ACS Appl. Mater. Interfaces.* **2015,** *7*, 15978-15987.

(61) Lei, T.; Dou, J. H.; Cao, X. Y.; Wang, J. Y.; Pei, J., Electron-deficient poly(p-phenylene vinylene) provides electron mobility over 1 cm(2) V(-1) s(-1) under ambient conditions. *J. Am. Chem. Soc.* **2013,** *135*, 12168-12171.

(62) Jo, J.; Lee, D., Turn-On Fluorescence Detection of Cyanide in Water: Activation of Latent Fluorophores through Remote Hydrogen Bonds That Mimic Peptide β-Turn Motif. *J. Am. Chem. Soc.* **2009,** *131*, 16283-16291.

(63) Moroni, M.; Le Moigne, J.; Pham, T. A.; Bigot, J. Y., Rigid Rod Conjugated Polymers for Nonlinear Optics. 3. Intramolecular H Bond Effects on Poly(phenyleneethynylene) Chains. *Macromolecules* **1997,** *30*, 1964-1972.

(64) Hu, W.; Yan, Q.; Zhao, D., Oligo(p-phenylene-ethynylene)s with Backbone Conformation Controlled by Competitive Intramolecular Hydrogen Bonds. *Chem. Eur. J.* **2011,** *17*, 7087-7094.

(65) Rao, Y.-L.; Amarne, H.; Zhao, S.-B.; McCormick, T. M.; Martić, S.; Sun, Y.; Wang, R.-Y.; Wang, S., Reversible Intramolecular C−C Bond Formation/Breaking and Color Switching Mediated by a N,C-Chelate in (2-ph-py)BMes2 and (5-BMes2-2-ph-py)BMes2. *J. Am. Chem. Soc.* **2008,** *130*, 12898-12900.

(66) Pais, V. F.; Alcaide, M. M.; López-Rodríguez , R.; Collado, D.; Nájera, F.; Pérez-Inestrosa, E.; Álvarez, E.; Lassaletta, J. M.; Fernández, R.; Ros, A.; Pischel, U., Strongly Emissive and Photostable Four-Coordinate Organoboron N,C Chelates and Their Use in Fluorescence Microscopy. *Chem. Eur. J.* **2015,** *21*, 15369-15376.

(67) Shaikh, A. C.; Ranade, D. S.; Thorat, S.; Maity, A.; Kulkarni, P. P.; Gonnade, R. G.; Munshi, P.; Patil, N. T., Highly emissive organic solids with remarkably broad color tunability based on N,C-chelate, four-coordinate organoborons. *Chem. Commun.* **2015,** *51*, 16115-16118.

(68) Ishida, N.; Moriya, T.; Goya, T.; Murakami, M., Synthesis of Pyridine−Borane Complexes via Electrophilic Aromatic Borylation. *J. Org. Chem.* **2010,** *75*, 8709-8712.

(69) Crossley, D. L.; Cade, I. A.; Clark, E. R.; Escande, A.; Humphries, M. J.; King, S. M.; Vitorica-Yrezabal, I.; Ingleson, M. J.; Turner, M. L., Enhancing electron affinity and tuning band gap in donor–acceptor organic semiconductors by benzothiadiazole directed C–H borylation. *Chem. Sci.* **2015,** *6*, 5144-5151.

(70) Liu, K.; Lalancette, R. A.; Jäkle, F., B–N Lewis Pair Functionalization of Anthracene: Structural Dynamics, Optoelectronic Properties, and O2 Sensitization. *J. Am. Chem. Soc.* **2017,** *139*, 18170-18173.

(71) Grandl, M.; Sun, Y.; Pammer, F., Generation of an N→B Ladder-type Structure by Regioselective Hydroboration of an Alkenyl-Functionalized Quaterpyridine. *Chem. Eur. J.* **2016,** *22*, 3976-3980.

(72) Grandl, M.; Kaese, T.; Krautsieder, A.; Sun, Y.; Pammer, F., Hydroboration as an Efficient Tool for the Preparation of Electronically and Structurally Diverse N→B-Heterocycles. *Chem. Eur. J.* **2016,** *22*, 14373-14382.

(73) Shimogawa, H.; Yoshikawa, O.; Aramaki, Y.; Murata, M.; Wakamiya, A.; Murata, Y., 4,7-Bis[3-(dimesitylboryl)thien-2-yl]benzothiadiazole: Solvato-, Thermo-, and Mechanochromism Based on the Reversible Formation of an Intramolecular B−N Bond. *Chem. Eur. J.* **2017,** *23*, 3784-3791.

(74) Grandl, M.; Rudolf, B.; Sun, Y.; Bechtel, D. F.; Pierik, A. J.; Pammer, F., Intramolecular N→B Coordination as a Stabilizing Scaffold for π-Conjugated Radical Anions with Tunable Redox Potentials. *Organometallics* **2017**.

(75) Dou, C.; Long, X.; Ding, Z.; Xie, Z.; Liu, J.; Wang, L., An Electron-Deficient Building Block Based on the B←N Unit: An Electron Acceptor for All-Polymer Solar Cells. *Angew. Chem. Int. Ed.* **2016,** *55*, 1436-1440.

(76) Long, X.; Gao, Y.; Tian, H.; Dou, C.; Yan, D.; Geng, Y.; Liu, J.; Wang, L., Electron-transporting polymers based on a double B-N bridged bipyridine (BNBP) unit. *Chem. Commun.* **2017,** *53*, 1649-1652.

(77) Fei, Z.; Pattanasattayavong, P.; Han, Y.; Schroeder, B. C.; Yan, F.; Kline, R. J.; Anthopoulos, T. D.; Heeney, M., Influence of Side-Chain Regiochemistry on the Transistor Performance of High-Mobility, All-Donor Polymers. *J. Am. Chem. Soc.* **2014,** *136*, 15154–15157.

(78) Murphy, A. R.; Fréchet, J. M. J.; Chang, P.; Lee, J.; Subramanian, V., Organic thin film transistors from a soluble oligothiophene derivative containing thermally removable solubilizing groups. *J. Am. Chem. Soc.* **2004,** *126*, 1596-1597.

(79) Yang, H.; Shin, T. J.; Yang, L.; Cho, K.; Ryu, C. Y.; Bao, Z., Effect of Mesoscale Crystalline Structure on the Field-Effect Mobility of Regioregular Poly(3-hexyl thiophene) in Thin-Film Transistors. *Adv. Funct. Mater.* **2005,** *15*, 671-676.

(80) Zhang, R.; Li, B.; Iovu, M. C.; Jeffries-El, M.; Sauve, G.; Cooper, J.; Jia, S.; Tristram-Nagle, S.; Smilgies, D. M.; Lambeth, D. N.; McCullough, R. D.; Kowalewski, T., Nanostructure dependence of field-effect mobility in regioregular poly(3-

hexylthiophene) thin film field effect transistors. *J. Am. Chem. Soc.* **2006,** *128*, 3480-3481.

(81) Thompson, B. C.; Kim, B. J.; Kavulak, D. F.; Sivula, K.; Mauldin, C.; Fréchet, J. M. J., Influence of Alkyl Substitution Pattern in Thiophene Copolymers on Composite Fullerene Solar Cell Performance. *Macromolecules* **2007,** *40*, 7425-7428.

(82) Tian, Y.-H.; Kertesz, M., Ladder-Type Polyenazine Based on Intramolecular S···N Interactions: A Theoretical Study of a Small-Bandgap Polymer. *Macromolecules* **2009,** *42*, 6123-6127.

(83) Özen, A. S.; Atilgan, C.; Sonmez, G., Noncovalent Intramolecular Interactions in the Monomers and Oligomers of the Acceptor and Donor Type of Low Band Gap Conducting Polymers. *J. Phys. Chem. C* **2007,** *111*, 16362-16371.

(84) Henson, Z. B.; Welch, G. C.; van der Poll, T.; Bazan, G. C., Pyridalthiadiazole-Based Narrow Band Gap Chromophores. *J. Am. Chem. Soc.* **2012,** *134*, 3766-3779.

(85) Fei, Z.; Boufflet, P.; Wood, S.; Wade, J.; Moriarty, J.; Gann, E.; Ratcliff, E. L.; McNeill, C. R.; Sirringhaus, H.; Kim, J.-S.; Heeney, M., Influence of Backbone Fluorination in Regioregular Poly(3-alkyl-4-fluoro)thiophenes. *J. Am. Chem. Soc.* **2015,** *137*, 6866-6879.

(86) Wolf, J.; Cruciani, F.; El Labban, A.; Beaujuge, P. M., Wide Band-Gap 3,4-Difluorothiophene-Based Polymer with 7% Solar Cell Efficiency: An Alternative to P3HT. *Chem. Mater.* **2015,** *27*, 4184-4187.

(87) Gao, Y.; Deng, Y.; Tian, H.; Zhang, J.; Yan, D.; Geng, Y.; Wang, F., Multifluorination toward High-Mobility Ambipolar and Unipolar n-Type Donor–Acceptor Conjugated Polymers Based on Isoindigo. *Adv. Mater.* **2017,** *29*, 1606217.

(88) Kawashima, K.; Fukuhara, T.; Suda, Y.; Suzuki, Y.; Koganezawa, T.; Yoshida, H.; Ohkita, H.; Osaka, I.; Takimiya, K., Implication of Fluorine Atom on Electronic Properties, Ordering Structures, and Photovoltaic Performance in Naphthobisthiadiazole-Based Semiconducting Polymers. *J. Am. Chem. Soc.* **2016,** *138*, 10265-10275.

(89) Yum, S.; An, T. K.; Wang, X.; Lee, W.; Uddin, M. A.; Kim, Y. J.; Nguyen, T. L.; Xu, S.; Hwang, S.; Park, C. E.; Woo, H. Y., Benzotriazole-Containing Planar Conjugated Polymers with Noncovalent Conformational Locks for Thermally Stable and Efficient Polymer Field-Effect Transistors. *Chem. Mater.* **2014,** *26*, 2147-2154.

(90) Guo, X.; Liao, Q.; Manley, E. F.; Wu, Z.; Wang, Y.; Wang, W.; Yang, T.; Shin, Y.-E.; Cheng, X.; Liang, Y.; Chen, L. X.; Baeg, K.-J.; Marks, T. J.; Guo, X., Materials Design via Optimized Intramolecular Noncovalent Interactions for High-Performance Organic Semiconductors. *Chem. Mater.* **2016,** *28*, 2449-2460.

(91) Huang, H.; Chen, Z.; Ortiz, R. P.; Newman, C.; Usta, H.; Lou, S.; Youn, J.; Noh, Y.-Y.; Baeg, K.-J.; Chen, L. X.; Facchetti, A.; Marks, T., Combining Electron-Neutral Building Blocks with Intramolecular "Conformational Locks" Affords Stable, High-Mobility P- and N-Channel Polymer Semiconductors. *J. Am. Chem. Soc.* **2012,** *134*, 10966-10973.

(92) Lv, L.; Wang, X.; Dong, T.; Wang, X.; Wu, X.; Yang, L.; Huang, H., Significantly improving the efficiency of polymer solar cells through incorporating noncovalent conformational locks. *Mater. Chem. Front.* **2017**.

(93) Huang, H.; Zhou, N.; Ortiz, R. P.; Chen, Z.; Loser, S.; Zhang, S.; Guo, X.; Casado, J.; López Navarrete, J. T.; Yu, X.; Facchetti, A.; Marks, T. J., Alkoxy-Functionalized Thienyl-Vinylene Polymers for Field-Effect Transistors and All-Polymer Solar Cells. *Adv. Funct. Mater.* **2014,** *24*, 2782-2793.

(94) Jaenicke, R.; Böhm, G., The stability of proteins in extreme environments. *Curr. Opin. Struct. Biol.* **1998,** *8*, 738-748.

(95) Gilli, P.; Pretto, L.; Bertolasi, V.; Gilli, G., Predicting Hydrogen-Bond Strengths from Acid−Base Molecular Properties. The pKa Slide Rule: Toward the Solution of a Long-Lasting Problem. *Acc. Chem. Res.* **2009,** *42*, 33-44.

(96) Guo, X.; Quinn, J.; Chen, Z.; Usta, H.; Zheng, Y.; Xia, Y.; Hennek, J. W.; Ortiz, R. P.; Marks, T. J.; Facchetti, A., Dialkoxybithiazole: A New Building Block for Head-to-Head Polymer Semiconductors. *J. Am. Chem. Soc.* **2013,** *135*, 1986-1996.

(97) Sun, Y.; Welch, G. C.; Leong, W. L.; Takacs, C. J.; Bazan, G. C.; Heeger, A. J., Solution-processed small-molecule solar cells with 6.7% efficiency. *Nat. Mater.* **2012,** *11*, 44-48.

(98) Kim, B.-G.; Jeong, E. J.; Chung, J. W.; Seo, S.; Koo, B.; Kim, J., A molecular design principle of lyotropic liquid-crystalline conjugated polymers with directed alignment capability for plastic electronics. *Nat. Mater.* **2013,** *12*, 659-664.

(99) Grozema, F. C.; van Duijnen, P. T.; Berlin, Y. A.; Ratner, M. A.; Siebbeles, L. D. A., Intramolecular charge transport along isolated chains of conjugated polymers: Effect of torsional disorder and polymerization defects. *J. Phys. Chem. B* **2002,** *106*, 7791-7795.

(100) Levitus, M.; Schmieder, K.; Ricks, H.; Shimizu, K. D.; Bunz, U. H. F.; Garcia-Garibay, M. A., Steps To Demarcate the Effects of Chromophore Aggregation and Planarization in Poly(phenyleneethynylene)s. 1. Rotationally Interrupted Conjugation in the Excited States of 1,4-Bis(phenylethynyl)benzene. *J. Am. Chem. Soc.* **2001,** *123*, 4259-4265.

(101) Shu, J.; Dudenko, D.; Esmaeili, M.; Park, J. H.; Puniredd, S. R.; Chang, J. Y.; Breiby, D. W.; Pisula, W.; Hansen, M. R., Coexistence of Helical Morphologies in Columnar Stacks of Star-Shaped Discotic Hydrazones. *J. Am. Chem. Soc.* **2013,** *135*, 11075-11086.

(102) Chen, S.; Slattum, P.; Wang, C.; Zang, L., Self-Assembly of Perylene Imide Molecules into 1D Nanostructures: Methods, Morphologies, and Applications. *Chem. Rev.* **2015,** *115*, 11967-11998.

(103) Huang, C.-F.; Wu, S.-L.; Huang, Y.-F.; Chen, Y.-C.; Chang, S.-T.; Wu, T.-Y.; Wu, K.-Y.; Chuang, W.-T.; Wang, C.-L., Packing Principles for Donor–Acceptor Oligomers from Analysis of Single Crystals. *Chem. Mater.* **2016,** *28*, 5175-5190.

(104) Sutton, C.; Risko, C.; Brédas, J.-L., Noncovalent Intermolecular Interactions in Organic Electronic Materials: Implications for the Molecular Packing vs Electronic Properties of Acenes. *Chem. Mater.* **2016,** *28*, 3-16.

(105) Balakrishnan, K.; Datar, A.; Oitker, R.; Chen, H.; Zuo, J.; Zang, L., Nanobelt Self-Assembly from an Organic n-Type Semiconductor: Propoxyethyl-PTCDI. *J. Am. Chem. Soc.* **2005,** *127*, 10496-10497.

(106) Che, Y.; Datar, A.; Balakrishnan, K.; Zang, L., Ultralong Nanobelts Self-Assembled from an Asymmetric Perylene Tetracarboxylic Diimide. *J. Am. Chem. Soc.* **2007,** *129*, 7234-7235.

(107) Hong, J.-H.; Atta, A. K.; Jung, K.-B.; Kim, S.-B.; Heo, J.; Cho, D.-G., Conformationally Locked Tolans, β-Sheet Structures, and Photophysical Properties. *Org. Lett.* **2015,** *17*, 6222-6225.

(108) Jones, I. M.; Hamilton, A. D., Designed Molecular Switches: Controlling the Conformation of Benzamido-diphenylacetylenes. *Org. Lett.* **2010,** *12*, 3651-3653.

(109) Wakamiya, A.; Yamaguchi, S., Designs of Functional π-Electron Materials based on the Characteristic Features of Boron. *Bull. Chem. Soc. Jpn.* **2015,** *88*, 1357-1377.

(110) Thu, H.-Y.; Yu, W.-Y.; Che, C.-M., Intermolecular Amidation of Unactivated sp2 and sp3 C−H Bonds via Palladium-Catalyzed Cascade C−H Activation/Nitrene Insertion. *J. Am. Chem. Soc.* **2006,** *128*, 9048-9049.

(111) Cary, J. M.; Moore, J. S., Hydrogen Bond-Stabilized Helix Formation of a m-Phenylene Ethynylene Oligomer. *Org. Lett.* **2002,** *4*, 4663-4666.

(112) Wyrembak, P. N.; Hamilton, A. D., Alkyne-Linked 2,2-Disubstituted-indolin-3-one Oligomers as Extended β-Strand Mimetics. *J. Am. Chem. Soc.* **2009,** *131*, 4566-4567.

(113) Miljanić, O. Š.; Han, S.; Holmes, D.; Schaller, G. R.; Vollhardt, K. P. C., Hindered rotation in an "exploded" biphenyl. *Chem. Commun.* **2005**, 2606-2608.

(114) Morozov, A. V.; Kortemme, T.; Tsemekhman, K.; Baker, D., Close agreement between the orientation dependence of hydrogen bonds observed in protein structures and quantum mechanical calculations. *Proc. Natl. Acad. Sci. USA* **2004,** *101*, 6946-6951.

(115) Gellman, S. H.; Dado, G. P.; Liang, G. B.; Adams, B. R., Conformation-directing effects of a single intramolecular amide-amide hydrogen bond: variable-temperature NMR and IR studies on a homologous diamide series. *J. Am. Chem. Soc.* **1991,** *113*, 1164-1173.

(116) K.Lonsdale; H.J.Milledge; K.E.Sayed, Anthraquinone. *Acta Crystallogr.* **1966,** *20*, 1.

(117) Mavridis, A.; Moustakali-Mavridis, I., Diphenylacetylene. *Acta Crystallogr., Sect. B: Struct. Crystallogr. Cryst. Chem.* **1977,** *33*, 3612.

(118) Li, Y.; Chen, Y.; Liu, X.; Wang, Z.; Yang, X.; Tu, Y.; Zhu, X., Controlling Blend Film Morphology by Varying Alkyl Side Chain in Highly Coplanar Donor–Acceptor Copolymers for Photovoltaic Application. *Macromolecules* **2011,** *44*, 6370-6381.

(119) Kastler, M.; Pisula, W.; Wasserfallen, D.; Pakula, T.; Müllen, K., Influence of Alkyl Substituents on the Solution- and Surface-Organization of Hexa-peri-hexabenzocoronenes. *J. Am. Chem. Soc.* **2005,** *127*, 4286-4296.

(120) Qie, L.; Chen, W.; Xiong, X.; Hu, C.; Zou, F.; Hu, P.; Huang, Y., Sulfur-Doped Carbon with Enlarged Interlayer Distance as a High-Performance Anode Material for Sodium-Ion Batteries. *Adv. Sci.* **2015,** *2*.

(121) Zhao, D.; Moore, J. S., Shape-persistent arylene ethynylene macrocycles: syntheses and supramolecular chemistry. *Chem. Commun.* **2003**, 807-818.

(122) Chen, Z.; Lohr, A.; Saha-Möller, C. R.; Würthner, F., Self-assembled π-stacks of functional dyes in solution: structural and thermodynamic features. *Chem. Soc. Rev.* **2009,** *38*, 564-584.

(123) Zhang, C.; Yu, C.; Long, H.; Denman, R. J.; Jin, Y.; Zhang, W., Synthesis of Phenylene Vinylene Macrocycles through Acyclic Diene Metathesis Macrocyclization and Their Aggregation Behavior. *Chem. Eur. J.* **2015,** *21*, 16935-16940.

(124) Chen, Z.; Lohr, A.; Saha-Moller, C. R.; Wurthner, F., Self-assembled small pi-stacks of functional dyes in solution: structural and thermodynamic features. *Chem. Soc. Rev.* **2009,** *38*, 564-584.

(125) Luo, J.; Lei, T.; Wang, L.; Ma, Y.; Cao, Y.; Wang, J.; Pei, J., Highly Fluorescent Rigid Supramolecular Polymeric Nanowires Constructed Through Multiple Hydrogen Bonds. *J. Am. Chem. Soc.* **2009,** *131*, 2076-2077.

(126) Pauling, L.; Corey, R. B.; Branson, H. R., The structure of proteins: Two hydrogen-bonded helical configurations of the polypeptide chain. *Proc. Natl. Acad. Sci. U. S. A.* **1951,** *37*, 205-211.

(127) Voet, D.; Voet, J. G., *Biochemistry*. Wiley, **2010**.

(128) Dado, G. P.; Gellman, S. H., Intramolecular Hydrogen Bonding in Derivatives of .beta.-Alanine and .gamma.-Amino Butyric Acid; Model Studies for the Folding of Unnatural Polypeptide Backbones. *J. Am. Chem. Soc.* **1994,** *116*, 1054-1062.

(129) Kondo, T., The relationship between intramolecular hydrogen bonds and certain physical properties of regioselectively substituted cellulose derivatives. *J. Polym. Sci., Part B: Polym. Phys.* **1997,** *35*, 717-723.

(130) Terao, T.; Maeda, S.; Saika, A., High-resolution solid-state carbon-13 NMR of poly(vinyl alcohol): enhancement of tacticity splitting by intramolecular hydrogen bonds. *Macromolecules* **1983,** *16*, 1535-1538.

(131) Nakahira, T.; Lin, F.; Boon, C. T.; Karato, T.; Annaka, M.; Yoshikuni, M.; Iwabuchi, S., Intramolecular Hydrogen Bonding in Isotactic Poly(methacrylamide)s and Its Implications for Control of Side-Chain Orientation. *Polym. J.* **1997,** *29*, 701.

(132) Hulvat, J. F.; Sofos, M.; Tajima, K.; Stupp, S. I., Self-Assembly and Luminescence of Oligo(p-phenylene vinylene) Amphiphiles. *J. Am. Chem. Soc.* **2005,** *127*, 366-372.

(133) Sato, H.; Murakami, R.; Padermshoke, A.; Hirose, F.; Senda, K.; Noda, I.; Ozaki, Y., Infrared Spectroscopy Studies of CH···O Hydrogen Bondings and Thermal Behavior of Biodegradable Poly(hydroxyalkanoate). *Macromolecules* **2004,** *37*, 7203-7213.

(134) Sato, H.; Ando, Y.; Dybal, J.; Iwata, T.; Noda, I.; Ozaki, Y., Crystal Structures, Thermal Behaviors, and C−H···O═C Hydrogen Bondings of Poly(3-hydroxyvalerate) and Poly(3-hydroxybutyrate) Studied by Infrared Spectroscopy and X-ray Diffraction. *Macromolecules* **2008,** *41*, 4305-4312.

(135) Peng, M.; Xiao, G.; Tang, X.; Zhou, Y., Hydrogen-Bonding Assembly of Rigid-Rod Poly(p-sulfophenylene terephthalamide) and Flexible-Chain Poly(vinyl alcohol) for

Transparent, Strong, and Tough Molecular Composites. *Macromolecules* **2014,** *47*, 8411-8419.

(136) Stals, P. J. M.; Gillissen, M. A. J.; Nicolaÿ, R.; Palmans, A. R. A.; Meijer, E. W., The balance between intramolecular hydrogen bonding, polymer solubility and rigidity in single-chain polymeric nanoparticles. *Polym. Chem.* **2013,** *4*, 2584-2597.

(137) Cheuk, K. K. L.; Lam, J. W. Y.; Chen, J.; Lai, L. M.; Tang, B. Z., Amino Acid-Containing Polyacetylenes: Synthesis, Hydrogen Bonding, Chirality Transcription, and Chain Helicity of Amphiphilic Poly(phenylacetylene)s Carrying l-Leucine Pendants. *Macromolecules* **2003,** *36*, 5947-5959.

(138) Nomura, R.; Nishiura, S.; Tabei, J.; Sanda, F.; Masuda, T., Stereoregular Poly(N-propargylcarbamates) Having Helical Conformation Stabilized by the Intramolecular Hydrogen Bonds. *Macromolecules* **2003,** *36*, 5076-5080.

(139) Okoshi, K.; Sakurai, S.-i.; Ohsawa, S.; Kumaki, J.; Yashima, E., Control of Main-Chain Stiffness of a Helical Poly(phenylacetylene) by Switching On and Off the Intramolecular Hydrogen Bonding through Macromolecular Helicity Inversion. *Angew. Chem. Int. Ed.* **2006,** *45*, 8173-8176.

(140) Ferrand, Y.; Huc, I., Designing Helical Molecular Capsules Based on Folded Aromatic Amide Oligomers. *Acc. Chem. Res.* **2018,** *51*, 970-977.

(141) Karle, I. L.; Gopi, H. N.; Balaram, P., Crystal structure of a hydrophobic 19-residue peptide helix containing three centrally located D amino acids. *Proc. Natl. Acad. Sci. U. S. A.* **2003,** *100*, 13946-13951.

(142) Kooijman, E. E.; Tieleman, D. P.; Testerink, C.; Munnik, T.; Rijkers, D. T. S.; Burger, K. N. J.; de Kruijff, B., An Electrostatic/Hydrogen Bond Switch as the Basis for the Specific Interaction of Phosphatidic Acid with Proteins. *J. Biol. Chem.* **2007,** *282*, 11356-11364.

(143) Nomura, R.; Tabei, J.; Masuda, T., Biomimetic Stabilization of Helical Structure in a Synthetic Polymer by Means of Intramolecular Hydrogen Bonds. *J. Am. Chem. Soc.* **2001,** *123*, 8430-8431.

(144) Yang, K.; He, T.; Chen, X.; Cheng, S. Z. D.; Zhu, Y., Patternable Conjugated Polymers with Latent Hydrogen-Bonding on the Main Chain. *Macromolecules* **2014,** *47*, 8479-8486.

(145) Guo, Z.-H.; Ai, N.; McBroom, C. R.; Yuan, T. Y.; Lin, Y. H.; Roders, M.; Zhu, C. Z.; Ayzner, A. L.; Pei, J.; Fang, L., A side-chain engineering approach to solvent-resistant semiconducting polymer thin films. *Polym. Chem.* **2016,** *7*, 648-655.

(146) McDowell, C.; Bazan, G. C., Organic solar cells processed from green solvents. *Current Opinion in Green and Sustainable Chemistry* **2017,** *5*, 49-54.

(147) Fang, L.; Zhou, Y.; Yao, Y.-X.; Diao, Y.; Lee, W.-Y.; Appleton, A. L.; Allen, R.; Reinspach, J.; Mannsfeld, S. C. B.; Bao, Z., Side-Chain Engineering of Isoindigo-Containing Conjugated Polymers Using Polystyrene for High-Performance Bulk Heterojunction Solar Cells. *Chem. Mater.* **2013,** *25*, 4874-4880.

(148) Iwashita, K.; Katoh, H.; Ohta, Y.; Yokozawa, T., Photodeprotectable N-Alkoxybenzyl Aromatic Polyamides. *Polymers* **2017,** *9*, 246.

(149) Badoux, M.; Drechsler, S.; Pal, S.; Kilbinger, A. F. M., Facile Synthesis of a High Molecular Weight Amphiphilic Aramid–ROMP Block Copolymer. *Macromolecules* **2017,** *50*, 9307-9314.

(150) Smith, Z. C.; Meyer, D. M.; Simon, M. G.; Staii, C.; Shukla, D.; Thomas, S. W., Thiophene-Based Conjugated Polymers with Photolabile Solubilizing Side Chains. *Macromolecules* **2015,** *48*, 959-966.

(151) Cheng, C.-C.; Chu, Y.-L.; Chang, F.-C.; Lee, D.-J.; Yen, Y.-C.; Chen, J.-K.; Chu, C.-W.; Xin, Z., New bioinspired hole injection/transport materials for highly efficient solution-processed phosphorescent organic light-emitting diodes. *Nano Energy* **2015,** *13*, 1-8.

(152) Stansbury, J. W.; Idacavage, M. J., 3D printing with polymers: Challenges among expanding options and opportunities. *Dent. Mater.* **2016,** *32*, 54-64.

(153) Hwang, M. C.; Jang, J.-W.; An, T. K.; Park, C. E.; Kim, Y.-H.; Kwon, S.-K., Synthesis and Characterization of New Thermally Stable Poly(naphthodithiophene)

Derivatives and Applications for High-Performance Organic Thin Film Transistors. *Macromolecules* **2012,** *45*, 4520-4528.

(154) Jiang, Z., GIXSGUI is available for download: http://www.aps.anl.gov/Sectors/Sector8/Operations/GIXSGUI.html.

(155) Gaussian 09 (Gaussian, Inc., Wallingford, CT, USA, 2009).

(156) Ajayaghosh, A., Chemistry of Squaraine-Derived Materials: Near-IR Dyes, Low Band Gap Systems, and Cation Sensors. *Acc. Chem. Res.* **2005,** *38*, 449-459.

(157) Prabhakar, C.; Yesudas, K.; Krishna Chaitanya, G.; Sitha, S.; Bhanuprakash, K.; Rao, V. J., Near-Infrared Absorption in Symmetric Squarylium and Croconate Dyes: A Comparative Study Using Symmetry-Adapted Cluster-Configuration Interaction Methods. *J. Phys. Chem. A.* **2005,** *109*, 8604-8616.

(158) Meier, C.; Gondorf, A.; Lüttjohann, S.; Lorke, A.; Wiggers, H., Silicon nanoparticles: Absorption, emission, and the nature of the electronic bandgap. *J. Appl. Phys.* **2007,** *101*, 103112.

(159) Lu, H.; Mack, J.; Yang, Y.; Shen, Z., Structural modification strategies for the rational design of red/NIR region BODIPYs. *Chem. Soc. Rev.* **2014,** *43*, 4778-4823.

(160) Gierschner, J.; Cornil, J.; Egelhaaf, H. J., Optical Bandgaps of π-Conjugated Organic Materials at the Polymer Limit: Experiment and Theory. *Adv. Mater.* **2007,** *19*, 173-191.

(161) Hwang, B. K.; Gu, Q. M.; Sih, C. J., Enzyme-catalyzed peptide segment condensation using 5(4H)-oxazolones as acyl donors. *J. Am. Chem. Soc.* **1993,** *115*, 7912-7913.

(162) Zhang, Q. T.; Tour, J. M., Alternating Donor/Acceptor Repeat Units in Polythiophenes. Intramolecular Charge Transfer for Reducing Band Gaps in Fully Substituted Conjugated Polymers. *J. Am. Chem. Soc.* **1998,** *120*, 5355-5362.

(163) Müllen, K.; Pisula, W., Donor–Acceptor Polymers. *J. Am. Chem. Soc.* **2015,** *137*, 9503-9505.

(164) Roncali, J., Synthetic Principles for Bandgap Control in Linear π-Conjugated Systems. *Chem. Rev.* **1997,** *97*, 173-206.

(165) Roncali, J., Molecular Engineering of the Band Gap of π-Conjugated Systems: Facing Technological Applications. *Macromol. Rapid Commun.* **2007,** *28*, 1761-1775.

(166) Cheng, Y.-J.; Yang, S.-H.; Hsu, C.-S., Synthesis of Conjugated Polymers for Organic Solar Cell Applications. *Chem. Rev.* **2009,** *109*, 5868-5923.

(167) Chou, C.-M.; Saito, S.; Yamaguchi, S., Heterotriangulenes π-Expanded at Bridging Positions. *Org. Lett.* **2014,** *16*, 2868-2871.

(168) Kim, B.-G.; Ma, X.; Chen, C.; Ie, Y.; Coir, E. W.; Hashemi, H.; Aso, Y.; Green, P. F.; Kieffer, J.; Kim, J., Energy Level Modulation of HOMO, LUMO, and Band-Gap in Conjugated Polymers for Organic Photovoltaic Applications. *Adv. Funct. Mater.* **2013,** *23*, 439-445.

(169) Dou, C.; Ding, Z.; Zhang, Z.; Xie, Z.; Liu, J.; Wang, L., Developing Conjugated Polymers with High Electron Affinity by Replacing a C-C Unit with a B←N Unit. *Angew. Chem. Int. Ed.* **2015,** *54*, 3648-3652.

(170) Ando, S.; Murakami, R.; Nishida, J.-i.; Tada, H.; Inoue, Y.; Tokito, S.; Yamashita, Y., n-Type Organic Field-Effect Transistors with Very High Electron Mobility Based on Thiazole Oligomers with Trifluoromethylphenyl Groups. *J. Am. Chem. Soc.* **2005,** *127*, 14996-14997.

(171) Yan, H.; Chen, Z.; Zheng, Y.; Newman, C.; Quinn, J. R.; Dotz, F.; Kastler, M.; Facchetti, A., A high-mobility electron-transporting polymer for printed transistors. *Nature* **2009,** *457*, 679-686.

(172) Zade, S. S.; Bendikov, M., From Oligomers to Polymer: Convergence in the HOMO−LUMO Gaps of Conjugated Oligomers. *Org. Lett.* **2006,** *8*, 5243-5246.

(173) Jin, X.-H.; Sheberla, D.; Shimon, L. J. W.; Bendikov, M., Highly Coplanar Very Long Oligo(alkylfuran)s: A Conjugated System with Specific Head-To-Head Defect. *J. Am. Chem. Soc.* **2014,** *136*, 2592-2601.

(174) Wang, X.-Y.; Lin, H.-R.; Lei, T.; Yang, D.-C.; Zhuang, F.-D.; Wang, J.-Y.; Yuan, S.-C.; Pei, J., Azaborine Compounds for Organic Field-Effect Transistors: Efficient Synthesis, Remarkable Stability, and BN Dipole Interactions. *Angew. Chem. Int. Ed.* **2013,** *52*, 3117-3120.

(175) Wang, X.-Y.; Zhuang, F.-D.; Wang, R.-B.; Wang, X.-C.; Cao, X.-Y.; Wang, J.-Y.; Pei, J., A Straightforward Strategy toward Large BN-Embedded π-Systems: Synthesis, Structure, and Optoelectronic Properties of Extended BN Heterosuperbenzenes. *J. Am. Chem. Soc.* **2014,** *136*, 3764-3767.

(176) Wang, X.-Y.; Wang, J.-Y.; Pei, J., BN Heterosuperbenzenes: Synthesis and Properties. *Chem. Eur. J.* **2015,** *21*, 3528-3539.

(177) Hudson, Z. M.; Ko, S.-B.; Yamaguchi, S.; Wang, S., Modulating the Photoisomerization of N,C-Chelate Organoboranes with Triplet Acceptors. *Org. Lett.* **2012,** *14*, 5610-5613.

(178) Li, D.; Zhang, H.; Wang, Y., Four-coordinate organoboron compounds for organic light-emitting diodes (OLEDs). *Chem. Soc. Rev.* **2013,** *42*, 8416-8433.

(179) Wakamiya, A.; Murakami, T.; Yamaguchi, S., Benzene-fused BODIPY and fully-fused BODIPY dimer: impacts of the ring-fusing at the b bond in the BODIPY skeleton. *Chem. Sci.* **2013,** *4*, 1002-1007.

(180) Hao, Q.; Yu, S.; Li, S.; Chen, J.; Zeng, Y.; Yu, T.; Yang, G.; Li, Y., Locked Planarity: A Strategy for Tailoring Ladder-Type π-Conjugated Anilido–Pyridine Boron Difluorides. *J. Org. Chem.* **2014,** *79*, 459-464.

(181) Crossley, D. L.; Cid, J.; Curless, L. D.; Turner, M. L.; Ingleson, M. J., Facile Arylation of Four-Coordinate Boron Halides by Borenium Cation Mediated Boro-desilylation and -destannylation. *Organometallics* **2015,** *34*, 5767-5774.

(182) Sengupta, A.; Doshi, A.; Jäkle, F.; Peetz, R. M., Segmented conjugated macromolecules containing silicon and boron: ADMET synthesis and luminescent properties. *J. Polym. Sci., Part A: Polym. Chem.* **2015,** *53*, 1707-1718.

(183) Hermanek, S., Boron-11 NMR spectra of boranes, main-group heteroboranes, and substituted derivatives. Factors influencing chemical shifts of skeletal atoms. *Chem. Rev.* **1992,** *92*, 325-362.

(184) Cui, C.; Bonder, E. M.; Jäkle, F., Weakly Coordinating Amphiphilic Organoborate Block Copolymers. *J. Am. Chem. Soc.* **2010,** *132*, 1810-1812.

(185) Ledoux, A.; Larini, P.; Boisson, C.; Monteil, V.; Raynaud, J.; Lacôte, E., Polyboramines for Hydrogen Release: Polymers Containing Lewis Pairs in their Backbone. *Angew. Chem. Int. Ed.* **2015,** *54*, 15744-15749.

(186) Yesudas, K.; Chaitanya, G. K.; Prabhakar, C.; Bhanuprakash, K.; Rao, V. J., Structure, Bonding, and Lowest Energy Transitions in Unsymmetrical Squaraines: A Computational Study. *J. Phys. Chem. A.* **2006,** *110*, 11717-11729.

(187) Srinivas, K.; Prabhakar, C.; Devi, C. L.; Yesudas, K.; Bhanuprakash, K.; Rao, V. J., Enhanced Diradical Nature in Oxyallyl Derivatives Leads to Near Infra Red Absorption: A Comparative Study of the Squaraine and Croconate Dyes Using Computational Techniques†. *J. Phys. Chem. A.* **2007,** *111*, 3378-3386.

(188) He, B.; Dai, J.; Zherebetskyy, D.; Chen, T. L.; Zhang, B. A.; Teat, S. J.; Zhang, Q.; Wang, L.; Liu, Y., A divergent route to core- and peripherally functionalized diazacoronenes that act as colorimetric and fluorescence proton sensors. *Chem. Sci.* **2015,** *6*, 3180-3186.

(189) Chen, J.; Lalancette, R. A.; Jäkle, F., Chiral Organoborane Lewis Pairs Derived from Pyridylferrocene. *Chem. Eur. J.* **2014,** *20*, 9120-9129.

(190) Steciuk, I.; Durka, K.; Gontarczyk, K.; Dabrowski, M.; Lulinski, S.; Wozniak, K., Nitrogen-boron coordination versus OH[three dots, centered]N hydrogen bonding in pyridoxaboroles - aza analogues of benzoxaboroles. *Dalton Trans.* **2015,** *44*, 16534-16546.

(191) Luisier, N.; Scopelliti, R.; Severin, K., Supramolecular gels based on boronate esters and imidazolyl donors. *Soft Matter* **2016,** *12*, 588-593.

(192) McRae, E. G., Theory of Solvent Effects on Molecular Electronic Spectra. Frequency Shifts. *J. Phys. Chem.* **1957,** *61*, 562-572.

(193) Lee, F. S.; Chu, Z. T.; Warshel, A., Microscopic and semimicroscopic calculations of electrostatic energies in proteins by the POLARIS and ENZYMIX programs. *J. Comput. Chem.* **1993,** *14*, 161-185.

(194) Limantara, L.; Sakamoto, S.; Koyama, Y.; Nagae, H., Effects of Nonpolar and Polar Solvents on the Qx and QY Energies of Bacteriochlorophyll a and Bacteriopheophytin a. *Photochem. Photobiol.* **1997,** *65*, 330-337.

(195) Strong Lewis basic solvents such as DMF, acetonitrile, and pyridine are excluded in this study because they have very large dielectric constants (DMF, 38.3; acetonitrile, 36.6; pyridine, 12.3). Data source: American Chemical Society (https://www.organicdivision.org/orig/organic_solvents.html). Fluride reagents were also excluded because 48 and 50 decomposed in solution upon the addition of TBAF and KF.

(196) Maria, P. C.; Gal, J. F., A Lewis basicity scale for nonprotogenic solvents: enthalpies of complex formation with boron trifluoride in dichloromethane. *J. Phys. Chem.* **1985,** *89*, 1296-1304.

(197) Lämmermann, A.; Szatmári, I.; Fülöp, F.; Kleinpeter, E., Inter- or Intramolecular N···H−O or N−H···O Hydrogen Bonding in 1,3-Amino-α/β-naphthols: An Experimental NMR and Computational Study. *J. Phys. Chem. A.* **2009,** *113*, 6197-6205.

(198) Icli, B.; Sheepwash, E.; Riis-Johannessen, T.; Schenk, K.; Filinchuk, Y.; Scopelliti, R.; Severin, K., Dative boron-nitrogen bonds in structural supramolecular chemistry: multicomponent assembly of prismatic organic cages. *Chem. Sci.* **2011,** *2*, 1719-1721.

(199) Wang, L.; Wang, K.; Zhang, H.; Jiao, C.; Zou, B.; Ye, K.; Zhang, H.; Wang, Y., The facile realization of RGB luminescence based on one yellow emissive four-coordinate organoboron material. *Chem. Commun.* **2015,** *51*, 7701-7704.

(200) Wheeler, S. E., Understanding substituent effects in noncovalent interactions involving aromatic rings. *Acc. Chem. Res.* **2013,** *46*, 1029-1038.

(201) Wheeler, S. E., Local Nature of Substituent Effects in Stacking Interactions. *J. Am. Chem. Soc.* **2011,** *133*, 10262-10274.

(202) Wheeler, S. E.; Bloom, J. W. G., Anion-[small pi] interactions and positive electrostatic potentials of N-heterocycles arise from the positions of the nuclei, not changes in the [small pi]-electron distribution. *Chem. Commun.* **2014,** *50*, 11118-11121.

(203) Yin, X.; Chen, J.; Lalancette, R. A.; Marder, T. B.; Jäkle, F., Highly Electron-Deficient and Air-Stable Conjugated Thienylboranes. *Angew. Chem. Int. Ed.* **2014,** *53*, 9761-9765.

(204) Geese, K.; Prehm, M.; Tschierske, C., Bent-core mesogens with thiophene units. *J. Mater. Chem.* **2010,** *20*, 9658-9665.

(205) Chen, L.; Baumgarten, M.; Guo, X.; Li, M.; Marszalek, T.; Alsewailem, F. D.; Pisula, W.; Mullen, K., Alkyl substituted dithienothieno[2,3-d;2[prime or minute],3[prime or minute]-d[prime or minute]]benzo[1,2-b:4,5-b[prime or minute]]dithiophenes as solution-processable hexathiaheptacenes. *J. Mater. Chem. C* **2014,** *2*, 3625-3630.

(206) Cai, Z.; Lo, W.-Y.; Zheng, T.; Li, L.; Zhang, N.; Hu, Y.; Yu, L., Exceptional Single-Molecule Transport Properties of Ladder-Type Heteroacene Molecular Wires. *J. Am. Chem. Soc.* **2016,** *138*, 10630-10635.

(207) Zheng, T.; Cai, Z.; Ho-Wu, R.; Yau, S. H.; Shaparov, V.; Goodson, T.; Yu, L., Synthesis of Ladder-Type Thienoacenes and Their Electronic and Optical Properties. *J. Am. Chem. Soc.* **2016,** *138*, 868-875.

(208) Jin, Z.; Teo, Y. C.; Teat, S. J.; Xia, Y., Regioselective Synthesis of [3]Naphthylenes and Tuning of Their Antiaromaticity. *J. Am. Chem. Soc.* **2017,** *139*, 15933-15939.

(209) Wang, Y.; Guo, H.; Ling, S.; Arrechea-Marcos, I.; Wang, Y.; López Navarrete, J. T.; Ortiz, R. P.; Guo, X., Ladder-type Heteroarenes: Up to 15 Rings with Five Imide Groups. *Angew. Chem. Int. Ed.* **2017,** *56*, 9924-9929.

(210) Cai, Z.; Awais, M. A.; Zhang, N.; Yu, L., Exploration of Syntheses and Functions of Higher Ladder-type π-Conjugated Heteroacenes. *Chem* **2018,** *4*, 2538-2570.

(211) Cai, Z.; Zhang, N.; Awais, M. A.; Filatov, A. S.; Yu, L., Synthesis of Alternating Donor–Acceptor Ladder-Type Molecules and Investigation of Their Multiple Charge-Transfer Pathways. *Angew. Chem. Int. Ed.* **2018,** *57*, 6442-6448.

(212) Stec, G. J.; Lauchner, A.; Cui, Y.; Nordlander, P.; Halas, N. J., Multicolor Electrochromic Devices Based on Molecular Plasmonics. *ACS Nano* **2017,** *11*, 3254-3261.

(213) Wetzel, C.; Brier, E.; Vogt, A.; Mishra, A.; Mena-Osteritz, E.; Bäuerle, P., Fused Thiophene-Pyrrole-Containing Ring Systems up to a Heterodecacene. *Angew. Chem. Int. Ed.* **2015,** *54*, 12334-12338.

(214) Gu, Y.; Wu, X.; Gopalakrishna, T. Y.; Phan, H.; Wu, J., Graphene-like Molecules with Four Zigzag Edges. *Angew. Chem. Int. Ed.* **2018,** *130*, 6541-6545.

(215) Woodward, A. N.; Kolesar, J. M.; Hall, S. R.; Saleh, N.-A.; Jones, D. S.; Walter, M. G., Thiazolothiazole Fluorophores Exhibiting Strong Fluorescence and Viologen-Like Reversible Electrochromism. *J. Am. Chem. Soc.* **2017,** *139*, 8467-8473.

(216) Guoping, L.; Letian, X.; Weidong, Z.; Kun, Z.; Yousong, D.; Fenglin, L.; Xiaoming, H.; Gang, H., Narrow-Bandgap Chalcogenoviologens for Electrochromism and Visible-Light-Driven Hydrogen Evolution. *Angew. Chem. Int. Ed.* **2018,** *130*, 4897-4901.

(217) Qiu, F.; Zhang, F.; Tang, R.; Fu, Y.; Wang, X.; Han, S.; Zhuang, X.; Feng, X., Triple Boron-Cored Chromophores Bearing Discotic 5,11,17-Triazatrinaphthylene-Based Ligands. *Org. Lett.* **2016,** *18*, 1398-1401.

(218) Wang, X.-Y.; Narita, A.; Feng, X.; Müllen, K., B2N2-Dibenzo[a,e]pentalenes: Effect of the BN Orientation Pattern on Antiaromaticity and Optoelectronic Properties. *J. Am. Chem. Soc.* **2015,** *137*, 7668-7671.

(219) Dou, C.; Liu, J.; Wang, L., Conjugated polymers containing B←N unit as electron acceptors for all-polymer solar cells. *Science China Chemistry* **2017,** *60*, 450-459.

(220) Alahmadi, A. F.; Lalancette, R. A.; Jäkle, F., Highly Luminescent Ladderized Fluorene Copolymers Based on B–N Lewis Pair Functionalization. *Macromol. Rapid Commun.* **2018,** *39*, 1800456.

(221) Yusuf, M.; Liu, K.; Guo, F.; Lalancette, R. A.; Jäkle, F., Luminescent organoboron ladder compounds via directed electrophilic aromatic C–H borylation. *Dalton Trans.* **2016,** *45*, 4580-4587.

(222) Yang, D.-T.; Mellerup, S. K.; Peng, J.-B.; Wang, X.; Li, Q.-S.; Wang, S., Substituent Directed Phototransformations of BN-Heterocycles: Elimination vs Isomerization via Selective B–C Bond Cleavage. *J. Am. Chem. Soc.* **2016,** *138*, 11513-11516.

(223) Hou, Q.; Liu, L.; Mellerup, S. K.; Wang, N.; Peng, T.; Chen, P.; Wang, S., Stimuli-Responsive B/N Lewis Pairs Based on the Modulation of B–N Bond Strength. *Org. Lett.* **2018,** *20*, 6467–6470.

(224) Ji, L.; Edkins, R. M.; Lorbach, A.; Krummenacher, I.; Brückner, C.; Eichhorn, A.; Braunschweig, H.; Engels, B.; Low, P. J.; Marder, T. B., Electron Delocalization in Reduced Forms of 2-(BMes2)pyrene and 2,7-Bis(BMes2)pyrene. *J. Am. Chem. Soc.* **2015,** *137*, 6750-6753.

(225) Ji, L.; Griesbeck, S.; Marder, T. B., Recent developments in and perspectives on three-coordinate boron materials: a bright future. *Chem. Sci.* **2017,** *8*, 846-863.

(226) Su, Y.; Kinjo, R., Boron-containing radical species. *Coord. Chem. Rev.* **2017,** *352*, 346-378.

(227) Luo, D.; Lee, S.; Zheng, B.; Sun, Z.; Zeng, W.; Huang, K.-W.; Furukawa, K.; Kim, D.; Webster, R. D.; Wu, J., Indolo[2,3-b]carbazoles with tunable ground states: how

Clar's aromatic sextet determines the singlet biradical character. *Chem. Sci.* **2014,** *5*, 4944-4952.

(228) Janosik, T.; Rannug, A.; Rannug, U.; Wahlström, N.; Slätt, J.; Bergman, J., Chemistry and Properties of Indolocarbazoles. *Chem. Rev.* **2018,** *118*, 9058-9128.

(229) Maeda, C.; Nagahata, K.; Ema, T., Carbazole-based BODIPYs with ethynyl substituents at the boron center: solid-state excimer fluorescence in the VIS/NIR region. *Org. Biomol. Chem.* **2017,** *15*, 7783-7788.

(230) Maeda, C.; Todaka, T.; Ueda, T.; Ema, T., Synthesis of carbazole-based BODIPY dimers showing red fluorescence in the solid state. *Org. Biomol. Chem.* **2017,** *15*, 9283-9287.

(231) Curiel, D.; Más-Montoya, M.; Usea, L.; Espinosa, A.; Orenes, R. A.; Molina, P., Indolocarbazole-Based Ligands for Ladder-Type Four-Coordinate Boron Complexes. *Org. Lett.* **2012,** *14*, 3360-3363.

(232) Knowles, C. M.; Watt, G. W., The Reduction of Benzoxazoles and Benzothiazole in Liquid Ammonia. *J. Org. Chem.* **1942,** *07*, 56-62.

(233) Loudet, A.; Burgess, K., BODIPY Dyes and Their Derivatives: Syntheses and Spectroscopic Properties. *Chem. Rev.* **2007,** *107*, 4891-4932.

(234) Ulrich, G.; Ziessel, R.; Harriman, A., The Chemistry of Fluorescent Bodipy Dyes: Versatility Unsurpassed. *Angew. Chem. Int. Ed.* **2008,** *47*, 1184-1201.

(235) Mehta, G.; Uma, R., Stereoelectronic Control in Diels−Alder Reaction of Dissymmetric 1,3-Dienes. *Acc. Chem. Res.* **2000,** *33*, 278-286.

(236) Alabugin, I. V.; Gilmore, K. M.; Peterson, P. W., Hyperconjugation. *Wiley Interdisciplinary Reviews: Computational Molecular Science* **2011,** *1*, 109-141.

(237) Ajayakumar, M. R.; Asthana, D.; Mukhopadhyay, P., Core-Modified Naphthalenediimides Generate Persistent Radical Anion and Cation: New Panchromatic NIR Probes. *Org. Lett.* **2012,** *14*, 4822-4825.

(238) Dyer, A. L.; Grenier, C. R. G.; Reynolds, J. R., A Poly(3,4-alkylenedioxythiophene) Electrochromic Variable Optical Attenuator with Near-Infrared Reflectivity Tuned Independently of the Visible Region. *Adv. Funct. Mater.* **2007,** *17*, 1480-1486.

(239) Mortimer, R. J., Electrochromic Materials. *Annu. Rev. Mater. Res.* **2011,** *41*, 241-268.

(240) Yao, C.-J.; Zhong, Y.-W.; Nie, H.-J.; Abruña, H. D.; Yao, J., Near-IR Electrochromism in Electropolymerized Films of a Biscyclometalated Ruthenium Complex Bridged by 1,2,4,5-Tetra(2-pyridyl)benzene. *J. Am. Chem. Soc.* **2011,** *133*, 20720-20723.

(241) Mee, S. P. H.; Lee, V.; Baldwin, J. E., Stille Coupling Made Easier—The Synergic Effect of Copper(I) Salts and the Fluoride Ion. *Angew. Chem. Int. Ed.* **2004,** *43*, 1132-1136.

(242) Jiang, W.; Tang, J.; Ban, X.; Sun, Y.; Duan, L.; Qiu, Y., Ideal Bipolar Host Materials with Bis-benzimidazole Unit for Highly Efficient Solution-Processed Green Electrophosphorescent Devices. *Org. Lett.* **2014,** *16*, 5346-5349.

(243) Hankache, J.; Wenger, O. S., Organic Mixed Valence. *Chem. Rev.* **2011,** *111*, 5138-5178.

(244) Hansmann, M. M.; Melaimi, M.; Bertrand, G., Organic Mixed Valence Compounds Derived from Cyclic (Alkyl)(amino)carbenes. *J. Am. Chem. Soc.* **2018,** *140*, 2206-2213.

(245) Krygowski, T. M.; Cyrański, M. K., Structural Aspects of Aromaticity. *Chem. Rev.* **2001,** *101*, 1385-1420.

(246) Lu, T.; Chen, F., Multiwfn: A multifunctional wavefunction analyzer. *J. Comput. Chem.* **2012,** *33*, 580-592.

(247) Ke, X.-S.; Hong, Y.; Lynch, V. M.; Kim, D.; Sessler, J. L., Metal-Stabilized Quinoidal Dibenzo[g,p]chrysene-Fused Bis-dicarbacorrole System. *J. Am. Chem. Soc.* **2018,** *140*, 7579-7586.

(248) Tomoda, S.; Senju, T., Natural bond orbital analysis of hyperconjugative stabilization effects in the transition states of cyclohexanone reduction with LiAlH4. *Chem. Commun.* **1999**, 423-424.

(249) Kwon, O.; Sevin, F.; McKee, M. L., Density Functional Calculations of Methyllithium, t-Butyllithium, and Phenyllithium Oligomers: Effect of Hyperconjugation on Conformation. *J. Phys. Chem. A.* **2001,** *105*, 913-922.

(250) Alam Sk, M.; Xi, H.-W.; Lim, K. H., Structure, Bonding, and Hyperconjugation of Germaallene: A Theoretical Study. *Organometallics* **2009,** *28*, 3678-3685.